ADAPTIVE ESTIMATION AND CONTROL WITH APPLICATION TO VISION-BASED AUTONOMOUS FORMATION FLIGHT

A Thesis
Presented to
The Academic Faculty

by

Ramachandra Sattigeri

In Partial Fulfillment
of the Requirements for the Degree
Doctor of Philosophy in the
School of Aerospace Engineering

Georgia Institute of Technology
August 2007

ADAPTIVE ESTIMATION AND CONTROL WITH APPLICATION TO VISION-BASED AUTONOMOUS FORMATION FLIGHT

Approved by:

Dr. Anthony J. Calise, Advisor
School of Aerospace Engineering
Georgia Institute of Technology

Dr. Allen Tannenbaum
School of Electrical and Computer Engineering
Georgia Institute of Technology

Dr. Eric N. Johnson
School of Aerospace Engineering
Georgia Institute of Technology

Dr. Byoung Soo Kim
School of Mechanical and Aerospace Engineering
Gyeongsang National University, Gyeongnam, SOUTH KOREA

Dr. J.V.R. Prasad
School of Aerospace Engineering
Georgia Institute of Technology

Date Approved: 15 May 2007

DEDICATION

To my parents

ACKNOWLEDGEMENTS

I would like to thank my advisor Dr. Anthony J. Calise for providing me with the opportunity to study and conduct research at one of the best engineering schools in the country. I thank him for his wisdom, continuous support and persistent encouragement without which this research and thesis would not have been possible. I would also like to thank my committee members: Dr. Byoung Soo Kim (Gyeongsang National University, South Korea), Dr. J.V.R. Prasad, Dr. Eric Johnson and Dr. Allen Tannenbaum (ECE) for taking the time to review my thesis and providing valuable suggestions to improve the quality and presentation of the thesis. In this, I would like to give special thanks to Dr. Byoung Soo Kim whose research and active supervision made possible two chapters of this thesis. Many thanks to Dr. Naira Hovakimyan (Virginia Tech) for inspiring and working tirelessly towards improving the theoretical aspects of our research.

I would like to acknowledge the contributions of Dr. Bong-Jun Yang, Dr. Venkatesh Madyastha, Dr. Suraj Unnikrishnan and Konstantin Volyanskyy with whom I had extensive discussions regarding fundamental theoretical aspects of this research. I would like to thank Matthew Johnson, Dr. Suresh Kannan, Yoko Watanabe and Nimrod Rooz for their help in implementing my algorithms in simulation. I thank them all for the time and effort they spent in advising and helping me. I would also like to thank Johnny Evers of AFRL/MNGN, Eglin Air Force Base, FL, for inspiring my research topic and for his comments and collaborative efforts during the conduct of this research. I would also like to acknowledge the CERT at Georgia Tech and AFOSR for funding this research.

I am grateful for the time spent with other colleagues at Georgia Tech, both past and present, including Dr. Moshe Idan, Dr. Manu Sharma, Dr. Nakwan Kim, Dr. Ali Kutay, Dr. Yoong-Hyun Shin, Dr. Manuj Dhingra, Dr. Cheng Chang, Jongki Moon, Alison Proctor, Jincheol Ha, Seung-Min Oh, Adrian Koller, Allen Wu, Claus Christmann, Girish Chowdhary, Jonathan Muse, Kilsoo Kim and Dongwon Jung. I have enjoyed and learnt from our interactions. I would also like to thank my room-mate Dr. Sriram Rallabhandi for his support and friendship during the last two years of this PhD. I deeply appreciate the friendship of my room-mates over the past few years including Dr. Venkatesh Madyastha, Dr. Suraj Unnikrishnan and Chirag Patel. I enjoyed the time that we spent on things other than research and academics.

Finally, I would like to thank my family particularly my parents, Jayant Sattigeri and Smitha Sattigeri, and my brother Naveen Sattigeri, for their endless support and encouragement. I am also thankful to my uncles Shrikant Sattigeri and Ashok Shahapurkar, and many others who have always prayed and wished for my success.

TABLE OF CONTENTS

LIST OF FIGURES

SUMMARY

The role of vision as an additional sensing mechanism has received a lot of attention in recent years in the context of autonomous flight applications. Modern Unmanned Aerial Vehicles (UAVs) are equipped with vision sensors because of their light-weight, low-cost characteristics and also their ability to provide a rich variety of information of the environment in which the UAVs are navigating in. Vision sensors have also been used as passive sensors to detect and track neighboring aircraft in autonomous formation flight type scenarios.

The problem of vision based autonomous flight is very difficult and challenging since it requires bringing together concepts from image processing and computer vision, target tracking and state estimation, and flight guidance and control. This thesis focuses on the adaptive state estimation, guidance and control problems involved in vision-based formation flight. Specifically, the thesis presents a composite adaptation approach to the partial state estimation of a class of nonlinear systems with unmodeled dynamics. In this approach, a linear time-varying Kalman filter is the nominal state estimator which is augmented by the output of an adaptive neural network (NN) that is trained with two error signals. The benefit of the proposed approach is in its faster and more accurate adaptation to the modeling errors over a conventional approach. In the context of the formation flight problem, the proposed adaptive state estimator is robust to unmodeled leader aircraft acceleration.

The thesis also presents two approaches to the design of adaptive guidance and control (G&C) laws for line-of-sight formation flight. In the first approach, the guidance and autopilot systems are designed separately and then combined together by assuming time-scale separation. The second approach is based on integrating the guidance and autopilot design process. The developed G&C laws using both approaches are adaptive to

unmodeled leader aircraft acceleration and to own aircraft aerodynamic uncertainties. The second approach results in an adaptive integrated guidance and control law that is shown to be capable of achieving higher bandwidth for the combined G&C dynamics compared to the adaptive G&C law based on time-scale separation. Both the approaches assume that true values of the line-of-sight variables are available for feedback.

The thesis also presents theoretical justification based on Lyapunov-like stability analysis for integrating the adaptive state estimation and adaptive G&C designs. Comparison results between the two integrated adaptive estimation guidance and control designs are presented to showcase the best overall design for vision-based formation flight. All the developed designs are validated in nonlinear, 6DOF fixed-wing aircraft simulations. The adaptive state estimation design is integrated with image processing algorithms and validated in real-time simulation software.

Finally, the thesis presents a decentralized coordination strategy for vision-based multiple-aircraft formation control. In this approach, each aircraft in formation regulates range from up to two nearest neighboring aircraft while simultaneously tracking nominal desired trajectories common to all aircraft and avoiding static obstacles.

CHAPTER 1

INTRODUCTION

The problem of vision based autonomous flight is very difficult and challenging since it requires bringing together concepts from image processing and computer vision, target tracking and state estimation, and flight guidance and control. This chapter offers a broad perspective on this problem by providing a survey of the relevant literature and outlines the problems that this thesis is expected to solve.

1.1 Autonomous Formation Flight

The subject of autonomous formation flight has received a tremendous amount of research interest from the aerospace community in the last few years. One motivating factor has been the aerodynamic benefits of close formation flight [1]-[3]. A close or tight formation is one in which the lateral separation between aircraft is less than a wingspan. In this case, aerodynamic coupling is introduced into the formation's dynamics, above and beyond the kinematically induced coupling. By properly positioning the follower aircraft relative to the leader aircraft, the aerodynamic forces created by the leader's vortex can be used to reduce the fuel consumption of the follower aircraft. Thus, alternating aircraft in and out of the lead position can potentially increase the range and endurance of the formation of aircraft.

In particular, control of the leader-follower formation has been investigated extensively. The various approaches include Proportional-Integral-Derivative (PID) control [4], Linear Quadratic Regulator (LQR) based decentralized control [5], and nonlinear, adaptive approaches [6]-[10]. In Refs. [8], [9], baseline constant gain control laws are compared through simulation studies with adaptive control laws that adapt to the uncertainties induced by the aerodynamic interactions. In Ref. [10], a formation flight

autopilot is designed for the follower aircraft using feedforward Neural Networks (NNs), direct Model Reference Adaptive Control and online extremum-seeking command generation to enable bounded output tracking that minimizes the effect of vortex uncertainty. Formation control has also been considered in the context of coordinated motion of a group of vehicles [11]-[14]. Such approaches ignore the aerodynamic coupling in the formation of aircraft and only focus on the coupling of the aircraft kinematics due to their measurement and control strategies. These approaches have been more widely researched in the mobile ground robotics community [15]-[20].

Almost all of the control approaches described in the literature above assume that some measurements of the leader position and velocity, and angular attitudes are available for feedback in the formation controller. Each vehicle in formation is assumed to be equipped with an independent navigation system to acquire its own position and velocity information. To this end, at least one radio communication channel is needed to send leader aircraft data to the follower. In such cases, damage to the receiver or transmitter may be critical to mission success. This then requires methods to be developed that maintain stability of the formation in the face of communication failures or delays. Vehicles with defective sensors are commanded to leave the formation and the formation is reconfigured [21], [22]. Communication delay also affects the formation [23]. Military missions generally prefer low-bandwidth communication, and if possible, radio silence for stealth purposes. As an example, unmanned aerial vehicles (UAVs) operating in close proximity to enemy forces provide real-time information difficult to obtain from other sources, without risk to human pilots. Technology demonstration programs such as Unmanned Combat Aerial Vehicle illustrate the trend toward developments of UAVs that will dominate enemy airspace through maintenance of a continuous presence over the battlefield. Among the weapons employed by these UAVs will be flocks of cooperative miniature or micro autonomous vehicles operating in close proximity to terrain or structures that will gather information on enemy movements and,

under human supervision, seek out, identify, and attack targets of opportunity. They will be expected to maintain a formation while at the same time executing searches in a congested environment. Stealth like operations will also be important, implying the need to maintain autonomy and to minimize communication. Methods enabling the passive detection of another vehicle and maintaining the formation would be thus preferred to methods that depend on two-way data links. One option for passive detection of neighboring vehicles is to use vision sensors onboard the vehicle.

1.2 Vision-based Flight Applications

There has been a lot of work done recently with respect to the use of vision sensors onboard aircraft. One of the most prevalent areas of research is in the development of UAVs that utilize vision in conjunction with other sensors. Vision has been used in trajectory planning or for the precise determination of a relative position [24], [25]. Ref. [26] presented a method for the autonomous landing of a rotorcraft UAV. The corners of a landing area are marked with red beacons whose position can be detected in the camera image through fast image processing algorithms. Then the locations of the corners are used as measurements for an Extended Kalman Filter (EKF) that is designed to estimate the relative position, velocity, attitude and angular rates of the aircraft. Other research has involved replacing a traditional sensor on a UAV with a vision sensor. Ref. [27] described a project in which a small glider flies autonomously relative to a window using only vision for guidance, navigation and control. Ref. [28] presented a method for vision-aided inertial navigation, where the output of a vision sensor and an inertial measurement unit (IMU) are used in tandem to allow autonomous navigation of a rotorcraft UAV without the use of Global Positioning System (GPS) updates. The motivation for this research is the possible loss of GPS links while navigating in urban and indoor areas and the problem of GPS jamming while operating in adversarial environments. Work has also been done in vision-based approaches to

obstacle modeling and obstacle avoidance. Ref. [29] uses Structure-From-Motion techniques fused with inertial measurements to estimate 3D obstacle feature points and an adaptive learning algorithm to estimate the environment from the 3D feature points. Ref. [30] detects obstacle edges as lines in the image instead of obstacle feature points and uses an EKF to construct 3D obstacle models. In the area of ground robotics, vision systems have been used in the formulation of control algorithms that do not require estimates of position and velocity. Such controllers are called image-based visual servo controllers [31, 32] but the extension of such control designs to a six degree-of-freedom (DOF) dynamical system such as an UAV is difficult and very few results are available in this direction.

Refs. [33-36] present vision-based algorithms for application in autonomous formation flight and the closely related field of autonomous aerial refueling. Uniquely identifiable light markers (beacons) are placed on the leader aircraft and on the refueling drogue to facilitate relative navigation. Work on autonomous aerial refueling is motivated by the fact that current UAVs are limited in flight range and endurance and need to be carried onto the battlefield and launched from there. In Ref. [35,36] the beacons are Light Emitting Diodes (LEDs) that emit structured light modulated with a known waveform. The vision sensor onboard the follower aircraft filters the received light energy from the LEDs so that much of the ambient energy is ignored and thus target detection can be achieved in a noisy, ambient environment. Based on the vision data collected, a nonlinear estimation routine is used to estimate the relative position and orientation of the vision sensor relative to the refueling drogue. Refs. [33,34] follow similar logic for the detection of a leader aircraft in formation flight by placing infrared LEDs on the leader aircraft emitting different colored lights. Then a pose estimation algorithm is utilized to estimate the relative leader position and attitude. The need for uniquely identifiable markers comes from the need of exactly associating a known LED 3D position on the target (leader, drogue) with its 2D projection onto the image plane. Refs. [37,38] employ the

method of active contours in the image processing algorithms and Kalman filtering to track the target (leader) aircraft across several image frames. The approach here does not require the use of uniquely identifiable optical markers to be placed all over the target aircraft. Active contours can be regarded as autonomous processes that can conform to various object shapes and motions. Data derived by the use of active contours is used to drive an EKF that produces estimates of range, line-of-sight (LOS) angle and their rates. The next section focuses on the specific problem of vision-based formation flight and the challenges involved in solving this problem.

1.3 Vision-based Formation Flight

The problem of leader-follower formation flight in which the follower aircraft is equipped with only an onboard camera to track the leader aircraft is quite challenging. The follower aircraft is tasked with the objective of maintaining a desired relative position, usually a commanded range and sometimes a relative orientation, from the leader aircraft. This problem requires simultaneous sensor data processing, state estimation and tracking control in the presence of unmodeled disturbances (leader acceleration) and measurement uncertainties. Figure 1 shows the block diagram of the follower aircraft with a vision-in-the-loop flight control system.

Although tracking in the presence of disturbances is a classical control issue, the problem at hand is very difficult and challenging due to the highly uncertain nature of the disturbance. Sensor data processing involves fast converging computer vision algorithms that track the leader aircraft in the presence of background clutter and derive noisy measurements of the leader aircraft's position relative to itself [33-38]. In this respect, the problem of vision-in-the-loop tracking differs from standard tracking problems in that the feedback signal is measured using vision sensors. The feedback signal is extracted by the

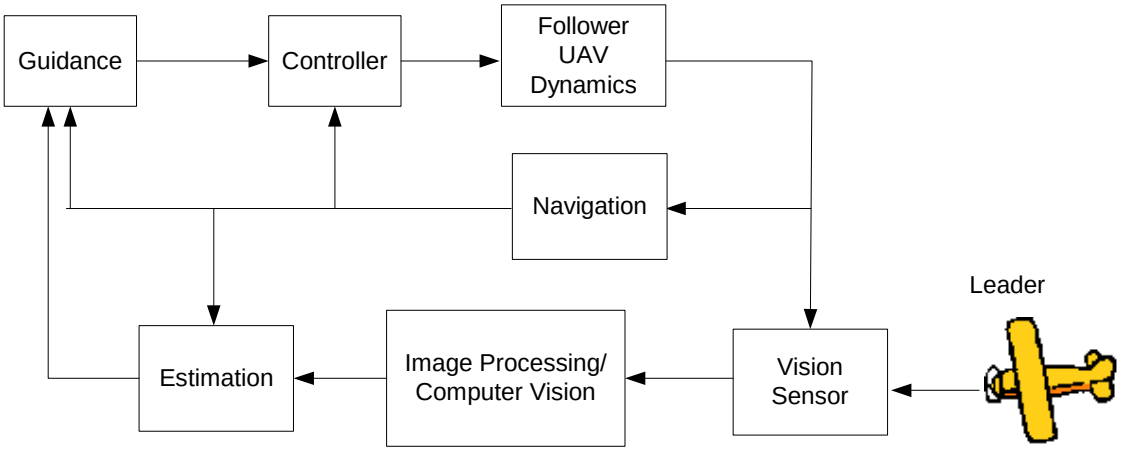

Figure 1. Vision-in-the-loop Flight Control System for Follower Aircraft

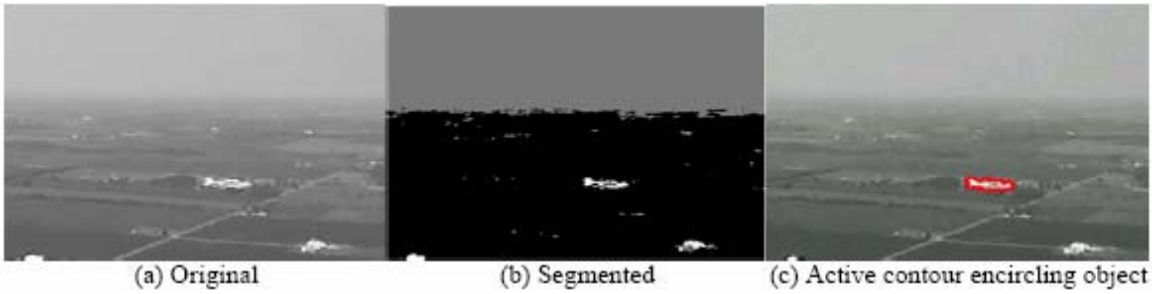

Figure 2. Sample image processing with background clutter [39]

uncertainties arise from sensor noise and the assumptions embedded in the computer vision and reasoning algorithms, for example, the likelihood of various hypotheses. In this thesis, we *do not* focus on the development of the computer vision algorithms and instead rely on the algorithms in [37, 38] and related references. These algorithms use active contours or snakes to track various features of interest over time across several image frames as shown in Figure 2. Active contours have the capability of conforming to

objects in the image plane, making them ideal for segmentation, edge detection, shape modeling and visual tracking. Efforts to make these algorithms robust to background noise and temporary loss of image data due to target occlusion etc. are ongoing [39].

A consequence of using a monocular fixed camera is that the range to the leader or target aircraft is not available as a direct measurement. So the measurements from the image processing algorithms have to be processed by a nonlinear filter, for example, an EKF, that computes estimates of range and other line-of-sight (LOS) variables that are required in the guidance and control algorithms [38]. There are several problems that affect the reliability of the estimation process. First, the measurements are always corrupted by noise. Secondly, the measurements can drop-out, i.e., the measurements are not available at some instants of time due to the target going out of the field-of-view (FOV) of the camera, lack of convergence of the computer vision algorithms, etc. Thirdly, the rate at which the measurements are available for use in the control loop is low (~20 Hz) relative to the required update rate of the control loop (~100 Hz). A critical source for uncertainty in the estimation process is the lack of knowledge of the target motion. Unmodeled target maneuvers lead to bias in the estimates of the range and LOS variables and in some cases can lead to divergence. The estimation process has to be to be made robust to all such uncertainties before being employed in closed-loop control. This is one of the *areas of focus* of this thesis and a comprehensive survey of the literature in this area is provided in Section 1.4.

Assuming reliable estimates are available from an estimator, guidance and control laws that utilize these estimates for control of the range and other LOS variables have to be designed. Most guidance and control laws are designed by assuming the separation principle [72] is valid and the estimation and guidance algorithms can be designed independently. However, the separation principle assumed implicitly in the separate design of the estimation and control algorithms has not been proven to be theoretically valid for general nonlinear systems even though there have been many practical

implementations of control designs based on this assumption. Any stability analysis of the control design has to take into account the lag due to the estimation process. This is another *area of focus* for this thesis and relevant literature survey is provided in Section 1.5. Finally, the intended application of the vision-based formation flight algorithms is for UAVs. The control design for UAVs must take into account modeling inaccuracies due to uncertainties in the aerodynamic parameters, actuator limitations and maneuverability requirements for operating in congested, adversarial environments and tracking maneuvering targets, etc. Conventional approaches to guidance and flight control design employ a time-scale separation argument to justify the separate design of the guidance and autopilot subsystems. The nominal performance of these designs is less than what can be achieved. Therefore, the development of an IGC design is another *area of focus* of this thesis and relevant literature survey is provided in Section 1.6.

1.4 Target Tracking and Adaptive State Estimation

The primary objective of target tracking is to estimate the state trajectories of a moving object. One of the major challenges for target tracking arises from target motion uncertainty. This uncertainty refers to the fact that an accurate dynamic model of the target being tracked is not available to the tracker. In addition, any measurements of the target being tracked are corrupted by noise and time delays. A Kalman filter is usually used in the tracking problem but its performance may be seriously degraded unless the estimation error due to unknown target maneuvers is compensated. Two different approaches have been widely used to handle the case of unknown target maneuvers: model-based adaptive filtering and input estimation.

Various mathematical models of target motion have been developed over the past three decades. The models may: 1) approximate the actually nonrandom target maneuver as a random process of certain properties, or 2) describe typical target trajectories by some representative motion models with properly designed parameters. In the class of

models where the target maneuver is modeled as a random process, the simplest model is the so-called white-noise acceleration model [40]. This model assumes that the target acceleration is an independent, white noise process. The intensity of this white noise can be adjusted online, which is the basis of some adaptive Kalman filter based target tracking algorithms [41-43]. Ref. [41] suggested a method in which the process noise covariance matrix can be estimated from the lagged prediction error covariance. This estimate is then directly utilized to compute the Kalman gain. Ref. [42] suggested techniques to independently estimate both the measurement noise covariance matrix and the process noise covariance matrix. The process noise covariance matrix is estimated by adjusting its value such that the statistics of the filter residual approach those of the optimum Kalman filter. Ref. [43] provided a procedure for adaptive computation of the process noise covariance matrix in an EKF for ballistic target tracking. The second next simplest model for target maneuver is the so-called white noise jerk model [40], which assumes that the derivative of the acceleration of the target is an independent, white noise process. While white noise models have the advantage of simplicity, they rarely capture to a sufficient degree the full range of maneuvers that targets are capable of performing. For many applications, a better approach is to use Markov process models. An example is the Singer model [44] which assumes that the target acceleration is a zero-mean first-order stationary Markov process. This formulation of the target maneuver model suppresses the bias in the state estimates to a certain degree but can exhibit poorer performance than simpler models when there is no target maneuver. More sophisticated approaches include the variable-dimension filter approach [45] in which extra states are introduced in the filter when an input is detected and the interacting multiple model (IMM) technique [46] in which the change of the plant is modeled as a Markovian parameter having a transition probability. Kinematic approaches to modeling the target maneuver include the circular motion model [47] and the more general curvilinear motion model [48]. Another technique has been to incorporate kinematic constraints as a pseudo-

measurement in the Kalman filter [49]. An example of kinematic constraint is that the acceleration vector is always perpendicular to the velocity vector for a constant speed target. A comprehensive survey on target tracking using target models is given in Ref. [50]. In general for model-based approaches to target state estimation, filter performance may not be satisfactory when the target maneuver does not comply with the model, and every approach can be defeated with a suitably chosen target maneuver.

Input estimation is a different approach in which the existence of target maneuvers is first detected and then the magnitude of the target maneuver (input) is estimated [51-55]. Ref. [51] proposes an input estimation technique using the least-squares method to calculate the input magnitude. Ref. [52] derives a recursive input estimation technique based on multiple-model filtering. Ref. [53] proposes a technique in which the unknown target maneuver is modeled as a linear combination of basis functions, which are some elementary functions of time. The coefficients of each basis function are estimated. A comprehensive survey on target tracking techniques using decision-based methods that include input detection and estimation is given in Ref. [54]. Ref. [55] employs a constant velocity filter, an input estimator and a maneuver detector implemented in parallel. This filter structure is similar to that of the two-stage Kalman filter [56] where the target acceleration is treated as a "bias" term. In the two-stage Kalman filter approach, two filters are implemented in parallel. A constant velocity filter represents the "bias-free" filter and the acceleration filter represents the "bias" filter [56].

Neural Network (NN) based adaptive estimation and identification schemes have been proposed to take into account modeling errors in the system and/or the measurement model [57-64]. The universal approximation property of NNs permits treatment of systems with modeling uncertainties that are not linear in the unknown system parameters. Refs. [58-60] propose approaches for augmenting a linear *time invariant* observer with a NN while [61-64] propose approaches for augmenting an EKF with a NN. The approaches in [58,59,61,62] require that the dimension of the system be known

while the approaches in [60,63,64] do not impose this condition allowing the application of the latter approaches to a certain class of systems with unmodeled dynamics. The adaptive nature of these estimators provides robustness to both parametric uncertainty and unmodeled dynamics. The main challenge in these approaches is in the derivation of an error signal to update the NN weights. The observer in [58] introduces a strictly positive real (SPR) filter that enables writing the NN weight update laws in terms of the only available error signal, i.e., the output error or residual. However, the filter needed to satisfy the SPR condition may not always exist, particularly for systems with multiple outputs. The observers in [60,64] do not employ the SPR filter but instead utilize an *error observer* that generates estimates of the state estimation error vector to train the NN.

In Ref. [63] the NN is trained online with the residuals of the EKF and designed to estimate the unknown target maneuvers in real-time and compensate the EKF. Ref. [65] modified the approach in [63] by deriving an additional error signal to train the NN. The modification was motivated by a particular target tracking application where it was difficult to identify a fixed set of NN design parameters that could give reasonable target acceleration estimates for varying target maneuvers. This in turn gave rise to state estimation errors that were larger than expected. The modified approach in [65] is similar in spirit to the composite adaptation approach [66], the combined direct and indirect adaptive control approach [67] and the Q-mod approach to adaptive control [68] that employ additional error signals to improve the performance of the adaptive component in the system. The difference is that the approaches in Ref. [66-68] were applied to adaptive control problems with state feedback, while the approach in [65] is developed for an adaptive state estimation problem. When compared to Ref. [63], the approach in [65] is limited thus far to the state estimation of linear, time-invariant systems. Ref. [69] provides another approach to adaptive state estimation in the presence of bounded disturbances and time-varying parameters. Neural networks are employed to approximate state and control-dependent continuous functional uncertainties and adaptive bounding

technique is used to reject the effect of bounded disturbances. However, SPR-like conditions have to be imposed on the system whose states are being estimated. A linear time-invariant observer is designed to estimate the linear part of the system.

1.5 Integrated Adaptive Estimation and Control

Guidance and control laws that attempt to position the follower aircraft at a desired location relative to the leader aircraft in order to obtain the benefits of drag reduction have been described in Section 1.1 [1-10]. In comparison, there have been very few attempts to formulate guidance and control laws for vision-based formation flight or for formation flight not requiring continuous data communication between vehicles in formation. Ref. [13] formulates guidance laws for multiple-vehicle formation flight using LOS information only. The LOS information set includes the LOS angle, range and their respective rates assumed to be available from vision sensors or radar. The formulation is valid for motions restricted to the two dimensional horizontal plane and issues of leader maneuvers are not considered in the formulation. Ref. [12] proposes an adaptive guidance solution for multiple-vehicle formation flight. Range and LOS angle information is assumed to be available from vision sensors and the ability of follower aircraft to maintain range from one or more neighboring vehicles is demonstrated. The guidance solution enables adaptation to the maneuvers of the neighboring vehicles. However, this solution also assumes that motion is restricted to the two-dimensional horizontal plane and that velocity and heading are achieved with a simple first-order lag. Ref. [14] proposed the concept of leaderless formations using the problem formulation in [12]. The approach was motivated by the need to increase the robustness of the formation to failure in the leader or more vehicles. Ref. [33] proposes speed and heading command based guidance laws that are formed by the action of PID controllers on position errors in the follower aircraft wind frame. The position errors refer to the error of the follower aircraft's current position with respect to a desired position from the leader aircraft. The

position errors are also augmented with the errors in the speed and heading of the follower aircraft with respect to the leader for better guidance law performance. However, this implies that the leader aircraft speed and heading should be available to the follower aircraft, which is assumed to be through radio communication. Issues of leader aircraft maneuvers are not considered. Ref. [70] proposed an adaptive guidance solution for regulating the range from a maneuvering leader aircraft in a 6 DOF leader-follower formation. The adaptive guidance solution was integrated with an adaptive autopilot and simulation results showed range tracking performance robust to leader aircraft maneuvers. However, this approach assumed that the true values of range and LOS angles of azimuth and elevation are available.

A drawback of the preceding guidance laws is that they are predicated on a deterministic perfect-information scenario. That is, the guidance laws are designed by assuming that the variables required for control of formation flight, for e.g., range, range-rate, LOS rates etc, are available instantaneously and are not distorted by noise. However, this assumption ignores the fact that the above variables are obtained from a nonlinear filter like an EKF, which is driven by noisy measurements. Similar assumptions are made in the derivation of the classical missile guidance laws of Proportional Navigation (PN) and Augmented Proportional Navigation (APN) [71]. The practice of integrating a perfect information guidance law with a separately designed estimator in effect assumes that the separation principle [72] is valid. However the separation principle has not been proven valid for a nonlinear system. This implies the need for an integrated design of the estimation and guidance laws [73, 74]. Ref. [74] invokes a General Separation Theorem (GST) that states that the estimator can be designed separately from the guidance law, yet when designing the guidance law the estimator has to be considered.

Ref. [64] provides an example of an integrated estimation and control law design applied to missile target tracking, obstacle avoidance and formation flight problems. The estimator is an EKF augmented with a NN to compensate for the effect of target

maneuvers. When integrating the estimator with the control law, the control law is implemented with the estimates of the states. Stability (ultimate boundedness of the system errors) of the integrated system is shown by imposing a linear-growth type condition on the control law as a function of the states. Other examples of integrated, adaptive estimation and controller design are given in refs. [75-80]. Ref. [75] constructs an adaptive NN observer providing state estimates to an adaptive NN controller for robotic type systems. The NN in the observer approximates the state-dependent uncertainty and the NN in the controller approximates a nonlinear function of the tracking error, states of the system and the state estimation error. Lyapunov-like stability analysis is used to show uniform ultimate boundedness (UUB) of the system errors. Ref. [76] presents an approach in which an adaptive NN observer is coupled with a backstepping controller for nonlinear systems with uncertainties that are functions of the output of the system. Similar adaptive observer based controller design approaches are presented in Ref. [77-79] for full relative degree systems. Ref. [80] presents an approach in which the state observer based linear control law is augmented with the error observer based adaptive observer [60], such that adaptive estimation and adaptive control is achieved through a single NN. The presented approach is applicable to nonlinear systems with known nominal linear models and with both matched and unmatched uncertainties. In Refs. [75-80], a linear time-invariant observer is designed for the linear part of the system. Another set of interesting results is found in Refs. [99-101] where the guidance laws are designed to enhance the accuracy of the estimation process. In these applications, range is not available as a measurement and the range and range-rate have to be estimated by using only passive measurements. Such problems are well known in literature as bearings-only target tracking problems [102]. There have been several approaches for the design of a guidance law that enhances the accuracy of the estimation process. The nominal guidance laws in [99] and [100] are augmented by a term that induces oscillations in the LOS angle and by a term proportional to the rate of the trace of

the Fisher information matrix respectively. In Ref. [101], the guidance law is obtained by maximizing the inverse of the error covariance matrix of the EKF.

1.6 Integrated Guidance and Control Design

Conventional approaches to guidance and flight control design employ a time-scale separation argument to justify the separate design of the guidance and autopilot subsystems. Once designed, the two subsystems are integrated together and tuned till the performance objectives are satisfied. While this approach to design has been successfully implemented on many flight vehicle systems, the design usually results in an overall performance that is less than what can be achieved. Secondly, in high performance applications like intercepting a highly maneuvering target, or maintaining range from a maneuvering leader aircraft in a formation, the time-scale separation argument does not hold. In such cases the guidance subsystem can drive the autopilot and the overall system unstable with commands that cannot be achieved by the autopilot.

Integrated approaches to guidance and control design have been indicated in literature as a way to overcome the shortcomings of the conventional approach. Its been stated that an integrated guidance and control (IGC) formulation can directly compensate for the effect of autopilot lag and improve missile intercept performance [81,82]. An integrated approach also helps avoid the iterative procedure involved in tuning the guidance and autopilot subsystems, if designed separately. The integrated design is also less susceptible to saturation and stability problems. Feedback linearization of the relative cross-range and altitude to target and the roll-angle is employed in Refs. [81,82] for the IGC formulation. Sliding mode control theory is employed in Ref. [83] for the IGC formulation. In Ref. [84], a single-plane linear IGC problem formulation is considered and a game-theoretic control synthesis approach is utilized. In Ref. [85], the IGC problem is formulated as a finite-time horizon nonlinear disturbance attenuation problem. An approximate solution approach to the above problem is developed that is referred to as

the state-dependent Riccati differential (difference) equation (SDRDE) technique. Monte Carlo simulation results using this technique showed that it performed favorably compared to a benchmark guidance and control system and resulted in much smaller overall system time constants. The SDRDE technique however is computationally intensive owing to the need to solve Riccati difference equations online at each sample instant. An adaptive backstepping based approach to IGC design is presented in [86]. The missile dynamics have to be written in the strict-feedback form [87] in order to use the backstepping approach. The advantage is that the backstepping approach can directly address plants with unmatched uncertainties. Adaptation is included to provide robustness to parametric uncertainty in the missile dynamics. In Ref. [88], the flight control system design is done via a conventional inner and outer-loop design approach. The linear compensator gains in the inner and outer-loops are chosen such that the combined error dynamics of both the loops are asymptotically stable in the absence of modeling uncertainties, and thus mitigate inner and outer-loop interaction. Adaptation is included in both loops to address any modeling uncertainties. Pseudo-Control Hedging [89] is used in the inner-loop to prevent adaptation to actuator saturation and dynamics. Hedging is also used in the outer-loop to prevent adaptation to inner-loop dynamics. An adaptive approach to IGC design for LOS based formation flight using a combination of output feedback inversion and backstepping techniques is given in Ref. [90]. It is shown that an IGC design employing only feedback inversion results in a deficiency in turn coordination. So feedback inversion is combined with backstepping, where the backstepping design is employed only to address the portion of the dynamics wherein the inverting solution is deficient. NN based adaptation is included to address any modeling uncertainties that arise in the process of dynamic inversion due to parametric uncertainty in the aircraft aerodynamic data and ignored nonlinearities.

1.7 Multiple-Aircraft Formation Control

Another objective of this thesis is to present an approach to multiple-aircraft formation control with the assumption that there is little to no communication between the aircraft. The focus of this research is to consider formation control only in the context of coordinated group motion as in [11] and to ignore the aerodynamic interaction effects due to closed-coupled formation flight as in Refs. [1]-[10]. Although imperfectly understood, flocking behavior of birds, schooling behavior of fish, and even studies of swarming insects have provided inspiration for concepts of coordinated multi-vehicle operation [117]. Existing works on coordinated group motion include a distributed behavioral approach to synthesizing the flocking motion of boids [113] (bird and fish-like objects). This approach assumes a flock is the result of the interaction between the behaviors of individual boids (used here to refer to individual autonomous agents operating in a coordinated manner). It was similarly shown in Ref. [118] that coordinated multi-robot motion could be constructed by using a small *basis* set of behaviors. A control-theoretic approach to formation control is given in [15]. The control laws derived using input-output feedback linearization theory, allow each follower vehicle in the formation to regulate range and relative orientation with respect to one leader vehicle, or range with respect to two leader vehicles, or range with respect to a leader vehicle while maintaining safe distance from obstacles. Switching between the control laws leads to changes in formation shape. Related work on formation control includes assignment of feasible formations [119] and moving into formation [16].

Standard approaches for formation control could be categorized into the leader-follower, behavior-based and the virtual structure approaches. In leader-follower based approach, one vehicle is designated as a leader and the remaining vehicles as followers [12], [14]. The followers track the range from the leader and other followers to desired values. The leader sets a nominal trajectory for the formation to follow and may cooperate with the followers in regulating range. In the virtual structure approach, the

entire formation is treated as a single entity [120], [121]. Desired motion is assigned to this single entity, the virtual structure, which traces out trajectories for each member in the formation to track. In behavior-based approaches, several desired behaviors are prescribed for each vehicle and the final control is derived from a weighting of the relative importance of each behavior [17], [118]. Since in the leader-follower and virtual structure based approaches, coordination is with respect to a central agent, the formation controls lack robustness. Behavior-based approaches are decentralized and are significantly easier to implement. However, these are difficult to analyze mathematically and formation convergence to desired configurations is not guaranteed.

In Refs. [12], [13], adaptive guidance strategies are formulated that enable vehicles to fly in formation and avoid static obstacles with the restriction of no communication between the vehicles. True values of range and LOS angles to the neighboring vehicles are assumed to be available by means of a passive vision sensor. The lack of relative velocity vector information with respect to neighboring vehicles is treated as modeling uncertainty, whose effect on LOS range regulation is canceled by the output of an adaptive NN that is updated online. Ref. [13] also proposes a coordination scheme that does not depend on a *unique* leader. The coordination scheme results in so called *leaderless* formations, in which each vehicle regulates range to up to two nearest vehicles while simultaneously navigating towards a common set of waypoints and avoiding obstacles. In this thesis, the approaches in [12], [13] are modified by assuming that the subtended angle is a measurement in place of the range. The measurements are also assumed to be corrupted with zero-mean white noise. Relative velocity with respect to neighboring vehicles is estimated by implementing a Kalman filter augmented with an adaptive NN as the target state estimator.

1.8 Why Neural-Network based Adaptation?

The sections preceding this one have referred to NN based adaptive control and adaptive estimation approaches in the literature without explaining why NNs are preferred over other adaptive mechanisms. This section discusses very briefly the motivation for NN based adaptive approaches. Traditional approaches of dealing with uncertainties in control system design are based on robust control techniques. Uncertainties include parametric uncertainty and unmodeled dynamics. The approach in robust control is to design a feedback control law that guarantees stability and performance specifications for all uncertainties within given bounds. The design process requires both a nominal model and some characterization of the uncertainties. An alternate way of dealing with uncertainties is to use adaptive control. In adaptive control, a linear/nonlinear parameterization of the uncertainty is assumed without assuming that the bounds on the uncertainty are known. Controller parameters are updated online using available system signals to approximate the uncertainty.

Conventional adaptive control methods have been most successful in applications where the uncertainty is a linear parameterization of known basis functions. The difficulty lies in finding the correct parameterization to use, since this is problem dependent. In many cases a linear parameterization of the uncertainty is simply not known. Neural network (NN) based adaptive control methods offer the potential to overcome the drawbacks of conventional adaptive control methods. NNs and other nonlinear approximator structures like fuzzy systems are universal approximators [92], [105-107], [123-125]. That is, they have the ability to approximate a continuous function to an arbitrary degree of accuracy over a compact set. The practical benefits of applying NNs are more significant. The burden of finding the right parameterization for the uncertainty function is left to the NN. Reduction in function approximation error can be obtained by a linear increase in the size of the NN. The size of the NN is given by the number of tunable parameters, i.e., the weights and biases of the NN. The NN parameters

are updated online by typically applying gradient descent algorithms on the tracking error, which is a filtered difference between the output of the NN and the unknown function to be approximated by the NN.

1.9 Thesis Objectives and Outline

The main goal of the thesis is to develop an adaptive and integrated estimation, guidance and control design that can be applied to the problem of vision-based formation flight. The approach in this thesis is to treat the estimation design problem and guidance and control design problem separately and provide a theoretical foundation to integrate the two designs. Towards this end, Chapter 3 presents an approach to adaptive state estimation and Chapters 4 and 5 present two different approaches to adaptive guidance and control design. Integration of the adaptive estimation and adaptive guidance and control designs is presented in Chapter 6.

Chapter 2 lists the mathematical definitions and theorems from Lyapunov stability theory and neural network (NN) approximation theory. The idea is to summarize the basic mathematical results that are important to the development and presentation of the main ideas in the thesis.

Chapter 3 presents an approach for augmenting a linear, time-varying Kalman filter with an adaptive NN for the partial state estimation of a class of nonlinear systems in the presence of unknown system inputs. Lyapunov-like stability analysis shows uniform ultimate boundedness of all the error signals in the system. Simulation results with application of the approach to a leader aircraft tracking problem in an autonomous formation flight scenario illustrate the effectiveness of the approach. The approach is also validated in software-in-the-loop simulations by integrating the adaptive estimator with image processing, guidance and flight control algorithms.

Chapter 4 presents an adaptive approach to the guidance and control design for a follower aircraft maintaining range from a maneuvering leader aircraft. This approach

assumes a time-scale separation between the guidance related variables (slow LOS kinematics) and the autopilot related variables (fast attitude dynamics). It is also assumed that the true values of range, the line-of-sight (LOS) angles, and their rates are available for feedback. NN based adaptation is included in the guidance law design to compensate for the unknown leader aircraft maneuvers and neglected LOS kinematics. The autopilot includes NN based adaptation to compensate for uncertainty in the aircraft dynamics. Simulation results using a nonlinear 6DOF fixed-wing aircraft simulation model are presented for different leader maneuvers.

Chapter 5 presents an integrated guidance and control (IGC) design for LOS formation flight using a combination of adaptive output feedback and backstepping techniques. This approach also assumes the true values of range, LOS angles, and their rates are available for feedback. Adaptive NNs are trained online with available measurements to compensate for unmodeled nonlinearities in the design process. These include uncertainties due to unknown leader aircraft acceleration, and the modeling error due to parametric uncertainties in the aircraft aerodynamic derivatives. Simulation results using a nonlinear 6DOF simulation model are presented to illustrate the efficacy of the approach by comparing the performance with the time-scale separation based guidance and control (TSSGC) design presented in Chapter 4.

Chapter 6 presents a method to integrate adaptive estimation and adaptive control designs for a class of nonlinear systems. The method is based on Lyapunov-like stability analysis of all the errors in the integrated closed-loop system. The analysis method is then applied to integrate the adaptive estimator solution in Chapter 3 with the adaptive guidance and control solutions presented in Chapters 4 and 5 for enabling vision-based formation flight. Simulation results are presented using a nonlinear 6DOF fixed-wing UAV simulation model to illustrate the feasibility and efficacy of the approach. Comparison results between the integrated adaptive estimation and TSSGC law, and the

integrated adaptive estimation and IGC law are also presented to show case the best overall design for enabling vision-based formation flight.

Chapter 7 presents a conceptual approach to multiple-aircraft formation control. It is assumed that the aircraft utilize passive vision sensors to track neighboring aircraft and that there is little to no communication between the aircraft. Formation controllers are designed that allow each vehicle in formation to maintain separation and relative orientation with respect to neighboring vehicles, while avoiding static obstacles. These controllers are integrated with adaptive NN augmented Kalman filters that generate estimates of the position and velocity of the neighboring aircraft. A multi-aircraft coordination scheme is proposed that does not depend on a unique leader in the formation. The resulting formations are called leaderless formations. Each aircraft in the formation maintains desired range to up to two nearest vehicles while simultaneously navigating towards a common set of waypoints and avoiding obstacles. Illustrative simulation results for a set of desired formation trajectories are shown.

Chapter 8 summarizes the thesis contributions, the conclusions drawn from the study, and recommends future work based on the research in the thesis.

Throughout the manuscript bold symbols are introduced for vectors, capital letters for matrices, small letters for scalars, $\|\cdot\|$ is the Euclidean 2-norm, $\|\cdot\|_F$ is the Frobenius norm of a matrix, that is, $\|A\|_F = \sqrt{\mathrm{tr}\left(AA^T\right)}$.

CHAPTER 2

MATHEMATICAL PRELIMINARIES

This chapter presents mathematical results and tools required in the development of the adaptive state estimation and control algorithms in the subsequent chapters.

Equation Chapter 2 Section 2

2.1 Lyapunov Stability Theory for Nonautonomous Systems

Consider the nonlinear dynamical system

$$\dot{\boldsymbol{x}} = \boldsymbol{f}(t, \boldsymbol{x}), \;\; \boldsymbol{x}(t_0) = \boldsymbol{x}_0 \tag{2.1}$$

where $\boldsymbol{f} : [0,\infty) \text{ x } D \rightarrow R^n$ is continuously differentiable, $D = \left\{ \boldsymbol{x} \in R^n \mid \|\boldsymbol{x}\| < r \right\}$, and the Jacobian matrix $\left[\frac{\partial \boldsymbol{f}}{\partial \boldsymbol{x}} \right]$ is bounded and Lipschitz on D, uniformly in t.

Exponential Stability Results

Definition 1 [104]: Let $\boldsymbol{x} = 0$ be an equilibrium point for the nonlinear system in (2.1). The equilibrium point $\boldsymbol{x} = 0$ is exponentially stable (ES) if

$$\|\boldsymbol{x}(t)\| \le k \|\boldsymbol{x}(t_0)\| e^{-\lambda(t-t_0)}, \;\; k > 0, \;\; \lambda > 0, \;\; \forall t \ge t_0 \ge 0, \;\; \forall \|\boldsymbol{x}(t_0)\| < c \tag{2.2}$$

where c is a positive constant independent of t_0; and is globally exponentially stable (GES) if this condition is satisfied for any initial state.

Theorem 1 [104]: Let $\boldsymbol{x} = 0$ be an equilibrium point for the nonlinear system in (2.1) where $\boldsymbol{f} : [0,\infty) \text{ x } D \rightarrow R^n$ is continuously differentiable, $D = \left\{ \boldsymbol{x} \in R^n \mid \|\boldsymbol{x}\| < r \right\}$, and the Jacobian matrix $\left[\frac{\partial \boldsymbol{f}}{\partial \boldsymbol{x}} \right]$ is bounded and Lipschitz on D, uniformly in t. Let k, λ and

r_0 be positive constants with $r_0 < \frac{r}{k}$. Let $D_0 = \{\boldsymbol{x} \in R^n \mid \|\boldsymbol{x}\| < r_0\}$. Assume that the trajectory of the system satisfies

$$\|\boldsymbol{x}(t)\| \le k\|\boldsymbol{x}(t_0)\| e^{-\lambda(t-t_0)}, \ \forall t \ge t_0 \ge 0, \ \ \forall \|\boldsymbol{x}(t_0)\| < c \tag{2.3}$$

Then there is a continuously differentiable function $V : [0,\infty)$ x $D_0 \ \rightarrow R$ that satisfies the inequalities

$$\begin{aligned} & c_1\|\boldsymbol{x}\|^2 \le V(t,\boldsymbol{x}) \le c_2\|\boldsymbol{x}\|^2 \\ & \frac{\partial V}{\partial t} + \frac{\partial V}{\partial \boldsymbol{x}} \boldsymbol{f}(t,\boldsymbol{x}) \le -c_3\|\boldsymbol{x}\|^2 \\ & \left\| \frac{\partial V}{\partial \boldsymbol{x}} \right\| \le c_4\|\boldsymbol{x}\| \end{aligned} \tag{2.4}$$

for some positive constants c_1, c_2, c_3 and c_4.

Theorem 2 [104]: Let $\boldsymbol{x} = 0$ be an equilibrium point for the nonlinear system in (2.1). Let $D_0 = \{\boldsymbol{x} \in R^n \mid \|\boldsymbol{x}\| < r_0\}$. Let $V : [0,\infty)$ x $D_0 \rightarrow R$ be a continuously differentiable function such that

$$W_1(\boldsymbol{x}) \le V(t,\boldsymbol{x}) \le W_2(\boldsymbol{x}) \tag{2.5}$$

$$\dot{V}(t,\boldsymbol{x}) = \frac{\partial V}{\partial t} + \frac{\partial V}{\partial \boldsymbol{x}} \boldsymbol{f}(t,\boldsymbol{x}) \le 0 \tag{2.6}$$

$$\int_t^{t+\delta} \dot{V}\left(\tau, \boldsymbol{\varphi}(\tau,t,\boldsymbol{x})\right) \, d\tau \le -\lambda V(t,\boldsymbol{x}), \ \ 0 < \lambda < 1 \tag{2.7}$$

$\forall t \ge 0, \ \ \forall \boldsymbol{x} \in D_0$, for some $\delta > 0$, where $W_1(\boldsymbol{x})$ and $W_2(\boldsymbol{x})$ are continuous positive definite functions on D_0 and $\boldsymbol{\varphi}(\tau,t,\boldsymbol{x})$ is the solution of the system that starts at $(t,\boldsymbol{x})$. Then, the origin is uniformly asymptotically stable (UAS). If all the assumptions hold globally and $W_1(\boldsymbol{x})$ is radially unbounded, then the origin is globally asymptotically

stable (GAS). If $W_1(\boldsymbol{x}) \geq k_1 \|\boldsymbol{x}\|^c$, $W_2(\boldsymbol{x}) \leq k_2 \|\boldsymbol{x}\|^c$, $k_1 > 0$, $k_2 > 0$, $c > 0$, then the origin is ES.

Boundedness and Ultimate Boundedness Results

Definition 2 [104]: A continuous function $\alpha : [0, a) \mapsto \Re^+$ belongs to class K if it is strictly increasing and $\alpha(0) = 0$. It belongs to class K_∞ if $a = \infty$ and $\alpha(r) \to \infty$ as $r \to \infty$.

Definition 3 [104]: A continuous function $\beta : [0, a)$ x $\Re^+ \mapsto \Re^+$ belongs to class KL if $\beta(r, s)$ is class K with respect to r for every fixed s, and $\beta(r, s)$ is decreasing in s for every fixed r and $\beta(r, s) \to 0$ as $s \to \infty$.

Definition 4 [104]: The solutions of the nonlinear system in (2.1) are

- uniformly bounded if there exists a positive constant γ, independent of t_0, such that for every $\delta \in (0, \gamma)$, there is a $\beta = \beta(\delta) > 0$, independent of t_0, such that $\|\boldsymbol{x}_0\| \leq \delta$ implies $\|\boldsymbol{x}(t)\| \leq \beta$, $\forall t \geq t_0$.
- globally uniformly bounded if for every $\delta \in (0, \infty)$, there is a $\beta = \beta(\delta) > 0$, independent of t_0, such that $\|\boldsymbol{x}_0\| \leq \delta$ implies $\|\boldsymbol{x}(t)\| \leq \beta$, $\forall t \geq t_0$.
- uniformly ultimately bounded with ultimate bound $b > 0$ if there exists $\gamma > 0$ such that for every $\delta \in (0, \gamma)$, there exists a $T = T(\delta, b) > 0$ such that $\|\boldsymbol{x}_0\| \leq \delta$ implies $\|\boldsymbol{x}(t)\| \leq b$, $\forall t \geq T$.
- globally uniformly ultimately bounded if for every $\delta \in (0, \infty)$, there exists a $T = T(\delta, b) > 0$ such that $\|\boldsymbol{x}_0\| \leq \delta$ implies $\|\boldsymbol{x}(t)\| < b$, $\forall t \geq T$.

Next a Theorem is stated that presents sufficient conditions for uniform ultimate boundedness and ultimate boundedness.

Theorem 3 [104]: Let $\boldsymbol{x} = 0$ be an equilibrium point for the nonlinear system in (2.1). Let $D_0 = \left\{ \boldsymbol{x} \in R^n \mid \left\| \boldsymbol{x} \right\| < r_0 \right\}$. Let $V : [0, \infty)$ x $D_0 \to R$ be a continuously differentiable function, $\alpha_1(\cdot)$ and $\alpha_2(\cdot)$ are class K functions, and $W : D_0 \mapsto R$ is a positive definite function such that:

$$\alpha_1(\boldsymbol{x}) \le V(t, \boldsymbol{x}) \le \alpha_2(\boldsymbol{x}) \tag{2.8}$$

$$\dot{V}(t, \boldsymbol{x}) \le -W(\boldsymbol{x}), \ \left\| \boldsymbol{x} \right\| > \mu, \ \boldsymbol{x} \in D_0 \tag{2.9}$$

$$\mu > \alpha_2^{-1}(\alpha_1(r)) \tag{2.10}$$

where r is the radius of the ball $B_r = \left\{ \boldsymbol{x} \ : \ \left\| \boldsymbol{x} \right\| \le r \right\} \subset D_0$. Then there exists a class KL function β such that for every initial state $\boldsymbol{x}(t_0)$, satisfying $\left\| \boldsymbol{x}(t_0) \right\| \le \alpha_2^{-1}(\alpha_1(r))$, there is a $T \ge 0$ dependent on $\boldsymbol{x}(t_0)$ and μ such that the solution of (2.1) satisfies:

$$\left\| \boldsymbol{x}(t) \right\| \le \beta\left(\left\| \boldsymbol{x}(t_0) \right\|, t - t_0 \right), \ \ \forall t_0 \le t \le t_0 + T \tag{2.11}$$

$$\left\| \boldsymbol{x}(t) \right\| \le \alpha_1^{-1}(\alpha_2(\mu)), \ \ \forall t \ge t_0 + T \tag{2.12}$$

Moreover if $D_0 = R^n$ and if $\alpha_1(\cdot)$ is a class K_∞ function, then (2.11) and (2.12) hold for any initial state $\boldsymbol{x}(t_0)$, no matter how large μ is, i.e., the results are global.

2.2 Neural Networks as Universal Approximators

Theorem 4 [105], [106], [107]: Given an arbitrary $\varepsilon^* > 0$, any continuous function $\boldsymbol{f}(\boldsymbol{x}) : R^n \mapsto R^m$ can be parameterized via a suitably chosen set of basis functions on a compact set $\boldsymbol{x} \in D \subset R^n$

$$\boldsymbol{f}(\boldsymbol{x}) = W^T \boldsymbol{\sigma}(\boldsymbol{x}) + \boldsymbol{\varepsilon}(\boldsymbol{x}),\ \left\|\boldsymbol{\varepsilon}(\boldsymbol{x})\right\| < \varepsilon^* \tag{2.13}$$

where the basis functions $\boldsymbol{\sigma}(\cdot)$ are shifted sigmoids. The sigmoidal basis function is smooth, uniformly bounded and monotonically increasing and is given by

$$\sigma(x) = \frac{1}{1+e^{-ax}} \tag{2.14}$$

where $a > 0$ is the activation potential.

Theorem 5 [91]: Assume that a n dimensional state vector $\boldsymbol{x}(t)$ of an observable time-invariant system

$$\begin{aligned} \dot{\boldsymbol{x}} &= \boldsymbol{f}(\boldsymbol{x}) \\ \boldsymbol{y} &= \boldsymbol{h}(\boldsymbol{x}) \end{aligned} \tag{2.15}$$

evolves on a n dimensional ball of radius $\bar{r}$ in R^n, $B_{\bar{r}} = \left\{\boldsymbol{x} \in R^n \mid \left\|\boldsymbol{x}\right\| < \bar{r}\right\}$. Also assume that the system output $\boldsymbol{y}(t) \in R^m$ and its derivatives up to the order $(n-1)$ are bounded. Then given arbitrary $\varepsilon^* > 0$, there exists a set of constant, bounded weights W and a positive time delay $d > 0$, such that the function $\boldsymbol{f}(\boldsymbol{x})$ in (2.15) can be approximated over the compact set $B_{\bar{r}}$ by a linearly parameterized NN

$$\boldsymbol{f}(\boldsymbol{x}) = W^T \boldsymbol{\sigma}(\bar{\boldsymbol{\mu}}) + \boldsymbol{\varepsilon}(\bar{\boldsymbol{\mu}}),\ \left\|W\right\|_F \le W^*,\ \left\|\boldsymbol{\varepsilon}(\bar{\boldsymbol{\mu}})\right\| \le \varepsilon^*,\ \left\|\bar{\boldsymbol{\mu}}\right\| \le \mu^*, \tag{2.16}$$

using the input vector

$$\bar{\boldsymbol{\mu}}(\boldsymbol{y}(t), d) = \left[\Delta_d^{(0)} \boldsymbol{y}^T(t) \ \ \ldots \ \ \Delta_d^{(n-1)} \boldsymbol{y}^T(t)\right] \ \in R^{nm} \tag{2.17}$$

where $\Delta_d^{(0)} \boldsymbol{y}^T(t) = \boldsymbol{y}^T(t)$, $\Delta_d^{(k)} \boldsymbol{y}^T(t) = \dfrac{\Delta_d^{(k-1)} \boldsymbol{y}^T(t) - \Delta_d^{(k-1)} \boldsymbol{y}^T(t-d)}{d}$, $k = 1, 2, \ldots,$, $\mu^* > 0$ is a uniform bound on $B_{\bar{r}}$.

CHAPTER 3

COMPOSITE ADAPTATION APPROACH TO ADAPTIVE STATE ESTIMATION

The problem of target tracking is essentially a state estimation problem in the presence of target motion uncertainty. The uncertainty refers to the fact that a model that adequately captures all possible maneuvers of a target is often not known. The state estimation problem in such cases is nonlinear and time-varying, with rapidly changing dynamics. Using a linear, time-invariant observer based on a nominal model of the target motion is not preferred for such applications. Time-varying observers with the ability to capture unmodeled dynamics are required in such applications. This chapter presents an approach for augmenting a linear, time-varying Kalman filter with an adaptive neural network (NN) for the partial state estimation of a class of nonlinear systems in the presence of unknown system inputs. The nonlinear systems have a known nominal linear model. The unknown system inputs represent the effect of unmodeled dynamics acting on the system and are assumed to be continuous and bounded. The NN is trained online to estimate the unknown inputs. The training signal for the NN consists of two error signals. The first error signal is the residual of the Kalman filter that is augmented with the NN output. The second error signal is obtained after deriving a linear parameterization model of available system signals in terms of the ideal, unknown NN weights that linearly parameterize the unknown system inputs. The combination of two different sources of error signals to train the NN represents a composite adaptation type approach to adaptive state estimation. Lyapunov-like stability analysis shows uniform ultimate boundedness of all the error signals in the system. Simulation results with application of the approach to a leader aircraft tracking problem in an autonomous formation flight scenario illustrate the

effectiveness of the approach. The approach is also validated in software-in-the-loop simulations by integrating the adaptive estimator with image processing, guidance and flight control algorithms. An extension to the multi-input multi-output case is also presented.

Equation Chapter 3 Section 1

3.1 Problem Formulation

Consider the following *bounded* single-input-single-output (SISO) nonlinear system

$$\begin{aligned} \dot{\boldsymbol{x}} &= A\boldsymbol{x} + Bg\left(\boldsymbol{x}, z\right), \qquad \boldsymbol{x}(0) = \boldsymbol{x}_0 \\ \dot{z} &= \boldsymbol{f}_z\left(\boldsymbol{x}, z\right), \qquad\quad z(0) = z_0 \\ y &= C\boldsymbol{x} \end{aligned} \tag{3.1}$$

where $\boldsymbol{x} \in D_x \subseteq R^{n_x}$ and $z \in D_z \subseteq R^{n_z}$ are the states of the system such that $\boldsymbol{x}$ represents the modeled states and z represents the unmodeled states, D_x and D_z are compact sets, $\boldsymbol{f}_z(\boldsymbol{x}, z) : R^{n_x} \times R^{n_z} \to R^{n_z}$ is an unknown, bounded function and represents the unmodeled dynamics, $g(\boldsymbol{x}, z) : R^{n_x} \times R^{n_z} \to R$ is an unknown, uniformly bounded and continuous function and represents the way in which the unmodeled dynamics is coupled to the system dynamics, for which n_z is also unknown but bounded, $y \in R$ represents the available measurement which is assumed to be bounded, the matrices $\left(A, B, C\right)$ are known and the pair $\left(A, C\right)$ is observable.

Remark 3.1: The function $g\left(\boldsymbol{x}, z\right)$ acts as the unknown system input or disturbance to the nominal linear system given by the matrices $\left(A, B, C\right)$.

Objective: Design a state estimator to estimate the states $\boldsymbol{x}$ of the system in (3.1) with bounded estimation error in the presence of the unknown system input $g\left(\boldsymbol{x}, z\right)$.

3.2 Adaptive Estimator and Error Signal Derivation

Using Theorem 5 in Chapter 2, consider the following NN approximation of $g(\boldsymbol{x},\boldsymbol{z})$

$$g(\boldsymbol{x},\boldsymbol{z}) = \boldsymbol{W}^T\boldsymbol{\sigma}(\bar{\boldsymbol{\mu}}) + \varepsilon(\bar{\boldsymbol{\mu}}),\ \|\boldsymbol{W}\|_F \le W^*,\ \|\varepsilon(\bar{\boldsymbol{\mu}})\| \le \varepsilon^*,\ \|\bar{\boldsymbol{\mu}}\| \le \mu^* \tag{3.2}$$

$\forall(\boldsymbol{x},\boldsymbol{z}) \in D_g \subset D_{\boldsymbol{x}}$ x $D_{\boldsymbol{z}}$, D_g is a compact set, $\boldsymbol{\sigma}(\bar{\boldsymbol{\mu}}) = \left[\sigma_1(\bar{\boldsymbol{\mu}}),\ldots,\sigma_N(\bar{\boldsymbol{\mu}})\right]^T$ is a vector of *shifted* sigmoidal functions $\sigma_i(\cdot)$ [106, 107], W^* and ε^* are the bounds on the Frobenius norms of the ideal, unknown weight vector $\boldsymbol{W}$ and of the NN functional approximation error ε respectively, N is the number of neurons, and the input vector $\bar{\boldsymbol{\mu}} = \bar{\boldsymbol{\mu}}(y(t),d)$ is the vector of difference quotients of the output y

$$\bar{\boldsymbol{\mu}}(y(t),d) = \left[1,\ \Delta_d^{(0)}y^T(t)\ \ \ldots\ \ \Delta_d^{(n-1)}y^T(t)\right] \tag{3.3}$$

where $\Delta_d^{(0)}y^T(t) = y^T(t)$, $\Delta_d^{(k)}y^T(t) = \dfrac{\Delta_d^{(k-1)}y^T(t) - \Delta_d^{(k-1)}y^T(t-d)}{d}$, $k = 1,2,\ldots,$ and $d > 0$ is a time delay. The sigmoidal functions are uniformly bounded [92], that is, $\left|\sigma_i(\bar{\mu})\right| \le 1$.

Consider the following time-varying adaptive estimator to estimate the states of the system in (3.1):

$$\begin{aligned} \dot{\hat{\boldsymbol{x}}}(t) &= A\hat{\boldsymbol{x}}(t) + K(t)\left(y(t) - \hat{y}(t)\right) + B\nu_{ad}, \qquad \hat{\boldsymbol{x}}(0) = \hat{\boldsymbol{x}}_0 \\ \hat{y}(t) &= C\hat{\boldsymbol{x}}(t) \end{aligned} \tag{3.4}$$

where $K(t)$ is the Kalman gain obtained through the following set of matrix differential Ricatti equations [93]

$$\begin{aligned} \dot{P}(t) &= AP(t) + P(t)A^T - P(t)C^T R^{-1} CP(t) + Q \\ K(t) &= P(t)C^T R^{-1} \end{aligned} \tag{3.5}$$

where $P(0) = P_0 > 0,\ Q = Q^T > 0,\ R = R^T > 0$. The solution $P(t)$ of (3.5) is bounded, symmetric, positive definite and continuously differentiable. The output of the NN ν_{ad} is given by

$$\nu_{ad} = \hat{\boldsymbol{W}}(t)^T \boldsymbol{\sigma}(\bar{\boldsymbol{\mu}}) \tag{3.6}$$

where $\hat{\boldsymbol{W}}(t)$ is the estimate of the weight vector $\boldsymbol{W}$ in (3.2) and ν_{ad} is designed to approximate the bounded disturbance $g(\boldsymbol{x}, \boldsymbol{z})$. The formulation so far replicates the formulation in Ref. [63] applied to the system in (3.1). The residual signal of the adaptive estimator $\tilde{y}(t) = y(t) - \hat{y}(t)$ is the *first* error signal that is used to train the NN.

Next we address the derivation of the second error signal to train the NN. The objective here is to establish a linear parameterization model of the ideal but unknown NN weight vector $\boldsymbol{W}$ in terms of available system signals. To do this, consider the following non-adaptive estimator for the system in (3.1):

$$\begin{aligned} \dot{\hat{\boldsymbol{x}}}_1(t) &= A\hat{\boldsymbol{x}}_1(t) + K_1(t)\big(y(t) - \hat{y}_1(t)\big), \qquad \hat{\boldsymbol{x}}_1(0) = \hat{\boldsymbol{x}}_{10} \\ \hat{y}_1(t) &= C\hat{\boldsymbol{x}}_1(t) \end{aligned} \tag{3.7}$$

where $\tilde{y}_1(t) = y(t) - \hat{y}_1(t)$ is the residual of the non-adaptive estimator in (3.7), and $K_1(t)$ is the Kalman gain obtained through the following set of matrix differential Ricatti equations [93]:

$$\begin{aligned} \dot{P}_1(t) &= AP_1(t) + P_1(t)A^T - P_1(t)C^T R_1^{-1} CP_1(t) + Q_1 \\ K_1(t) &= P_1(t)C^T R_1^{-1} \end{aligned} \tag{3.8}$$

where $P_1(0) = P_{10} = P_0 > 0,\ Q_1 = Q_1^T \geq 0,\ R_1 = R_1^T > 0$. The solution $P_1(t)$ of (3.8) is bounded, symmetric, positive definite and continuously differentiable.

Consider the estimation error dynamics of the non-adaptive estimator in (3.7). Define $\tilde{\boldsymbol{x}}_1 = \boldsymbol{x} - \hat{\boldsymbol{x}}_1$ and $\bar{A}_1(t) = A - K_1(t)C$. Then we have the following estimation error dynamics:

$$\begin{aligned} \dot{\tilde{\boldsymbol{x}}}_1 &= \bar{A}_1(t)\tilde{\boldsymbol{x}}_1 + Bg(\boldsymbol{x}, z) \\ \tilde{y}_1 &= C\tilde{\boldsymbol{x}}_1 \end{aligned} \tag{3.9}$$

Next, we state and prove a key lemma.

Lemma 3.1: The estimation error dynamics of the unforced system

$$\begin{aligned} \dot{\tilde{\boldsymbol{x}}}_1 &= \bar{A}_1(t)\tilde{\boldsymbol{x}}_1 \\ \tilde{y}_1 &= C\tilde{\boldsymbol{x}}_1 \end{aligned} \tag{3.10}$$

are Globally Exponentially Stable (GES). This implies that

$$\Phi(t, t_0)\tilde{\boldsymbol{x}}_1(t_0) \to 0, \text{ as } t \to \infty, \ \forall t \geq t_0 \geq 0 \tag{3.11}$$

where $\Phi(\tau, t)$ is the state transition matrix of the system (3.10). The above result implies that in presence of bounded input $g(\boldsymbol{x}, z)$ to the system in (3.10), the estimation error vector $\tilde{\boldsymbol{x}}_1(t)$ and the residual $\tilde{y}_1(t)$ are bounded.

Proof: We prove the above result via Lyapunov stability analysis of the dynamics in (3.10). Before starting the Lyapunov analysis, we derive Eqs. (3.12)-(3.14) that are used in the analysis. The matrix differential equation (3.8) can be re-written as

$$\dot{P}_1(t) = \bar{A}_1(t)P_1(t) + P_1(t)\bar{A}_1(t)^T + P_1(t)C^T R_1^{-1} C P_1(t) + Q_1 \tag{3.12}$$

Invoking the identity $P_1(t)P_1(t)^{-1} = I$ and differentiating, we have:

$$\dot{P}_1^{-1}(t) = -P_1^{-1}(t)\bar{A}_1(t) - \bar{A}_1(t)^T P_1^{-1}(t) - \tilde{Q}_1(t) \tag{3.13}$$

$$\tilde{Q}_1(t) = C^T R_1^{-1} C + P_1^{-1}(t) Q_1 P_1^{-1}(t) \geq 0 \tag{3.14}$$

Now consider the Lyapunov candidate function $V_1(t,\tilde{\boldsymbol{x}}_1)=\tilde{\boldsymbol{x}}_1^T P_1^{-1}(t)\tilde{\boldsymbol{x}}_1$. Since $P_1(t)$ is bounded, symmetric and positive definite, there exist positive constants ρ_1 and ρ_2, $\rho_1>\rho_2>0$, such that

$$0<\frac{1}{\rho_1}\|\tilde{\boldsymbol{x}}_1\|^2\le V_1(t,\tilde{\boldsymbol{x}}_1)\le\frac{1}{\rho_2}\|\tilde{\boldsymbol{x}}_1\|^2 \tag{3.15}$$

So $V_1(t,\tilde{\boldsymbol{x}}_1)$ is decresent and radially unbounded [104]. Differentiating $V_1(t,\tilde{\boldsymbol{x}}_1)$

$$\dot{V}_1(t,\tilde{\boldsymbol{x}}_1)=\dot{\tilde{\boldsymbol{x}}}_1^T P_1(t)^{-1}\tilde{\boldsymbol{x}}_1+\tilde{\boldsymbol{x}}_1^T P_1(t)^{-1}\dot{\tilde{\boldsymbol{x}}}+\tilde{\boldsymbol{x}}_1^T\dot{P}_1(t)^{-1}\tilde{\boldsymbol{x}}_1 \tag{3.16}$$

Substituting for $\dot{\tilde{\boldsymbol{x}}}_1$ from (3.10) and $\dot{P}_1^{-1}(t)$ from (3.13), Eq. (3.16) simplifies to

$$\dot{V}_1(t,\tilde{\boldsymbol{x}}_1)=-\tilde{\boldsymbol{x}}_1^T\tilde{Q}_1(t)\tilde{\boldsymbol{x}}_1\le 0 \tag{3.17}$$

where $\tilde{Q}_1(t)$ is given by (3.14). Since $Q_1\ge 0$, we have $P_1(t)^{-1}Q_1P_1(t)^{-1}\ge 0$. This implies that

$$\dot{V}_1(t,\tilde{\boldsymbol{x}}_1)\le-\tilde{\boldsymbol{x}}_1^T C^T R_1^{-1}C\tilde{\boldsymbol{x}}_1\le 0 \tag{3.18}$$

The solution of the linear time-varying system (3.10) starting at $(t,\tilde{\boldsymbol{x}}_1)$ is given by

$$\boldsymbol{\varphi}(\tau,t,\tilde{\boldsymbol{x}}_1)=\Phi(\tau,t)\tilde{\boldsymbol{x}}_1(t) \tag{3.19}$$

Therefore for some $\delta>0$, we have,

$$\int_t^{t+\delta}\dot{V}_1\left(\tau,\boldsymbol{\varphi}(\tau,t,\tilde{\boldsymbol{x}}_1)\right)\,d\tau\le-\tilde{\boldsymbol{x}}_1^T\left[\int_t^{t+\delta}\Phi^T(\tau,t)L^T\;L\;\Phi(\tau,t)d\tau\right]\tilde{\boldsymbol{x}}_1=-\tilde{\boldsymbol{x}}_1^T W_1(t,t+\delta)\tilde{\boldsymbol{x}}_1 \tag{3.20}$$

where $L=R_1^{-1/2}C$. The matrix $W_1(t,t+\delta)$ is the observability gramian of the pair $(\bar{A}_1(t),L)=(A-P_1(t)C^TR_1^{-1}C,R_1^{-1/2}C)$. Observability of the pair (A,C) guarantees uniform observability of the pair $(\bar{A}_1(t),L)=(A-P_1(t)C^TR_1^{-1}C,R_1^{-1/2}C)$.

The above fact guarantees that $W_1(t,t+\delta) \geq kI > 0$, $\forall t \geq 0$, where $k < \frac{1}{\rho_2}$. This implies that

$$\int_t^{t+\delta} \dot{V}_1\left(\tau, \boldsymbol{\varphi}(\tau,t,\tilde{\boldsymbol{x}}_1)\right)\, d\tau \leq -k\left\|\tilde{\boldsymbol{x}}_1\right\|^2 \leq -k\rho_2 V_1(t,\tilde{\boldsymbol{x}}_1) \tag{3.21}$$

Eqs. (3.15), (3.18) and (3.21) satisfy the sufficient conditions of Theorem 2 in Chapter 2 with $W_1(\tilde{\boldsymbol{x}}_1) = \frac{1}{\rho_1}\left\|\tilde{\boldsymbol{x}}_1\right\|^2$ and $W_2(\tilde{\boldsymbol{x}}_1) = \frac{1}{\rho_2}\left\|\tilde{\boldsymbol{x}}_1\right\|^2$. This implies that the origin $\tilde{\boldsymbol{x}}_1(t) \equiv 0$ of the unforced system (3.10) is GES. Considering the time-domain solution of (3.10), we have

$$\tilde{\boldsymbol{x}}_1(t) = \Phi(t,t_0)\tilde{\boldsymbol{x}}_1(t_0), \quad \forall t \geq t_0 \geq 0 \tag{3.22}$$

Applying Definition 1 in Chapter 2 implies that

$$\left\|\tilde{\boldsymbol{x}}_1(t)\right\| = \left\|\Phi(t,t_0)\tilde{\boldsymbol{x}}_1(t_0)\right\| \leq k\left\|\tilde{\boldsymbol{x}}_1(t_0)\right\| e^{-\lambda(t-t_0)} \tag{3.23}$$

for some positive constants k and λ and for $\tilde{\boldsymbol{x}}_1(t_0) \in R^n$. This implies that

$$\Phi(t,t_0)\tilde{\boldsymbol{x}}_1(t_0) \to 0, \text{ as } t \to \infty, \quad \forall t \geq t_0 \geq 0 \tag{3.24}$$

Since the estimation error dynamics in (3.10) are GES, in the presence of the bounded disturbance $g(\boldsymbol{x},\boldsymbol{z})$ the estimation error vector $\tilde{\boldsymbol{x}}_1$ of the system in (3.9), is input-to-state stable [104]. This implies that $\tilde{\boldsymbol{x}}_1(t)$ is bounded as long as $g(\boldsymbol{x},\boldsymbol{z})$ is bounded. This also implies that the residual $\tilde{y}_1(t)$ is bounded as long as $g(\boldsymbol{x},\boldsymbol{z})$ is bounded.

□

Next, we show that the time-domain solution for $\tilde{y}_1$ is a linear parameterization model in terms of the unknown NN weight vector $\boldsymbol{W}$. Eq. (3.9) can be written in terms of the linear parameterization of $g(\boldsymbol{x},\boldsymbol{z})$ in Eq. (3.2) as

$$\begin{aligned}\dot{\tilde{\boldsymbol{x}}}_1 &= \bar{A}_1(t)\tilde{\boldsymbol{x}}_1 + B\boldsymbol{W}^T\boldsymbol{\sigma}(\bar{\boldsymbol{\mu}}) + B\varepsilon \\ \tilde{y}_1 &= C\tilde{\boldsymbol{x}}_1\end{aligned} \tag{3.25}$$

where $\|\boldsymbol{W}\|_F \le W^*$, $\|\varepsilon(\bar{\boldsymbol{\mu}})\| \le \varepsilon^*$. The time domain solution for the residual $\tilde{y}_1$ is given by

$$\tilde{y}_1(t) = C\Phi(t,t_0)\tilde{\boldsymbol{x}}_1(t_0) + \int_{t_0}^{t} C\Phi(t,\tau)B\boldsymbol{W}^T\boldsymbol{\sigma}(\bar{\boldsymbol{\mu}})\ d\tau + \int_{t_0}^{t} C\Phi(t,\tau)B\varepsilon\ d\tau \tag{3.26}$$

Since $g(\boldsymbol{x},\boldsymbol{z}) \in R$ and $\boldsymbol{W}$ is a constant vector, Eq. (3.26) can be re-written as

$$\tilde{y}_1(t) = C\Phi(t,t_0)\tilde{\boldsymbol{x}}_1(t_0) + \left[\int_{t_0}^{t} C\Phi(t,\tau)B\boldsymbol{\sigma}^T(\bar{\boldsymbol{\mu}})\ d\tau\right]\boldsymbol{W} + \varepsilon_f(t,t_0) \tag{3.27}$$

where $\varepsilon_f(t,t_0)$ is the output of the following dynamical system,

$$\begin{aligned}\dot{\boldsymbol{x}}_\varepsilon &= \bar{A}_1(t)x_\varepsilon + B\varepsilon, \quad \boldsymbol{x}_\varepsilon(t_0) = 0 \\ \varepsilon_f &= C\boldsymbol{x}_\varepsilon\end{aligned} \tag{3.28}$$

and ε_f is always bounded since it is the output of the GES system in (3.10) with bounded input ε. Let $\|\varepsilon_f(t,t_0)\| \le \varepsilon_f^*$. Eq. (3.27) can now be written as

$$\tilde{y}_1(t) = C\Phi(t,t_0)\tilde{\boldsymbol{x}}_1(t_0) + \boldsymbol{q}(t,t_0)\boldsymbol{W} + \varepsilon_f(t,t_0) \tag{3.29}$$

where $\boldsymbol{q}(t,t_0)$ is a row vector given by

$$\boldsymbol{q}(t,t_0) = \left[\sigma_{f1}(t,t_0)\ \sigma_{f2}(t,t_0)\ \ldots\ \sigma_{fN}(t,t_0)\right] \tag{3.30}$$

and the $\sigma_{fi}(t,t_0)$, $i = 1,2,\ldots,N$ are the outputs of the GES system in (3.10) with uniformly bounded inputs $\sigma_i(\bar{\boldsymbol{\mu}})$, $i = 1,2,\ldots,N$, i.e.,

$$\begin{aligned}\dot{\boldsymbol{x}}_{fi} &= \bar{A}_1(t)\boldsymbol{x}_{fi} + B\sigma_i\left(\bar{\boldsymbol{\mu}}(t)\right), \quad \boldsymbol{x}_{fi}(t_0) = 0, \;\; i = 1,2,\ldots,N \\ \sigma_{fi} &= C\boldsymbol{x}_{fi}\end{aligned} \tag{3.31}$$

The boundedness of $\sigma_i(\bar{\boldsymbol{\mu}})$ implies the boundedness of $\sigma_{fi}(t,t_0)$ which in turn implies the boundedness of the row vector $\boldsymbol{q}(t,t_0)$. The initial condition $\tilde{\boldsymbol{x}}_1(t_0)$ and the filtered NN approximation error $\varepsilon_f(t,t_0)$ are not available. Eq. (3.24) shows that the contribution of the initial estimation error term $\tilde{\boldsymbol{x}}_1(t_0)$ converges exponentially fast to zero and Eq. (3.28) established that $\varepsilon_f(t,t_0)$ is always bounded.

Eq. (3.29) is a linear parameterization model in terms of the available residual signal $\tilde{y}_1(t)$ and the unknown, constant NN weight vector $\boldsymbol{W}$. Consider an estimate of the residual $\tilde{y}_1(t)$ by replacing $\boldsymbol{W}$ by its estimate $\hat{\boldsymbol{W}}(t)$

$$\hat{\tilde{y}}_1(t) = \boldsymbol{q}(t,t_0)\hat{\boldsymbol{W}}(t) \tag{3.32}$$

The signal formed by the difference between $\tilde{y}_1(t)$ and $\hat{\tilde{y}}_1(t)$ is the second error signal used to train the NN and is given by

$$e_1(t) = \tilde{y}_1(t) - \hat{\tilde{y}}_1(t) = \tilde{y}_1(t) - \boldsymbol{q}(t,t_0)\hat{\boldsymbol{W}}(t) \tag{3.33}$$

Remark 3.2: It requires $(N+1)$ time-varying filters (Eqs. (3.7) and (3.31)) to generate the error signal $e_1(t)$.

Let the NN adaptive law be given by

$$\dot{\hat{\boldsymbol{W}}} = -\Gamma_W\left\{-\boldsymbol{\sigma}(\bar{\boldsymbol{\mu}})\tilde{y} - \boldsymbol{q}^T(t,t_0)e_1 + \lambda_W\hat{\boldsymbol{W}}\right\} \tag{3.34}$$

with the NN design constants $\Gamma_W > 0$, and $\lambda_W > 0$, where Γ_W are the adaptation gains and λ_W is the sigma-mod parameter [94].

Remark 3.3: The form of the adaptive law containing the error term $e_1(t)$ is the gradient descent approach [66] to minimizing $e_1(t)$. Other potential approaches include the standard least-squares minimization, least-squares with exponential forgetting [66], etc. Figure 3 shows a block diagram of the composite adaptation based state estimator.

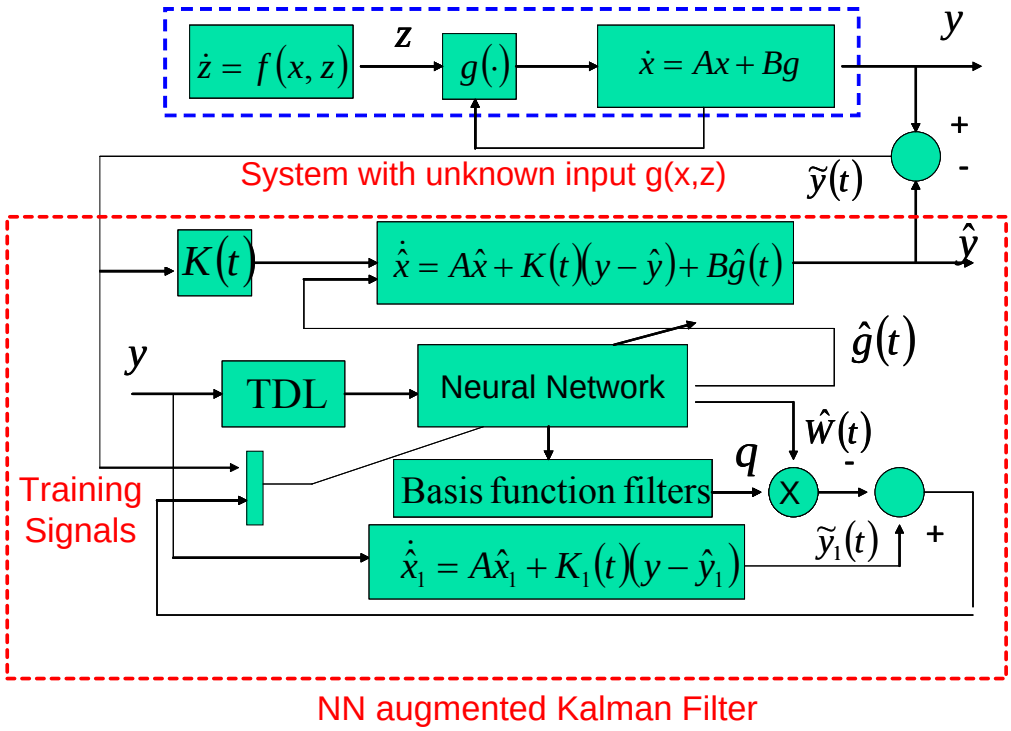

Figure 3. Composite Adaptation based Adaptive State Estimation

3.3 Error Boundedness Analysis

The boundedness of the state estimation errors and NN weight estimation errors is shown via Lyapunov-like analysis. Before starting the boundedness analysis, a few results are presented in the forms that are directly used in the analysis.

Define the state estimation error vector $\tilde{\boldsymbol{x}} = \boldsymbol{x} - \hat{\boldsymbol{x}}$, the NN weight estimation error vector $\tilde{\boldsymbol{W}} = \boldsymbol{W} - \hat{\boldsymbol{W}}$ and $\bar{A}(t) = A - K(t)C$. Using Eqs. (3.1), (3.2), (3.4), and (3.6), the state estimation error dynamics can be written as

$$\begin{aligned} \dot{\tilde{\boldsymbol{x}}} &= \bar{A}(t)\tilde{\boldsymbol{x}} + B\tilde{\boldsymbol{W}}^T\boldsymbol{\sigma}(\bar{\boldsymbol{\mu}}) + B\varepsilon(\bar{\boldsymbol{\mu}}) \\ \tilde{y} &= C\tilde{\boldsymbol{x}} \end{aligned} \tag{3.35}$$

where $\tilde{y}$ is the residual of the adaptive estimator. The NN weight estimation error dynamics can be written using Eqs. (3.34) and (3.35) as,

$$\dot{\tilde{\boldsymbol{W}}} = -\dot{\hat{\boldsymbol{W}}} = \Gamma_W\left(-\boldsymbol{\sigma}(\bar{\boldsymbol{\mu}})C\tilde{\boldsymbol{x}} - \boldsymbol{q}^T(t,t_0)e_1 + \lambda_W\boldsymbol{W} - \lambda_W\tilde{\boldsymbol{W}}\right) \tag{3.36}$$

Applying the approach in Eqs. (3.12)-(3.14), the following identity can be written for $P^{-1}(t)$, where $P(t)$ is the positive definite, symmetric and bounded solution of the matrix differential equation (3.5)

$$\dot{P}^{-1}(t) = -P^{-1}(t)\bar{A}(t) - \bar{A}(t)^T P^{-1}(t) - \tilde{Q}(t) \tag{3.37}$$

$$\tilde{Q}(t) = C^T R^{-1} C + P^{-1}(t) Q P^{-1}(t) > 0 \tag{3.38}$$

The following bounds on $P^{-1}(t)$ are used in the analysis [64],

$$\rho_1 I \le P(t) \le \rho_2 I \Rightarrow \frac{1}{\rho_2} I \le P^{-1}(t) \le \frac{1}{\rho_2} I \tag{3.39}$$

The second error signal used to train the NN can be written as follows using Eqs. (3.33) and (3.29),

$$e_1(t) = C\Phi(t,t_0)\tilde{\boldsymbol{x}}_1(t_0) + \boldsymbol{q}(t,t_0)\tilde{\boldsymbol{W}} + \varepsilon_f(t,t_0) \tag{3.40}$$

Define the error vector

$$\boldsymbol{\varsigma} = \begin{bmatrix} \tilde{\boldsymbol{x}}^T & \tilde{\boldsymbol{W}}^T \end{bmatrix}^T \tag{3.41}$$

and the positive definite Lyapunov candidate function for the boundedness analysis as

$$V(\varsigma) = V\left(\tilde{\boldsymbol{x}}, \tilde{\boldsymbol{W}}\right) = \tilde{\boldsymbol{x}}^T P^{-1}(t)\,\tilde{\boldsymbol{x}} + \tilde{\boldsymbol{W}}^T \Gamma_W^{-1} \tilde{\boldsymbol{W}} \tag{3.42}$$

Note that the NN approximation for the unmodeled dynamics (3.2) is defined over a compact set D_g. In the space of the error vector ς, consider the largest level set of $V(\varsigma)$ such that its projection on the subspace of the NN input variables lies completely in D_g. Define the largest ball that lies within that level set as $B_M \triangleq \{\varsigma : \|\varsigma\| \le M\}$ and let α be the minimum value of $V(\varsigma)$ on the boundary of B_M:

$$\alpha \triangleq \min_{\|\varsigma\|=M} V(\varsigma) \tag{3.43}$$

Introduce the set

$$\Omega_\alpha = \{\varsigma \in B_M \mid V(\varsigma) \le \alpha\} \tag{3.44}$$

The definition of the candidate Lyapunov function (3.42) shows that there exist class K functions κ_1 and κ_2 such that

$$\kappa_1(\|\varsigma\|) \le V(\varsigma) \le \kappa_2(\|\varsigma\|)$$

where

$$\begin{aligned} \kappa_1(\|\varsigma\|) &= \frac{1}{\rho_2^2}\|\tilde{\boldsymbol{x}}\|^2 + \lambda_{\min}\left(\Gamma_W^{-1}\right)\|\tilde{\boldsymbol{W}}\|^2 \\ \kappa_2(\|\varsigma\|) &= \frac{1}{\rho_1^2}\|\tilde{\boldsymbol{x}}\|^2 + \lambda_{\max}\left(\Gamma_W^{-1}\right)\|\tilde{\boldsymbol{W}}\|^2 \end{aligned} \tag{3.45}$$

where the bounds on $P^{-1}(t)$ in (3.39) are applied.

Assumption 1: Let

$$M > \kappa_1^{-1}(\kappa_2(\gamma)) \tag{3.46}$$

where γ is defined as

$$\gamma \triangleq \frac{\sqrt{m_1^2 + \left(m_4^2 + m_5^2\right) + \lambda_W W^{*2}}}{\min\left(\sqrt{\frac{\lambda_{\min}(Q)}{\rho_2^2} - 2}, \sqrt{\lambda_W - \left(m_2^2 + 2\right)}\right)} \tag{3.47}$$

$$\begin{aligned} m_1 &= \left\| P^{-1}(t) B \right\| \varepsilon^* \\ m_2 &= \left\| P^{-1}(t) B - C^T \right\| \sqrt{N} \\ m_3 &= \left\| q(t, t_0) \right\| \\ m_4 &= m_3 k \|C\| \left\| \tilde{\boldsymbol{x}}_1(t_0) \right\| \\ m_5 &= m_3 \varepsilon_f^* \end{aligned} \tag{3.48}$$

where N is the number of basis functions, $k > 0$ comes from (3.23) and $\left|\varepsilon_f(t, t_0)\right| \le \varepsilon_f^*$.

Let $\lambda_{\min}(Q) > 2\rho_2^2$ and $\lambda_W > m_2^2 + 2$. Now the main result on the error boundedness can be stated.

Theorem 3.1: Let Assumption 1 hold and the initial error vector $\varsigma(t_0) \in \Omega_\alpha$. For the system formulation in (3.1) and the NN parameterization in (3.2), let the adaptive estimator be given by (3.4) with the NN adaptive law given by (3.34). Then the state estimation error $\tilde{\boldsymbol{x}}$ and NN weight estimation error $\tilde{\boldsymbol{W}}$ are uniformly ultimately bounded.

Proof: Refer to Appendix A.

Remark 3.4: The bound on the NN approximation error ε appears in the expression for the ultimate bounds in (3.47) through the terms m_1 and m_5 in (3.48). These terms can be made arbitrarily small by choosing sufficiently large number of neurons of the NN. This has to be balanced with the computational requirements of the adaptive estimator implementation.

3.4 Simulation Results

A. Problem Formulation

A 3 DOF leader-follower formation flight configuration is considered to illustrate the simulation results. A leader aircraft is the maneuvering target to be tracked. The follower aircraft tracks the leader aircraft at a commanded range of 5 meters, which is approximately two wing-span lengths of the follower. Since the approach presented in Section 3.2 is applicable for adaptive state estimation only, the state estimates are not used in the guidance law. The guidance law in Ref. [70] that assumes true values of the range R, LOS azimuth angle λ_A and LOS elevation angle λ_E and LOS rates $\dot{R}$, $\dot{\lambda}_A$, and $\dot{\lambda}_E$ is implemented in this simulation. We consider the relative LOS kinematics of the target with respect to the follower in the inertial Cartesian coordinate frame

$$\frac{d}{dt}\begin{bmatrix} R_X \\ \dot{R}_X \\ R_Y \\ \dot{R}_Y \\ R_Z \\ \dot{R}_Z \end{bmatrix} = \underbrace{\begin{bmatrix} 0 & 1 & 0 & 0 & 0 & 0 \\ 0 & 0 & 0 & 0 & 0 & 0 \\ 0 & 0 & 0 & 1 & 0 & 0 \\ 0 & 0 & 0 & 0 & 0 & 0 \\ 0 & 0 & 0 & 0 & 0 & 1 \\ 0 & 0 & 0 & 0 & 0 & 0 \end{bmatrix}}_{A} \begin{bmatrix} R_X \\ \dot{R}_X \\ R_Y \\ \dot{R}_Y \\ R_Z \\ \dot{R}_Z \end{bmatrix} + \underbrace{\begin{bmatrix} 0 & 0 & 0 \\ 1 & 0 & 0 \\ 0 & 0 & 0 \\ 0 & 1 & 0 \\ 0 & 0 & 0 \\ 0 & 0 & 1 \end{bmatrix}}_{B} \begin{bmatrix} a_{T_X} \\ a_{T_Y} \\ a_{T_Z} \end{bmatrix} + \begin{bmatrix} 0 & 0 & 0 \\ 1 & 0 & 0 \\ 0 & 0 & 0 \\ 0 & 1 & 0 \\ 0 & 0 & 0 \\ 0 & 0 & 1 \end{bmatrix} \begin{bmatrix} -a_{F_X} \\ -a_{F_Y} \\ -a_{F_Z} \end{bmatrix} \tag{3.49}$$

where R_X, R_Y and R_Z are respectively the projections of the range vector from the follower to the target aircraft onto the inertial X, Y and Z axes, and the subscripts *T* and *F* refer to target (leader) and follower aircraft respectively. The relationship between the inertial frame components of the LOS range vector R_X, R_Y and R_Z and the spherical coordinate frame components R, λ_A and λ_E is given by (3.50) and represented graphically in Figure 4,

$$
\begin{aligned}
R_X &= R\cos\lambda_A\cos\lambda_E \\
R_Y &= R\sin\lambda_A\cos\lambda_E \\
R_Z &= -R\sin\lambda_E
\end{aligned}
\tag{3.50}
$$

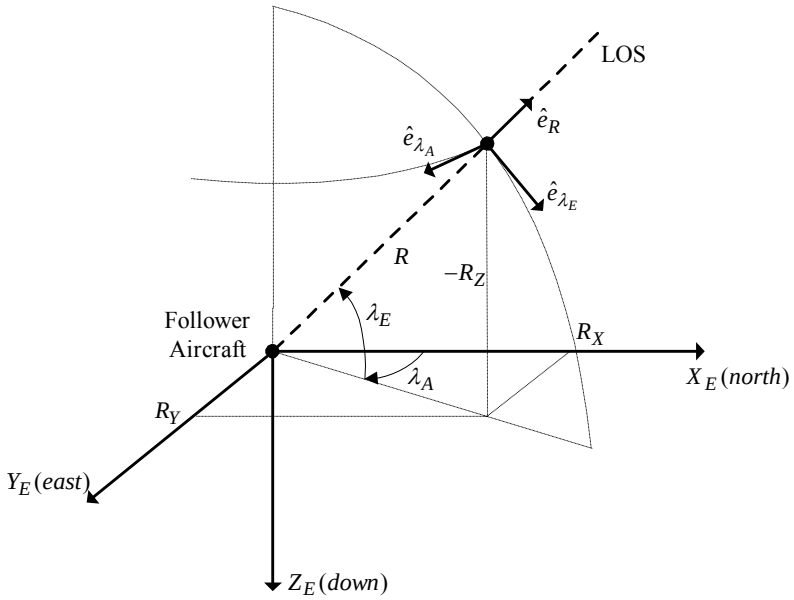

Figure 4. Line-of-Sight (LOS) Variables in the Inertial Coordinates

We assume that there is a vision sensor onboard the follower aircraft that can measure the subtended angle α, the azimuth angle λ_A, and the elevation angle λ_E with zero-mean additive measurement white noise of standard deviation 0.01 radians for each measurement [38]. The subtended angle measures the maximum size subtended by the target aircraft on the follower image plane. Using these raw measurements, we can create pseudo-measurements of R_X, R_Y and R_Z using the relationship between subtended angle, azimuth angle and elevation angle and range [38]

$$
\begin{aligned}
R_m &= \frac{b}{2\tan\left(\frac{\alpha_m}{2}\right)} \\
R_{X_m} &= R_m \cos\left(\lambda_{A_m}\right)\cos\left(\lambda_{E_m}\right) \\
R_{Y_m} &= R_m \sin\left(\lambda_{A_m}\right)\cos\left(\lambda_{E_m}\right) \\
R_{Z_m} &= -R_m \sin\left(\lambda_{E_m}\right)
\end{aligned}
\tag{3.51}
$$

where the subscript *m* indicates the variables are measurements, and b is the target size (wing-span length), assumed constant and known for this simulation. The conversion of the image plane noisy measurements of α, λ_A and λ_E into the measurements of R_X, R_Y and R_Z allows us to use the following linear, measurement model for the LOS kinematics in (3.49)

$$
\underbrace{\begin{bmatrix} y_1 \\ y_2 \\ y_3 \end{bmatrix}}_{Y} = \underbrace{\begin{bmatrix} 1 & 0 & 0 & 0 & 0 & 0 \\ 0 & 0 & 1 & 0 & 0 & 0 \\ 0 & 0 & 0 & 0 & 1 & 0 \end{bmatrix}}_{C} \underbrace{\begin{bmatrix} R_X \\ \dot{R}_X \\ R_Y \\ \dot{R}_Y \\ R_Z \\ \dot{R}_Z \end{bmatrix}}_{X} + \begin{bmatrix} \nu_X \\ \nu_Y \\ \nu_Z \end{bmatrix}
\tag{3.52}
$$

where ν_X, ν_Y and ν_Z are now state-dependent measurement noise terms.

Estimator Design Objective: The objective is to design a state estimator that can produce reliable estimates of the state vector $\left[R_X, \dot{R}_X, R_Y, \dot{R}_Y, R_Z, \dot{R}_Z\right]^T$ in Eq. (3.49) in the absence of knowledge of the target acceleration vector $\left[a_{T_X}, a_{T_Y}, a_{T_Z}\right]^T$ using only the noisy image measurements $\left[R_{X_m}, R_{Y_m}, R_{Z_m}\right]^T$.

We evaluate the adaptive state estimation approach on the basis of estimation accuracy of the range R, range-rate $\dot{R}$, azimuth rate $\dot{\lambda}_A$, elevation rate $\dot{\lambda}_E$, and the target acceleration $\left[a_{T_X},\ a_{T_Y},\ a_{T_Z}\right]^T$. These variables are the most important from point of view of implementation in the guidance law. The range, range-rate, azimuth rate and elevation rate terms are related to the states of the LOS kinematics model in Eq. (3.49) through the following relations:

$$\begin{aligned} R &= \sqrt{R_X^2 + R_Y^2 + R_Z^2} \\ \dot{R} &= \frac{R_X \dot{R}_X + R_Y \dot{R}_Y + R_Z \dot{R}_Z}{R} \end{aligned} \tag{3.53}$$

$$\begin{aligned} \lambda_A &= \tan^{-1}\left(\frac{R_Y}{R_X}\right) \\ \dot{\lambda}_A &= \frac{1}{\sqrt{R_X^2 + R_Y^2}}\left(\dot{R}_Y \cos\lambda_A - \dot{R}_X \sin\lambda_A\right) \end{aligned} \tag{3.54}$$

$$\begin{aligned} \lambda_E &= -\sin^{-1}\left(\frac{R_Z}{R}\right) \\ \dot{\lambda}_E &= -\frac{1}{R}\left[\dot{R}_Z \cos\lambda_E + \dot{R}_X \cos\lambda_A \sin\lambda_E + \dot{R}_Y \sin\lambda_A \sin\lambda_E\right] \end{aligned} \tag{3.55}$$

Note that even though the system in Eqs.(3.49) and (3.52) is multi-input multi-output (MIMO), each input-output channel is completely decoupled and we can use the theory developed in Section 3.2 for implementation.

B. Simulation Results and Discussion

We implement the composite adaptation based adaptive estimator for the system in Eqs. (3.49) and (3.52) and compare the performance with a linear, time-varying Kalman filter and the adaptive estimator in Ref. [63]. The linear, time-varying Kalman filter is designed using the relative LOS kinematics in Eq. (3.49) and linear measurement model in Eq. (3.52). The target acceleration components along the X, Y and Z axes are

modeled as independent, zero-mean, white noise processes in the design of the filter. The adaptive state estimator in Ref. [63] also augments a time-varying Kalman filter with a NN, but uses only one source of error signals, namely, the residuals of the filter to train the NN. The leader aircraft tracks waypoints in the inertial 3D space. The waypoints can be arranged so as to result in various target maneuvers. For example, in this chapter we consider two specific target maneuvers. The first target maneuver is the 'square-box trajectory' maneuver (Figure 5a). This maneuver is generated by making the target aircraft track waypoints at the corners of a square box in the horizontal plane. This maneuver is characterized by sharp heading changes at the corners of the square box followed by larger segments of constant velocity flight. The second target maneuver is a 'circular trajectory' maneuver (Figure 5b). This maneuver is generated by making the target aircraft track waypoints on a circle in the horizontal plane. The resulting target maneuver is a smaller amplitude maneuver than the square-box trajectory maneuver but the duration of constant velocity flight is much reduced in this case. The two maneuvers are thus different from each other and can be used to check the consistency of performance of the adaptive state estimation method presented in the previous sections.

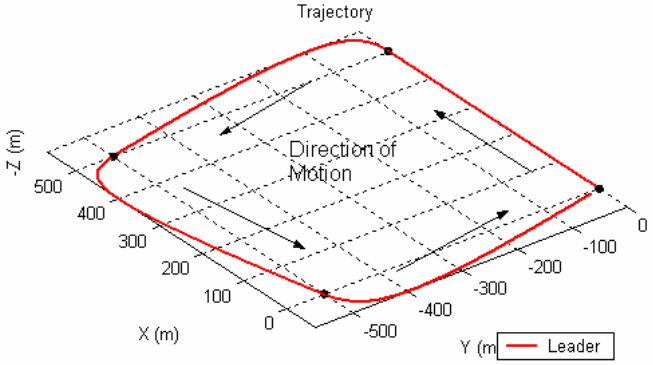

a

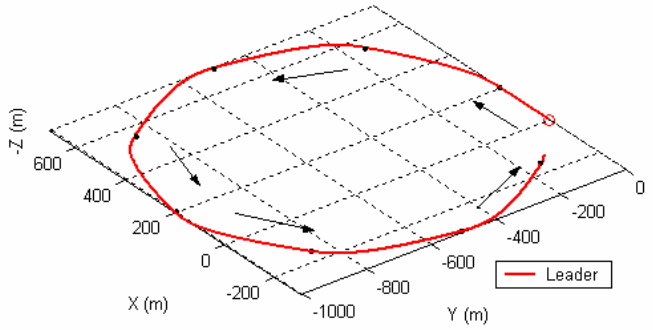

b

Figure 5. Leader Aircraft Trajectories (m), a) Square-box Trajectory, b) Circular Trajectory

The first sets of results are shown for the square-box trajectory target maneuver. Figure 6 shows the range estimation error in meters for the square-box trajectory target maneuver. Since the target size b is assumed to be known, the range estimate is expectedly quite accurate. The range estimation error in Figure 6c appears like white noise, indicating near optimal performance of the composite adaptation based state estimator. Figure 7 shows the azimuth-rate estimation performance. The sub-plots at the top of the Figure 7 show the true azimuth-rate (red solid line) and the estimated azimuth-rate (blue dashed line) in deg/s. The sub-plots at the bottom show the azimuth-rate estimation error in deg/s. At time $t = 20, 40$ and 60 s, the target initiates a heading change and Figure 7 shows that the estimation errors peak just after these target maneuvers. The reasons for the peaking of the estimation errors is that the white-noise process models used in the design of the Kalman filter are in no way representative of the true target acceleration components along the X, Y and Z axes. The estimation errors go towards zero when the target stops maneuvering. Comparing the performances of the estimators, it can be seen that the composite adaptation based state estimator results in estimation errors with the smaller peaks. This is most clearly visible right after the first target maneuver at about 20 seconds where the reduction in estimation error is at least 50 % smaller than with the other two estimators. The simulation is stopped at about 84 seconds when the leader aircraft reaches the last waypoint in the maneuver.

Figure 8 shows the range-rate estimation performance. This figure shows the significant reduction in the estimation error peak after the first target maneuver at about 20 seconds with the composite adaptation based state estimator compared with the other two estimators. The reason for the better performance of the composite adaptation based estimator is that the target maneuver is captured more accurately. This is shown in Figure 9. The 3 sub-plots show the target acceleration estimation along the inertial X, Y and Z axes respectively. The true acceleration is shown in red, and the target acceleration estimate, which is the output of the NN, is shown by the blue dashed line.

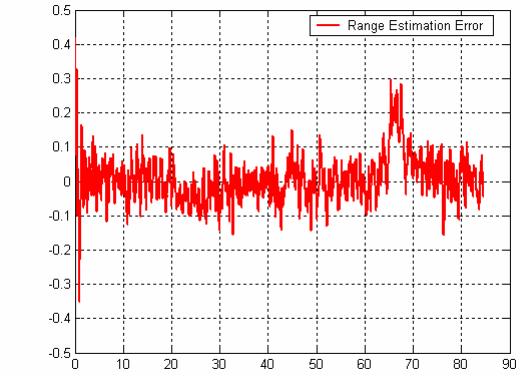

a

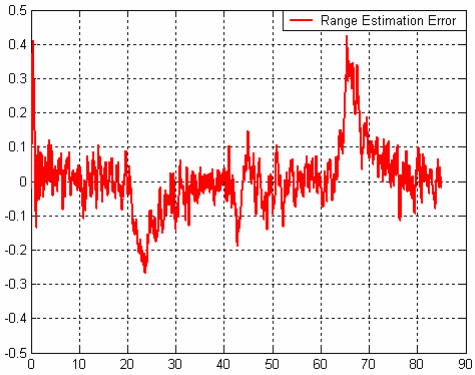

b

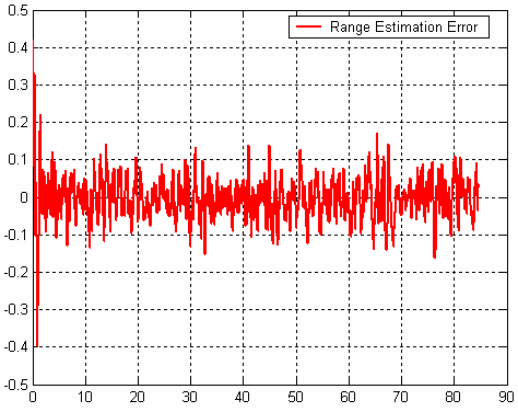

c

Figure 6. Range Estimation Error in meters, a) No Adaptation, b) Conventional Adaptation [63], and c) Composite Adaptation, Square-box Trajectory Maneuver

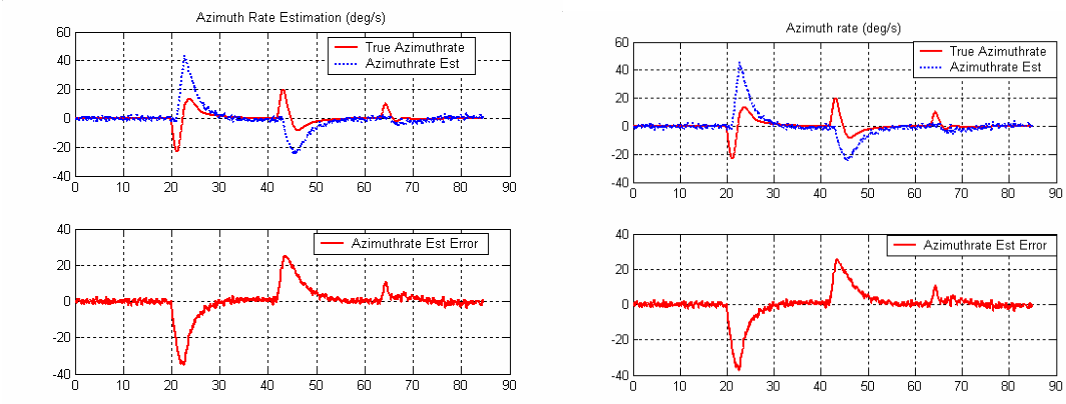

a **b**

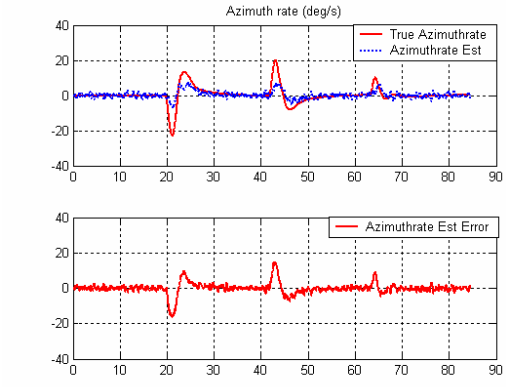

c

Figure 7. Azimuth-rate Estimation in deg/s, a) No Adaptation, b) Conventional Adaptation [63], and c) Composite Adaptation, Square-box Trajectory Maneuver

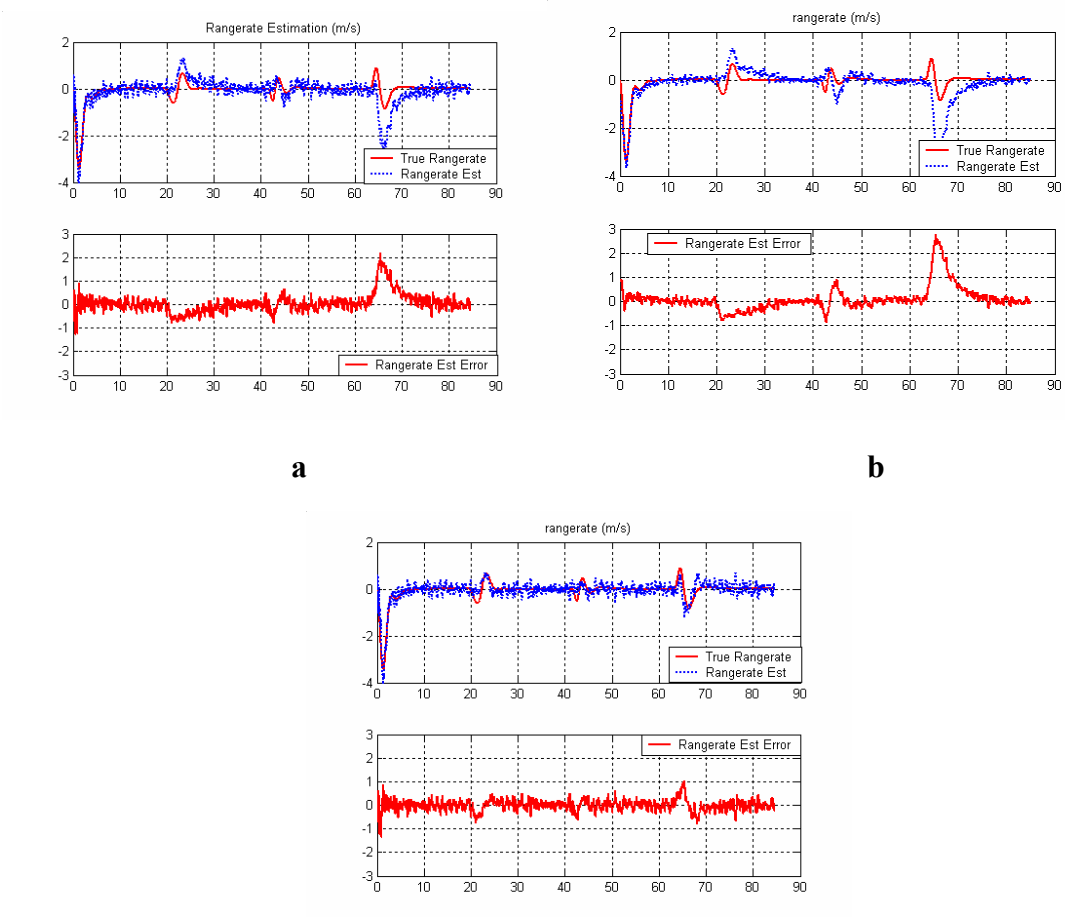

Figure 8. Range-rate Estimation Error in m/s, a) No Adaptation, b) Conventional Adaptation [63], and c) Composite Adaptation, Square-box Trajectory Maneuver

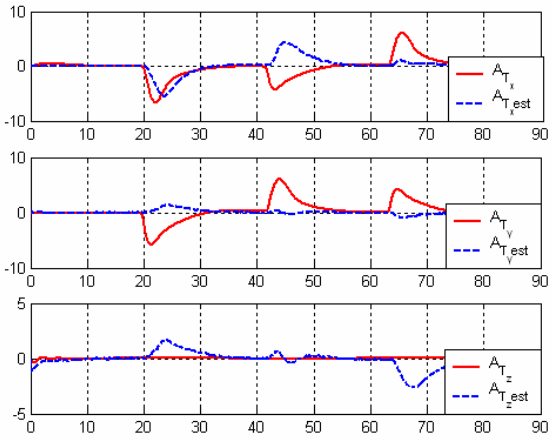

a

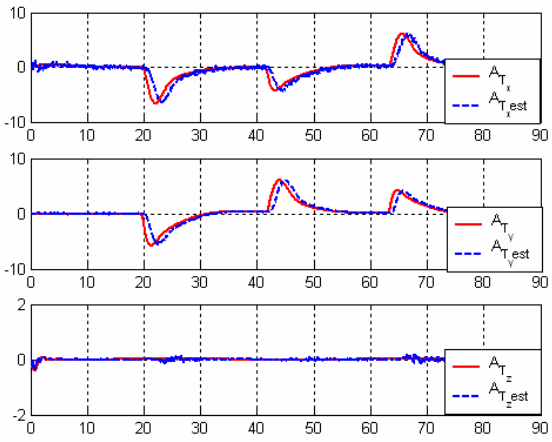

b

Figure 9. Target Acceleration Estimation in m/s^2, a) Conventional Adaptation [63], and b) Composite Adaptation, Square-box Trajectory Maneuver

The next sets of results are shown for the 'circular trajectory' target maneuver. For this case, we only show the plots that show significant differences in the estimation performance with the three estimators. Figure 10 shows the azimuth-rate estimation performance. It is seen again that the composite adaptation based state estimator results in estimation errors with the smallest peaks, up to 50% less than with the other two estimators. The estimation performance is consistent over the entire target maneuver. Figure 11 shows the target acceleration estimation performance with the two adaptive estimators. The composite adaptation based estimator again captures the target maneuver very accurately compared to the conventional adaptation based estimator. These results show that the target acceleration estimation performance does not change significantly when the target maneuver is changed.

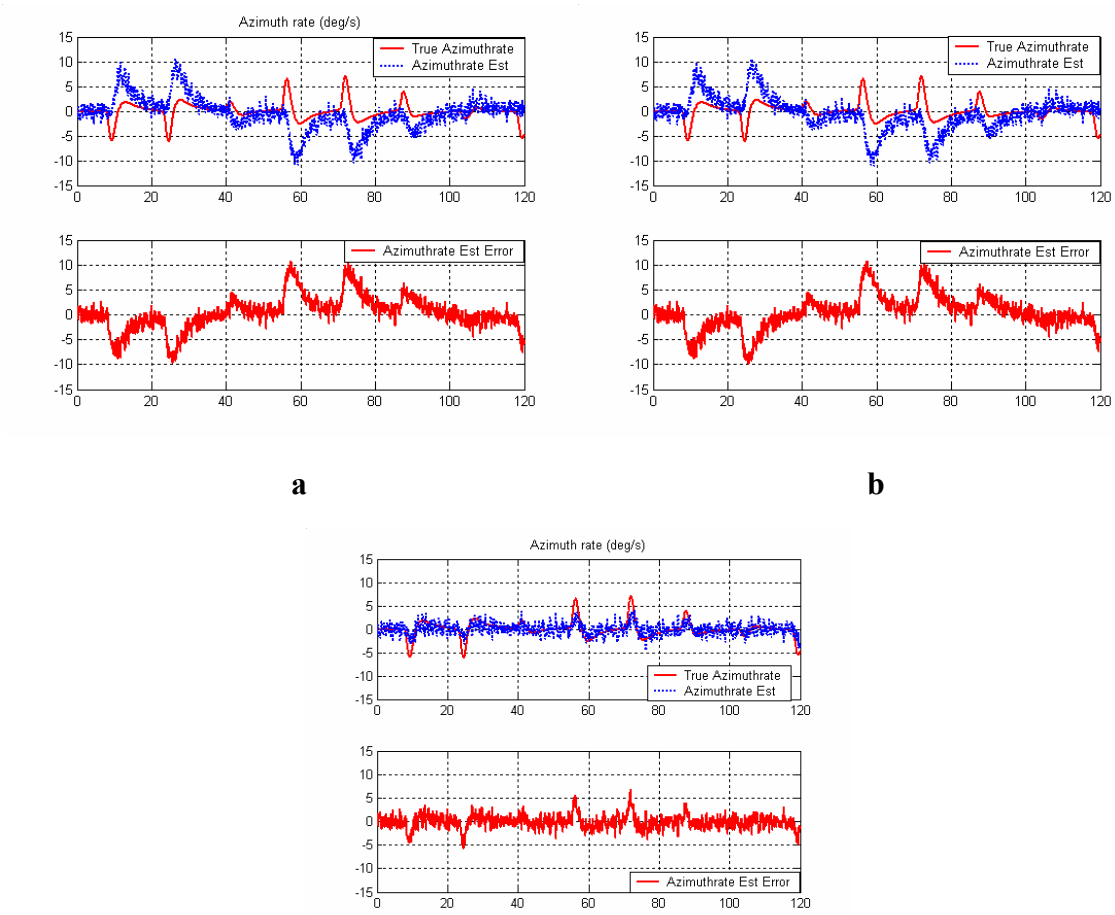

Figure 10. Azimuth-rate Estimation in deg/s, a) No Adaptation, b) Conventional Adaptation [63], c) Composite Adaptation, Circular Trajectory Maneuver

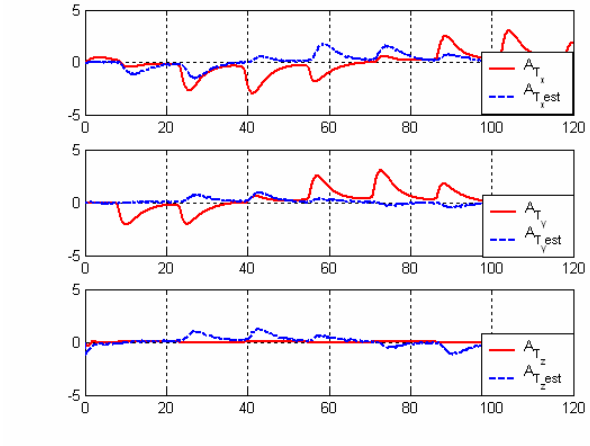

a

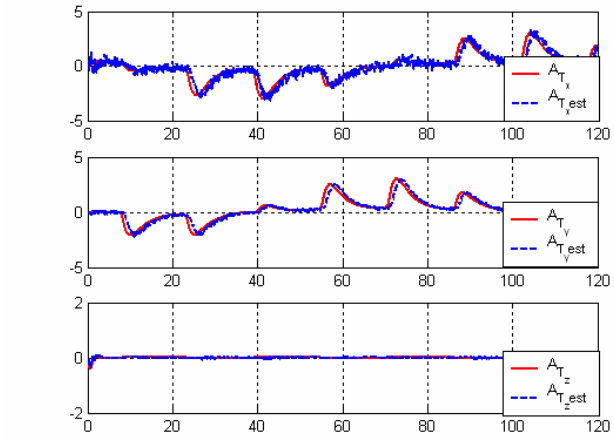

b

Figure 11. Target Acceleration Estimation in m/s^2, a) Conventional Adaptation [63], and b) Composite Adaptation, Circular Trajectory Maneuver

C. Validation in 6DOF Real-Time Simulation with Image Processing and Flight Tests

The adaptive state estimation algorithm presented in Sections 3.1-3.4 was integrated with the image processing, guidance and flight control algorithms in the Georgia Tech Unmanned Systems Testbed (GUST) Real-Time Simulation Software [108]. The image processing, a non-adaptive Extended Kalman Filter (EKF) as the target state estimator, and the guidance and flight control algorithms have been separately validated. These have been flight-tested in closed-loop and completely autonomous formation flight test results between two UAVs in a leader-follower configuration were reported in [109].

The adaptive state estimation algorithm is validated in software-in-the-loop simulations using the GUST software. Figure 12 shows a screenshot of the simulation. The 'src' screenshot is the frame-grabber window which is used by the image processing algorithm to capture the leader aircraft center (green crosshair) and wingtips (red crosshairs). The 'Scene Window 1' and 'Scene Window 2' screenshots depict the formation view from the top and from behind the follower aircraft respectively. The green circles in these screenshots depict the target estimator's estimate of the leader position.

The measurements obtained from the image processing are the unit vector in the camera fixed axes $\left[u_{x_m}, u_{y_m}, u_{z_m}\right]^T$ and the subtended angle α_m. The subscript *'m'* indicates measurement. The unit vector measurements are transformed into the inertial coordinate (NED) frame $\left[u_{Xm}, u_{Ym}, u_{Zm}\right]^T$. The linear, time-varying Kalman filter augmented by an adaptive NN in Section 3.3 is implemented as the adaptive target state estimator. The measurements to this filter are constructed as follows:

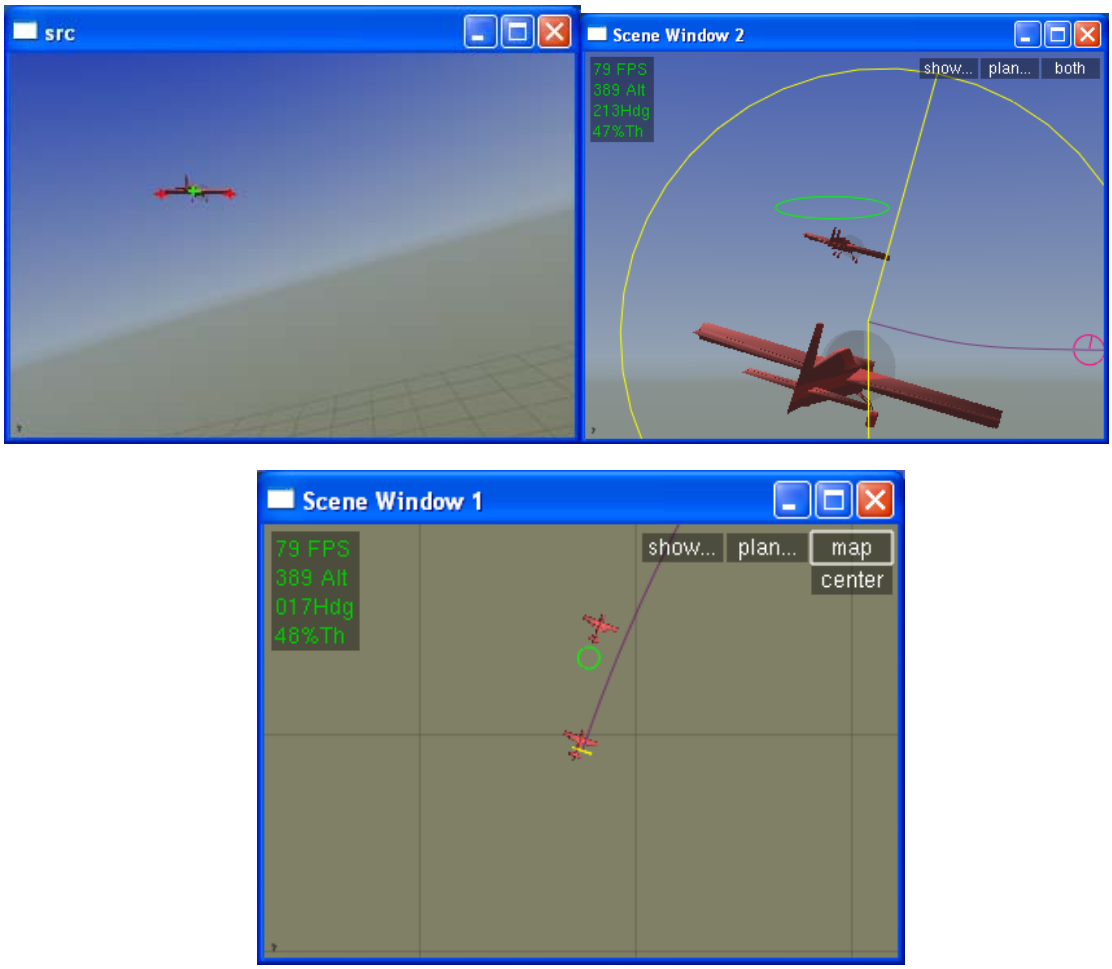

Figure 12. Screenshot of Vision-based Formation Flight in Real-Time Simulation

$$
\begin{aligned}
R_{Xm} &= \frac{b}{2\tan\left(\alpha_m/2\right)} u_{Xm} \\
R_{Ym} &= \frac{b}{2\tan\left(\alpha_m/2\right)} u_{Ym} \\
R_{Zm} &= \frac{b}{2\tan\left(\alpha_m/2\right)} u_{Zm}
\end{aligned}
\tag{3.56}
$$

where the target wing-span b is assumed to be known. The leader aircraft is flying in a circle in the horizontal plane at a constant heading rate. The follower aircraft is tasked

with maintaining specified separation distances along the x-, y- and z-axes of the follower body-fixed frame. The follower is first put into the desired formation using only GPS communicated data of the leader inertial position, velocity and acceleration. The leader GPS data is communicated at about 5 Hz and is filtered to produce leader state estimates at the rate required (~50 Hz) by the follower aircraft guidance and flight control algorithms. Once the leader aircraft is at the desired separation distance, the image processing and target state estimation algorithms are switched on. The estimates of the leader position, velocity and acceleration from using the vision-based target state estimator are blended in with the corresponding GPS estimates to produce the leader state estimates that are used in the guidance and flight control algorithms for formation keeping.

The formation separation commands for the results shown below are given by $[\mathrm{dx},\mathrm{dy},\mathrm{dz}]_{com} = [60,15,10]$ ft. Figure 13 shows the flags pertaining to the image processing and adaptive estimation. The 'IP flag' indicates if the image processing (IP) has returned a measurement. The 'useVision Fraction' flag indicates the fraction of the vision-based leader position, velocity and acceleration estimates used in the guidance law relative to GPS estimates of the same. Figure 13 shows that the vision estimates are first blended in (about 50 %) at about 140 seconds, and the vision estimates are in complete control of the follower aircraft at about 290 seconds. The 'NN switch' flag indicates if the NN augmenting the nominal Kalman filter is switched on/off.

Figure 14 plots the IP relative position measurements along the inertial coordinate axes along with their corresponding GPS measurements. On the right hand side, the difference between these measurements is shown. The apparent chattering in the plot is due to the chattering of the GPS measurements. This plot shows that the image processing measurements are consistent with the corresponding GPS measurements.

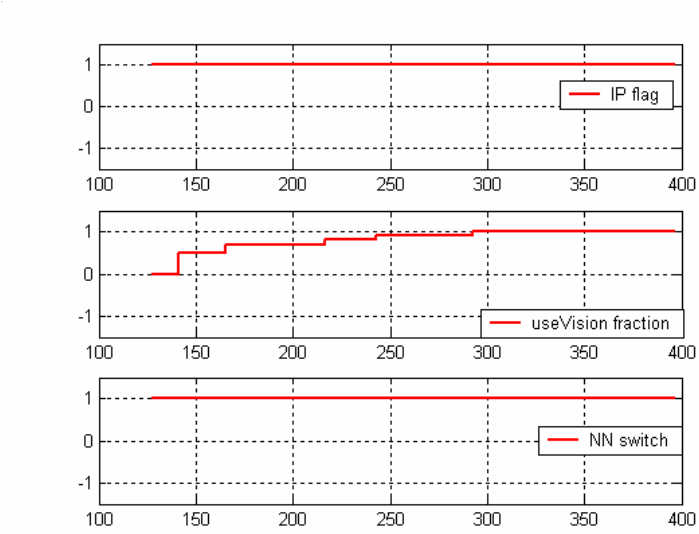

Figure 13. Image Processing (IP) flag, use Vision fraction, and NN on/off switch, with Adaptive Estimation

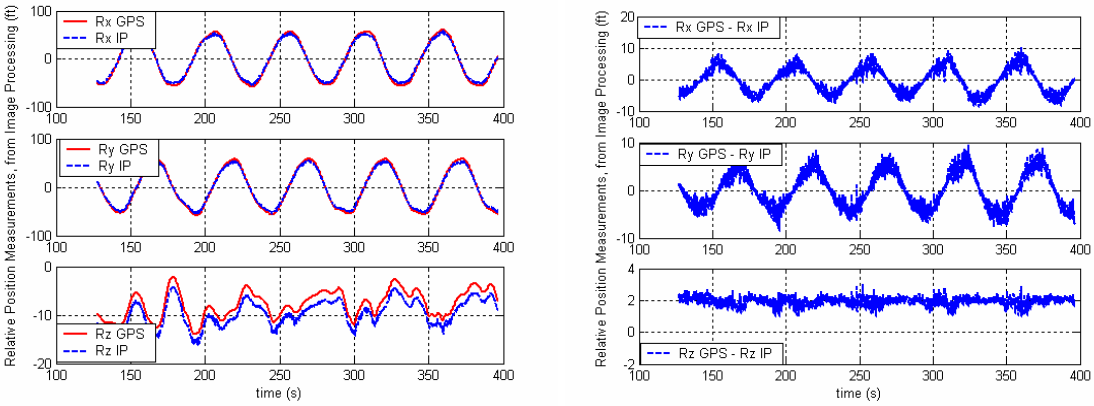

a b

Figure 14. IP Relative Position Measurements and corresponding GPS measurements (ft)

Figure 15 plots the formation position command tracking performance. The magnitudes of the tracking errors are within acceptable bounds, but there is clearly room for improvement. Since the overall control architecture involves integration of several different components, it is difficult to pinpoint the exact steps to take to improve the

performance. The accuracy of the tracking is definitely related to the accuracy of the image measurements relative to the GPS measurements shown in Figure 14. The image measurements chosen depend on the choice of the coordinates (rectangular or spherical) used to construct the target state estimator. At large separation distances, the subtended angle α_m becomes very small and the accuracy of the measurements in (3.56) is decreased. The target state estimator using the modified spherical coordinates [109] is more robust to inaccuracies in α_m.

Figure 16-Figure 18 show the leader position, velocity and acceleration estimation performance. In Figure 18, the estimates of the leader acceleration are the outputs of the adaptive state estimator. The plots show reasonable estimation performance.

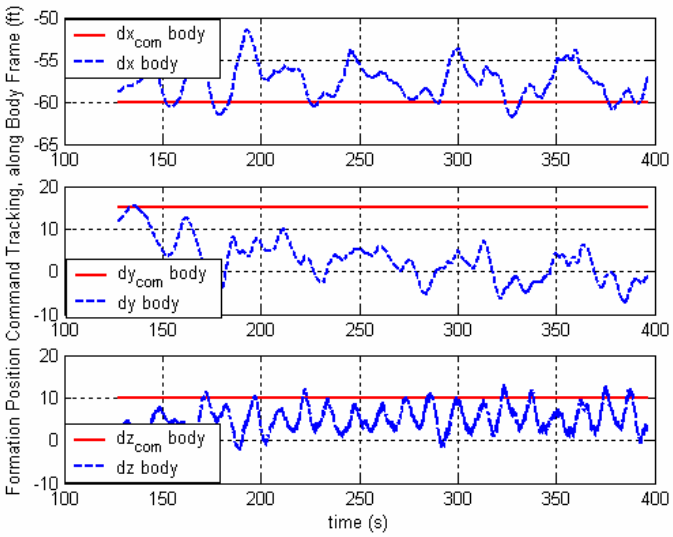

Figure 15. Formation Position Command Tracking, with blend of vision and GPS, Adaptive Estimation in the loop

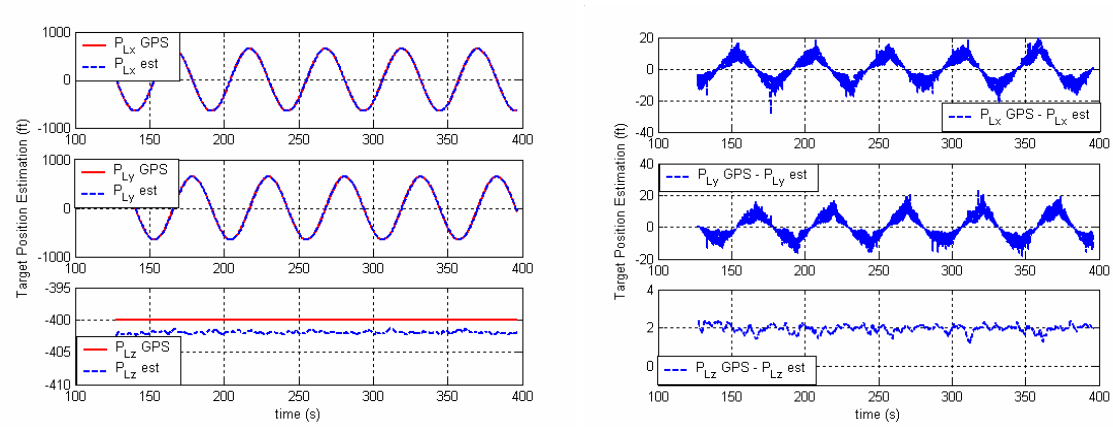

a b

Figure 16. Leader Position Estimation Performance (ft)

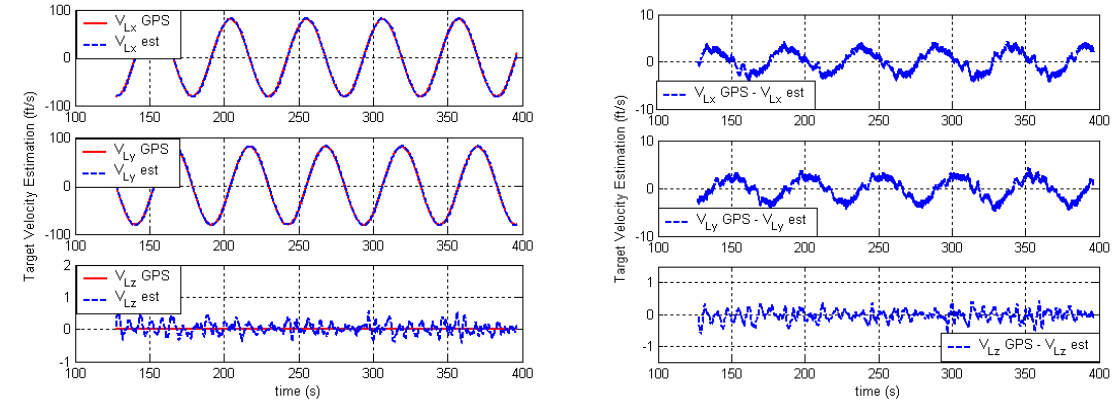

a b

Figure 17. Leader Velocity Estimation Performance (ft/s)

Figure 19 and Figure 20 show the result if the NN augmenting the Kalman filter is switched off. As soon as the vision estimates are blended in (20% vision at about 148 seconds), the 'IP' flag is temporarily zero suggesting loss of convergence. As the percentage of vision estimates used increases (40% vision at about 175 seconds), the range diverges. Without adaptation in the estimation, the leader aircraft just drifts out the field-of-view causing loss of visual track and ultimately range divergence.

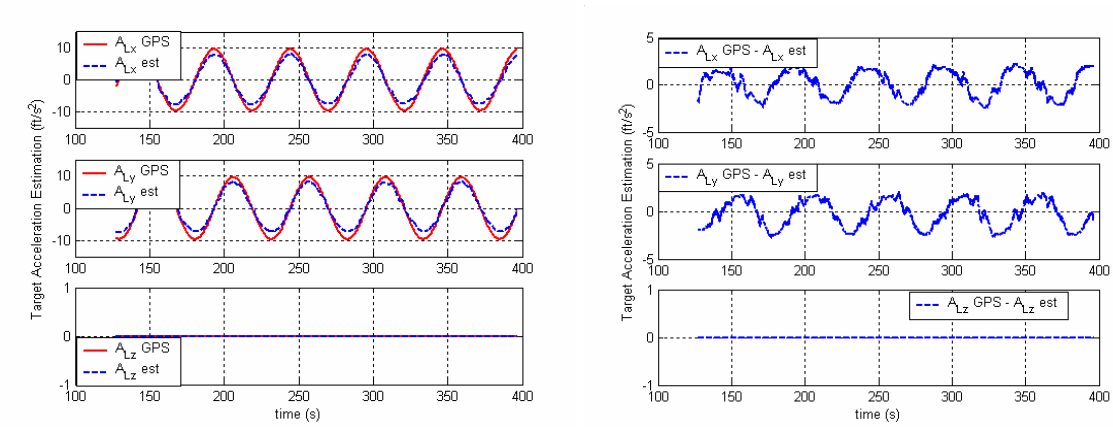

a b

Figure 18. Leader Acceleration Estimation Performance (ft/s^2)

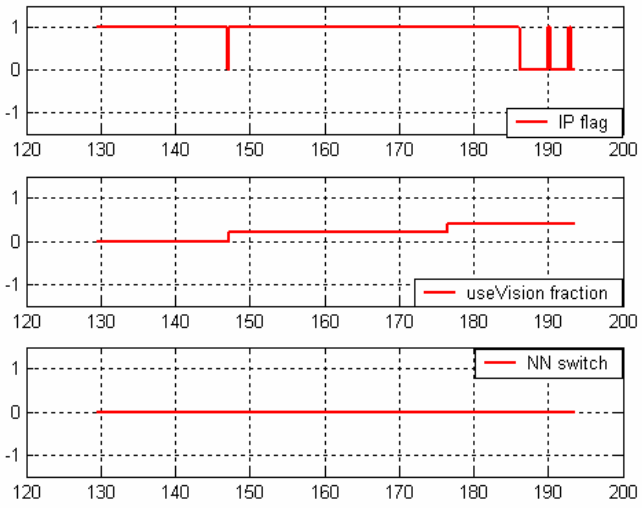

Figure 19. Image Processing (IP) flag, use Vision fraction, and NN on/off switch, without Adaptive Estimation

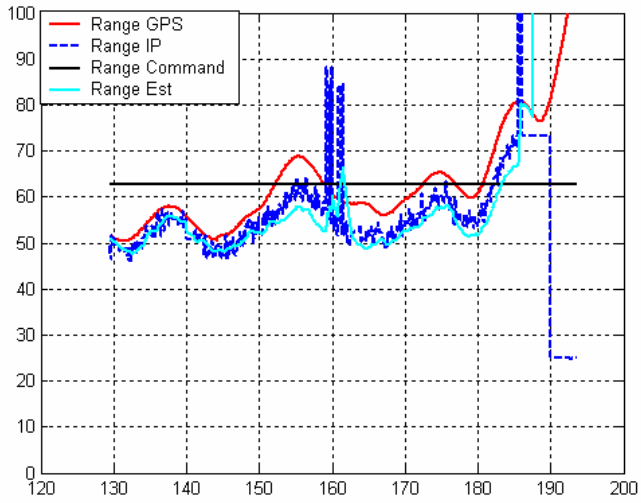

Figure 20. Range Estimation, without Adaptive Estimation

3.5 Extension to Multi-Input Multi-Output (MIMO) Systems

This section presents an extension of the composite adaptation approach to partial state estimation of the class of MIMO nonlinear systems given by

$$\begin{aligned} \dot{\boldsymbol{x}} &= A\boldsymbol{x} + B\boldsymbol{g}(\boldsymbol{x},\boldsymbol{z}), \qquad \boldsymbol{x}(0) = \boldsymbol{x}_0 \\ \dot{\boldsymbol{z}} &= \boldsymbol{f}_z(\boldsymbol{x},\boldsymbol{z}), \qquad\quad \boldsymbol{z}(0) = \boldsymbol{z}_0 \\ \boldsymbol{y} &= C\boldsymbol{x} \end{aligned} \tag{3.57}$$

where the conditions on the system are the same as described in the problem formulation in Section 3.1 with the exception that $\boldsymbol{g}(\boldsymbol{x},\boldsymbol{z}) : R^{n_x} \times R^{n_z} \to R^m$ and $\boldsymbol{y} \in \Re^m$ are column vectors, and $B \in \Re^{n_x \times m}$ and $C \in \Re^{m \times n_x}$ are known, constant matrices of full column and row rank respectively.

The procedure for deriving the second error signal to train the NN is the only thing that is notably different from the SISO case and this is discussed below. The following equation is written to facilitate this derivation. The vector $B\boldsymbol{g}(\boldsymbol{x},\boldsymbol{z})$ is written as follows:

$$B\boldsymbol{g}(\boldsymbol{x},\boldsymbol{z}) = \sum_{i=1}^{m} \boldsymbol{b}_i g_i'(\boldsymbol{x},\boldsymbol{z}) \tag{3.58}$$

where $\boldsymbol{b}_i$ is a column vector of zeros with only the i^{th} element equal to 1. We assume that the following NN parameterization for $g_i'(\boldsymbol{x},\boldsymbol{z})$ similar to the parameterization in (3.2):

$$\begin{aligned} g_i'(\boldsymbol{x},\boldsymbol{z}) &= \boldsymbol{W}_i^T \boldsymbol{\sigma}(\bar{\boldsymbol{\mu}}) + \varepsilon_i'(\bar{\boldsymbol{\mu}}), \quad \|\boldsymbol{W}_i\|_F \le W_i^* \le W^*, \quad \|\varepsilon_i'(\bar{\boldsymbol{\mu}})\| \le \varepsilon_i^* \le \varepsilon^*, \\ \bar{\boldsymbol{\mu}} &\in B_{\mu^*} = \{\bar{\boldsymbol{\mu}} \mid \|\bar{\boldsymbol{\mu}}\| \le \mu^*\}, \quad i = 1,2,\cdots,m \end{aligned} \tag{3.59}$$

$\forall(\boldsymbol{x},\boldsymbol{z}) \in D_g \subset D_x \text{ x } D_z$, where D_g is a compact set. Using Eqs. (3.59) and (3.58) in (3.57), we have,

$$\begin{aligned} \dot{\boldsymbol{x}} &= A\boldsymbol{x} + \sum_i^m \boldsymbol{b}_i \boldsymbol{W}_i^T \boldsymbol{\sigma}(\bar{\boldsymbol{\mu}}) + \sum_i^m \boldsymbol{b}_i \varepsilon_i'(\bar{\boldsymbol{\mu}}), \qquad \boldsymbol{x}(0) = \boldsymbol{x}_0 \\ \dot{\boldsymbol{z}} &= \boldsymbol{f}_z(\boldsymbol{x},\boldsymbol{z}), \qquad\qquad z(0) = z_0 \\ \boldsymbol{y} &= C\boldsymbol{x} \end{aligned} \tag{3.60}$$

The NN augmented Kalman estimator for the system in (3.60) is given by:

$$\begin{aligned} \dot{\hat{\boldsymbol{x}}}(t) &= A\hat{\boldsymbol{x}}(t) + K(t)\big(\boldsymbol{y}(t) - \hat{\boldsymbol{y}}(t)\big) + \sum_i^m \boldsymbol{b}_i \hat{\boldsymbol{W}}_i^T(t)\boldsymbol{\sigma}(\bar{\boldsymbol{\mu}}), \qquad \hat{\boldsymbol{x}}(0) = \hat{\boldsymbol{x}}_0 \\ \hat{\boldsymbol{y}}(t) &= C\hat{\boldsymbol{x}}(t) \end{aligned} \tag{3.61}$$

where $K(t)$ is given as in (3.5), $\hat{\boldsymbol{W}}_i$ is an estimate for the ideal but unknown NN weight vector $\boldsymbol{W}_i$. The residual vector $\tilde{\boldsymbol{y}}(t) = \boldsymbol{y}(t) - \hat{\boldsymbol{y}}(t)$ is the first training signal for the NN. Next, we will show the derivation of the second training signal for the NN using the non-adaptive Kalman estimator given by

$$\begin{aligned} \dot{\hat{\boldsymbol{x}}}_1(t) &= A\hat{\boldsymbol{x}}_1(t) + K_1(t)\big(\boldsymbol{y}(t) - \hat{\boldsymbol{y}}_1(t)\big), \qquad \hat{\boldsymbol{x}}_1(0) = \hat{\boldsymbol{x}}_{10} \\ \hat{\boldsymbol{y}}_1(t) &= C\hat{\boldsymbol{x}}_1(t) \end{aligned} \tag{3.62}$$

The state estimation error dynamics for the non-adaptive Kalman filter become

$$\begin{aligned}\dot{\tilde{\boldsymbol{x}}}_1 &= \bar{A}_1(t)\,\tilde{\boldsymbol{x}}_1 + \sum_i^m \boldsymbol{b}_i \boldsymbol{W}_i^T \boldsymbol{\sigma}(\bar{\boldsymbol{\mu}}) + \sum_i^m \boldsymbol{b}_i \varepsilon_i'(\bar{\boldsymbol{\mu}}) \\ \tilde{\boldsymbol{y}}_1 &= C\tilde{\boldsymbol{x}}_1\end{aligned} \tag{3.63}$$

where $\bar{A}_1(t) = A - K_1(t)C$, $\tilde{\boldsymbol{x}}_1 \triangleq \boldsymbol{x} - \hat{\boldsymbol{x}}_1$ and $\tilde{\boldsymbol{y}}_1 \triangleq \boldsymbol{y} - \hat{\boldsymbol{y}}_1$. The time domain solution for the residual $\tilde{\boldsymbol{y}}_1$ of the non-adaptive Kalman filter is given by:

$$\tilde{\boldsymbol{y}}_1(t) = C\Phi(t,t_0)\tilde{\boldsymbol{x}}_1(t_0) + \sum_i^m \int_{t_0}^t C\Phi(t,\tau)\boldsymbol{b}_i \boldsymbol{W}_i^T \boldsymbol{\sigma}(\bar{\boldsymbol{\mu}})\; d\tau + \sum_i^m \int_{t_0}^t C\Phi(t,\tau)\boldsymbol{b}_i \varepsilon_i'\; d\tau \tag{3.64}$$

where $\Phi(t,t_0)$ is the state transition matrix associated with the matrix $\bar{A}_1(t)$. Eq. (3.64) can be re-written as

$$\tilde{\boldsymbol{y}}_1(t) = T\left(\tilde{\boldsymbol{x}}_1(t_0), \varepsilon_{f1}', \varepsilon_{f2}', \cdots, \varepsilon_{fm}'\right) + \sum_i^m \int_{t_0}^t \underbrace{\left[C\Phi(t,\tau)\boldsymbol{b}_i \boldsymbol{\sigma}^T(\bar{\boldsymbol{\mu}})\, d\tau\right]}_{Q_{fi}} \boldsymbol{W}_i^T \tag{3.65}$$

where $T\left(\tilde{\boldsymbol{x}}_1(t_0), \varepsilon_{f1}', \varepsilon_{f2}', \cdots, \varepsilon_{fm}'\right) = C\Phi(t,t_0)\tilde{\boldsymbol{x}}_1(t_0) + \sum_i^m \int_{t_0}^t C\Phi(t,\tau)\boldsymbol{b}_i \varepsilon_i'\; d\tau$ is an unknown vector that is always bounded using the result of *Lemma 3.1*, and Q_{fi} is the filtered basis function *matrix* obtained by solving the following matrix differential equation:

$$\begin{aligned}\dot{\Omega}_{fi} &= \bar{A}_1(t)\Omega_{fi} + \boldsymbol{b}_i \boldsymbol{\sigma}^T(\bar{\boldsymbol{\mu}}), \;\; \Omega_{fi}(t_0) = 0 \\ Q_{fi} &= C\Omega_{fi}\end{aligned} \tag{3.66}$$

The matrix $\Omega_{fi} \in \Re^{n_x \text{ x } N}$, N is the number of neurons, is always bounded, again using the result of *Lemma 3.1* and the output matrix $Q_{fi} \in \Re^{m \text{ x } N}$ is similarly bounded. An estimate of $\tilde{\boldsymbol{y}}_1(t)$ is obtained by using $\hat{\boldsymbol{W}}_i$ in place of $\boldsymbol{W}_i$ in (3.65)

$$\hat{\tilde{\boldsymbol{y}}}_1(t) = \sum_i^m Q_{fi}\hat{\boldsymbol{W}}_i \tag{3.67}$$

So, the second error signal to train the NN is given by

$$\boldsymbol{e}_1(t) = \tilde{\boldsymbol{y}}_1(t) - \hat{\tilde{\boldsymbol{y}}}_1(t) = T\left(\tilde{\boldsymbol{x}}_1(t_0), \varepsilon'_{f1}, \varepsilon'_{f2}, \cdots, \varepsilon'_{fm}\right) + \sum_i^m Q_{fi}\tilde{\boldsymbol{W}}_i \tag{3.68}$$

The NN weight update law is given by

$$\dot{\hat{\boldsymbol{W}}}_i = -\Gamma_{W_i}\left\{-\boldsymbol{\sigma}(\bar{\boldsymbol{\mu}})\tilde{y}_i - Q_{fi}^T\boldsymbol{e}_1 + \lambda_W\hat{\boldsymbol{W}}_i\right\} \tag{3.69}$$

where $\tilde{y}_i$ is the i^{th} element of the residual vector $\tilde{\boldsymbol{y}}$ and $\Gamma_{W_i} > 0$ and $\lambda_W > 0$ are the NN design constants.

The error boundedness analysis for the MIMO case follows exactly the same steps as for the SISO case. The details are skipped here and simply referred to the Proof of Theorem 3.1 and Theorem 6.1 in Chapter 6.

3.6 Conclusions

A composite adaptation approach to the partial state estimation of a class of nonlinear systems with unmodeled dynamics is presented. The state estimator is a linear, time-varying Kalman filter augmented with an adaptive neural network. The key benefit of the composite adaptation approach over a conventional approach to adaptive state estimation [63] is faster and more accurate approximation of the modeling errors that degrade the accuracy of the estimation process. Another benefit of the adaptive approach to state estimation is the limited reliance on elaborate target maneuver models for target tracking.

CHAPTER 4

ADAPTIVE GUIDANCE AND CONTROL DESIGN FOR LINE-OF-SIGHT FORMATION FLIGHT

This chapter presents an adaptive approach to the guidance and control design for a follower aircraft maintaining range from a maneuvering leader aircraft. The approach is based on a deterministic, perfect-information scenario, i.e., it is assumed that the true values of range and line-of-sight (LOS) angles are available for feedback. The objective of the guidance and control design is for the follower aircraft to regulate the range and LOS rates to commanded values. The LOS angles are not regulated since it is not desirable to restrict the follower aircraft to a particular orientation with respect to the leader aircraft, particularly in the presence of leader maneuvers. The LOS rates are obtained by low-pass differentiation on the LOS angles. The range and LOS rate kinematics are inverted to obtain inertial acceleration commands for the follower aircraft. The inertial acceleration commands are transformed to body-axes specific force and bank angle commands and sent to the autopilot. Neural network (NN) based adaptation is included in the guidance law design to compensate for unknown leader aircraft maneuvers and neglected LOS kinematics. This approach assumes that there is a natural time-scale separation between the guidance related variables (slow LOS kinematics) and the autopilot related variables (fast attitude dynamics). The autopilot includes NN based adaptation to compensate for uncertainty in the aircraft dynamics. The adaptive guidance and control design for the follower aircraft is applied in a nonlinear, 6 DOF fixed-wing aircraft simulation. The leader aircraft tracks waypoints in the 3D inertial coordinate space. Simulation results for different leader maneuvers are presented and discussed.

Equation Chapter 4 Section 1

4.1 Follower Aircraft Guidance

A. Problem Formulation

Consider the normal form [98] of a Multi-Input Multi-Output (MIMO) nonlinear system given by

$$\begin{aligned}
&\dot{\boldsymbol{Z}} = \boldsymbol{f}_{\boldsymbol{Z}}\left(\boldsymbol{\xi}, \boldsymbol{Z}\right) \\
&\dot{\xi}_i^1 = \xi_i^2 \\
&\quad \vdots \\
&\dot{\xi}_i^{(r_i-1)} = \xi_i^{(r_i)} \\
&\dot{\xi}_i^{(r_i)} = \alpha_i^0\left(\boldsymbol{\xi}\right) + \alpha_i^1\left(\boldsymbol{\xi}, \boldsymbol{Z}\right) + \beta_i\left(y_1, \cdots, y_m\right) u_i \\
&y_i = \xi_i^1, \quad i = 1, 2, \cdots, m
\end{aligned} \tag{4.1}$$

where $\boldsymbol{\xi} \triangleq \left[\begin{array}{cccccccc} \xi_i^1 & \xi_i^2 & \cdots & \xi_i^{(r_i)} & \cdots & \xi_m^1 & \xi_m^2 & \cdots & \xi_m^{(r_m)} \end{array}\right]^T \in D_\xi \subset \Re^r$, $\boldsymbol{Z} \in D_{\boldsymbol{Z}} \subset \Re^{n-r}$ are the states associated with the internal dynamics, u_i are the control inputs, y_i are the regulated outputs, r_i is the relative degree of the i^{th} output, and $r = r_1 + r_2 + \cdots r_m \leq n$. $\boldsymbol{f}_{\boldsymbol{Z}}\left(\boldsymbol{\xi}, \boldsymbol{Z}\right)$ is a completely unknown continuous function, $\alpha_i^1\left(\boldsymbol{\xi}, \boldsymbol{Z}\right)$ and $\beta_i\left(y_1, \cdots, y_m\right)$ are partially known continuous functions, $\alpha_i^0\left(\boldsymbol{\xi}\right)$ is a known continuous function. Let $\boldsymbol{x} \triangleq \left[\boldsymbol{\xi}^T, \boldsymbol{Z}^T\right]^T \in D_x \subset \Re^n$ be the state vector of the system where $D_x = D_\xi \text{ x } D_{\boldsymbol{Z}}$.

Assumption 4.1: $\beta_i\left(y_1, \cdots, y_m\right)$ is continuous and non-zero for every $\boldsymbol{x} \in D_x$.

Assumption 4.2: The function $\boldsymbol{f}_{\boldsymbol{Z}}\left(\cdot, \cdot\right)$ is a bounded function of its arguments and $\boldsymbol{Z}\left(t\right)$ is bounded for all t.

Remark 4.1: The normal form in (4.1) is an adequate representation for the LOS kinematics which are of interest in designing the adaptive guidance law. In (4.1), the states $\boldsymbol{\xi}$ represent the states associated with the LOS kinematics, namely, the range, LOS

angles and their rates. The regulated outputs y_i refer to outputs of interest from the formation control point of view, which in this case are the range and the azimuth and elevation components of LOS rate. The states $\boldsymbol{Z}$ represent the bounded accelerations of the leader aircraft. The functions $\alpha_i^1(\boldsymbol{\xi}, \boldsymbol{Z})$ represent how the leader acceleration terms influence the LOS kinematics. Likewise, the term $\beta_i(y_1, \cdots, y_m)u_i$ represents the influence of the follower accelerations or control inputs u_i on the LOS kinematics.

Control Design Objective: Design a control law as a function of available measurements such that $y_i(t)$ track smooth, bounded reference trajectories $y_{c,i}(t)$, $i = 1, 2, \cdots, m$ with bounded errors.

Remark 4.2: The LOS formation flight problem formulated above can be treated using the theory for MIMO Adaptive Output Feedback Control [95], [96]. In the following sub-sections, an adaptive guidance law is derived by applying the theory in Ref. [96]. The objective is to regulate the range and LOS rates with respect to the leader aircraft to commanded values. The steps in the design include the derivation of LOS kinematics, NN augmented dynamic inversion of the LOS kinematics to give the commanded follower accelerations, followed by transformation of the commanded accelerations into appropriate autopilot commands.

B. Derivation of LOS Kinematics

The local North-East-Down (NED) coordinate frame is assumed to be the inertial coordinate axes for the derivation of the LOS kinematics. We also assume that the NED frame is parallel to the Vehicle-Carried frame, which is a frame attached to the body of the follower aircraft and translating with the follower aircraft. These are reasonable assumptions in small UAV applications where the UAVs don't fly at very high altitudes

or at very high (supersonic or faster) speeds. The LOS variables in spherical coordinates consist of the range (R) to the leader, azimuth angle (λ_A) from the inertial X-axis to the projection of the LOS vector onto the X-Y plane, and elevation angle (λ_E) to the horizontal (inertial X-Y plane). These are depicted in Figure 4. The relationships between the rectangular inertial frame components of the LOS range vector R_X, R_Y, R_Z and the spherical coordinate components R, λ_A and λ_E are given by Eqs. (3.50), (3.53)-(3.55). The first derivatives of R, λ_A and λ_E given by Eqs. (3.53)-(3.55) are repeated below for convenience:

$$\dot{R} = \dot{R}_X \cos\lambda_A \cos\lambda_E + \dot{R}_Y \sin\lambda_A \cos\lambda_E - \dot{R}_Z \sin\lambda_E \tag{4.2}$$

$$\dot{\lambda}_A = \frac{1}{R\cos\lambda_E}\left(-\dot{R}_X \sin\lambda_A + \dot{R}_Y \cos\lambda_A\right) \tag{4.3}$$

$$\dot{\lambda}_E = -\frac{1}{R}\left(\dot{R}_X \cos\lambda_A \sin\lambda_E + \dot{R}_Y \sin\lambda_A \sin\lambda_E + \dot{R}_Z \cos\lambda_E\right) \tag{4.4}$$

where $\dot{R}_X, \dot{R}_Y, \dot{R}_Z$ denote the relative velocity components between the leader and follower aircraft expressed in the rectangular inertial coordinate system. The inverse relationships between $\dot{R}_X, \dot{R}_Y, \dot{R}_Z$ and $\dot{R}$, $\dot{\lambda}_A$ and $\dot{\lambda}_E$ are given as follows:

$$\dot{R}_X = \dot{R}\cos\lambda_A \cos\lambda_E - R\dot{\lambda}_A \sin\lambda_A \cos\lambda_E - R\dot{\lambda}_E \cos\lambda_A \sin\lambda_E \tag{4.5}$$

$$\dot{R}_Y = \dot{R}\sin\lambda_A \cos\lambda_E + R\dot{\lambda}_A \cos\lambda_A \cos\lambda_E - R\dot{\lambda}_E \sin\lambda_A \sin\lambda_E \tag{4.6}$$

$$\dot{R}_Z = -\dot{R}\sin\lambda_E - R\dot{\lambda}_E \cos\lambda_E \tag{4.7}$$

Differentiating Eqs. (4.2)-(4.4) and utilizing Eqs. (4.5)-(4.7), the following relationships between the relative accelerations and the second time derivatives of the range and LOS angles are derived:

$$\ddot{R} = R\left[\dot{\lambda}_A^2 \cos^2\lambda_E + \dot{\lambda}_E^2\right] + \left[a_X \cos\lambda_A \cos\lambda_E + a_Y \sin\lambda_A \cos\lambda_E - a_Z \sin\lambda_E\right] \tag{4.8}$$

$$\ddot{\lambda}_A = \frac{1}{\cos\lambda_E}\left\{-2\dot{\lambda}_A\left[\left(\frac{\dot{R}}{R}\right)\cos\lambda_E - \dot{\lambda}_E\sin\lambda_E\right] + \left(\frac{1}{R}\right)\left[-a_X\sin\lambda_A + a_Y\cos\lambda_A\right]\right\} \tag{4.9}$$

$$\begin{aligned}\ddot{\lambda}_E = &-2\left(\frac{\dot{R}}{R}\right)\dot{\lambda}_E - \dot{\lambda}_A^2\sin\lambda_E\cos\lambda_E \\ &-\left(\frac{1}{R}\right)\left[a_X\cos\lambda_A\sin\lambda_E + a_Y\sin\lambda_A\sin\lambda_E + a_Z\cos\lambda_E\right]\end{aligned} \tag{4.10}$$

where $a_X = a_{L_X} - a_{F_X} \equiv \ddot{R}_X$, $a_Y = a_{L_Y} - a_{F_Y} \equiv \ddot{R}_Y$, $a_Z = a_{L_Z} - a_{F_Z} \equiv \ddot{R}_Z$ are the relative accelerations of the leader with respect to the follower in the rectangular coordinates. Subscripts '*L*' and '*F*' denote leader and follower aircraft, respectively. The right hand sides of Eqs. (4.8)-(4.10) can be simplified as:

$$\ddot{R} = R\left[\dot{\lambda}_A^2\cos^2\lambda_E + \dot{\lambda}_E^2\right] + \left[a_{L_R} - a_{F_R}\right] \tag{4.11}$$

$$\ddot{\lambda}_A = \frac{1}{\cos\lambda_E}\left\{-2\dot{\lambda}_A\left[\left(\frac{\dot{R}}{R}\right)\cos\lambda_E - \dot{\lambda}_E\sin\lambda_E\right] + \left(\frac{1}{R}\right)\left[a_{L_{\lambda,A}} - a_{F_{\lambda,A}}\right]\right\} \tag{4.12}$$

$$\ddot{\lambda}_E = -2\left(\frac{\dot{R}}{R}\right)\dot{\lambda}_E - \dot{\lambda}_A^2\sin\lambda_E\cos\lambda_E - \left(\frac{1}{R}\right)\left[a_{L_{\lambda,E}} - a_{F_{\lambda,E}}\right] \tag{4.13}$$

where the terms a_{L_R}, $a_{L_{\lambda,A}}$, $a_{L_{\lambda,E}}$ represent leader aircraft accelerations along the LOS and perpendicular to the LOS respectively, and likewise for the follower aircraft.

C. Dynamic Inversion of LOS Kinematics

Eqs. (4.11)-(4.13) are inverted to construct the follower aircraft acceleration commands. The first step in the dynamic inversion process is to re-write Eqs. (4.11)-(4.13) as

$$\ddot{R} = \nu_R + \left\{R\left(\dot{\lambda}_E^2 + \dot{\lambda}_A^2\cos^2\lambda_E\right) + a_{L_R}\right\} = \nu_R + \Delta_R \tag{4.14}$$

$$\ddot{\lambda}_A = \nu_{\lambda_A} + \frac{1}{\cos\lambda_E}\left\{-2\dot{\lambda}_A\left[\left(\frac{\dot{R}}{R}\right)\cos\lambda_E - \dot{\lambda}_E\sin\lambda_E\right] + \left(\frac{a_{L_{\lambda,A}}}{R}\right)\right\} = \nu_{\lambda_A} + \Delta_{\lambda_A} \tag{4.15}$$

$$\ddot{\lambda}_E = \nu_{\lambda_E} + \left[-2\left(\frac{\dot{R}}{R}\right)\dot{\lambda}_E - \dot{\lambda}_A^2 \sin\lambda_E \cos\lambda_E - \left(\frac{a_{L_{\lambda,E}}}{R}\right)\right] = \nu_{\lambda_E} + \Delta_{\lambda_E} \tag{4.16}$$

where ν_R, ν_{λ_A} and ν_{λ_E} are the so-called 'pseudo-controls'. These represent an approximation of the $\ddot{R}$, $\ddot{\lambda}_A$ and $\ddot{\lambda}_E$ dynamics. The terms Δ_R, Δ_{λ_A} and Δ_{λ_E} represent the inversion error due to the terms that are ignored in the approximation. From Eqs. (4.11)-(4.16), we have:

$$\nu_R = -a_{F_R} \tag{4.17}$$

$$\nu_{\lambda_A} = \frac{-a_{F_{\lambda,A}}}{R\cos\lambda_E} \tag{4.18}$$

$$\nu_{\lambda_E} = \frac{a_{F_{\lambda,E}}}{R} \tag{4.19}$$

The acceleration commands in the spherical coordinates for the follower aircraft are thus given by:

$$a_{F_{R,com}} = -\nu_R \tag{4.20}$$

$$a_{F_{\lambda,A,com}} = -R\cos\lambda_E \nu_{\lambda_A} \tag{4.21}$$

$$a_{F_{\lambda,E,com}} = R\nu_{\lambda_E} \tag{4.22}$$

where ν_R, ν_{λ_A} and ν_{λ_E} are constructed such that they represent desired $\ddot{R}$, $\ddot{\lambda}_A$ and $\ddot{\lambda}_E$ dynamics. The construction of the pseudo-controls is addressed in the next sub-section. The follower acceleration commands in the rectangular inertial coordinate frame are obtained by the following coordinate transformation:

$$\begin{bmatrix} a_{F_{X,com}} \\ a_{F_{Y,com}} \\ a_{F_{Z,com}} \end{bmatrix} = \begin{bmatrix} \cos\lambda_A & -\sin\lambda_A & 0 \\ \sin\lambda_A & \cos\lambda_A & 0 \\ 0 & 0 & 1 \end{bmatrix} \begin{bmatrix} \cos\lambda_E & 0 & \sin\lambda_E \\ 0 & 1 & 0 \\ -\sin\lambda_E & 0 & \cos\lambda_E \end{bmatrix} \begin{bmatrix} a_{F_{R,com}} \\ a_{F_{\lambda,A,com}} \\ a_{F_{\lambda,E,com}} \end{bmatrix} \tag{4.23}$$

D. Construction of the Pseudo-Control Signals

The process of dynamic inversion ignores certain nonlinearities and leader acceleration terms in Eqs. (4.14)-(4.16) giving rise to the modeling error vector

$$\boldsymbol{\Delta}\left(\boldsymbol{x}_{LOS},\boldsymbol{a}_{L}\right)=\begin{bmatrix}\Delta_{R}\left(\boldsymbol{x}_{LOS},\boldsymbol{a}_{L}\right)\\ \Delta_{\lambda_A}\left(\boldsymbol{x}_{LOS},\boldsymbol{a}_{L}\right)\\ \Delta_{\lambda_E}\left(\boldsymbol{x}_{LOS},\boldsymbol{a}_{L}\right)\end{bmatrix} \tag{4.24}$$

where $\boldsymbol{x}_{LOS}=\begin{bmatrix}R & \dot{R} & \lambda_A & \dot{\lambda}_A & \lambda_E & \dot{\lambda}_E\end{bmatrix}^T$ is the LOS state vector and $\boldsymbol{a}_{LOS}=\begin{bmatrix}a_{L_X} & a_{L_Y} & a_{L_Z}\end{bmatrix}^T$ is the leader acceleration vector. To compensate for these modeling errors, the pseudo-controls are augmented with the output of an adaptive NN that is trained online with the available measurements.

The pseudo-control vector $\boldsymbol{\nu}=\begin{bmatrix}\nu_{\lambda_A},\nu_{\lambda_E},\nu_{\lambda_R}\end{bmatrix}^T$ is constructed as,

$$\boldsymbol{\nu}=\boldsymbol{\nu}_{crm}+\boldsymbol{\nu}_{dc}-\boldsymbol{\nu}_{ad} \tag{4.25}$$

where $\boldsymbol{\nu}_{crm}$, $\boldsymbol{\nu}_{dc}$ and $\boldsymbol{\nu}_{ad}$ represent the outputs of reference models, linear compensators and the adaptive NN respectively. Since the relative degree of R is two with respect to the follower acceleration terms, the range command R_{com} is filtered through a 2nd order reference model. The LOS rates are relative degree one each, so the LOS rate commands $\dot{\lambda}_{A_{com}}$ and $\dot{\lambda}_{E_{com}}$ are filtered through 1st order reference models. The outputs of the reference models are given by $\boldsymbol{\nu}_{\boldsymbol{crm}}=\begin{bmatrix}\nu_{crm_{\lambda,A}},\nu_{crm_{\lambda,E}},\nu_{crm_R}\end{bmatrix}^T$:

$$\begin{aligned}\nu_{crm_R}&=\omega_{n_R}^2\left(R_{com}-R_c\right)-2\zeta_R\omega_{n_R}\dot{R}_c\\ \nu_{crm_{\lambda,A}}&=\frac{1}{\tau_{\lambda_A}}\left(\dot{\lambda}_{A_{com}}-\dot{\lambda}_{A_c}\right)\\ \nu_{crm_{\lambda,E}}&=\frac{1}{\tau_{\lambda_E}}\left(\dot{\lambda}_{E_{com}}-\dot{\lambda}_{E_c}\right)\end{aligned} \tag{4.26}$$

where $R_c, \dot{R}_c, \dot{\lambda}_{A_c}, \dot{\lambda}_{E_c}$ are states of the respective reference models, and $\omega_{n_R}^2, \varsigma_R, \tau_{\lambda_A}, \tau_{\lambda_E}$ are design parameters set by choosing a desired form of response based on rise time, settling time, and maximum overshoot.

The linear compensator for controlling the range is chosen as a 1st order dynamic compensator. For controlling the LOS rates, the linear compensators are just proportional error controllers. A low-pass differentiator (derivative filter) is used to estimate the LOS rates from the LOS angles. Note that we could similarly obtain an estimate of the range-rate and use a proportional-derivative (PD) controller for the range dynamics. We simply chose instead to use a lead compensator in this case. The linear compensator outputs are given by $\boldsymbol{\nu}_{\boldsymbol{dc}} = \left[\nu_{dc_{\lambda,A}}, \nu_{dc_{\lambda,E}}, \nu_{dc_R} \right]^T$:

$$\begin{aligned}
\dot{\eta} &= a_c \eta + b_c \left(R_c - R \right) \\
\nu_{dc_R} &= c_c \eta + d_c \left(R_c - R \right) \\
\nu_{dc_{\lambda,A}} &= K_{\lambda_A} \left(\dot{\lambda}_{A_c} - \hat{\dot{\lambda}}_A \right) \\
\nu_{dc_{\lambda,E}} &= K_{\lambda_E} \left(\dot{\lambda}_{E_c} - \hat{\dot{\lambda}}_E \right)
\end{aligned} \tag{4.27}$$

where η is the state of the 1st order dynamic compensator, $\left(a_c, b_c, c_c, d_c \right)$ are the parameters of this compensator, $K_{\lambda_A}, K_{\lambda_E}$ are the proportional controller gains, and $\hat{\dot{\lambda}}_A, \hat{\dot{\lambda}}_E$ are the estimated LOS rates.

Define the tracking error vector to be

$$\boldsymbol{E} \triangleq \begin{bmatrix} e_R \\ \dot{e}_R \\ e_{\lambda_A} \\ e_{\lambda_E} \\ \eta \end{bmatrix} = \begin{bmatrix} R_c - R \\ \dot{R}_c - \dot{R} \\ \dot{\lambda}_{A_c} - \hat{\dot{\lambda}}_A \\ \dot{\lambda}_{E_c} - \hat{\dot{\lambda}}_E \\ \eta \end{bmatrix} \tag{4.28}$$

The tracking error dynamics are obtained by substituting for the pseudo-control vector $\boldsymbol{v}$ in Eqs. (4.14)-(4.16) using Eqs. (4.25)-(4.28):

$$\begin{aligned} \dot{\boldsymbol{E}} &= \bar{A}\boldsymbol{E} + \bar{B}\left[\boldsymbol{v}_{ad} - \boldsymbol{\Delta}\right] \\ \boldsymbol{z} &= \bar{C}\boldsymbol{E} \end{aligned} \tag{4.29}$$

where

$$\boldsymbol{z} = \begin{bmatrix} e_R \\ e_{\lambda_A} \\ e_{\lambda_E} \\ \eta \end{bmatrix} \tag{4.30}$$

and

$$\bar{A} = \begin{bmatrix} 0 & 1 & 0 & 0 & 0 \\ -d_c & 0 & 0 & 0 & -c_c \\ 0 & 0 & -K_{\lambda_A} & 0 & 0 \\ 0 & 0 & 0 & -K_{\lambda_E} & 0 \\ b_c & 0 & 0 & 0 & a_c \end{bmatrix}, \; \bar{B} = \begin{bmatrix} 0 & 0 & 0 \\ 1 & 0 & 0 \\ 0 & 1 & 0 \\ 0 & 0 & 1 \\ 0 & 0 & 0 \end{bmatrix}, \; \bar{C} = \begin{bmatrix} 1 & 0 & 0 & 0 & 0 \\ 0 & 0 & 0 & 0 & 0 \\ 0 & 0 & 1 & 0 & 0 \\ 0 & 0 & 0 & 1 & 0 \\ 0 & 0 & 0 & 0 & 1 \end{bmatrix} \tag{4.31}$$

The linear compensator parameters are chosen such that the $\bar{A}$ matrix is Hurwitz. This implies that the closed-loop tracking error dynamics in Eq. (4.29) are asymptotically stable in the absence of any modeling uncertainty.

The construction of the NN output vector $\boldsymbol{v}_{ad}$ is discussed next. Eq. (4.29) shows that if $\boldsymbol{v}_{ad} \equiv \boldsymbol{\Delta}$, the tracking error dynamics are asymptotically stable. So the objective for the design of the NN is to compensate as accurately as possible the modeling error $\boldsymbol{\Delta}$. So, consider a parameterization of $\boldsymbol{\Delta}$ using a Linear-in-Parameters (LIP) NN [96]:

$$\boldsymbol{\Delta}\left(\boldsymbol{x}_{LOS}, \boldsymbol{a}_L\right) = W^T \boldsymbol{\sigma}\left(\bar{\boldsymbol{\mu}}\right) + \boldsymbol{\varepsilon}\left(\bar{\boldsymbol{\mu}}\right), \;\; \left\|W\right\|_F \le W^*, \;\; \left\|\boldsymbol{\varepsilon}\left(\bar{\boldsymbol{\mu}}\right)\right\| \le \varepsilon^* \tag{4.32}$$

where $\left(\boldsymbol{x}_{LOS}, \boldsymbol{a}_L\right)$ is assumed to evolve over a compact domain, W is the matrix of NN weights, $\boldsymbol{\sigma}$ is a vector of *shifted* sigmoidal basis functions [106, 107], $\bar{\boldsymbol{\mu}}$ is the input

vector to the NN and $\boldsymbol{\varepsilon}$ is the NN function approximation error. The input vector is given by

$$\bar{\boldsymbol{\mu}}(t)=\left[1 \;\; \boldsymbol{R}_{\boldsymbol{d}}^{\boldsymbol{T}}(t) \;\; \boldsymbol{\lambda}_{\boldsymbol{A},\boldsymbol{d}}^{\boldsymbol{T}}(t) \;\; \boldsymbol{\lambda}_{\boldsymbol{E},\boldsymbol{d}}^{\boldsymbol{T}}(t) \;\; \boldsymbol{a}_{\boldsymbol{F_X},\boldsymbol{d}}^{\boldsymbol{T}}(t) \;\; \boldsymbol{a}_{\boldsymbol{F_Y},\boldsymbol{d}}^{\boldsymbol{T}}(t) \;\; \boldsymbol{a}_{\boldsymbol{F_Z},\boldsymbol{d}}^{\boldsymbol{T}}(t)\right]^T \tag{4.33}$$

where the subscript d signifies vectors of delayed values of the signals. The measurements $\left[R \;\lambda_A \;\lambda_E \;a_{F_X} \;a_{F_Y} \;a_{F_Z}\right]^T$ are normalized and passed through a tapped-delay line that generates the delayed values with a time delay $d>0$

$$\begin{aligned}
&\boldsymbol{R}_{\boldsymbol{d}}=\left[R_{norm}(t) \;R_{norm}(t-d) \;R_{norm}(t-2d) \;\cdots\right]^T \\
&\vdots \qquad\qquad\qquad \vdots \qquad\qquad\qquad \vdots \\
&\boldsymbol{a}_{\boldsymbol{F_Z},\boldsymbol{d}}=\left[a_{F_{Z,norm}}(t) \;a_{F_{Z,norm}}(t-d) \;a_{F_{Z,norm}}(t-2d) \;\cdots\right]^T
\end{aligned} \tag{4.34}$$

The number of delayed values is chosen to be sufficiently larger than the dimension of the outputs being regulated [95], [96]. For implementation, the number of delayed values was set to four for each measurement.

Since the ideal NN weight matrix W is unknown, an estimate $\hat{W}$ is considered to form the output of the LIP NN:

$$\boldsymbol{v}_{ad}=\hat{W}^T\boldsymbol{\sigma}(\bar{\boldsymbol{\mu}}) \tag{4.35}$$

The NN weight estimate $\hat{W}$ is updated online. For full state-feedback applications, the NN weight update laws are in terms of the error vector $\boldsymbol{E}$. However, $\dot{R}$ is not directly available to form the signal $\dot{e}_R$. As noted earlier, a low-pass differentiator could be used to estimate the range-rate too and construct $\dot{e}_R$. However, in this case, we employ an error observer [96] to estimate the entire error vector $\boldsymbol{E}$ by defining $\hat{\boldsymbol{E}}=\left[\hat{e}_R,\;\hat{\dot{e}}_R,\;\hat{e}_{\lambda_A},\;\hat{e}_{\lambda_E},\;\hat{\eta}\;\right]^T$. A reduced order error observer could be employed to

estimate the partial error vector $\left[\hat{e}_R,\ \dot{\hat{e}}_R\ \right]^T$ [110]. In this case, we chose to design a full order error observer. The error observer dynamics is given by,

$$\dot{\hat{\boldsymbol{E}}} = \left(\bar{A} - K_{obs}\bar{C}\right)\hat{\boldsymbol{E}} + K_{obs}\boldsymbol{z} \tag{4.36}$$

where $\tilde{A} = \bar{A} - K_{obs}\bar{C}$ is an asymptotically stable matrix and K_{obs} is the error observer gain matrix. The error observer gain matrix is designed by pole placement techniques by specifying the eigenvalues of $\tilde{A}$ to be significantly faster (at least three times) than that of $\bar{A}$.

The NN weights are updated online with the adaptive law [96]

$$\dot{\hat{W}} = -\Gamma_W\left(\boldsymbol{\sigma}\left(\bar{\boldsymbol{\mu}}\right)\hat{\boldsymbol{E}}^T P\bar{B} + \lambda_W\hat{W}\right) \tag{4.37}$$

where the term $\hat{\boldsymbol{E}}^T P\bar{B}$ is the training signal for the NN, $\Gamma_W > 0$ is the NN learning rate and $\lambda_W > 0$ is the sigma-mod parameter. The P matrix in the training signal is obtained by solving the following Lyapunov equation

$$\bar{A}^T P + P\bar{A} = -Q,\ \ Q = Q^T > 0 \tag{4.38}$$

Lyapunov-like stability analysis is used to show uniform ultimate boundedness of all error signals and the NN weight estimation errors [96].

Remark 4.3: The NN adaptive law can be derived without constructing an error observer by applying the direct approach in [95]. The training signal for the NN in this case is obtained by filtering the tracking error through a strictly positive real (SPR) filter.

In summary, the output of the adaptive guidance law is a vector of follower acceleration commands given by Eq. (4.23), which are obtained from Eqs. (4.20)-(4.22),

which in turn are obtained by solving for the pseudo-controls vector as described in this section.

E. Pseudo-Control Hedging

Pseudo-Control Hedging (PCH) is introduced to protect the adaptive law from effects due to actuator rate and position limits, unmodeled actuator dynamics and to protect the adaptive process when it is not in control of the plant [89]. The main idea behind the PCH methodology is to modify the reference command in order to prevent the adaptive element from adapting to these actuator characteristics. This is commonly done by generating the command using a reference model for the desired response. The reference model is 'hedged' by an amount equal to the difference between the commanded and an estimate for the achieved pseudo-control [89]. Note that since we are commanding acceleration, the acceleration autopilot appears like an actuator to the adaptive guidance law. So, hedging is applied to the autopilot dynamics and limitations in achieving the commanded acceleration.

The estimate of the achieved pseudo-control is given by

$$\hat{\nu}_{\lambda_A} = \frac{-a_{F_{\lambda,A}}}{R\cos\lambda_E} \tag{4.39}$$

$$\hat{\nu}_{\lambda_E} = \frac{a_{F_{\lambda,E}}}{R} \tag{4.40}$$

$$\hat{\nu}_R = -a_{F_R} \tag{4.41}$$

where the acceleration signals $a_{F_{\lambda,A}}, a_{F_{\lambda,E}}$ and a_{F_R} are computed from the achieved acceleration along the rectangular coordinate axes and by inverse transforming Eq. (4.23). The hedge signals are given by

$$\begin{bmatrix} \nu_{h_R} \\ \nu_{h_{\lambda,A}} \\ \nu_{h_{\lambda,E}} \end{bmatrix} = \begin{bmatrix} \nu_R - \hat{\nu}_R \\ \nu_{\lambda_A} - \hat{\nu}_{\lambda_A} \\ \nu_{\lambda_E} - \hat{\nu}_{\lambda_E} \end{bmatrix} \tag{4.42}$$

The reference models are then updated with the hedge signals as shown below,

$$\begin{aligned} \ddot{R}_c &= \nu_{crm_R} - \nu_{h_R} \\ \ddot{\lambda}_{A_c} &= \nu_{crm_{\lambda,A}} - \nu_{h_{\lambda,A}} \\ \ddot{\lambda}_{E_c} &= \nu_{crm_{\lambda,E}} - \nu_{h_{\lambda,E}} \end{aligned} \tag{4.43}$$

Figure 21 shows a block diagram of the adaptive guidance law.

F. Converting Acceleration Commands into Autopilot Commands

The follower acceleration commands in Eq. (4.23), $\boldsymbol{a}_{F_{com}} = \begin{bmatrix} a_{F_{X,com}} & a_{F_{Y,com}} & a_{F_{Z,com}} \end{bmatrix}^T$, have to be transformed into commands for the autopilot. Henceforth, the subscript '*F*' is dropped for convenience. First, the commanded specific force vector along the rectangular inertial coordinate axes is computed by subtracting the gravity vector is subtracted from $\boldsymbol{a}_{com}$:

$$\boldsymbol{F}_{com} = \boldsymbol{a}_{com} - \begin{bmatrix} 0, & 0, & g \end{bmatrix}^T \tag{4.44}$$

where g is the acceleration due to gravity. The commands to the autopilot are the specific force commands along body-fixed coordinate x- and z-axis respectively, ${}_B f_{x_{com}}$, ${}_B f_{z_{com}}$, and the bank angle command Φ_{com}. The commanded specific force vector $\boldsymbol{F}_{com}$ is rotated into the body-fixed frame to form the above commands. This is accomplished by rotating through the Euler angles Ψ (heading), Θ (pitch), and Φ_{com} (roll). The intermediate frame formed after the Ψ and Θ rotations is called the 2-frame for convenience. The bank angle command Φ_{com} rotates the $\boldsymbol{F}_{com}$ components in the 2-frame ${}_2\boldsymbol{f}_{com}$, to the body frame components ${}_B\boldsymbol{f}_{com}$:

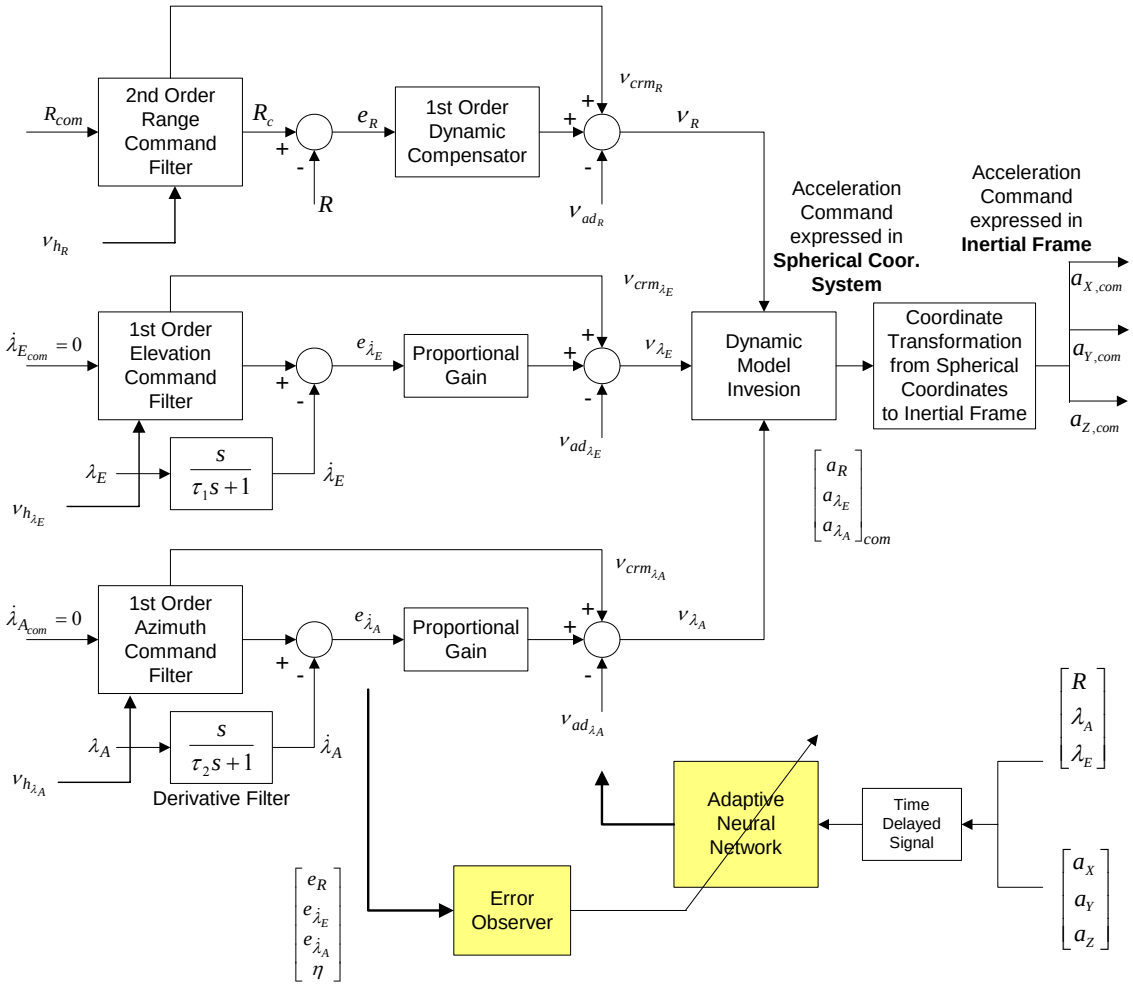

Figure 21. Follower Aircraft Adaptive Guidance Law for LOS Formation Flight

$$ {}_2\boldsymbol{f}_{com} = \left[L_{2V}\left(\Psi,\Theta\right)\right]\boldsymbol{F}_{com} \tag{4.45} $$

$$ \left[L_{2V}\left(\Psi,\Theta\right)\right] = \begin{bmatrix} \cos\Theta & 0 & -\sin\Theta \\ 0 & 1 & 0 \\ \sin\Theta & 0 & \cos\Theta \end{bmatrix} \begin{bmatrix} \cos\Psi & \sin\Psi & 0 \\ -\sin\Psi & \cos\Psi & 0 \\ 0 & 0 & 1 \end{bmatrix} \tag{4.46} $$

$$ {}_B\boldsymbol{f}_{com} = \left[L_{B2}\left(\Phi_{com}\right)\right] {}_2\boldsymbol{f}_{com} \tag{4.47} $$

The components of the commanded specific force vectors in Eqs. (4.45) and (4.47) are given by

$$ {}_2\boldsymbol{f}_{com} = \begin{bmatrix} {}_2 f_{x_{com}} \\ {}_2 f_{y_{com}} \\ {}_2 f_{z_{com}} \end{bmatrix}, \quad {}_B\boldsymbol{f}_{com} = \begin{bmatrix} {}_B f_{x_{com}} \\ {}_B f_{y_{com}} \\ {}_B f_{z_{com}} \end{bmatrix} \tag{4.48} $$

The situation after rotation into the 2-frame is shown in Figure 22 which depicts the view from the front of the aircraft, with the X-axis coming out of the page. The bank angle command is constructed as

$$ \Phi_{com} = \text{atan2}\left({}_2 f_{y_{com}}, -{}_2 f_{z_{com}} \right) \tag{4.49} $$

The body frame z-axis specific force command is given as

$$ {}_B f_{z_{com}} = -\sqrt{ {}_2 f_{y_{com}}^2 + {}_2 f_{z_{com}}^2 } \tag{4.50} $$

and the body frame x-axis specific force command is

$$ {}_B f_{x_{com}} = {}_2 f_{x_{com}} \tag{4.51} $$

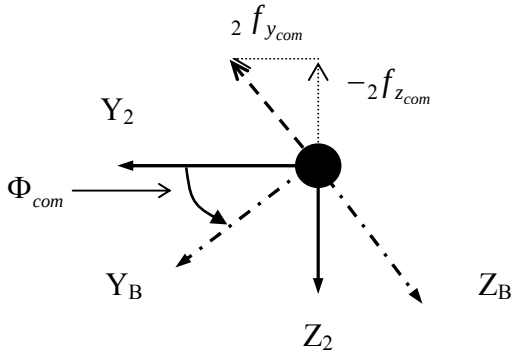

Figure 22. Front view of the 2-frame and body frame

4.2 Autopilot Design

Adaptive controllers are designed for tracking the normal acceleration command ${}_B f_{z_{com}}$, bank angle command Φ_{com}, and lateral acceleration ${}_B f_{y_{com}} = 0$ for turn coordination. The design of these adaptive controllers is not a contribution of this thesis. The details are referred to Appendix B.

The throttle controller is a proportional-integral (PI) controller with an anti-windup feature for tracking speed command V_{com} or a command formed by a combination of the longitudinal acceleration command ${}_B f_{x_{com}}$ and V_{com}. There is a stability issue when a pure acceleration command $e_{x_{cmd}} = f_{x_{cmd}} - f_x$ is input to the throttle controller of the follower aircraft. This stability issue is particular to the aircraft model used in the simulation and occurs when sharp heading turns are commanded. This is due to the fact that the guidance law generates an excessive negative acceleration command along the body X-axis when starting a heading turn and this causes saturation into the lower bound of the throttle, ultimately leading to instability of the entire closed-loop system. So, the command to the throttle controller of the follower aircraft is modified as,

$$e_{x_{cmd}} = V_{com} - V_F + K_x f_{x_{cmd}},\ 0 \le K_x \le 1 \tag{4.52}$$

where V_{com} is the commanded speed of the leader, V_F is the follower speed, and K_x is a design gain. Arguably, the commanded speed of the leader should also be unknown to the follower, but in this particular application, it is assumed known. There is a trade-off with the range tracking performance as a result of the command modification to the throttle controller. Using $e_{x_{cmd}}$ as throttle controller command for the follower aircraft, reduces the transient speed of response of the range variable and the desired steady-state with respect to range may not be achieved, even when the leader stops maneuvering. The gain K_x is chosen to get acceptable range tracking performance for a range of leader maneuvers while not saturating the throttle controller. In case there is no danger of saturating the

throttle by commanding negative acceleration along the body X-axis, for e.g., if spoilers can be deployed for additional drag, it should be possible to use $e_{x_{cmd}}$ as input to the throttle controller.

At a higher level, the command modification to the throttle controller illustrates a drawback of the process in which the guidance and autopilot systems are designed separately and then integrated together. This drawback manifests itself in reduced range tracking performance as the range commands become smaller and the leader maneuvers become more severe. In such cases the time-scale separation assumption that is inherent in the separate design of the guidance and autopilot systems may not be valid any more. This provides a motivation for pursuing the development of an integrated guidance and control law, which is the subject of the next chapter.

4.3 Simulation Results

A. Simulation Model

A nonlinear 6-DOF fixed-wing aircraft simulation is used for the testing of the control and guidance algorithms for formation flight. Data for the model was obtained from a flight test and system identification of a small fixed-wing unmanned aerial vehicle at Eglin Air Force Base. The simulation model is a rigid body aircraft model with 13 states, 3 for position with respect to the Earth-fixed frame, 3 for translational velocity expressed in the body frame, 4 for the quaternions and 3 for the angular velocity expressed in the body frame. Engine thrust is obtained from a linear interpolation map of throttle position. The actuators are modeled as first-order, stable linear filters with rate and position limits and time delays:

$$\dot{\delta}(t) = \text{sat}\left(\frac{1}{\tau_a}\left[\delta_{cmd}\left(t - \tau_d\right) - \text{sat}\left(\delta(t)\right)\right] \right) \tag{4.53}$$

where $\delta_{cmd}(t)$ is the actuator command signal at time t, $\delta(t)$ is the actuator output at time t, $\text{sat}(\cdot)$ is a linear saturation operator, τ_a is the actuator time constant, and τ_d is the time delay.

B. Simulation Results and Discussion

Closed-loop formation flight results are shown for three sets of leader aircraft maneuvers. The leader aircraft maneuvers by tracking waypoints in the inertial reference frame. Three sets of waypoints are prescribed: 1) waypoints in the inertial X-Z plane, requiring the leader to climb and descend, 2) waypoints at the corners of a square box in the inertial X-Y plane, requiring the leader to make sharp heading changes at the corners of the box while holding altitude, and 3) waypoints prescribed at the corners of a slanted box in 3D space, requiring sharp heading changes, climbing and descending motions of the leader. The three sets of waypoints require increasing levels of maneuvers from the leader. The objective is to investigate the range tracking performance of the follower aircraft. It will be shown that the range tracking performance deteriorates as the leader maneuver becomes more severe.

The range command is set to $R_{com} = 5$ meters, which is slightly less than 2 wing-span lengths. The wing-span length of the simulated aircraft is $b = 2.8$ meters. The nominal LOS rate commands are 0 deg/s, but these commands are modified to prevent drifts in the bearing angles to large values. The bearing angles are defined as:

$$\chi_A \equiv \lambda_A - \Psi$$
$$\chi_E \equiv \lambda_E - \Theta$$

where the angles Ψ (yaw), Θ (pitch) and Φ (roll) are the Euler attitude angles of the follower aircraft. These angles are of interest since χ_A and χ_E are computable from the Euler attitude angles and LOS measurements from an onboard camera fixed to the body

of the follower aircraft, with optical axis coincident with the X-body axis. The field-of-view (FOV) constraints of the onboard camera impose limits on the magnitude of measurable bearing angles. The idea of modifying the LOS rate commands is to prevent drifts in χ_A and χ_E to values larger than the FOV imposed limits. The method of generating the LOS rate command is shown using the dead-zone in Figure 23. Here χ represents either χ_A or χ_E and we have the corresponding LOS rate command. For χ within the dead-zone, $\dot{\lambda}_{com} = 0$ and if χ drifts outside the dead-zone, $\dot{\lambda}_{com} \neq 0$ is such that it brings χ back within the dead-zone. The boundaries of the dead-zone are dependent on the FOV constraints.

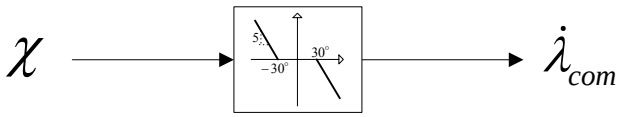

Figure 23. Dead-zone logic for generating LOS rate commands

The commanded speed of the leader aircraft is $V_{com} = 25$ meters/sec. The initial conditions for the leader and follower is the trim condition of steady, level flight. The leader initial position is at (0,0,0) meters and the follower initial position is at (-10,0,5) meters. The simulation is terminated when the leader aircraft flies through the last waypoint. The plots shown are used to demonstrate the tracking performance of the guidance and control law over the range of maneuvers.

Case 1: Waypoints in inertial X-Z plane

Figure 24 shows the 2D trajectory of the leader and follower. The red circle and blue triangle at the bottom right of the figure are the initial positions of the leader and follower respectively. Note that the Z-axis scale is magnified compared to the X axis. Figure 25 shows the range tracking performance. The 'hedged R_{ref}' signal in the figure shows the

hedged reference command signal that is being tracked. Note that the maximum overshoot from the commanded range is less than 1 meter in the presence of leader maneuvers. The performance is very much acceptable.

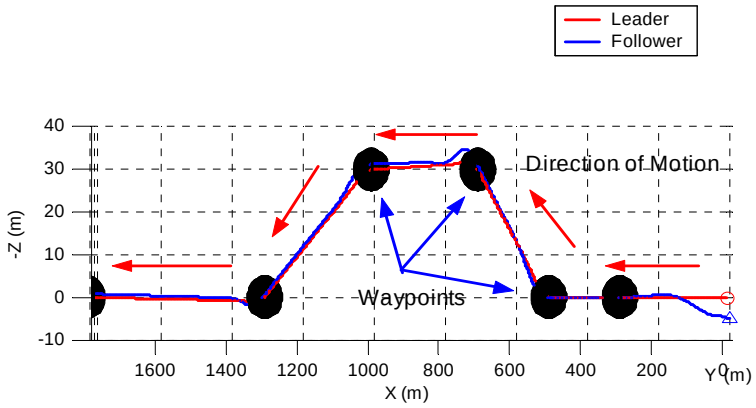

Figure 24. 2D Leader and Follower Trajectory, in meters (Case 1)

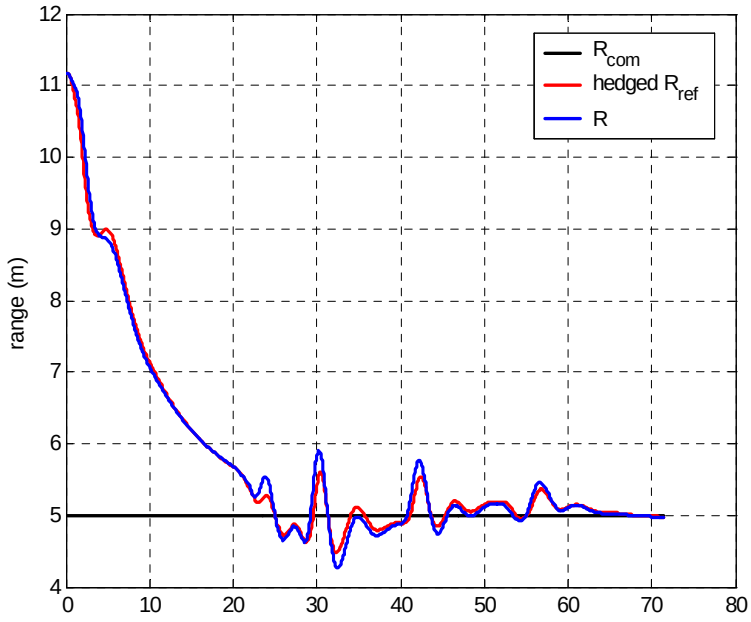

Figure 25. Range Tracking Performance, in meters (Case 1)

Case 2: Waypoints at the corner of square box in inertial X-Y plane

Figure 26 shows the 3D trajectory of the leader and follower from the top view. Figure 27 shows the range tracking history. Note that the maximum overshoot from the commanded range is less than 2 meters in the presence of leader maneuvers. This implies a slight deterioration compared to the tracking performance in Figure 25. The overshoots occur when the leader aircraft commands a change in heading after passing through a waypoint. Overall, the performance is still acceptable.

Case 3: Waypoints at the corner of slanted box in 3D inertial space

Figure 28 shows the 3D trajectory of leader and follower for the last maneuver. This maneuver differs from the preceding one in that after passing through the first waypoint the leader turns and climbs to 50 meters, does another turn while holding altitude, and finally returns to the starting point by turning and descending. Figure 29 shows the range tracking history. Note the deterioration in the range tracking performance compared to the results in Case 1 and Case 2. The overshoots are larger with a maximum overshoot of about 4.5 meters and slow convergence to commanded range.

Figure 30 shows the effectiveness of the adaptation. The NN output $\boldsymbol{\nu}_{ad}$ approximates closely the inversion error $\boldsymbol{\Delta}$. Figure 31 shows that the actuator deflection histories for the follower aircraft are quite reasonable. Figure 32 shows the range tracking performance diverges with NN off indicating that adaptation is critical to the stability of the tracking performance.

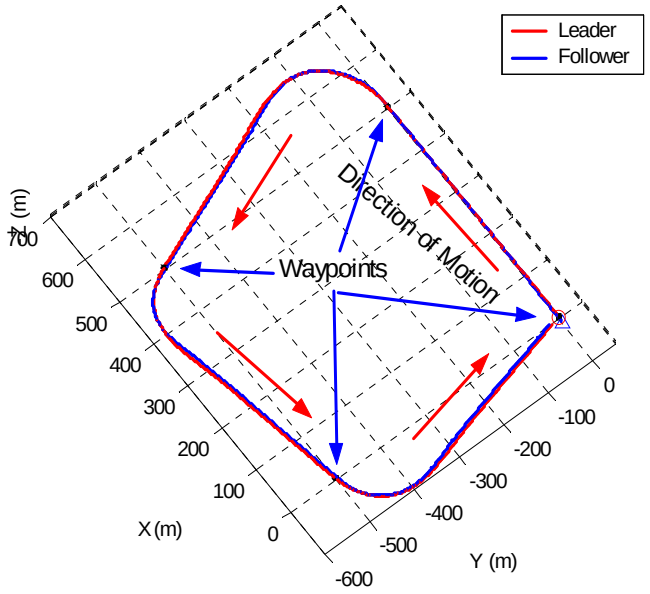

Figure 26. 3D Leader and Follower Trajectory, in meters (Case 2)

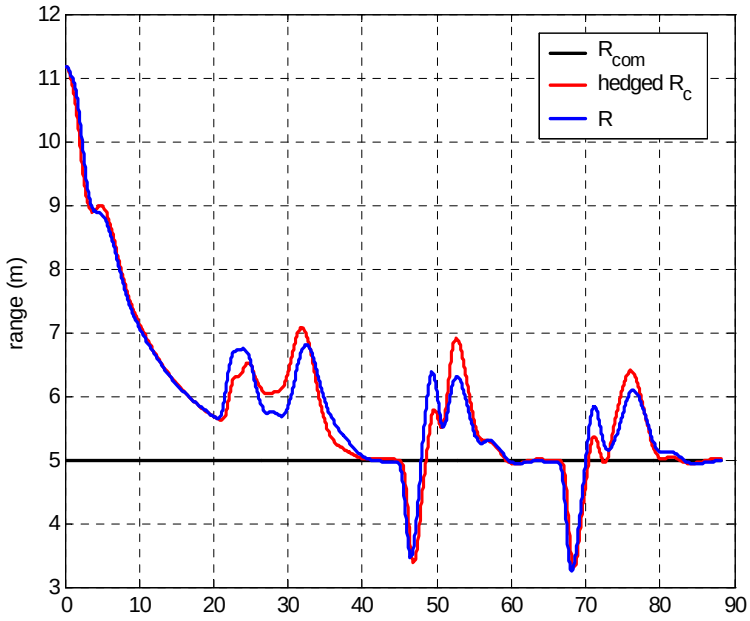

Figure 27. Range Tracking Performance, in meters (Case 2)

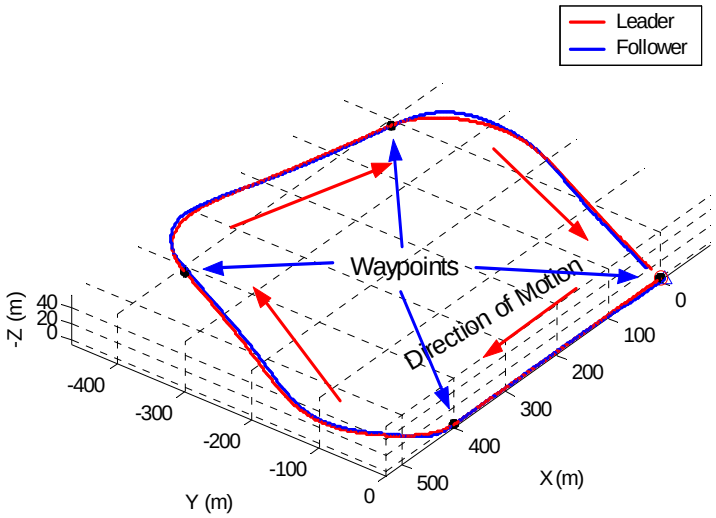

Figure 28. 3D Leader and Follower Trajectory, in meters (Case 3)

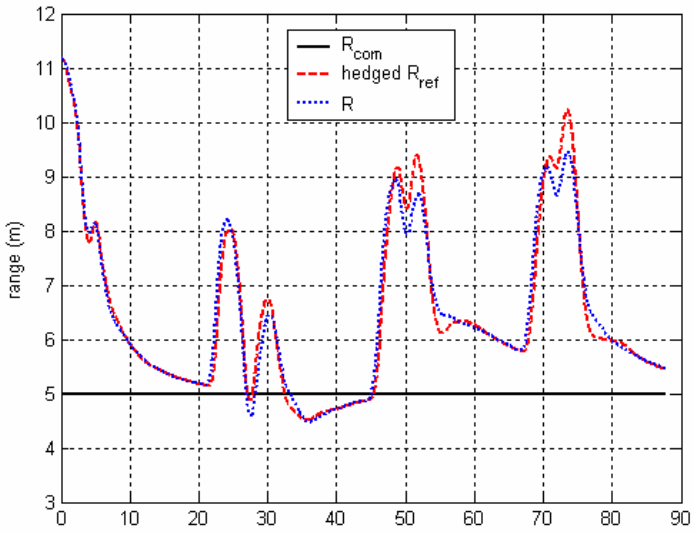

Figure 29. Range Tracking Performance, in meters (Case 3)

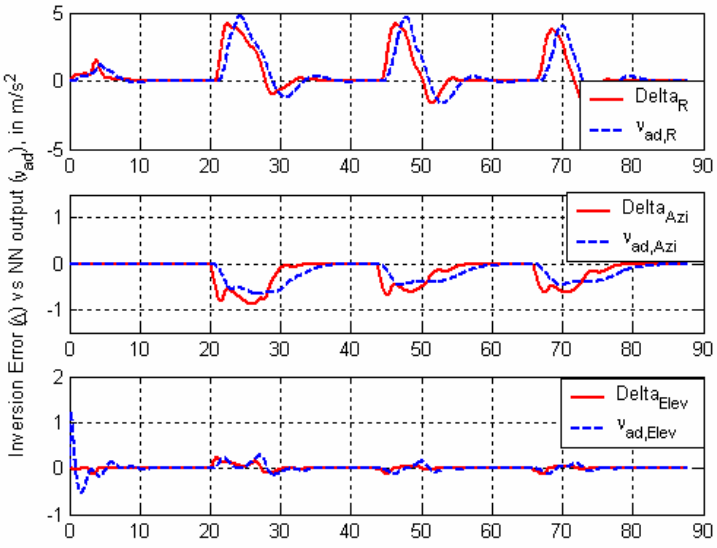

Figure 30. Inversion Error vs NN Output, in m/s^2 (Case 3)

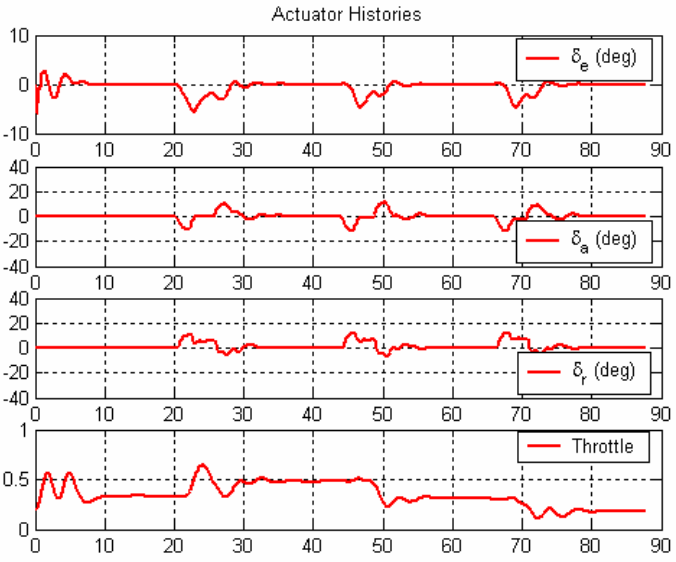

Figure 31. Follower Aircraft Actuator Histories, in deg (Case 3)

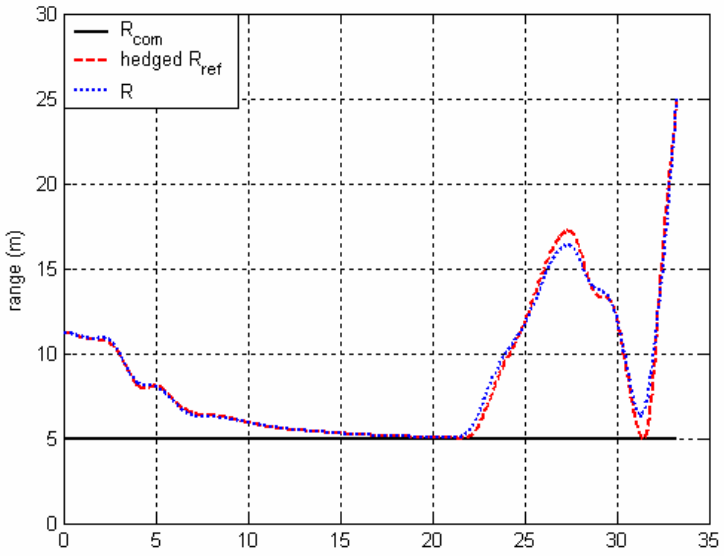

Figure 32. Range Tracking Performance in meters, NN off (Case 3)

4.4 Conclusions

This chapter presents the design of an adaptive guidance law for a follower aircraft maintaining range from a maneuvering leader aircraft. The results show that the NN based adaptation effectively compensates for unknown leader maneuvers and ignored LOS kinematics, enabling reasonable range tracking performance for a range of leader maneuvers. The guidance law assumes that true values of the range and LOS angles are available for feedback. This assumption is relaxed in Chapter 6 where the guidance law is integrated with the adaptive state estimator in Chapter 3. The results also showed that the range tracking deteriorates as the leader maneuver becomes more severe. This is a consequence of the scaling down of the longitudinal acceleration guidance command to the throttle controller to preserve stability in the presence of sharp turning maneuvers of the leader. This shows that when tracking severe leader maneuvers at close ranges, the time-scale separation assumption that is inherent in the separate design of the guidance

and autopilot systems may not be valid any more. In the next chapter, this limitation is overcome by developing an integrated guidance and control law for LOS formation flight.

CHAPTER 5

ADAPTIVE INTEGRATED GUIDANCE AND CONTROL DESIGN FOR LINE-OF-SIGHT FORMATION FLIGHT

This chapter presents an integrated guidance and control design for line-of-sight formation flight using a combination of adaptive output feedback and backstepping techniques. The design objective is for a follower aircraft to regulate range and two bearing angle rates from a maneuvering leader aircraft while maintaining turn coordination. The approach assumes the true values of range and line-of-sight angles are available for feedback. Adaptive neural networks are trained online with available measurements to compensate for unmodeled nonlinearities in the design process. These include uncertainties due to unknown leader aircraft acceleration, and the modeling error due to parametric uncertainties in the aircraft aerodynamic derivatives. One benefit of this approach is that the guidance and flight control design process is integrated. Simulation results using a nonlinear 6DOF simulation model are presented to illustrate the efficacy of the approach by comparing its performance with i time-scale separation based guidance and control design presented in Chapter 4.

5.1 Integrated Guidance and Control – Design 1

In this section, an adaptive integrated guidance and control (IGC) law is derived using the theory for adaptive output feedback control [96]. The approach here is similar to that used for the derivation of the adaptive guidance law in Chapter 4. The line-of-sight (LOS) range and two bearing angle rates are defined to be the regulated outputs. The LOS kinematics are expressed in the normal form [98] and inverted to give the expressions for commanded controls. The difference is that with the IGC law the

commanded controls are the commanded actuator deflections. This implies that the LOS kinematics have to be written in a form where the actuator deflection terms appear. This derivation is outlined in the following sub-sections. The modeling error that arises in the approximate dynamic inversion of the LOS kinematics is a nonlinear function of the leader aircraft accelerations, nonlinear LOS kinematics, and own-aircraft dynamics. Adaptive neural networks (NNs) are trained online to compensate the modeling error as in Chapter 4. The developed design is referred to as IGC Design 1, which is shown to result in a deficiency in turn coordination. This deficiency is resolved by modifying the azimuth channel portion of the inverting design using an adaptive backstepping algorithm. This modification is described in Section 5.2 and the modified design is referred to as IGC Design 2.

A. Problem Formulation

Consider the Multi-Input Multi-Output (MIMO) nonlinear system given by

$$\begin{aligned} \dot{\boldsymbol{x}}_1 &= A_1 \boldsymbol{x}_1 + B_1 \left[\boldsymbol{\varsigma}(\boldsymbol{x}_2) + \boldsymbol{g}(\boldsymbol{x}_1, z) \right] \\ \dot{z} &= \boldsymbol{f}_z(\boldsymbol{x}_1, z) \\ \dot{\boldsymbol{x}}_2 &= \boldsymbol{f}_2(\boldsymbol{x}_2) + G(\boldsymbol{x}_2)\boldsymbol{u} \\ \boldsymbol{y} &= \boldsymbol{h}(\boldsymbol{x}_1, \boldsymbol{x}_2) \end{aligned} \tag{5.1}$$

where $\boldsymbol{x}_1 \in D_{x_1} \subset \Re^{n_1}$ and $\boldsymbol{x}_2 \in D_{x_2} \subset \Re^{n_2}$ are the modeled states of the system available for feedback, $z \in D_z \subset \Re^{n_z}$ are the unmodeled states where n_z is also unknown but bounded, D_{x_1}, D_{x_2}, and D_z are open sets containing their respective origins, and $\boldsymbol{y} \in \Re^p$ and $\boldsymbol{u} \in \Re^p$ are the regulated outputs and control inputs of the system respectively. The matrices $A_1 \in \Re^{n_{x1} \text{ x } n_{x1}}$ and $B_1 \in \Re^{n_{x1} \text{ x } m}$ are known. The functions $\boldsymbol{\varsigma} : D_{x_2} \to \Re^m$ and $\boldsymbol{h} : D_{x_1} \text{ x } D_{x_2} \to \Re^p$ are known and continuous. The functions $\boldsymbol{f}_2 : D_{x_2} \to \Re^{n_2}$ and $G : D_{x_2} \to \Re^{n_2 \text{ x } m}$ are *partially* known and continuous. The function

$\boldsymbol{f}_z(\boldsymbol{x}_1, z) : D_{x_1} \times D_z \to \Re^{n_z}$ is unknown, continuous and represents the unmodeled dynamics. The function $\boldsymbol{g}(\boldsymbol{x}_1, z) : D_{x_1} \times D_z \to \Re^m$ is unknown, continuous and represents the way in which the unmodeled dynamics is coupled to the system dynamics. Let $\boldsymbol{x} = \left[\boldsymbol{x}_1^T, \boldsymbol{x}_2^T, \boldsymbol{z}^T \right]^T \in D_{\boldsymbol{x}} \subset \Re^n$, $n = n_{x_1} + n_{x_2} + n_z$, be the composite state vector of the system, where $D_{\boldsymbol{x}} = D_{x_1}$ x D_{x_2} x D_z.

Assumption 5.1: The function $\boldsymbol{f}_z(\cdot,\cdot)$ is a bounded function of its arguments and $\boldsymbol{z}(t)$ is bounded for all t.

Remark 5.1: In context of the formation flight problem, $\boldsymbol{x}_1$ represents the states of the LOS kinematics and $\boldsymbol{x}_2$ represents the states of the rigid body dynamics of the follower aircraft. In general, the complete state vector $\boldsymbol{x}_1$ is not available for feedback, but in the derivation of the IGC law in this chapter, $\boldsymbol{x}_1$ is assumed to be available. This assumption is eliminated in Chapter 5 when the IGC law is integrated with the adaptive state estimator presented in Chapter 3. The state vector $\boldsymbol{x}_2$ is assumed to be available by means of sensors such as accelerometers, rate-gyros, integrated INS-GPS, etc. The unknown functions $\boldsymbol{f}_z(\boldsymbol{x}_1, z)$ and $\boldsymbol{g}(\boldsymbol{x}_1, z)$ represent the leader acceleration dynamics and the effect of the leader accelerations on the LOS kinematics respectively. The function $\varsigma(\boldsymbol{x}_2)$ represents the effect of the follower accelerations on the LOS kinematics and hence it is reasonable to assume $\varsigma(\boldsymbol{x}_2)$ is known. The functions $\boldsymbol{f}_2(\boldsymbol{x}_2)$ and $G(\boldsymbol{x}_2)$ represent the follower aircraft dynamics and it is reasonable to assume that at least a linear model of the aircraft dynamics is available implying partial knowledge of $\boldsymbol{f}_2(\cdot)$ and $G(\cdot)$. The control inputs $\boldsymbol{u}$ represent the actuator deflections of the follower

aircraft. The regulated outputs $\boldsymbol{y}$ represent the outputs of interest, for example, range, bearing angle rates, bank or sideslip angle for turn coordination, etc for enabling formation flight with respect to a maneuvering leader.

Assumption 5.2: The dynamical system (5.1) satisfies the conditions for output feedback linearization [98] with vector relative degree $\boldsymbol{r} \triangleq \left[r_1, r_2, \cdots, r_p \right]^T$, $\boldsymbol{r} = r_1 + r_2 + \cdots + r_p \leq n$.

Then there exists a mapping $\boldsymbol{\xi} = \boldsymbol{\varphi}(\boldsymbol{x}) = \boldsymbol{\varphi}(\boldsymbol{x}_1, \boldsymbol{x}_2, \boldsymbol{z})$ which is given by

$$\boldsymbol{\varphi}(\boldsymbol{x}) = \begin{bmatrix} \boldsymbol{\varphi}_1 \\ \boldsymbol{\varphi}_1 \\ \vdots \\ \boldsymbol{\varphi}_p \end{bmatrix}, \ \boldsymbol{\varphi}_i = \begin{bmatrix} y_i \\ \dot{y}_i \\ \vdots \\ y_i^{(r_i-1)} \end{bmatrix} \tag{5.2}$$

that transforms the system in (5.1) into the normal form [98]:

$$\begin{aligned} \dot{\boldsymbol{Z}} &= \boldsymbol{f}_{\boldsymbol{Z}}(\boldsymbol{\xi}, \boldsymbol{Z}) \\ \dot{\xi}_i^1 &= \xi_i^2 \\ &\vdots \\ \dot{\xi}_i^{(r_i-1)} &= \xi_i^{(r_i)} \\ \dot{\xi}_i^{(r_i)} &= \alpha_i^0(\boldsymbol{x}_1, \boldsymbol{x}_2) + \alpha_i^1(\boldsymbol{x}_1, \boldsymbol{x}_2, \boldsymbol{z}, u_i) + \beta_i(y_1, y_2, \cdots, y_p, \boldsymbol{x}_2) u_i \\ y_i &= \xi_i^1, \quad i = 1, 2, \cdots, p \end{aligned} \tag{5.3}$$

where $\boldsymbol{\xi} \triangleq \left[\xi_i^1 \ \ \xi_i^2 \ \ \cdots \ \ \xi_i^{(r_i)} \ \ \cdots \ \ \xi_m^1 \ \ \xi_m^2 \ \ \cdots \ \ \xi_m^{(r_m)} \right]^T \in D_\xi \subset \Re^r$, $\boldsymbol{Z} \in D_{\boldsymbol{Z}} \subset \Re^{n-r}$ are the states associated with the internal dynamics, u_i are the control inputs, y_i are the regulated outputs, r_i is the relative degree of the i^{th} output, $\boldsymbol{f}_{\boldsymbol{Z}}(\boldsymbol{\xi}, \boldsymbol{Z})$ is a completely unknown continuous function representing the internal dynamics, $\alpha_i^0(\boldsymbol{x}_1, \boldsymbol{x}_2) = \alpha_i^0(\boldsymbol{\xi})$ and $\beta_i(y_1, y_2, \cdots, y_p, \boldsymbol{x}_2)$ are known continuous functions, and $\alpha_i^1(\boldsymbol{x}_1, \boldsymbol{x}_2, \boldsymbol{z}, u_i) = \alpha_i^1(\boldsymbol{\xi}, \boldsymbol{Z}, u_i)$ is an unknown continuous function.

Assumption 5.3: The function $\boldsymbol{f}_{\boldsymbol{Z}}(\cdot,\cdot)$ is a bounded function of its arguments and $\boldsymbol{Z}(t)$ is bounded for all t.

Assumption 5.4: $\beta_i\left(y_1,\cdots,y_p,\boldsymbol{x}_2\right)$ is continuous and non-zero for every $\boldsymbol{x}\in D_{\boldsymbol{x}}$.

Control Design Objective: Design a control law as a function of available measurements such that $y_i(t)$ track smooth, bounded reference trajectories $y_{c,i}(t)$, $i=1,2,\cdots,p$ with bounded errors.

Remark 5.2: The normal form in (5.3) is very similar to the normal form in (4.1). So, the same theory for adaptive output feedback control [96] is applied to solve for the control solution u_i in (5.3). The key difference is that for the IGC design the own (follower) aircraft dynamics and LOS kinematics are considered in the problem formulation, and the commanded controls are the actuator deflections. In the problem formulation for the adaptive guidance law in Chapter 4, only the LOS kinematics were considered and the commanded controls were the inertial accelerations of the follower aircraft, which were assumed to be achieved by means of a separately designed autopilot. The approach presented in this chapter integrates the guidance and flight control design process. In the next sub-section, the LOS kinematics is derived in a form where the actuator deflection terms appear. The existence of a well-defined vector relative degree is shown. Following this, the adaptive IGC control law is derived.

B. Derivation of LOS Kinematics

The formation flight objective is to regulate the range R and two bearing angle rates with respect to the leader aircraft while maintaining turn coordination. The bearing angles are defined as:

$$\chi_A \equiv \lambda_A - \Psi$$
$$\chi_E \equiv \lambda_E - \Theta \tag{5.4}$$

where the angles Ψ (yaw), Θ (pitch) and Φ (roll) are the Euler attitude angles of the follower aircraft. These angles are of interest since χ_A and χ_E are computable from the Euler attitude angles and LOS measurements from an onboard camera fixed to the body of the follower aircraft, with optical axis coincident with the X-body axis. A bank angle command Φ_{com} is constructed to maintain turn coordination, i.e., to nullify the acceleration along the body-fixed Y axis. So, the output vector for regulation is given by $\boldsymbol{y} = \left[R,\ \chi_A,\ \chi_E,\ \Phi\right]^T$.

The derivation of the LOS kinematics for the IGC law design starts with Eqs. (4.8)-(4.10), which are repeated below for convenience:

$$\ddot{R} = R\left[\dot{\lambda}_A^2 \cos^2 \lambda_E + \dot{\lambda}_E^2\right] + \left[a_X \cos\lambda_A \cos\lambda_E + a_Y \sin\lambda_A \cos\lambda_E - a_Z \sin\lambda_E\right] \tag{5.5}$$

$$\ddot{\lambda}_A = \frac{1}{\cos\lambda_E}\left\{-2\dot{\lambda}_A\left[\left(\frac{\dot{R}}{R}\right)\cos\lambda_E - \dot{\lambda}_E \sin\lambda_E\right] + \left(\frac{1}{R}\right)\left[-a_X \sin\lambda_A + a_Y \cos\lambda_A\right]\right\} \tag{5.6}$$

$$\begin{aligned}\ddot{\lambda}_E = &-2\left(\frac{\dot{R}}{R}\right)\dot{\lambda}_E - \dot{\lambda}_A^2 \sin\lambda_E \cos\lambda_E \\ &-\left(\frac{1}{R}\right)\left[a_X \cos\lambda_A \sin\lambda_E + a_Y \sin\lambda_A \sin\lambda_E + a_Z \cos\lambda_E\right]\end{aligned} \tag{5.7}$$

where $a_X = a_{L_X} - a_{F_X} \equiv \ddot{R}_X$, $a_Y = a_{L_Y} - a_{F_Y} \equiv \ddot{R}_Y$, $a_Z = a_{L_Z} - a_{F_Z} \equiv \ddot{R}_Z$ are the relative accelerations of the leader with respect to the follower in the rectangular coordinates. Subscripts '*L*' and '*F*' denote leader and follower aircraft, respectively. The next step is to replace the follower acceleration terms in the rectangular inertial coordinates in Eqs. (5.5)-(5.7) with the specific force vector in the follower body-fixed frame. This is accomplished by first subtracting the gravity vector as shown below:

$$\begin{bmatrix} f_{F_X}^B \\ f_{F_Y}^B \\ f_{F_Z}^B \end{bmatrix} = \left[L_x(\Phi)\right]\left[L_y(\Theta)\right]\left[L_z(\Psi)\right]\left(\begin{bmatrix} a_{F_X} \\ a_{F_Y} \\ a_{F_Z} \end{bmatrix} - \begin{bmatrix} 0 \\ 0 \\ g \end{bmatrix}\right) \tag{5.8}$$

where $\boldsymbol{f}^B = \left[\, f_{F_X}^B, f_{F_Y}^B, f_{F_Z}^B \,\right]^T$ is the specific force vector in the body-fixed frame, g is the acceleration due to gravity, and the $[L]$ matrices represent the rotation matrices that transform a vector from the NED frame to the body-fixed frame [103]. Eq. (5.8) can be inverted as

$$\begin{bmatrix} a_{F_X} \\ a_{F_Y} \\ a_{F_Z} \end{bmatrix} = \left[L_z(-\Psi)\right]\left[L_y(-\Theta)\right]\left[L_x(-\Phi)\right]\begin{bmatrix} f_{F_X}^B \\ f_{F_Y}^B \\ f_{F_Z}^B \end{bmatrix} + \begin{bmatrix} 0 \\ 0 \\ g \end{bmatrix} \tag{5.9}$$

It is assumed that only the X-component of $\boldsymbol{f}^B$ has a functional relation to the throttle among the control input variables $\{\delta T, \delta a, \delta e, \delta r\}$ of the follower aircraft. The Y- and Z-components are assumed to be independent of the control input variables since their dependency is secondary, whereas the X-component can be written as:

$$f_{F_X}^B = \Delta f_{F_X}^B \approx X_{\delta T}\delta T \tag{5.10}$$

where $\Delta f_{F_X}^B = \left(\Delta \Im_{A_X} + \Delta \Im_{T_X}\right)\Big/ m \approx X_{\delta T} \cdot \delta T$ is the perturbation from the trim condition, and $\Im_A, \Im_T$ refer to the external force due to aerodynamics and thrust respectively, and $X_{\delta T} \neq 0$ is the throttle control effectiveness. Combining Eqs. (5.9), (5.10) and substituting in Eqs. (5.5)-(5.7), we obtain:

$$\begin{aligned} \ddot{R} = {} & R\left[\dot{\lambda}_A^2 \cos^2 \lambda_E + \dot{\lambda}_E^2\right] + \left[a_{L_X} \cos\lambda_A \cos\lambda_E + a_{L_Y} \sin\lambda_A \cos\lambda_E - a_{L_Z} \sin\lambda_E\right] \\ & + \left(-\cos\chi_A \cos\lambda_E \cos\Theta - \sin\lambda_E \sin\Theta\right) X_{\delta T}\delta T + \Delta_R^1\left(\boldsymbol{x}_{AC}\right) \end{aligned} \tag{5.11}$$

$$
\begin{aligned}
\ddot{\lambda}_E = & -2\left(\frac{\dot{R}}{R}\right)\dot{\lambda}_E - \dot{\lambda}_A^2 \sin\lambda_E \cos\lambda_E \\
& -\left(\frac{1}{R}\right)\left[a_{L_X}\cos\lambda_A \sin\lambda_E + a_{L_Y}\sin\lambda_A \sin\lambda_E + a_{L_Z}\cos\lambda_E\right] \\
& +\left\{\left(\cos\chi_A \sin\lambda_E \cos\Theta - \cos\lambda_E \sin\Theta\right)/R\right\} X_{\delta T}\delta T + \Delta^1_{\lambda_E}\left(\boldsymbol{x}_{AC}\right)
\end{aligned}
\tag{5.12}
$$

$$
\begin{aligned}
\ddot{\lambda}_A = & \frac{1}{\cos\lambda_E}\left\{-2\dot{\lambda}_A\left[\left(\frac{\dot{R}}{R}\right)\cos\lambda_E - \dot{\lambda}_E \sin\lambda_E\right]\right\} + \left(\frac{1}{R\cos\lambda_E}\right)\left[-a_{L_X}\sin\lambda_A + a_{L_Y}\cos\lambda_A\right] \\
& +\left\{\left(-\sin\chi_A \cos\Theta\right)/\left(R\cos\lambda_E\right)\right\} X_{\delta T}\delta T + \Delta^1_{\lambda_A}\left(\boldsymbol{x}_{AC}\right)
\end{aligned}
\tag{5.13}
$$

where $\boldsymbol{x}_{AC} = \left[U\ V\ W\ p\ q\ r\ \Phi\ \Theta\ \Psi\right]^T$ is the rigid body dynamics state vector of the follower aircraft, $\left\{\Delta^1_R,\ \Delta^1_{\lambda_E},\ \Delta^1_{\lambda_A}\right\}$ are the modeling errors.

To derive the bearing rates' dynamics in terms of the remaining control effectors, the second derivatives of the Euler angles Ψ, Θ and Φ have to be obtained. To do this, first consider the relationship between the Euler angle rates and the angular velocities [103],

$$
\begin{aligned}
\dot{\Phi} &= p + \left(q\sin\Phi + r\cos\Phi\right)\tan\Theta \\
\dot{\Theta} &= q\cos\Phi - r\sin\Phi \\
\dot{\Psi} &= \left(q\sin\Phi + r\cos\Phi\right)\sec\Theta
\end{aligned}
\tag{5.14}
$$

and thus the second time derivatives of Euler angles $\left\{\Psi, \Theta, \Phi\right\}$ can be expressed in the form:

$$
\begin{aligned}
\ddot{\Phi} &= \dot{p} + \left(\dot{q}\sin\Phi + \dot{r}\cos\Phi\right)\tan\Theta \ +\ \Delta^1_{\Phi}\left(\boldsymbol{x}_{AC}\right) \\
\ddot{\Theta} &= \dot{q}\cos\Phi - \dot{r}\sin\Phi \ +\ \Delta^1_{\Theta}\left(\boldsymbol{x}_{AC}\right) \\
\ddot{\Psi} &= \left(\dot{q}\sin\Phi + \dot{r}\cos\Phi\right)\sec\Theta \ +\ \Delta^1_{\Psi}\left(\boldsymbol{x}_{AC}\right)
\end{aligned}
\tag{5.15}
$$

where $\left\{\Delta^1_{\Phi}, \Delta^1_{\Theta}, \Delta^1_{\Psi}\right\}$ are functions of the angular velocities and Euler angles. The derivatives of the angular velocities $\left\{\dot{p}, \dot{q}, \dot{r}\right\}$ depend mainly on the control surface perturbations $\{\delta a, \delta e, \delta r\}$,

$$\begin{aligned}\dot{p} &= \Delta_p\left(\boldsymbol{x}_{AC}\right) + L_{\delta a}\cdot\delta a \\ \dot{q} &= \Delta_q\left(\boldsymbol{x}_{AC}\right) + M_{\delta e}\cdot\delta e \\ \dot{r} &= \Delta_r\left(\boldsymbol{x}_{AC}\right) + N_{\delta r}\cdot\delta r\end{aligned} \tag{5.16}$$

where $\left\{\Delta_p, \Delta_q, \Delta_r\right\}$ are functions of the states of the aircraft dynamics, and $L_{\delta a}, M_{\delta e}$ and $N_{\delta r}$ are the non-zero aileron, elevator and rudder control effectiveness terms respectively. Note that we are ignoring the control-coupling effects of the aileron and rudder in the expressions for $\dot{p}$ and $\dot{r}$ in (5.16) respectively by assuming these effects are small. Using (5.16) in (5.15), we obtain:

$$\begin{aligned}\ddot{\Phi} &= \Delta_\Phi\left(\boldsymbol{x}_{AC}\right) + L_{\delta a}\cdot\delta a + M_{\delta e}\sin\Phi\tan\Theta\cdot\delta e + N_{\delta r}\cos\Phi\tan\Theta\cdot\delta r \\ \ddot{\Theta} &= \Delta_\Theta\left(\boldsymbol{x}_{AC}\right) + M_{\delta e}\cos\Phi\cdot\delta e - N_{\delta r}\sin\Phi\cdot\delta r \\ \ddot{\Psi} &= \Delta_\Psi\left(\boldsymbol{x}_{AC}\right) + M_{\delta e}\sin\Phi\sec\Theta\cdot\delta e + N_{\delta r}\cos\Phi\sec\Theta\cdot\delta r\end{aligned} \tag{5.17}$$

where $\left\{\Delta_\Phi, \Delta_\Theta, \Delta_\Psi\right\}$ are modeling error terms as functions of the aircraft states. Combining (5.17) with Eqs. (5.4) and (5.11)-(5.13), we have:

$$\underbrace{\begin{bmatrix}\ddot{R}\\ \ddot{\chi}_A\\ \ddot{\chi}_E\\ \ddot{\Phi}\end{bmatrix}}_{\boldsymbol{y}^{(r)}} = \underbrace{\begin{bmatrix}\Delta_R\left(\boldsymbol{x}_{AC},\boldsymbol{x}_{LOS},\boldsymbol{a}_L\right)\\ \Delta_{\chi_A}\left(\boldsymbol{x}_{AC},\boldsymbol{x}_{LOS},\boldsymbol{a}_L\right)\\ \Delta_{\chi_E}\left(\boldsymbol{x}_{AC},\boldsymbol{x}_{LOS},\boldsymbol{a}_L\right)\\ \Delta_\Phi\left(\boldsymbol{x}_{AC}\right)\end{bmatrix}}_{\boldsymbol{\Delta}\left(\boldsymbol{x}_{AC},\boldsymbol{x}_{LOS},\boldsymbol{a}_L\right)} + \left[\beta\left(\boldsymbol{x}_{AC},\boldsymbol{y}\right)\right]\underbrace{\begin{bmatrix}\delta T\\ \delta a\\ \delta e\\ \delta r\end{bmatrix}}_{\boldsymbol{u}} \tag{5.18}$$

where $\boldsymbol{\Delta}\left(\boldsymbol{x}_{AC},\boldsymbol{x}_{LOS},\boldsymbol{a}_L\right)$ is the modeling error vector obtained by combining the nonlinear LOS kinematics and leader acceleration terms in Eqs. (5.11)-(5.13) and $\left\{\Delta_\Phi, \Delta_\Theta, \Delta_\Psi\right\}$ in (5.17), and $\left[\beta\left(\boldsymbol{x}_{AC},\boldsymbol{y}\right)\right]$ is a known matrix given by

$$\left[\beta\left(\boldsymbol{x}_{AC},\boldsymbol{y}\right)\right] = \begin{bmatrix}-X_{\delta T}\left\{\cos\chi_A\cos\lambda_E\cos\Theta+\sin\lambda_E\sin\Theta\right\} & 0 & 0 & 0\\ -X_{\delta T}\sin\chi_A\cos\Theta/R\cos\lambda_E & 0 & -M_{\delta e}\sin\Phi\sec\Theta & -N_{\delta r}\cos\Phi\sec\Theta\\ X_{\delta T}\left\{\cos\chi_A\sin\lambda_E\cos\Theta-\cos\lambda_E\sin\Theta\right\}/R & 0 & -M_{\delta e}\cos\Phi & N_{\delta r}\sin\Phi\\ 0 & L_{\delta a} & M_{\delta e}\sin\Phi\tan\Theta & N_{\delta r}\cos\Phi\tan\Theta\end{bmatrix} \tag{5.19}$$

C. Vector Relative Degree and Dynamic Inversion

A well defined vector relative degree exists if and only if the matrix $\left[\beta\left(\boldsymbol{x}_{AC}, \boldsymbol{y}\right)\right]$ is non-singular. The determinant of $\left[\beta\left(\boldsymbol{x}_{AC}, \boldsymbol{y}\right)\right]$ is given by

$$\det\left[\beta\left(\boldsymbol{x}_{AC}, \boldsymbol{y}\right)\right] = X_{\delta T} L_{\delta a} M_{\delta e} N_{\delta r} \left\{\cos\chi_A \cos\lambda_E + \sin\lambda_E \tan\Theta\right\} \tag{5.20}$$

which is non-zero unless the term in the parenthesis is zero. The term in the parenthesis is the $(1,1)^{\text{th}}$ element of the $\left[\beta\left(\boldsymbol{x}_{AC}, \boldsymbol{y}\right)\right]$ matrix multiplied by $\sec\Theta$. So, $\det\left[\beta\left(\boldsymbol{x}_{AC}, \boldsymbol{y}\right)\right] = 0$ implies that the range is not controllable using the throttle δT. Geometrically, this happens when:

1. $\chi_A = \pi/2$ and $\lambda_E = 0$ OR $\chi_A = \pi/2$ and $\Theta = 0$

This condition implies that the follower heading is perpendicular to the LOS when the motion is in the horizontal plane.

2. $\lambda_E = \pm\pi/2$ and $\Theta = 0$ assuming $\left|\Theta\right| < \pi/2$

This condition implies that the follower is either directly above or below the leader aircraft.

To minimize the likelihood of these situations arising, we impose soft limits on the azimuth and elevation bearing angles $\left|\chi_A\right| \le \chi_{A_{\max}} < \pi/2$ and $\left|\chi_E\right| \le \chi_{E_{\max}} < \pi/2$ in our problem formulation. This is enabled by adjusting the bearing rate commands to prevent drifts in the bearing angles to values greater than maximum field-of-view widths. This design of the bearing rate commands is described in Chapter 4, Section 4.3. In our implementation, we set $\chi_{A_{\max}} = \chi_{A_{\max}} = \pi/6$. We also assume the initial conditions for the bearing angles satisfy these restrictions.

The important issue is that should the vector relative degree not exist at some point in time, the condition is only temporary, and an alternative strategy can be pursued when close to this condition. For example, for LOS conditions close to the two cases

shown above, we can give up on regulating range temporarily and an alternative feedback inversion control can be designed. The more serious issue is if there are any equilibrium conditions for which the vector relative degree does not exist. We have shown that by restricting the bearing angles to be less than 90^0, we have eliminated any such equilibrium conditions. In general, we can show that $\det\left[\beta\left(\boldsymbol{x}_{AC}, \boldsymbol{y}\right)\right] \neq 0$ subject to the constraints $\left|\Theta\right| < \pi/2$, $\left|\chi_A\right| \leq \chi_{A_{\max}} < \pi/2$ and $\left|\chi_E\right| \leq \chi_{E_{\max}} < \pi/2$ numerically.

The process of dynamic inversion ignores the nonlinearities and leader's acceleration terms in (5.18). Thus, an approximate feedback linearization is given as follows:

$$\begin{bmatrix} \delta T \\ \delta a \\ \delta e \\ \delta r \end{bmatrix} = \left[\beta\left(\boldsymbol{x}_{AC}, \boldsymbol{y}\right)\right]^{-1} \begin{bmatrix} \nu_R \\ \nu_{\chi_A} \\ \nu_{\chi_E} \\ \nu_\Phi \end{bmatrix} \tag{5.21}$$

where the vector $\boldsymbol{v} = \begin{bmatrix} \nu_R & \nu_{\chi_A} & \nu_{\chi_E} & \nu_\Phi \end{bmatrix}^T$ represents the pseudo-control input vector and represents the desired dynamics of the output vector $\boldsymbol{y} = \left[R,\ \chi_A,\ \chi_E,\ \Phi\right]^T$. Thus, the system dynamics, as far as the regulated output variables are concerned, from Eqs. (5.18) and (5.21), is given by:

$$\boldsymbol{y}^{(r)} = \boldsymbol{\Delta}\left(\boldsymbol{x}_{AC}, \boldsymbol{x}_{LOS}, \boldsymbol{a}_L\right) + \boldsymbol{v} \tag{5.22}$$

D. Construction of the Pseudo-Control Vector

The pseudo-control vector $\boldsymbol{v}$ is constructed as,

$$\boldsymbol{v} = \boldsymbol{v}_{crm} + \boldsymbol{v}_{dc} - \boldsymbol{v}_{ad} \tag{5.23}$$

where $\boldsymbol{v}_{crm}$, $\boldsymbol{v}_{dc}$ and $\boldsymbol{v}_{ad}$ represent the outputs of reference models, linear compensators and the adaptive NN respectively. The construction of $\boldsymbol{v}_{crm}$ and $\boldsymbol{v}_{dc}$ for controlling R, $\dot{\chi}_A$ and $\dot{\chi}_E$ is identical to the construction of $\boldsymbol{v}_{crm}$ and $\boldsymbol{v}_{dc}$ described in Chapter 4, Section 4.1 D and is not repeated here. The construction of $\boldsymbol{v}_{ad}$ for controlling R, $\dot{\chi}_A$ and $\dot{\chi}_E$ is done slightly differently for the IGC law. First, there is a NN for each output being regulated. This allows for separate tuning of each NN, and allows better overall performance. This also allows for modification of the design for individual outputs. This will be illustrated in Section 5.2 where the azimuth channel is designed separately using a backstepping approach. Secondly, since the modeling error $\Delta = \Delta\left(\boldsymbol{x}_{AC}, \boldsymbol{x}_{LOS}, \boldsymbol{a}_L\right)$, the input vector to the NN consists of delayed values of the LOS, delayed values of the follower aircraft acceleration and the state vector of the follower aircraft:

$$\bar{\boldsymbol{\mu}}(t) = \left[1 \quad \boldsymbol{R}_d^T(t) \quad \boldsymbol{\chi}_{A,d}^T(t) \quad \boldsymbol{\chi}_{E,d}^T(t) \quad \boldsymbol{a}_{F_X,d}^T(t) \quad \boldsymbol{a}_{F_Y,d}^T(t) \quad \boldsymbol{a}_{F_Z,d}^T(t) \; \boldsymbol{x}_{AC,norm}^T(t)\right]^T \tag{5.24}$$

All the inputs to the NN were normalized using an estimate for their maximum values. The bank angle command Φ_{com} is constructed to maintain turn coordination, that is, to nullify the acceleration along the Y-axis of the body fixed frame, $a_{F_{Y,com}}^B$. This can be accomplished in several ways. One such way is to use a PD controller to regulate $a_{F_{Y,com}}^B$ to zero as in Figure 33.

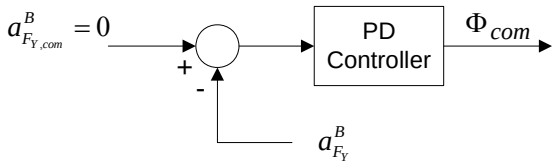

Figure 33. Bank angle command for Turn Coordination

A dynamic inversion controller augmented with an adaptive NN is considered for tracking Φ_{com}. Since Φ is relative degree 2 with respect to aileron deflection δa, a second order reference model is used to filter Φ_{com} and generate the reference command signals Φ_c and $\dot{\Phi}_c$. The bandwidth and damping ratio of the reference model is set with the design parameters $\omega_{n_\Phi}>0$ and $0<\zeta_\Phi<1$ respectively. A PD controller with gains $K_{p_\Phi}>0,\ K_{d_\Phi}>0$ is used as the linear compensator. The pseudo-control ν_Φ is constructed as below

$$
\begin{aligned}
\nu_\Phi &= \nu_{crm_\Phi} + \nu_{dc_\Phi} - \nu_{ad_\Phi} \\
\nu_{crm_\Phi} &= \omega_{n_\Phi}^2\left(\Phi_{com} - \Phi_c\right) - 2\zeta_\Phi\omega_{n_\Phi}\dot{\Phi}_c \\
\nu_{dc_\Phi} &= K_{p_\Phi}\left(\Phi_c - \Phi\right) + K_{d_\Phi}\left(\dot{\Phi}_c - \dot{\Phi}\right) \\
\nu_{ad_\Phi} &= \hat{\boldsymbol{W}}_\Phi^T\boldsymbol{\sigma}\left(\bar{\boldsymbol{\mu}}_{AC}\right) \\
\bar{\boldsymbol{\mu}}_{AC}\left(t\right) &= \left[1 \quad \boldsymbol{x}_{AC,norm}^T\left(t\right)\right]^T
\end{aligned}
\tag{5.25}
$$

where ν_{ad_Φ} is the output of the adaptive NN and $\bar{\boldsymbol{\mu}}_{AC}\left(t\right)$ is the normalized input vector to the NN. The pseudo-control ν_Φ is used to construct $\boldsymbol{\nu}$ which is used in Eq. (5.21) to solve for the actuator deflection commands.

The NN for each output being regulated is updated using the adaptive law in Eq. (4.37). The tracking error vector for bank angle control is given by $\boldsymbol{E}_\Phi = \left[\Phi_c - \Phi,\ \ \dot{\Phi}_c - \dot{\Phi}\right]^T$. If the complete tracking error vector is available as in the case of bank angle control, then an error observer is not required, and (4.37) is written using the actual error vector.

E. Pseudo-Control Hedging (PCH)

The motivation and approach for PCH was explained in Chapter 4, Section 4.1 E, and is not repeated here. The only thing described in this section is the construction of the

hedge signals and updating of the reference models. The estimate of the achieved pseudo-control vector is given as follows:

$$\begin{bmatrix} \hat{\nu}_R \\ \hat{\nu}_{\chi_A} \\ \hat{\nu}_{\chi_E} \\ \hat{\nu}_\Phi \end{bmatrix} = \left[\beta\left(\boldsymbol{x}_{AC}, \boldsymbol{y} \right) \right] \begin{bmatrix} \hat{\delta}T \\ \hat{\delta}a \\ \hat{\delta}e \\ \hat{\delta}r \end{bmatrix} \tag{5.26}$$

where the 'hat' above indicates estimates. The estimated actuator deflections are obtained by using an actuator model that filters the commanded actuator deflections in Eq. (5.21). The hedge signals are given by

$$\begin{bmatrix} \nu_{h_R} \\ \nu_{h_{\chi,A}} \\ \nu_{h_{\chi,E}} \\ \nu_{h_\Phi} \end{bmatrix} = \begin{bmatrix} \nu_R - \hat{\nu}_R \\ \nu_{\chi_A} - \hat{\nu}_{\chi_A} \\ \nu_{\chi_E} - \hat{\nu}_{\chi_E} \\ \nu_\Phi - \hat{\nu}_\Phi \end{bmatrix} \tag{5.27}$$

and the reference models are updated with the hedge signals as follows:

$$\begin{aligned} \ddot{R}_c &= \nu_{crm_R} - \nu_{h_R} \\ \ddot{\chi}_{A_c} &= \nu_{crm_{\chi,A}} - \nu_{h_{\chi,A}} \\ \ddot{\chi}_{E_c} &= \nu_{crm_{\chi,E}} - \nu_{h_{\chi,E}} \\ \ddot{\Phi}_c &= \nu_{crm_\Phi} - \nu_{h_\Phi} \end{aligned} \tag{5.28}$$

Figure 34 shows a block diagram of the adaptive IGC law. The range command is set to a constant value and the bearing rate commands are set to zero. The IGC design developed in this section is referred to as IGC Design 1.

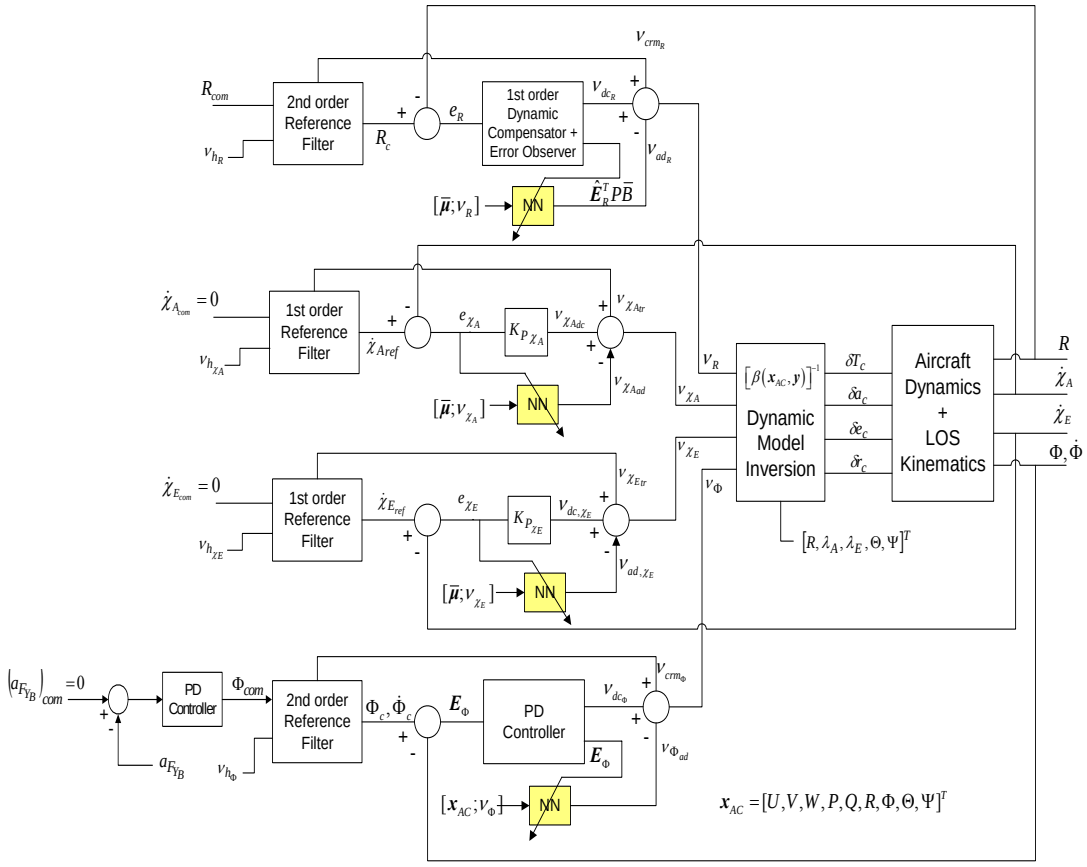

Figure 34. Adaptive Integrated Guidance and Control Block Diagram for LOS Formation Flight – IGC Design 1

Remark 5.3: IGC Design 1 leads to unacceptably large sideslip angles as will be shown in the simulation results. The problem here can be anticipated by examining the first three rows of (5.18) and the matrix $\left[\beta\left(\boldsymbol{x}_{AC}, \boldsymbol{y}\right)\right]$ in (5.19). It can be seen that the derivatives $\ddot{R}$, $\ddot{\chi}_A$ and $\ddot{\chi}_E$ do not contain the aileron deflection term δa. Specifically, the term $\ddot{\chi}_A$ shows strong dependence on the rudder deflection δr for small Φ and Θ. This implies that the rudder is used to generate a heading rate to regulate the azimuth bearing rate to zero. Using the rudder in this way causes uncoordinated turns leading to unacceptably large sideslip angles. In the next section, the azimuth channel is redesigned using the

approach of adaptive backstepping [86], [87], to avoid using the rudder to control the azimuth rate.

5.2 Integrated Guidance and Control – Design 2

The idea behind the redesign of the azimuth channel is to show that there exists a natural dependency of the azimuth rate derivative $\ddot{\lambda}_A$ on the bank angle Φ, and consequently on the aileron deflection δa. Then this natural dependency can be exploited in a strategy to implement adaptive backstepping in terms of three feedback loops as follows

$$(\dot{\lambda}_A) \rightarrow (\phi) \rightarrow (p) \rightarrow (\delta a)$$

A. Azimuth rate control via backstepping design

The first step is to re-write (5.6) as follows

$$\begin{aligned}\ddot{\lambda}_A = & \frac{-2\dot{\lambda}_A}{\cos\lambda_E}\left[\left(\frac{\dot{R}}{R}\right)\cos\lambda_E - \dot{\lambda}_E \sin\lambda_E\right] + \left(\frac{1}{R\cos\lambda_E}\right)\left[-a_{L_X}\sin\lambda_A + a_{L_Y}\cos\lambda_A\right] \\ & -\left(\frac{1}{R\cos\lambda_E}\right)\left[-a_{F_X}\sin\lambda_A + a_{F_Y}\cos\lambda_A\right]\end{aligned} \tag{5.29}$$

Then the following equality can be derived

$$-a_{F_X}\sin\lambda_A + a_{F_Y}\cos\lambda_A = -a^1_{F_X}\sin(\lambda_A - \Psi) + a^1_{F_Y}\cos(\lambda_A - \Psi) \tag{5.30}$$

where $a^1_{F_X}$ and $a^1_{F_Y}$ represent the X and Y-axis acceleration components of follower aircraft expressed in the coordinate frame obtained by a rotation about the inertial Z-axis by the Euler angle Ψ.

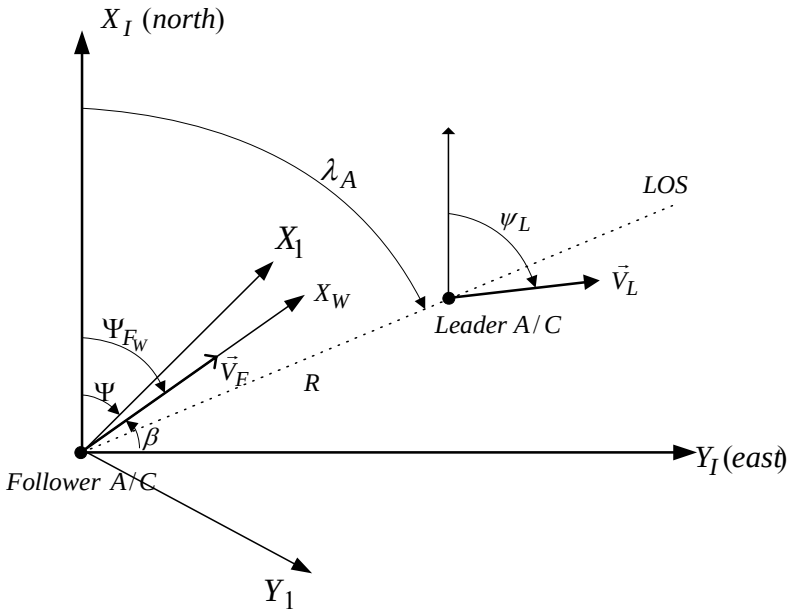

Figure 35. Coordinate Reference Frames in Horizontal Plane

From the pictorial representation of the coordinate frames in the inertial horizontal plane in Figure 35, the acceleration component $a^1_{F_Y}$ can be approximated as follows

$$a^1_{F_Y} \approx V_F \cos\Theta \cdot \dot{\Psi}_{F_W} \approx V_F \cos\Theta\left(\dot{\Psi} + \dot{\beta}\right) \tag{5.31}$$

where the subscript '*W*' indicates the wind axes, V_F is the follower speed, and β is the sideslip angle. Then, the following identities can be used to expand (5.31)

$$\dot{\Psi} = \left(q\sin\Phi + r\cos\Phi\right)\sec\Theta \tag{5.32}$$

$$\begin{aligned}\dot{\beta} = {} & p\sin\alpha - r\cos\alpha + \frac{1}{mV_F}\left(D\sin\beta + Y\cos\beta\right) \\ & + \frac{g}{V_F}\left(\cos\alpha\sin\beta\sin\Theta + \cos\beta\sin\Phi\cos\theta - \sin\alpha\sin\beta\cos\Phi\cos\Theta\right)\end{aligned} \tag{5.33}$$

where α is the angle of attack and D and Y are the aerodynamic drag and cross-wind forces.

Using $\chi_A = \lambda_A - \Psi$, $\ddot{\chi}_A$ can be written as follows by utilizing Eqs. (5.17), (5.29)-(5.33):

$$\ddot{\chi}_A = f_1\left(\boldsymbol{x}_{AC}, \boldsymbol{x}_{LOS}\right) + g_1\left(\boldsymbol{y}, \boldsymbol{x}_{AC}\right)\cdot\Phi + \Delta_{\chi_A}\left(\boldsymbol{x}_{AC}, \boldsymbol{x}_{LOS}, \boldsymbol{a}_L\right) \tag{5.34}$$

where

$$\begin{aligned} f_1\left(\boldsymbol{x}_{AC}, \boldsymbol{x}_{LOS}\right) &= \frac{-2\dot{\lambda}_A}{\cos\lambda_E}\left[\left(\frac{\dot{R}}{R}\right)\cos\lambda_E - \dot{\lambda}_E\sin\lambda_E\right] - \left(\frac{1}{R\cos\lambda_E}\right)a^1_{F_X}\sin\chi_A \\ g_1\left(\boldsymbol{y}, \boldsymbol{x}_{AC}\right) &= -\frac{\cos\chi_A}{R\cos\lambda_E}\left(V_F\, q + g\cos\beta\cos^2\Theta\right) \end{aligned} \tag{5.35}$$

are known, computable terms and $\Delta_{\chi_A} = \Delta_{\chi_A}\left(\boldsymbol{x}_{AC}, \boldsymbol{x}_{LOS}, \boldsymbol{a}_L\right)$ is the modeling error term. We also have

$$\begin{aligned} \dot{\Phi} &= f_2\left(\boldsymbol{x}_{AC}\right) + g_2 p \\ f_2\left(\boldsymbol{x}_{AC}\right) &= \left(q\sin\Phi + r\cos\Phi\right)\tan\Theta \\ g_2 &= 1 \end{aligned} \tag{5.36}$$

and

$$\begin{aligned} \dot{p} &= f_3\left(\boldsymbol{x}_{AC}\right) + g_3\delta a + \Delta_p\left(\boldsymbol{x}_{AC}, \delta a\right) \\ f_3\left(\boldsymbol{x}_{AC}\right) &= L_\beta\beta + L_p p + L_r r \\ g_3 &= L_{\delta a} \end{aligned} \tag{5.37}$$

where $f_2\left(\boldsymbol{x}_{AC}\right), f_3\left(\boldsymbol{x}_{AC}\right), g_2, g_3$ are also known, computable terms, $L_\beta, L_p, L_r, L_{\delta a}$ are lateral-directional aerodynamic derivatives obtained for a specific flight condition, and $\Delta_p = \Delta_p\left(\boldsymbol{x}_{AC}, \delta a\right)$ is the modeling error associated with the roll-rate dynamics. Eqs. (5.34)-(5.37) show that the bearing azimuth rate dynamics has a natural cascade form. That is, Φ can be used as a virtual control for the $\dot{\chi}_A$ dynamics, and p as a virtual control for the Φ dynamics, with the control δa finally being computed to ensure $\dot{\chi}_A$ command tracking. Let $x_1 = \dot{\chi}_A,\ x_2 = \Phi,\ x_3 = p,$ and $u = \delta a$. Then Eqs. (5.34)-(5.37) can be rewritten as follows:

$$\begin{aligned}\dot{x}_1 &= f_1(\boldsymbol{x}_{AC},\boldsymbol{x}_{LOS})+g_1(\boldsymbol{y},\boldsymbol{x}_{AC})x_2+\Delta_{\chi_A}\left(\boldsymbol{x}_{AC},\boldsymbol{x}_{LOS},\boldsymbol{a}_L\right)\\ \dot{x}_2 &= f_2\left(\boldsymbol{x}_{AC},x_2\right)+g_2x_3\\ \dot{x}_3 &= f_3(\boldsymbol{x}_{AC},x_3)+g_3u+\Delta_p\left(\boldsymbol{x}_{AC},u\right)\end{aligned} \tag{5.38}$$

The bearing azimuth rate dynamics in (5.38) are in the form suitable for the application of adaptive backstepping [86], [87]. We begin by defining the following error states

$$\begin{aligned}\zeta_1 &\equiv x_{1_c}-x_1\\ \zeta_2 &\equiv g_1\cdot(\overline{x}_2-x_2)\\ \zeta_3 &\equiv g_1\cdot(\overline{x}_3-x_3)\end{aligned} \tag{5.39}$$

where $\overline{x}_2$ and $\overline{x}_3$ are virtual commands to be constructed that will ensure that the reference command x_{1_c} is tracked. The reference command x_{1c} is obtained by filtering the raw azimuth bearing rate command $\dot{\chi}_{A_{com}}$ through a stable command filter that generates smooth, achievable trajectories.

Step 1: Differentiating ζ_1 applying Eqs. (5.38) and (5.39) yields

$$\dot{\zeta}_1 = \dot{x}_{1_c}-\dot{x}_1=\dot{x}_{1_c}-f_1-g_1x_2-\Delta_{\chi_A}=\dot{x}_{1_c}-f_1+\zeta_2-g_1\overline{x}_2-\Delta_1 \tag{5.40}$$

where $\overline{x}_2$ is viewed as a virtual control for the ζ_1 dynamics. Then to stabilize the ζ_1 dynamics, let

$$\overline{x}_2 = g_1^{-1}\left[K_1\zeta_1-f_1+\dot{x}_{1_c}-\nu_{ad_1}\right] \tag{5.41}$$

where ν_{ad_1} is an adaptive control term designed to cancel Δ_1 and $\Delta_1=\Delta_{\chi_A}$. Note that $|g_1|>0$ for (5.41) to be valid. Examining (5.35), this imposes a requirement that $|\chi_A|<\pi/2$. Hence, the bearing rate command $\dot{\chi}_{A_{com}}$ is constructed such that $|\chi_A|$ does not drift to large values. Then substituting (5.41) into (5.40) yields

$$\dot{\zeta}_1 = -K_1\zeta_1+\zeta_2+\nu_{ad_1}-\Delta_1 \tag{5.42}$$

Step 2: Differentiating ζ_2 yields

$$\begin{aligned}\dot{\zeta}_2 &= \dot{g}_1\left(\bar{x}_2 - x_2\right) + g_1\left(\dot{\bar{x}}_2 - \dot{x}_2\right) = \dot{g}_1\left(\bar{x}_2 - x_2\right) + g_1\dot{\bar{x}}_2 - g_1\dot{x}_2 \\ &= -\Delta_2 + \ddot{x}_{l_c} - g_1 x_3 - g_1 f_2 = -\Delta_2 + \ddot{x}_{l_c} - g_1 f_2 + \zeta_3 - g_1\bar{x}_3\end{aligned} \tag{5.43}$$

where $\Delta_2 \equiv -\left[\dot{g}_1\left(\bar{x}_2 - x_2\right) + g_1\dot{\bar{x}}_2 - \ddot{x}_{l_c}\right]$ since the derivatives of f_1 and g_1 contain unknown terms due to leader aircraft motion. Let

$$\bar{x}_3 = g_1^{-1}\left[\zeta_1 + K_2\zeta_2 + \ddot{x}_{l_c} - g_1 f_2 - \nu_{ad_2}\right] \tag{5.44}$$

so that

$$\dot{\zeta}_2 = -\zeta_1 - K_2\zeta_2 + \zeta_3 + \nu_{ad_2} - \Delta_2 \tag{5.45}$$

The purpose of introducing ζ_1 in (5.45) is to compensate for the coupling between the ζ_1 and ζ_2 dynamics. The sign of the ζ_1 in (5.45) is intentionally chosen as negative to set up a skew-symmetric matrix representing the complete error dynamics. This skew-symmetric structure is a key feature of backstepping controllers, and results in the cancellation of the coupling terms during Lyapunov stability analysis [87].

Step 3: Differentiating ζ_3 yields

$$\begin{aligned}\dot{\zeta}_3 &= \dot{g}_1\left(\bar{x}_3 - x_3\right) + g_1\left(\dot{\bar{x}}_3 - \dot{x}_3\right) = \dot{g}_1\left(\bar{x}_3 - x_3\right) + g_1\dot{\bar{x}}_3 - g_1\dot{x}_3 \\ &= \dot{g}_1\left(\bar{x}_3 - x_3\right) + g_1\dot{\bar{x}}_3 - g_1\left(f_3 + g_3 u + \Delta_P\right) \\ &= -\Delta_3 + \dddot{x}_{l_c} - g_1 f_3 - g_1 g_3 u\end{aligned} \tag{5.46}$$

where $\Delta_3 \equiv -\left[\dot{g}_1\left(\bar{x}_3 - x_3\right) + g_1\dot{\bar{x}}_3 - \dddot{x}_{l_c} - g_1\Delta_p\right]$. Let

$$u = \left(g_1 g_3\right)^{-1}\left[\zeta_2 + K_3\zeta_3 - g_1 f_3 + \dddot{x}_{l_c} - \nu_{ad_3}\right] \tag{5.47}$$

so that

$$\dot{\zeta}_3 = -\zeta_2 - K_3\zeta_3 + \nu_{ad_3} - \Delta_3 \tag{5.48}$$

Note that $|g_1 g_3| > 0$ since the aileron control effectiveness $g_3 = L_{\delta a}$ is non-zero in most aircraft control applications. Eqs .(5.42), (5.45) and (5.48) can be now expressed in state space form

$$\dot{\boldsymbol{\omega}} = \bar{A}\boldsymbol{\omega} + \boldsymbol{\nu}_{ad} - \boldsymbol{\Delta} \tag{5.49}$$

where $\boldsymbol{\omega} \equiv \left[\, \zeta_1, \zeta_2, \zeta_3 \,\right]^T$, $\boldsymbol{\nu}_{ad} \equiv \left[\, \nu_{ad_1}, \nu_{ad_2}, \nu_{ad_3} \,\right]^T$, $\boldsymbol{\Delta} \equiv \left[\, \Delta_1, \Delta_2, \Delta_3 \,\right]^T$, and

$$\bar{A} = \begin{bmatrix} -K_1 & 1 & 0 \\ -1 & -K_2 & 1 \\ 0 & -1 & -K_3 \end{bmatrix} \tag{5.50}$$

The gains $K_{1,2,3} > 0$ to ensure stability, but they also need to be tuned to obtain reasonable performance. The NN considered is a single-hidden-layer NN with output given by

$$\boldsymbol{\nu}_{ad} = \hat{W}^T \boldsymbol{\sigma}\left(\hat{V}^T \bar{\boldsymbol{\mu}}\right) \tag{5.51}$$

where $\hat{W}, \hat{V}$ are the output and input layer NN weight matrices respectively, $\boldsymbol{\sigma}$ is the vector of uniformly bounded and continuously differentiable sigmoidal basis functions [92], and $\bar{\boldsymbol{\mu}}$ is the normalized input vector to the NN given in (5.24). The NN weight update law is given by [86]

$$\begin{aligned} \dot{\hat{V}} &= -\left[\, \bar{\boldsymbol{\mu}} \boldsymbol{\omega}^T \hat{W}^T \hat{\sigma}' + \lambda_V \left\| \boldsymbol{\omega} \right\| \hat{V} \,\right] \Gamma_V \\ \dot{\hat{W}} &= -\left[\, \left(\hat{\boldsymbol{\sigma}} - \hat{\sigma}' \hat{V}^T \bar{\boldsymbol{\mu}} \right) \boldsymbol{\omega}^T + \lambda_W \left\| \boldsymbol{\omega} \right\| \hat{W} \,\right] \Gamma_W \end{aligned} \tag{5.52}$$

where $\hat{\boldsymbol{\sigma}} = \boldsymbol{\sigma}\left(\hat{V}^T \bar{\boldsymbol{\mu}}\right)$, $\hat{\sigma}'$ is the derivative of $\boldsymbol{\sigma}$ with respect to its argument, $\Gamma_{V,W} > 0$ are the NN learning rates, and $\lambda_{V,W} > 0$ are e-mod parameters [94]. The NN adaptive law itself is not a contribution of this thesis and details of the derivation of (5.52) and stability analysis are referred to Ref. [86] and references within.

The complete control policy is given by Eqs. (5.39), (5.41), (5.44), (5.47), (5.51) and (5.52). The block diagram for this control structure is given by Figure 36.

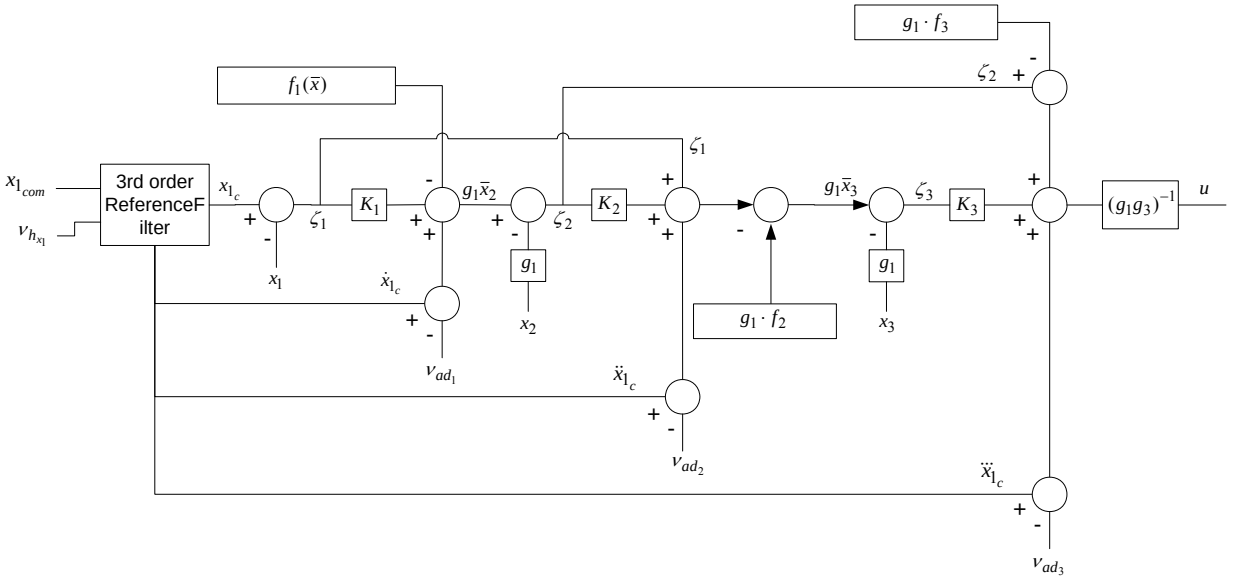

Figure 36. Azimuth Rate Control using Adaptive Backstepping Algorithm

B. Turn Coordination by Adaptive Lateral Acceleration Control

To maintain turn coordination, the lateral acceleration along the body-fixed Y-axis a_Y^B is regulated to zero. The control design consists of an outer-loop proportional-integral (PI) controller acting on the lateral acceleration command error and whose output $y_{lat,com}$ is a command for the blended output $y_{lat} = \beta + C_r r$ [111]. The signal $y_{lat,com}$ is input to an inner-loop inverting controller augmented by an adaptive NN that generates rudder deflection command δr_{com}. The details of the design are contained in the Appendix B. The derivative of the blended output y_{lat} can be given as

$$\dot{y}_{lat} = \dot{\beta} + C_r \dot{r} = \Delta_{y_{lat}}\left(\boldsymbol{x}_{AC}\right) + \left(\frac{Y_{\delta r}}{U_0} + C_r N_{\delta r}\right)\delta r \tag{5.53}$$

where $\Delta_{y_{lat}}(\boldsymbol{x}_{AC})$ is the modeling error associated with the dynamic inversion of the $\dot{y}_{lat}$ dynamics which is compensated for with the output of the adaptive NN.

C. Dynamic Inversion

In IGC Design 2, the outputs regulated via NN augmented dynamic inversion are $\boldsymbol{y}_2 = [R,\ \chi_E,\ y_{lat}]^T$. From Eqs. (5.18) and (5.53), we have,

$$\underbrace{\begin{bmatrix} \ddot{R} \\ \ddot{\chi}_E \\ \dot{y}_{lat} \end{bmatrix}}_{\boldsymbol{y}_2^{(r)}} = \underbrace{\begin{bmatrix} \Delta_R(\boldsymbol{x}_{AC}, \boldsymbol{x}_{LOS}, \boldsymbol{a}_L) \\ \Delta_{\chi_E}(\boldsymbol{x}_{AC}, \boldsymbol{x}_{LOS}, \boldsymbol{a}_L) \\ \Delta_{y_{lat}}(\boldsymbol{x}_{AC}) \end{bmatrix}}_{\boldsymbol{\Delta}_2(\boldsymbol{x}_{AC}, \boldsymbol{x}_{LOS}, \boldsymbol{a}_L)} + \left[\beta_2(\boldsymbol{x}_{AC}, \boldsymbol{y})\right] \begin{bmatrix} \delta T \\ \delta e \\ \delta r \end{bmatrix} \tag{5.54}$$

where $\left[\beta_2(\boldsymbol{x}_{AC}, \boldsymbol{y})\right]$ is a computable matrix given by

$$\beta_2(\boldsymbol{x}_{AC}, \boldsymbol{y}) = \begin{bmatrix} \{-\cos\chi_A \cos\lambda_E \cos\Theta - \sin\lambda_E \sin\Theta\} X_{\delta T} & 0 & 0 \\ \left\{\{\cos\chi_A \sin\lambda_E \cos\Theta - \cos\lambda_E \sin\Theta\}/R\right\} X_{\delta T} & M_{\delta e}\cos\Phi & -N_{\delta r}\sin\Phi \\ 0 & 0 & \dfrac{Y_{\delta r}}{U_0} + C_r N_{\delta r} \end{bmatrix} \tag{5.55}$$

A well defined vector relative degree exists if and only if the matrix $\left[\beta_2(\boldsymbol{x}_{AC}, \boldsymbol{y})\right]$ is non-singular. The determinant of $\left[\beta_2(\boldsymbol{x}_{AC}, \boldsymbol{y})\right]$ is given by

$$\det\left[\beta_2(\boldsymbol{x}_{AC}, \boldsymbol{y})\right] = -X_{\delta T} M_{\delta e} \left(\frac{Y_{\delta r}}{U_0} + C_r N_{\delta r}\right) \{\cos\chi_A \cos\lambda_E + \sin\lambda_E \tan\Theta\} \cos\Phi \tag{5.56}$$

which is non-zero unless the term in the parenthesis is zero. Thus, an approximate feedback linearization is given as follows:

$$\begin{bmatrix} \delta T \\ \delta e \\ \delta r \end{bmatrix} = \left[\beta_2(\boldsymbol{x}_{AC}, \boldsymbol{y})\right]^{-1} \begin{bmatrix} \nu_R \\ \nu_{\chi_E} \\ \nu_{y_{lat}} \end{bmatrix} \tag{5.57}$$

where the vector $\boldsymbol{\nu}_2 = \begin{bmatrix} \nu_R & \nu_{\chi_E} & \nu_{y_{lat}} \end{bmatrix}^T$ represents the pseudo-control input vector and represents the desired dynamics of the output vector $\boldsymbol{y}_2$. The rest of the inverting design is very similar to the design described in Section 5.1 C and beyond. This is not repeated in this section. Figure 37 shows a block diagram for IGC Design 2.

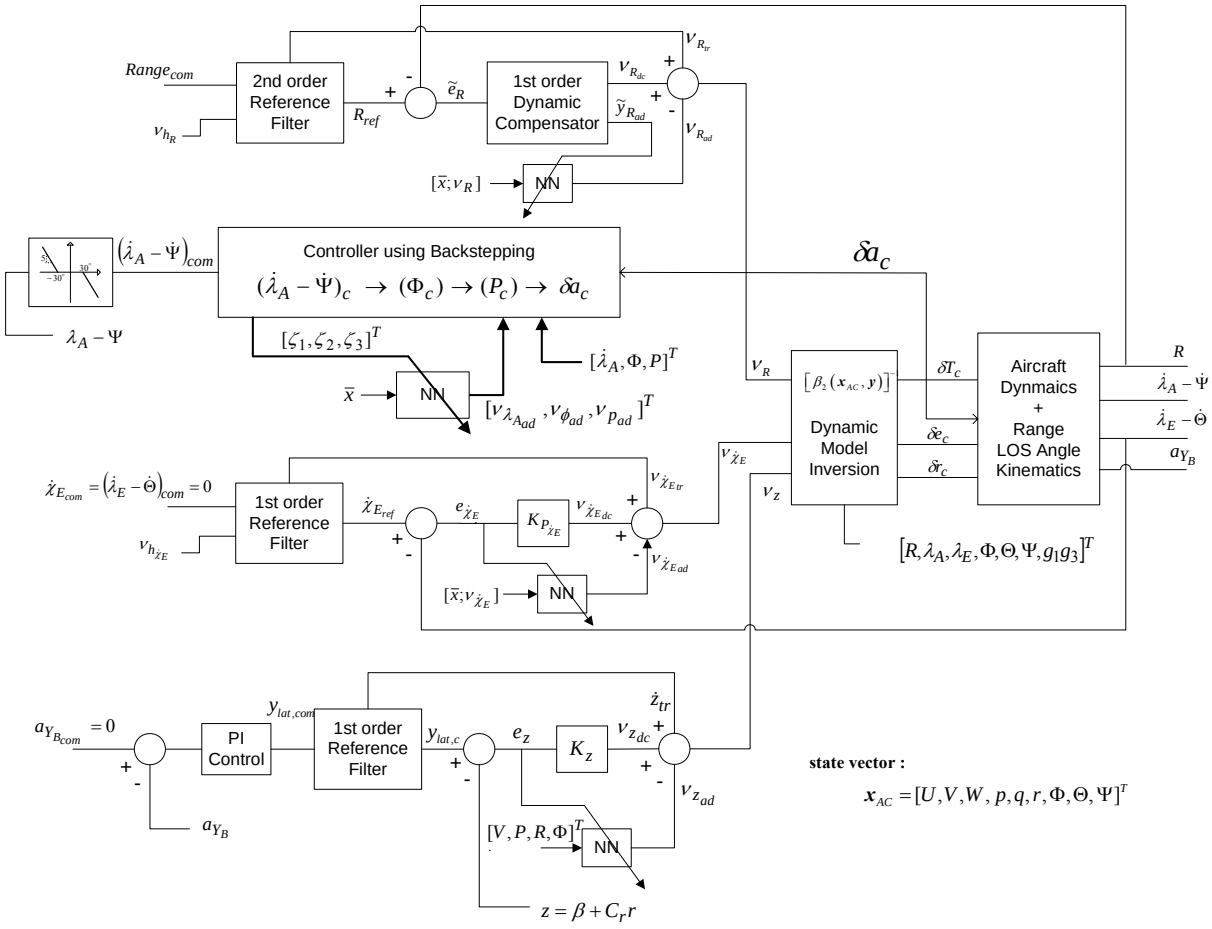

Figure 37. Adaptive Integrated Guidance and Control Block Diagram for LOS Formation Flight – Design 2

5.3 Simulation Results

We compare the range tracking performance of IGC Design 1 (IGC-1 henceforth) and IGC Design 2 (IGC-2 henceforth) with that of the time-scale separated adaptive guidance and control design presented in Chapter 4. We abbreviate the latter as the 'TSSGC' design for convenience in the discussion that follows. The 6DOF nonlinear simulation model has been described in Chapter 4, Section 4.3-A. The comparison between the three guidance and control designs will be shown for the case of the slanted 3D box maneuver of the leader aircraft. For this case, the waypoints are at the corners of a slanted box in 3D space, requiring sharp heading changes, combined with climbing and descending motions of the leader. This is referred to as Case-3 leader maneuver in the simulation results in Chapter 4. The performance with the TSSGC design was the 'worst' for this maneuver in comparison with the two other leader maneuvers considered in Chapter 4.

The range command is set to $R_{com} = 5$ meters, which is slightly less than 2 wing-span lengths. The LOS (bearing) rate commands for all three designs are nominally set to zero, and these commands are modified to prevent drifts in the bearing angles to large values using the dead-zone logic shown in Figure 23.

Figure 38 shows the range command tracking performance in meters with the TSSGC, IGC 1 and IGC 2 designs. The black solid line represents the commanded range $R_{com} = 5$ meters, the blue dotted line is the range, and the red dashed line represents the hedged reference signal. The range signal R tracks the hedged reference signal R_{ref}. It is clear that the performance with the IGC designs (Figure 38 b, c) is superior to the TSSGC design (Figure 38 a) by virtue of much smaller range overshoots (maximum of 1.5 meters for the IGC designs, versus 4.5 meters for the TSSGC design), and convergence to the commanded range in steady-state. The overshoots in range occur after the leader aircraft starts a maneuver.

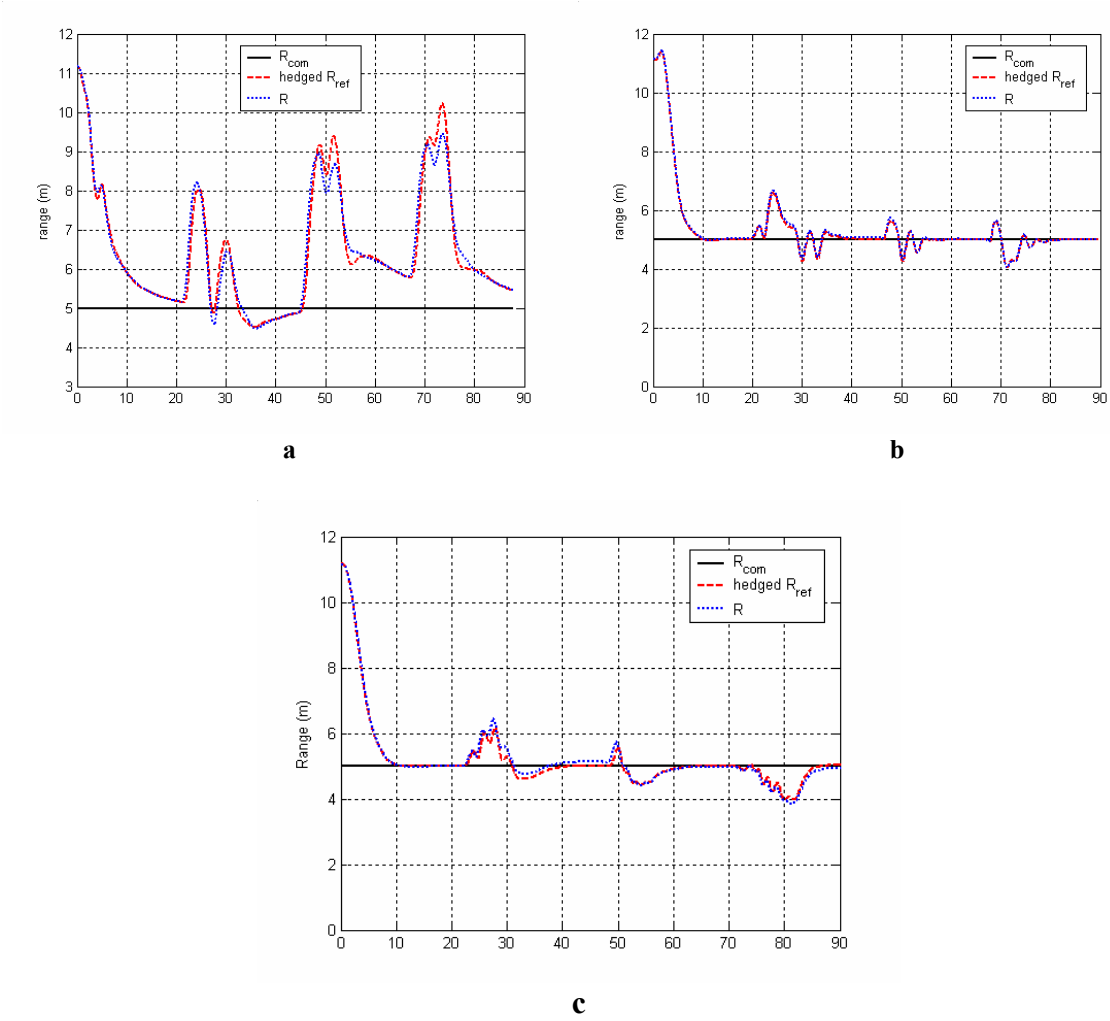

Figure 38. Range Command Tracking Performance (meters), a) TSSGC b) IGC-1 c) IGC-2

One of the reasons for the deficient performance of the TSSGC design when compared to the IGC designs is the choice of command to the throttle controller in the TSSGC design. This was explained in Chapter 4, Section 4.2. The throttle controller in the TSSGC design is a PI controller with anti-windup. There is a stability issue when the longitudinal acceleration command $f_{x_{cmd}}$ from the guidance law is input to the throttle controller for the case of a sharply turning leader aircraft. This is due to the fact that the

guidance logic generates an excessive negative acceleration command along the X-axis of the body frame (highly negative $f_{x_{cmd}}$) when starting a heading turn and this causes the throttle to saturate, ultimately leading to instability of the entire closed-loop system. As described in Chapter 4, Section 4.2, the throttle controller command is modified to be a blend of the longitudinal acceleration command $f_{x_{cmd}}$ and speed command V_{com}. The blended throttle controller command in Eq. (4.52) reduces the transient speed of response of the range variable and the desired steady-state with respect to range may not be exactly achieved even when the leader stops maneuvering. The consequence of the modification of the throttle command is a trade-off between range command tracking and closed-loop stability for the TSSGC design. This is not an issue in the IGC designs since the throttle command is obtained by dynamic inversion of the range and bearing rate dynamics (Eqs.(5.21) and (5.57)) with adaptive compensation for the modeling errors.

Figure 39 shows the angle of attack and sideslip angle histories in degrees for all three designs. It is clear that the sideslip angles with IGC-1 are unacceptably large (maximum 15 degrees). With the TSSGC design and IGC-2, the sideslip angle histories are acceptable (maximum 4 degrees). To further reduce the sideslip excursions in Figure 39 a, c, a simulation study was carried out by incorporating a washout filter in the yaw-rate feedback loop. However, this did not result in further improvement in the sideslip suppression performance. More work is needed to address this issue but it is not dealt with further in this thesis.

Figure 40 shows the bearing rates histories in deg/s. When the leader maneuvers, there are large overshoots in the LOS and bearing rates histories, but the overshoots with the IGC designs are much smaller than those with the TSSGC design. The red solid lines in Figure 40 are the hedged reference signals. Figure 40 a shows the reference signal dynamics are slower for the TSSGC design. This is because the reference model bandwidths in the TSSGC design are restricted by the limitations of the autopilot. In the

IGC designs, the reference models have higher bandwidths. This is a key point of the IGC design. The IGC design allows much higher controller bandwidths than a time-scale separated design, and hence can achieve better performance. In Figure 40 b and c, the apparent sign reversal of the reference signals is due to hedging of the IGC designs.

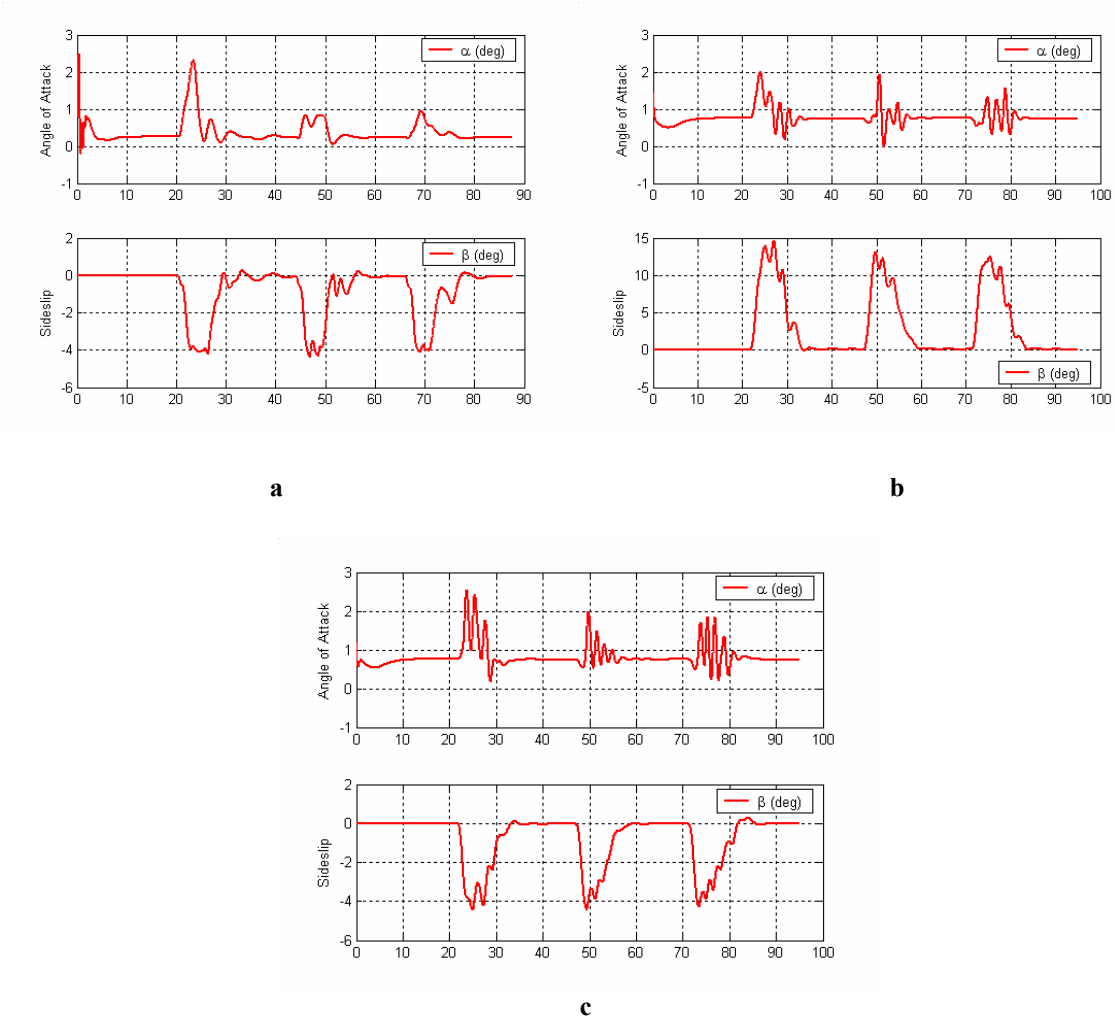

Figure 39. Aerodynamic Angles (deg) a) TSSGC b) IGC-1 c) IGC-2

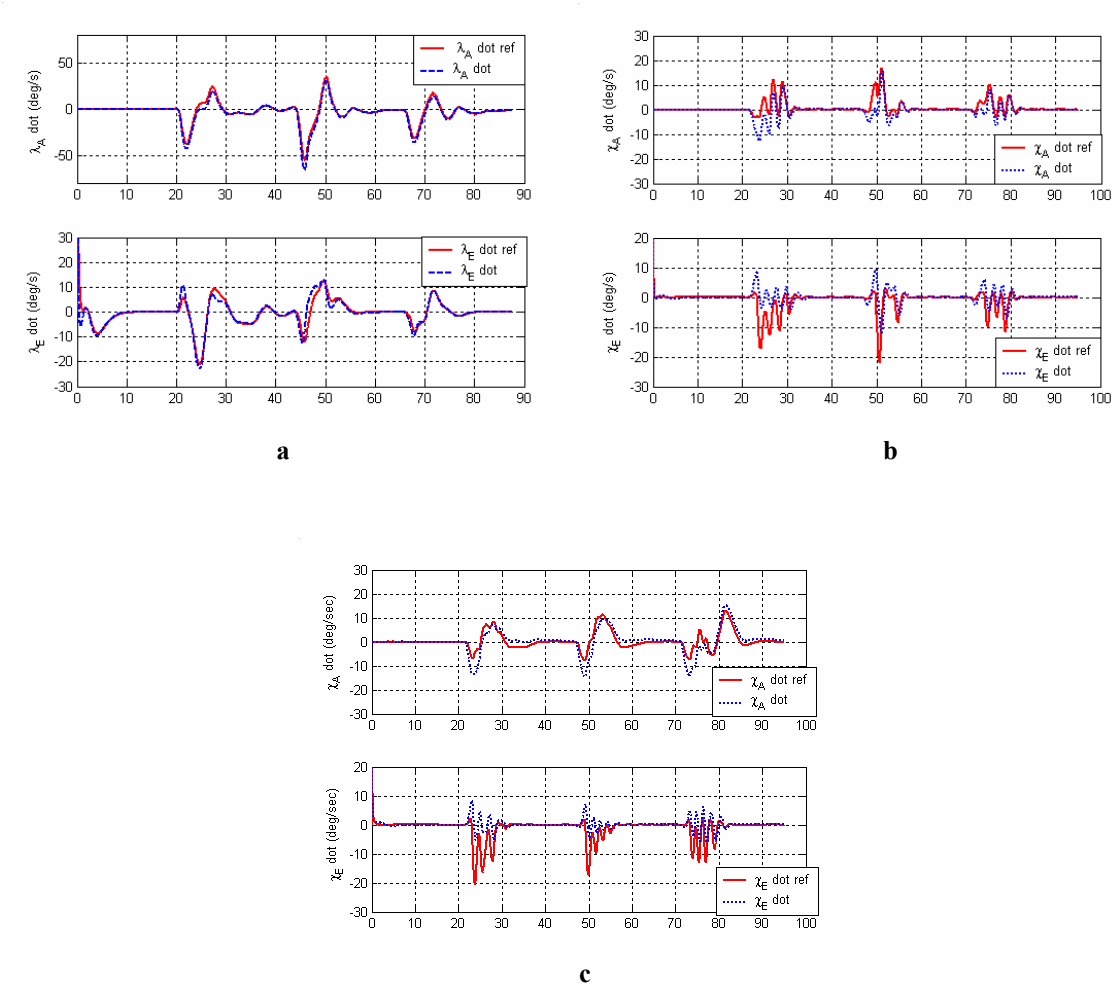

Figure 40. Bearing Rates Tracking Performance (deg/s), a) TSSGC Design, b) IGC-1, c) IGC-2

Figure 41 shows the bearing angles. With IGC-1 and IGC-2 designs, the bearing angles ride the boundaries of the dead-zone given by $\chi_{A_{\max}} = \chi_{A_{\max}} = \pi/6$ in the steady-state with transient overshoots of less than 10^0. With the TSSGC design, the overshoots are about 20^0, which again show that the bearing rate regulation with the IGC designs is superior to that of the TSSGC design.

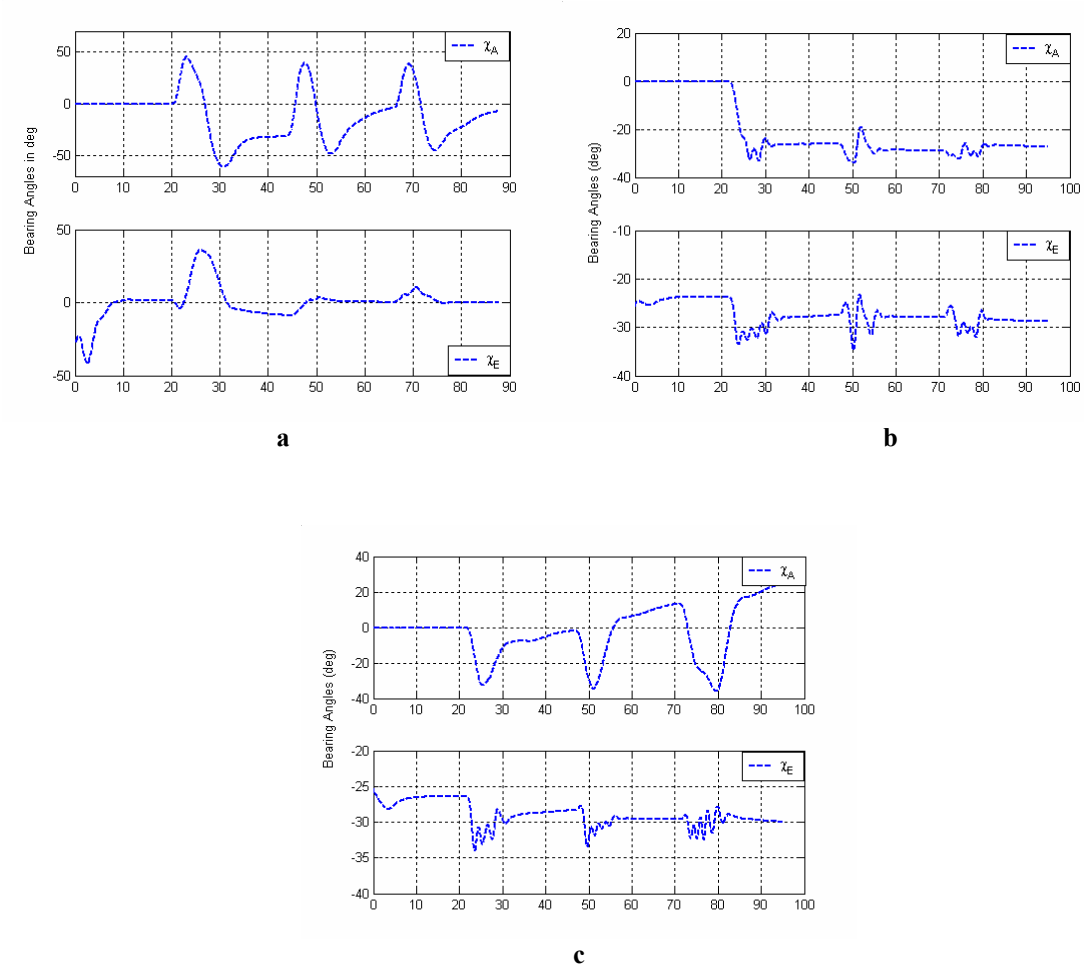

Figure 41. Bearing Angles (deg), a) TSSGC Design, b) IGC-1, c) IGC-2

Figure 42 shows the actuator deflections. There is lot more activity in the rudder and aileron channels with the IGC designs than with the TSSGC design, and the control histories have reasonable amplitude and frequency content.

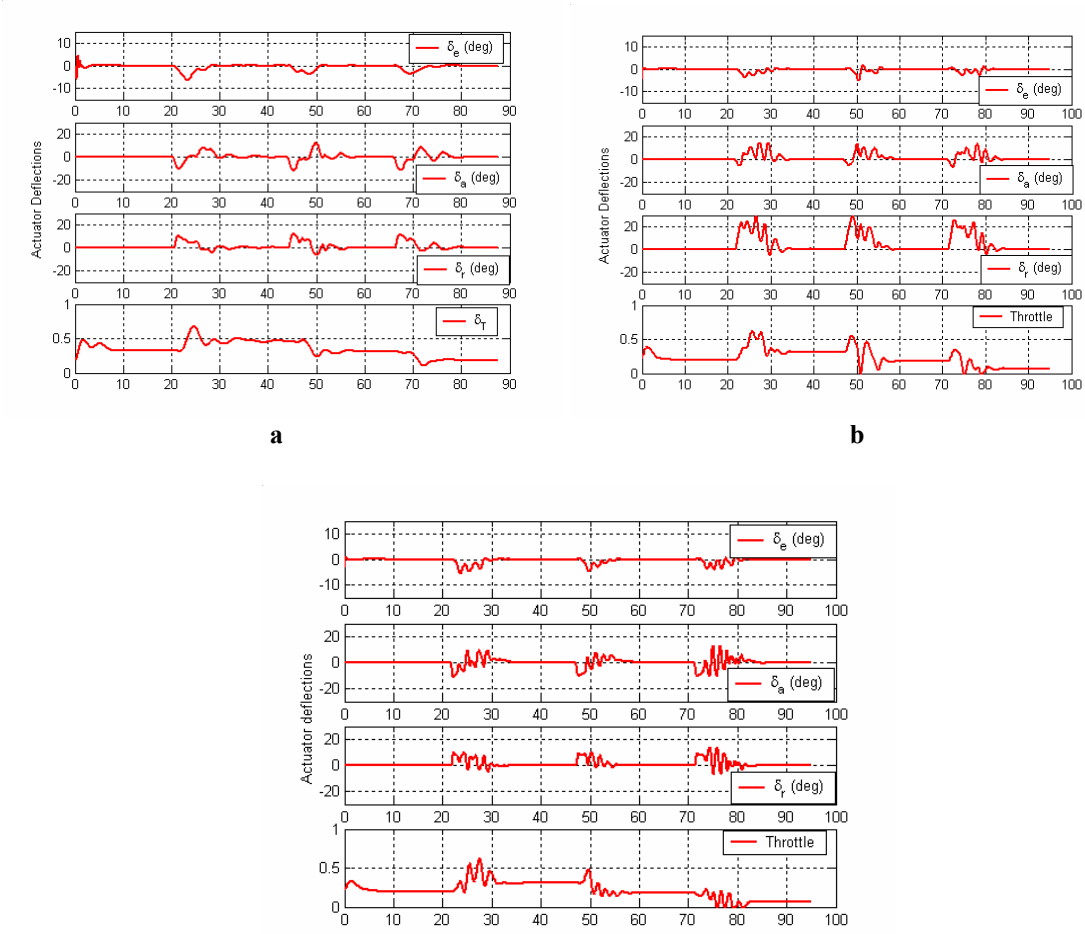

Figure 42. Actuator deflection histories a) TSSGC b) IGC-1 c) IGC-2

Figure 43 shows the NN approximation of the modeling error Δ for the IGC-1 and IGC-2 designs. The figure shows very good approximation indicating the effectiveness of adaptation. The corresponding plot for the TSSGC design is shown in Figure 30. If the adaptation is switched off, the tracking goes unstable for all three designs. Figure 44 shows the range tracking performance with NN off for just the IGC designs, which shows that the tracking diverges after the first leader maneuver. The corresponding plot for the TSSGC design is shown in Figure 32.

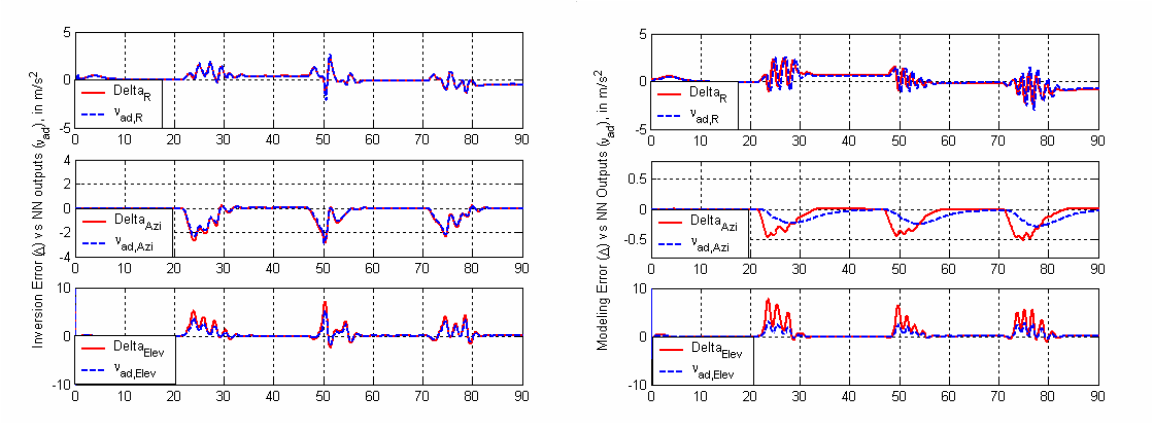

a **b**

Figure 43. Modeling Error Δ vs NN Outputs ν_{ad}, in m/s^2, a) IGC-1 b) IGC-2

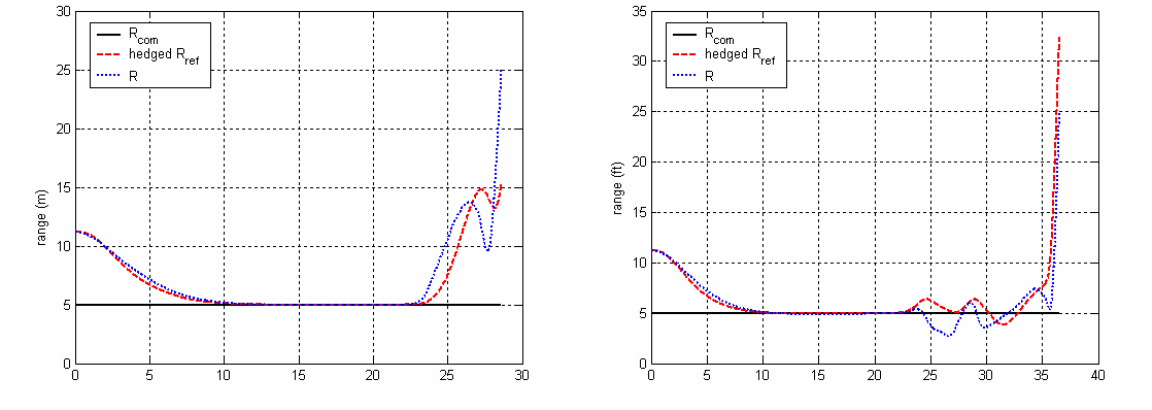

a **b**

Figure 44. Range Tracking Performance in meters, NN off, a) IGC-1 b) IGC-2

The next set of results is obtained for varying bandwidths of the G&C designs. The objective is to show that the IGC design is capable of achieving higher bandwidth than the TSSGC design for the combined G&C dynamics and to provide bandwidth metrics for the two designs. The bandwidth of the designs in this study is indicated by the time-constants of the reference models for range and LOS rates command tracking. In the following, the bandwidths of the reference models for LOS rates command tracking are

set to values such that increasing the bandwidths further result in destabilization of the tracking performance. Then the natural frequencies of the range command reference model (2^{nd} order stable linear systems for both TSSGC and IGC designs) are varied between spectrums of values and range tracking is noted. The smallest and highest values of the natural frequency for which reasonable range tracking performance (defined to be such that the overshoot in range response is less than 5 meters) is obtained are indicated for both the designs. The comparison between the two designs is illustrated for the slanted 3D box leader maneuver.

In the TSSGC design, the bandwidth of the guidance loop is dictated by the bandwidth of the inner-loop controller. So, the bandwidth of the guidance loop is chosen such that a time-scale separation between the guidance and controller designs is satisfied. The bandwidth of the guidance loop in the TSSGC design for which reasonable range tracking performance is obtained is given by:

$$0.6 \le \omega_{n,R} \le 1.7,\ \zeta_R = 1.0,\ \tau_{\dot{\chi}_A} = 1.5,\ \tau_{\dot{\chi}_E} = 1 \tag{5.58}$$

where $\omega_{n,R}$ and ζ_R are the natural frequency and damping ratio of the range command reference model, $\tau_{\dot{\chi}_A}$ and $\tau_{\dot{\chi}_E}$ are the time constants for the LOS azimuth and elevation bearing rates reference models respectively. The range tracking performance for $\omega_{n,R} = 0.6,\ 1.0,\ 1.7$ with other bandwidth parameters as in (5.58) is shown below in Figure 45.

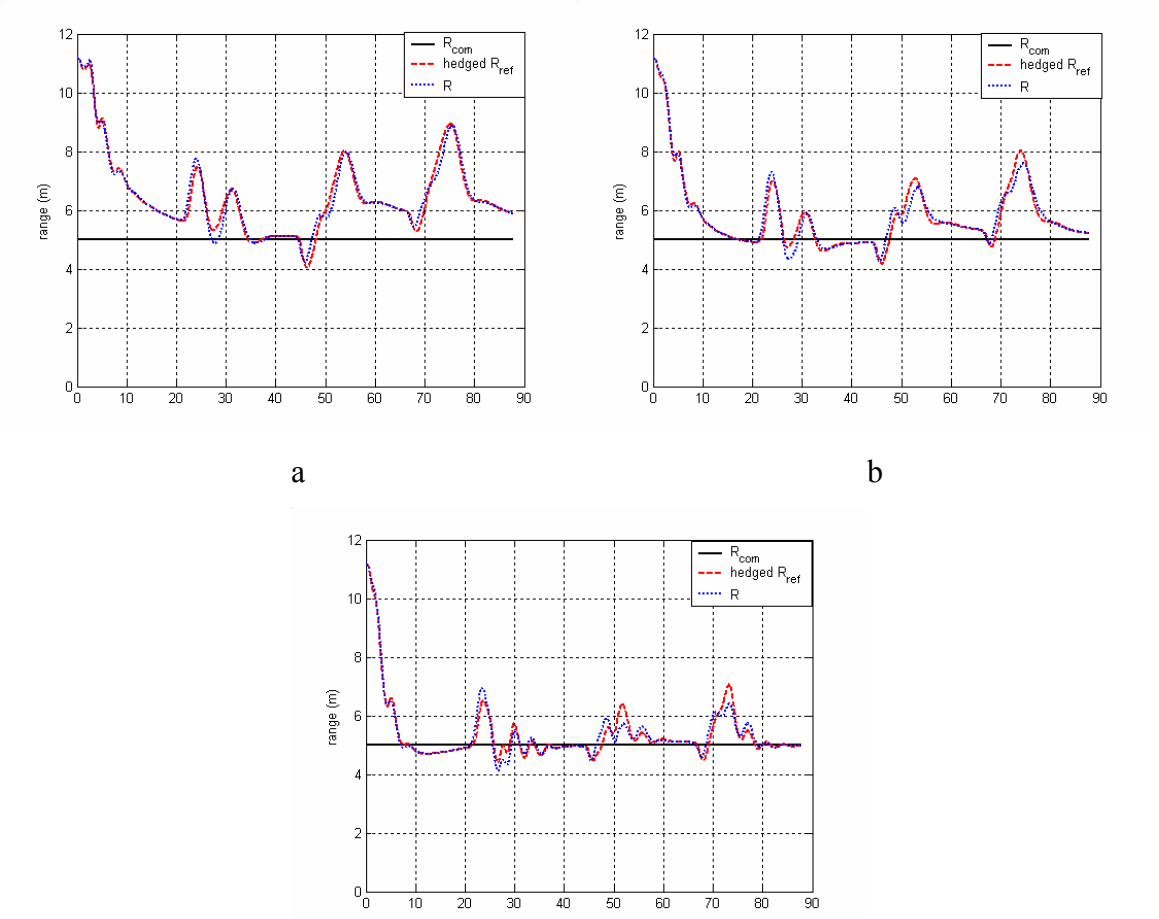

Figure 45. Range Tracking Performance for Varying Bandwidths, TSSGC design a) $\omega_{n,R} = 0.6$**, b)** $\omega_{n,R} = 1.0$**, c)** $\omega_{n,R} = 1.7$

For the IGC-2 design, the corresponding values for the bandwidths of the reference models are given by

$$0.25 \le \omega_{n,R} \le 0.75,\ \zeta_R = 1.0,\ \tau_{\dot{\chi}_A} = 0.9,\ \tau_{\dot{\chi}_E} = 0.05 \tag{5.59}$$

The range tracking performance for $\omega_{n,R} = 0.25,\ 0.5,\ 0.75$ with other bandwidth parameters as in (5.59) is shown in Figure 46.

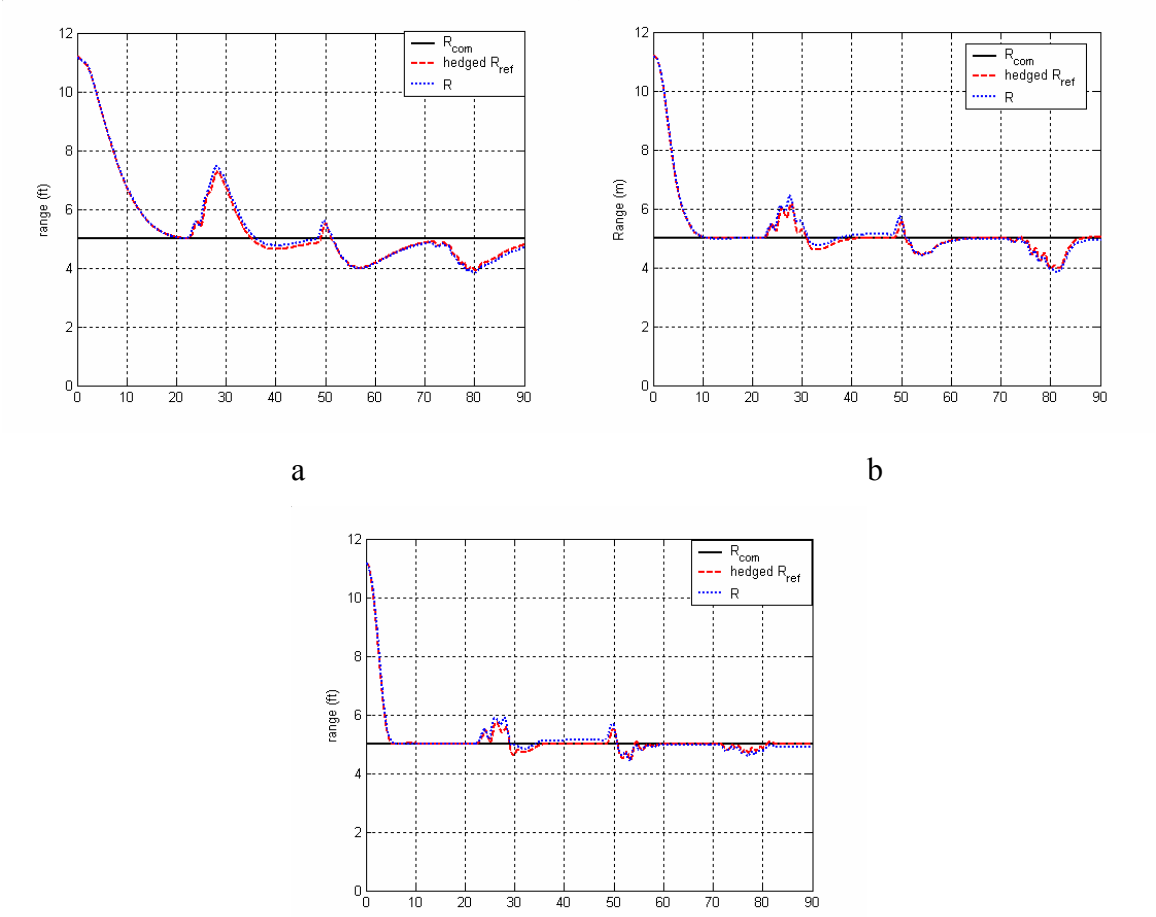

Figure 46. Range Tracking Performance for Varying Bandwidths, IGC-2 design

a) $\omega_{n,R} = 0.25$ **, b)** $\omega_{n,R} = 0.5$ **, c)** $\omega_{n,R} = 0.75$

Comparing the range tracking performances in Figure 45 and Figure 46, it can be concluded that the IGC design is capable of achieving a higher bandwidth than the TSSGC design. The bandwidths of the LOS rate command reference models have significant effect on the range tracking performance.

5.4 Conclusions

This chapter has presented an adaptive integrated guidance and control (IGC) design for line-of-sight formation flight using a combination of output feedback inversion

and backstepping techniques. Neural network based online adaptation is used to compensate for modeling errors in the design process, that include, uncertainties due to unknown leader aircraft acceleration, and the modeling error due to parametric uncertainties in the aircraft aerodynamic derivatives. One conclusion is that adaptation in the integrated design of guidance and flight control plays a critical role in this application. A second conclusion is that using feedback inversion alone results in a deficiency in maintaining turn coordination. This deficiency can be avoided by employing a backstepping approach for the azimuth portion of the design process. Attempting to address the full 6DOF problem using backstepping alone leads to a cumbersome design, whereas combining feedback inversion with backstepping appears leads to a complimentary design approach. Finally, when compared to an adaptive time-scale separated guidance and control design (TSSGC), the adaptive IGC design is capable of achieving a higher bandwidth design for the combined dynamics. The bandwidths of the LOS rate command reference models have significant effect on the range tracking performance. In the case of the TSSGC design, attempting to improve performance by increasing the bandwidth of the guidance design while maintaining sufficient time-scale separation with the autopilot leads to actuator saturation and instability. The main advantage of the IGC design is that it translates into better transient and steady-state range tracking performance as seen in the simulation results.

The next chapter presents a method of analysis for integrating the adaptive guidance and control designs developed in Chapters 4 and 5 with the adaptive state estimation design of Chapter 3. This makes the integrated estimation, guidance and control design practical from the point of view of enabling vision-in-the-loop formation flight.

CHAPTER 6

INTEGRATED ADAPTIVE ESTIMATION AND ADAPTIVE CONTROL

This chapter presents a method to integrate adaptive estimation and adaptive control designs for a class of nonlinear systems. The method is based on Lyapunov-like stability analysis of all the errors in the integrated closed-loop system. The analysis method is then applied to integrate the adaptive estimator solution in Chapter 3 with the adaptive guidance and control solutions presented in Chapters 4 and 5 for enabling vision-based formation flight. Simulation results are presented using a nonlinear 6DOF fixed-wing UAV simulation model to illustrate the feasibility and efficacy of the approach. Comparison results between the integrated adaptive estimation and time-scale separation based guidance and control law, and the integrated adaptive estimation and integrated guidance and control law are also presented to show case the best overall design for enabling vision-based formation flight.

Equation Chapter 6 Section 1

6.1 Problem Formulation

We start with the problem formulation similar to the one presented in Chapter 5, but with the important difference that the states $\boldsymbol{x}_1$ are not available for feedback. Consider the Multi-Input Multi-Output (MIMO) nonlinear system given by:

$$\begin{aligned}
\dot{\boldsymbol{x}}_1 &= A_1\boldsymbol{x}_1 + B_1\left[\varsigma\left(\boldsymbol{x}_2\right) + \boldsymbol{g}\left(\boldsymbol{x}_1, z\right)\right] \\
\boldsymbol{y}_1 &= C_1\boldsymbol{x}_1 \\
\dot{z} &= \boldsymbol{f}_z\left(\boldsymbol{x}_1, z\right) \\
\dot{\boldsymbol{x}}_2 &= \boldsymbol{f}_2\left(\boldsymbol{x}_2\right) + G\left(\boldsymbol{x}_2\right)\boldsymbol{u} \\
\boldsymbol{y} &= \boldsymbol{h}\left(\boldsymbol{y}_1, \boldsymbol{x}_2\right)
\end{aligned} \tag{6.1}$$

where $\boldsymbol{x}_1 \in D_{x_1} \subset \Re^{n_1}$ and $\boldsymbol{x}_2 \in D_{x_2} \subset \Re^{n_2}$ are the modeled states of the system, $\boldsymbol{y}_1 \in \Re^m$ and $\boldsymbol{x}_2$ are measurements available for feedback, $\boldsymbol{z} \in D_z \subset \Re^{n_z}$ are the unmodeled states where n_Z is also unknown but bounded, D_{x_1}, D_{x_2}, and D_z are open sets containing their respective origins, and $\boldsymbol{y} \in \Re^p$ and $\boldsymbol{u} \in \Re^p$ are the regulated outputs and control inputs of the system. The matrices $A_1 \in \Re^{n_{x1} \text{ x } n_{x1}}$, $B_1 \in \Re^{n_{x1} \text{ x } m}$ and $C_1 \in \Re^{m \text{ x } n_{x1}}$ are known, and the pair (A_1, C_1) is observable. The functions $\varsigma : D_{x_2} \to \Re^m$ and $\boldsymbol{h} : \Re^m \text{ x } D_{x_2} \to \Re^p$ are known and continuous. The functions $\boldsymbol{f}_2 : D_{x_2} \to \Re^{n_2}$ and $G : D_{x_2} \to \Re^{n_2 \text{ x } m}$ are *partially* known and continuous. The function $\boldsymbol{f}_z(\boldsymbol{x}_1, \boldsymbol{z}) : D_{x_1} \times D_z \to \Re^{n_z}$ is unknown, continuous and represents the unmodeled dynamics. The function $\boldsymbol{g}(\boldsymbol{x}_1, \boldsymbol{z}) : D_{x_1} \times D_z \to \Re^m$ is unknown, continuous and represents the way in which the unmodeled dynamics is coupled to the system dynamics. Let $\boldsymbol{x} = \left[\boldsymbol{x}_1^T, \boldsymbol{x}_2^T, \boldsymbol{z}^T \right]^T \in D_x \subset \Re^n$, $n = n_{x_1} + n_{x_2} + n_z$, be the composite state vector of the system, where $D_x = D_{x_1} \text{ x } D_{x_2} \text{ x } D_z$.

Assumption 6.1: The function $\boldsymbol{f}_z(\cdot, \cdot)$ is a bounded function of its arguments and $\boldsymbol{z}(t)$ is bounded for all t.

Remark 6.1: In context of the vision-based formation flight problem, $\boldsymbol{x}_1$ represents the states of the LOS kinematics, $\boldsymbol{x}_2$ represents the states of the rigid body dynamics of the follower aircraft, assumed to be all available, $\boldsymbol{z}$ represents the unknown states associated with the leader acceleration dynamics, $\boldsymbol{y}_1$ represents the measurements obtained via the use of a vision sensor, $\boldsymbol{u}$ represents the actuator deflections of the follower aircraft, and $\boldsymbol{y}$ represents the *measurable* regulated outputs of interest. The complete state vector $\boldsymbol{x}_1$

is not available for feedback which makes the problem formulation in (5.1) different from the one in (5.1). Another difference is in the definition of the regulated outputs $\boldsymbol{y}$. In (5.1), $\boldsymbol{y}$ represent the *measurable* regulated outputs, for example, subtended angle of the leader aircraft on image plane, or range to leader aircraft assuming leader wing-span size is known, bearing angles, and bank or sideslip angle for turn coordination. Since the bearing rates are not measurable, these cannot be treated directly using the problem formulation above. The bearing rates are handled as a special case and discussed later. The rest of the problem formulation in (5.1) has the same interpretation as in *Remark 5.1* and is not discussed further here.

Assumption 6.2: The dynamical system (5.1) satisfies the conditions for output feedback linearization [98] with vector relative degree $\boldsymbol{r} \triangleq \left[r_1, r_2, \cdots, r_p \right]^T$, $\boldsymbol{r} = r_1 + r_2 + \cdots + r_p \le n$.

Then there exists a mapping $\boldsymbol{\xi} = \boldsymbol{\varphi}(\boldsymbol{x}) = \boldsymbol{\varphi}(\boldsymbol{x}_1, \boldsymbol{x}_2, \boldsymbol{z})$ which is given by

$$\boldsymbol{\varphi}(\boldsymbol{x}) = \begin{bmatrix} \boldsymbol{\varphi}_1 \\ \boldsymbol{\varphi}_1 \\ \vdots \\ \boldsymbol{\varphi}_p \end{bmatrix}, \ \boldsymbol{\varphi}_i = \begin{bmatrix} y_i \\ \dot{y}_i \\ \vdots \\ y_i^{(r_i-1)} \end{bmatrix} \tag{6.2}$$

that transforms the system in (5.1) into the normal form [98]:

$$\begin{aligned} \dot{\boldsymbol{Z}} &= \boldsymbol{f}_{\boldsymbol{Z}}(\boldsymbol{\xi}, \boldsymbol{Z}) \\ \dot{\xi}_i^1 &= \xi_i^2 \\ &\vdots \\ \dot{\xi}_i^{(r_i-1)} &= \xi_i^{(r_i)} \\ \dot{\xi}_i^{(r_i)} &= \alpha_i^0(\boldsymbol{x}_1, \boldsymbol{x}_2) + \alpha_i^1(\boldsymbol{x}_1, \boldsymbol{x}_2, \boldsymbol{z}, u_i) + \beta_i(\boldsymbol{y}_1, \boldsymbol{x}_2) u_i \\ y_i &= \xi_i^1, \quad i = 1, 2, \cdots, m \end{aligned} \tag{6.3}$$

where $\boldsymbol{\xi} \triangleq \left[\xi_i^1 \;\; \xi_i^2 \;\; \cdots \;\; \xi_i^{(r_i)} \;\; \cdots \;\; \xi_m^1 \;\; \xi_m^2 \;\; \cdots \;\; \xi_m^{(r_m)} \right]^T \in D_\xi \subset \Re^r$, $\boldsymbol{Z} \in D_{\boldsymbol{Z}} \subset \Re^{n-r}$ are the states associated with the internal dynamics, u_i are the control inputs, y_i are the regulated outputs, r_i is the relative degree of the i^{th} output, $\boldsymbol{f}_{\boldsymbol{Z}}(\boldsymbol{\xi}, \boldsymbol{Z})$ is a completely unknown continuous function representing the internal dynamics, $\alpha_i^0(\boldsymbol{x}_1, \boldsymbol{x}_2) = \alpha_i^0(\boldsymbol{\xi})$ and $\beta_i(\boldsymbol{y}_1, \boldsymbol{x}_2)$ are known continuous functions, and $\alpha_i^1(\boldsymbol{x}_1, \boldsymbol{x}_2, z, u_i) = \alpha_i^1(\boldsymbol{\xi}, \boldsymbol{Z}, u_i)$ are unknown continuous functions.

Assumption 6.3: The function $\boldsymbol{f}_{\boldsymbol{Z}}(\cdot, \cdot)$ is a bounded function of its arguments and $\boldsymbol{Z}(t)$ is bounded for all t.

Assumption 6.4: $\beta_i(\boldsymbol{y}_1, \boldsymbol{x}_2)$ is continuous and non-zero for every $\boldsymbol{x} \in D_{\boldsymbol{x}}$.

Control Design Objective: Design a control law as a function of available measurements such that $y_i(t)$ track smooth, bounded reference trajectories $y_{c,i}(t)$, $i = 1, 2, \cdots, m$ with bounded errors.

Remark 6.2: Since the states $\boldsymbol{x}_1$ are not available, an estimator is utilized to provide estimates of $\boldsymbol{x}_1$ in the control solution. These estimates are used to construct estimates of the functions $\alpha_i^0(\boldsymbol{x}_1, \boldsymbol{x}_2)$ in the control solution. It is seen that the functions $\alpha_i^0(\boldsymbol{x}_1, \boldsymbol{x}_2)$ can be incorporated within the unknown functions $\alpha_i^1(\boldsymbol{x}_1, \boldsymbol{x}_2, z, u_i)$ and adaptive neural networks (NNs) could be employed to approximate the modified functions $\alpha_i^1(\boldsymbol{x}_1, \boldsymbol{x}_2, z, u_i)$. This was the approach followed in Chapters 4 and 5, where the states $\boldsymbol{x}_1$ were assumed to be available for feedback. Presumably the same approach

can be followed even if $\boldsymbol{x}_1$ is not available by using delayed values of the available measurements $\left[\boldsymbol{y}_1^T, \boldsymbol{x}_2^T, \boldsymbol{u}^T\right]^T$ as inputs to the NNs and relying on the approximation capabilities of the NNs to compensate for the functions $\alpha_i^1\left(\boldsymbol{x}_1, \boldsymbol{x}_2, \boldsymbol{z}, u_i\right)$. While this approach is theoretically treatable, there are practical considerations that make this approach undesirable. Treating $\alpha_i^0\left(\boldsymbol{x}_1, \boldsymbol{x}_2\right)$ as unknown and incorporating it within $\alpha_i^1\left(\boldsymbol{x}_1, \boldsymbol{x}_2, \boldsymbol{z}, u_i\right)$ makes the overall design a high-gain control design. In the presence of measurement noise and lags due to estimation, the high-gain control design can excite high frequency dynamics, cause actuator chattering and rate saturation, and even lead to instability. In general, available information about system nonlinearities should be incorporated within the control design to reduce the loop gain needed to achieve a desired performance level.

6.2 Adaptive State Estimation

A. Adaptive State Estimator

The objective of adaptive estimation is to provide estimates of the states $\boldsymbol{x}_1$ in (5.1). The estimator solution must be robust to the effect of unmodeled dynamics, $\boldsymbol{g}\left(\boldsymbol{x}_1, \boldsymbol{z}\right)$. The adaptive state estimator considered is a time-varying Kalman filter augmented with an adaptive neural network (NN) as presented in Chapter 3. The adaptive NN is updated online with two error signals using a composite adaptation approach.

We consider only the following subsystem for the purpose of adaptive estimation

$$\begin{aligned} \dot{\boldsymbol{x}}_1 &= A_1\boldsymbol{x}_1 + B_1\left[\varsigma\left(\boldsymbol{x}_2\right) + \boldsymbol{g}\left(\boldsymbol{x}_1, \boldsymbol{z}\right)\right], \quad \boldsymbol{x}_1(t_0) = \boldsymbol{x}_{10} \\ \boldsymbol{y}_1 &= C_1\boldsymbol{x}_1 \\ \dot{\boldsymbol{z}} &= \boldsymbol{f}_{\boldsymbol{z}}\left(\boldsymbol{x}_1, \boldsymbol{z}\right), \quad \boldsymbol{z}(t_0) = \boldsymbol{z}_0 \end{aligned} \tag{6.4}$$

As in (3.67), we assume that $B_1\boldsymbol{g}(\boldsymbol{x},\boldsymbol{z})$ can be written in the form

$$B_1\boldsymbol{g}(\boldsymbol{x}_1,\boldsymbol{z}) = \sum_{i=1}^{m} \boldsymbol{b}_i g_i'(\boldsymbol{x}_1,\boldsymbol{z}) \tag{6.5}$$

where $\boldsymbol{b}_i$ is a column vector of zeros with only the i^{th} element equal to 1. We assume the following NN parameterization for $g_i'(\boldsymbol{x}_1,\boldsymbol{z})$:

$$\begin{aligned} g_i'(\boldsymbol{x}_1,\boldsymbol{z}) &= \boldsymbol{W}_{o,i}{}^T\boldsymbol{\sigma}_o(\bar{\boldsymbol{\mu}}_o) + \varepsilon_{o,i}'(\bar{\boldsymbol{\mu}}_o), \quad \|\boldsymbol{W}_{o,i}\|_F \le W_{o,i}^* \le W_o^*, \quad \|\varepsilon_{o,i}'(\bar{\boldsymbol{\mu}})\| \le \varepsilon_{o,i}^* \le \varepsilon_o^*, \\ \bar{\boldsymbol{\mu}}_o &\in B_{\mu_o^*} = \{\bar{\boldsymbol{\mu}}_o \mid \|\bar{\boldsymbol{\mu}}_o\| \le \mu_o^*\}, \quad i = 1,2,\cdots,m \end{aligned} \tag{6.6}$$

$\forall(\boldsymbol{x}_1,\boldsymbol{x}_2,\boldsymbol{z}) \in D_g \subset D_{\boldsymbol{x}_1}$ x $D_{\boldsymbol{x}_2}$ x $D_{\boldsymbol{z}}$, where D_g is a compact set, the subscript 'o' stands for 'observer', $\boldsymbol{W}_{o,i} \in \Re^{N_o}$ is the ideal but unknown NN weight vector, $\varepsilon_{o,i}(\bar{\boldsymbol{\mu}}_o)$ is the NN functional approximation error, $\boldsymbol{\sigma}_o(\bar{\boldsymbol{\mu}}_o) = [\sigma_{o,1}(\bar{\boldsymbol{\mu}}_o),\ldots,\sigma_{o,N_o}(\bar{\boldsymbol{\mu}}_o)]^T$ is a vector of sigmoidal functions $\sigma_{o,i}(\cdot)$, N_o is the number of neurons, W_o^* and ε_o^* are the bounds on the Frobenius norms of $\boldsymbol{W}_{o,i}$ and $\varepsilon_{o,i}$ respectively, and the input vector $\bar{\boldsymbol{\mu}}_o = \bar{\boldsymbol{\mu}}_o(\boldsymbol{y}_1(t),\boldsymbol{\varsigma}(t-d),d)$ is a vector of difference quotients of the output vector $\boldsymbol{y}_1$ and known vector $\boldsymbol{\varsigma}$,

$$\begin{aligned} \bar{\boldsymbol{\mu}}_o(\boldsymbol{y}_1(t),\boldsymbol{\varsigma}(t-d),d) &= [1, \bar{\boldsymbol{y}}_{1,d}^T(t), \ \bar{\boldsymbol{\varsigma}}_d^T(t-d)]^T \\ \bar{\boldsymbol{y}}_{1,d}^T(t) &= [\Delta_d^{(0)}\boldsymbol{y}_1^T(t), \ \cdots, \Delta_d^{(n_1-1)}\boldsymbol{y}_1^T(t)]^T \\ \bar{\boldsymbol{\varsigma}}_d^T(t-d) &= [\Delta_d^{(0)}\boldsymbol{\varsigma}^T(t-d), \ \ldots \ \Delta_d^{(n_2-1)}\boldsymbol{\varsigma}^T(t-d)]^T \end{aligned} \tag{6.7}$$

where the definitions of the difference quotients $\Delta_d^{(k)}[\cdot]$, $k = 1,2,\cdots$ are as in (3.3), $n_1, n_2 \ge n$ are sufficiently large integers, and $d > 0$ is a time delay. The sigmoidal functions are uniformly bounded, that is, $|\sigma_{o,i}(\bar{\boldsymbol{\mu}}_o)| \le 1$. Using Eqs. (6.6) and (6.5) in Eq. (6.4), we have,

$$\begin{aligned}
\dot{\boldsymbol{x}}_1 &= A_1\boldsymbol{x}_1 + B_1\boldsymbol{\varsigma} + \sum_i^m \boldsymbol{b}_i \boldsymbol{W}_{o,i}{}^T \boldsymbol{\sigma}_o\left(\bar{\boldsymbol{\mu}}_o\right) + \sum_i^m \boldsymbol{b}_i \varepsilon'_{o,i}\left(\bar{\boldsymbol{\mu}}_o\right) \\
\dot{\boldsymbol{z}} &= \boldsymbol{f}_z\left(\boldsymbol{x}_1, \boldsymbol{z}\right), \\
\boldsymbol{y}_1 &= C_1\boldsymbol{x}_1
\end{aligned} \tag{6.8}$$

The adaptive estimator for the system in (6.8) is given by

$$\begin{aligned}
&\dot{\hat{\boldsymbol{x}}}_1(t) = A_1\hat{\boldsymbol{x}}_1(t) + K_1(t)\left(\boldsymbol{y}_1(t) - \hat{\boldsymbol{y}}_1(t)\right) + B_1\boldsymbol{\varsigma} + \sum_i^m \boldsymbol{b}_i \hat{\boldsymbol{W}}_{o,i}{}^T\left(t\right)\boldsymbol{\sigma}_o\left(\bar{\boldsymbol{\mu}}_o\right), \qquad \hat{\boldsymbol{x}}_1(t_0) = \hat{\boldsymbol{x}}_{10} \\
&\hat{\boldsymbol{y}}_1(t) = C_1\hat{\boldsymbol{x}}_1(t)
\end{aligned} \tag{6.9}$$

where $\hat{\boldsymbol{W}}_{o,i}\ \left(t\right)$ is an estimate of the ideal but unknown NN weight vector $\boldsymbol{W}_{o,i}$, $K_1(t)$ is the Kalman gain obtained through the following set of matrix differential Ricatti equations [93]

$$\begin{aligned}
\dot{P}_1(t) &= A_1P_1(t) + P_1(t)A_1^T - P_1(t)C_1^T R_1^{-1} C_1 P_1(t) + Q_1 \\
K_1(t) &= P_1(t)C_1^T R_1^{-1}
\end{aligned} \tag{6.10}$$

where $P_1(0) = P_0 > 0,\ Q_1 = Q_1^T > 0,\ R_1 = R_1^T > 0$. The solution $P_1(t)$ of (6.10) is bounded, symmetric, positive definite and continuously differentiable. Note that the adaptive estimator identified with subscript '1' in Eqs. (6.9)-(6.10) has no connection with the Kalman estimator given by Eqs. (3.7)-(3.8) identified with subscript '1'. The i^{th} output of the NN is given by

$$\hat{g}_i\left(t\right) = \hat{\boldsymbol{W}}_{o,i}\left(t\right)^T \boldsymbol{\sigma}_o\left(\bar{\boldsymbol{\mu}}_o\right),\ i = 1, 2, \cdots, m \tag{6.11}$$

The residual vector of the adaptive estimator $\tilde{\boldsymbol{y}}_1\left(t\right) = \boldsymbol{y}_1\left(t\right) - \hat{\boldsymbol{y}}_1\left(t\right)$ is the first set of error signals used to train the NN.

The derivation of the NN adaptive law is referred to Chapter 3, Section 5. The NN adaptive law is given by:

$$\dot{\hat{\boldsymbol{W}}}_{o,i} = -\Gamma_{o_i}\left\{-\boldsymbol{\sigma}_o\left(\bar{\boldsymbol{\mu}}_o\right)\tilde{y}_{1,i} - Q_{fl}^T \boldsymbol{e}_{na,1} + \lambda_o \hat{\boldsymbol{W}}_{o,i}\right\} \tag{6.12}$$

where $\Gamma_{o_i} > 0$ and $\lambda_o > 0$ are the NN design constants, $\tilde{y}_{1,i} = C_{1,i}\tilde{\boldsymbol{x}}_1$ is the i^{th} element of the residual vector $\tilde{\boldsymbol{y}}_1(t)$, $C_{1,i}$ is the i^{th} row of the C_1 matrix, $\boldsymbol{e}_{na,1}(t) = \tilde{\boldsymbol{y}}_{na,1}(t) - \hat{\tilde{\boldsymbol{y}}}_{na,1}(t)$ $= \tilde{\boldsymbol{y}}_{na,1}(t) - \sum_{i}^{m} Q_{fi}\hat{\boldsymbol{W}}_{o,i}(t)$ is the second error signal vector to train the NN, $\tilde{\boldsymbol{y}}_{na,1}(t) = \boldsymbol{y}_1(t) - \hat{\boldsymbol{y}}_{na,1}(t)$ is the residual vector of the time-varying non-adaptive Kalman filter given in (6.13):

$$\begin{aligned}
&\dot{\hat{\boldsymbol{x}}}_{na,1}(t) = A_1\hat{\boldsymbol{x}}_{na,1}(t) + K_{na,1}(t)\left(\boldsymbol{y}_1(t) - \hat{\boldsymbol{y}}_{na,1}(t)\right) + B_1\boldsymbol{\varsigma}, \qquad \hat{\boldsymbol{x}}_{na1}(t_0) = \hat{\boldsymbol{x}}_{na,10} \\
&\hat{\boldsymbol{y}}_{na,1}(t) = C_1\hat{\boldsymbol{x}}_{na,1}(t) \\
&\dot{P}_{na,1}(t) = A_1P_{na,1}(t) + P_{na,1}(t)A_1^T - P_{na,1}(t)C_1^TR_{na,1}^{-1}C_1P_{na,1}(t) + Q_{na,1} \\
&K_{na,1}(t) = P_{na,1}(t)C_1^TR_{na,1}^{-1}
\end{aligned} \tag{6.13}$$

where the subscript '*na*' is used to identify the second Kalman filter as a non-adaptive filter, and $Q_{fi} \in \Re^{n_{x1}\text{ x }N_o}$ is the filtered basis function *matrix* obtained by solving the matrix differential equation (6.14):

$$\begin{aligned}
&\dot{\Omega}_{fi} = \bar{A}_{na,1}(t)\Omega_{fi} + \boldsymbol{b}_i\boldsymbol{\sigma}^T(\bar{\boldsymbol{\mu}}), \;\; \Omega_{fi}(t_0) = 0, \; i = 1,2,\cdots,m \\
&Q_{fi} = C_1\Omega_{fi}
\end{aligned} \tag{6.14}$$

where $\bar{A}_{na,1}(t) = A_1 - K_{na,1}(t)C_1$. The matrix Ω_{fi} is always bounded by using the result of *Lemma 3.1* and the output matrix $Q_{fi} \in \Re^{m\text{ x }N_o}$ is similarly bounded.

Remark 6.3: Since $\tilde{\boldsymbol{y}}_{na,1}(t)$ is the output of a Globally Exponentially Stable filter using the result of *Lemma 3.1*, $\tilde{\boldsymbol{y}}_{na,1}(t)$ is bounded as long as the inputs to the filter, i.e., $g_i'(\boldsymbol{x}_1, \boldsymbol{z}), \; i = 1,2,\cdots,m,$ are bounded. The latter is true as long as the states $\boldsymbol{x}_1$ and $\boldsymbol{z}$ are bounded. Assumption 6.1 guarantees that the states $\boldsymbol{z}$ are always bounded. However, since this is a combined estimation and control problem, we cannot assume *a priori* that $\boldsymbol{x}_1$ is bounded. To get around this technical obstacle, we will make the assumption that if

the initial state estimation errors belong to a Lyapunov level set, then the states $\boldsymbol{x}_1$ belong to a compact set where the NN approximation is valid. Then the proof of boundedness will show that $\boldsymbol{x}_1$ remains within the compact set with ultimate bounds that are smaller then the bounds on the compact set. Thus the functions $g_i^{'}(\boldsymbol{x}_1, \boldsymbol{z})$, $i = 1, 2, \cdots, m,$ and consequently $\tilde{\boldsymbol{y}}_{na,1}(t)$ can be shown to be bounded at all time. The assumption mentioned above is standard in NN based output feedback control literature [80], [96].

B. Error Boundedness Analysis

The approach is to show boundedness of the errors in the adaptive state estimation system first and then show boundedness of all errors in the integrated adaptive estimation plus adaptive control system. This approach justifies the use of state estimates in the adaptive controller solution. The boundedness of the state estimation errors and observer NN weight estimation errors is shown via Lyapunov-like analysis. Before starting the boundedness analysis, a few results are presented in the forms that are directly used in the analysis.

Define the state estimation error vector $\tilde{\boldsymbol{x}}_1 = \boldsymbol{x}_1 - \hat{\boldsymbol{x}}_1$, the NN weight estimation error vector $\tilde{\boldsymbol{W}}_{o,i}(t) = \boldsymbol{W}_{o,i} - \hat{\boldsymbol{W}}_{o,i}(t)$ and $\bar{A}_1(t) = A_1 - K_1(t)C_1$. Using Eqs. (6.8) and (6.9), the state estimation error dynamics can be written as

$$\begin{aligned} \dot{\tilde{\boldsymbol{x}}}_1(t) &= \bar{A}_1(t)\tilde{\boldsymbol{x}}_1(t) + \sum_i^m \boldsymbol{b}_i \tilde{\boldsymbol{W}}_{o,i}^{\ T}(t)\boldsymbol{\sigma}_o(\bar{\boldsymbol{\mu}}_o) + \sum_i^m \boldsymbol{b}_i \varepsilon_{o,i}^{'}(\bar{\boldsymbol{\mu}}_o), \qquad \tilde{\boldsymbol{x}}_1(t_0) = \tilde{\boldsymbol{x}}_{10} \\ \tilde{\boldsymbol{y}}_1(t) &= C_1\tilde{\boldsymbol{x}}_1(t) \end{aligned} \tag{6.15}$$

The NN weight estimation error dynamics can be written using (6.12) as,

$$\dot{\tilde{\boldsymbol{W}}}_{o,i} = -\dot{\hat{\boldsymbol{W}}}_{o,i} = \Gamma_{o_i}\left(-\boldsymbol{\sigma}_o(\bar{\boldsymbol{\mu}}_o)C_{1,i}\tilde{\boldsymbol{x}}_1 - Q_{fi}^T \boldsymbol{e}_{na,1} + \lambda_o \boldsymbol{W}_{o,i} - \lambda_o \tilde{\boldsymbol{W}}_{o,i}\right) \tag{6.16}$$

Invoking the identity $P_1(t)P_1(t)^{-1} = I$ and differentiating:

$$\dot{P}_1^{-1}(t) = -P_1^{-1}(t)\bar{A}_1(t) - \bar{A}_1(t)^T P_1^{-1}(t) - \tilde{Q}_1(t) \tag{6.17}$$

$$\tilde{Q}_1(t) = C^T R_1^{-1} C + P_1^{-1}(t) Q_1 P_1^{-1}(t) > 0 \tag{6.18}$$

The following bounds on $P_1^{-1}(t)$ are used in the analysis [64],

$$\rho_1 I \le P_1(t) \le \rho_2 I \Rightarrow \frac{1}{\rho_2} I \le P_1^{-1}(t) \le \frac{1}{\rho_2} I \tag{6.19}$$

The second error signal used to train the NN can be written as in (3.68)

$$\boldsymbol{e}_{na,1}(t) = \tilde{\boldsymbol{y}}_{na,1}(t) - \hat{\tilde{\boldsymbol{y}}}_{na,1}(t) = T\left(\tilde{\boldsymbol{x}}_{na,1}(t_0), \varepsilon_{f1}^{'}, \varepsilon_{f2}^{'}, \cdots, \varepsilon_{fm}^{'}\right) + \sum_i^m Q_{fi} \tilde{\boldsymbol{W}}_{o,i} \tag{6.20}$$

where $T\left(\tilde{\boldsymbol{x}}_{na,1}(t_0), \varepsilon_{f1}^{'}, \varepsilon_{f2}^{'}, \cdots, \varepsilon_{fm}^{'}\right) = C_1 \Phi_{na,1}(t,t_0)\tilde{\boldsymbol{x}}_{na,1}(t_0) + \sum_i^m \int_{t_0}^{t} C_1 \Phi_{na,1}(t,t_0)\boldsymbol{b}_i \varepsilon_{o,i}^{'} \; d\tau$ is an unknown term that is always bounded using the result of *Lemma 3.1*.

Define the composite error vector

$$\boldsymbol{\zeta}_o = \left[\tilde{\boldsymbol{x}}_1^T \;\; \tilde{\boldsymbol{W}}_{o,1}^T \; \tilde{\boldsymbol{W}}_{o,2}^T \; \cdots \; \tilde{\boldsymbol{W}}_{o,m}^T\right]^T \tag{6.21}$$

and the positive definite Lyapunov candidate function for the boundedness analysis as

$$V_o(\boldsymbol{\zeta}_o) = \tilde{\boldsymbol{x}}_1^T P_1^{-1}(t)\tilde{\boldsymbol{x}}_1 + \sum_i^m \tilde{\boldsymbol{W}}_{o,i}^T \Gamma_{o_i}^{-1} \tilde{\boldsymbol{W}}_{o,i} \tag{6.22}$$

Note that the NN approximation for the unmodeled dynamics functions (6.6) is defined over a compact set D_g. In the space of the error vector $\boldsymbol{\zeta}_o$, consider the largest level set of $V_o(\boldsymbol{\zeta}_o)$ such that its projection on the subspace of the NN input variables lies completely in D_g. Define the largest ball that lies within that level set as $B_M \triangleq \left\{\boldsymbol{\zeta}_o : \left\|\boldsymbol{\zeta}_o\right\| \le M\right\}$ and let α be the minimum value of $V_o(\boldsymbol{\zeta}_o)$ on the boundary of B_M:

$$\alpha \triangleq \min_{\|\zeta_o\|=M} V_o\left(\zeta_o\right) \tag{6.23}$$

Introduce the set

$$\Omega_\alpha = \left\{\zeta_o \in B_M \mid V_o\left(\zeta_o\right) \le \alpha\right\} \tag{6.24}$$

The definition of the candidate Lyapunov function (6.22) shows that there exist class K functions κ_1 and κ_2 such that

$$\kappa_1\left(\left\|\zeta_o\right\|\right) \le V_o\left(\zeta_o\right) \le \kappa_2\left(\left\|\zeta_o\right\|\right)$$

where

$$\begin{aligned}
\kappa_1\left(\left\|\zeta_o\right\|\right) &= \frac{1}{\rho_2^2}\left\|\tilde{\boldsymbol{x}}_1\right\|^2 + \sum_i^m \lambda_{\min}\left(\Gamma_{o_i}^{-1}\right)\left\|\tilde{\boldsymbol{W}}_{o,i}\right\|^2 \\
\kappa_2\left(\left\|\zeta_o\right\|\right) &= \frac{1}{\rho_1^2}\left\|\tilde{\boldsymbol{x}}_1\right\|^2 + \sum_i^m \lambda_{\max}\left(\Gamma_{o_i}^{-1}\right)\left\|\tilde{\boldsymbol{W}}_{o,i}\right\|^2
\end{aligned} \tag{6.25}$$

where the bounds on $P_1^{-1}\left(t\right)$ in (6.19) are applied.

Assumption 6.5: Let

$$M > \kappa_1^{-1}\left(\kappa_2\left(\gamma\right)\right) \tag{6.26}$$

where γ is defined as

$$\gamma \triangleq \frac{\sqrt{\sum_i^m \left\{m_{1_i}^2 + m_{4_i}^2 + \lambda_o W_o^{*2}\right\}}}{\min\left(\sqrt{\frac{\lambda_{\min}\left(Q_1\right)}{\rho_2^2} - 2m}, \sqrt{\lambda_o - \left(m_{2_1}^2 + 2\right)}, \sqrt{\lambda_o - \left(m_{2_2}^2 + 2\right)}, \cdots \sqrt{\lambda_o - \left(m_{2_m}^2 + 2\right)}\right)} \tag{6.27}$$

$$\begin{aligned}
m_{1_i} &= \left\|P_1^{-1}\left(t\right)\boldsymbol{b}_i\right\|\varepsilon_o^* \\
m_{2_i} &= \left\|P_1^{-1}\left(t\right)\boldsymbol{b}_i - C_{1,i}^T\right\|\sqrt{N_o} \\
m_{4_i} &= \left\|Q_{fi}\right\|_F \left\|T\left(\tilde{\boldsymbol{x}}_{na,1}\left(t_0\right), \varepsilon_{f1}^{'}, \varepsilon_{f2}^{'}, \cdots, \varepsilon_{fm}^{'}\right)\right\|
\end{aligned} \tag{6.28}$$

where N_o is the number of neurons of the NN. Let $\lambda_{\min}(Q_1) > 2m\rho_2^2$ and $\lambda_o > \max\left\{m_{2_1}^2 + 2, m_{2_2}^2 + 2, \cdots, m_{2_m}^2 + 2\right\}$. Now the main result on the error boundedness can be stated.

Theorem 6.1: Let Assumptions 6.1 and 6.5 hold and the initial error vector $\boldsymbol{\zeta}_o(t_0) \in \Omega_\alpha$. For the system formulation in (6.4) and the NN parameterization in (6.5), (6.6), let the adaptive estimator be given by (6.9) with the NN adaptive law given by (6.12). Then the state estimation error $\tilde{\boldsymbol{x}}_1$ and NN weight estimation errors $\tilde{\boldsymbol{W}}_{o,i}$, $i = 1, 2, \cdots, m$ are uniformly ultimately bounded.

Proof: Refer to Appendix C.

6.3 Adaptive Control

We start with the normal form for the i^{th} regulated output given in (5.3):

$$\begin{aligned} y_i &= h_i(\boldsymbol{y}_1, \boldsymbol{x}_2) \\ y_i^{(r_i)} &= \alpha_i^0(\boldsymbol{x}_1, \boldsymbol{x}_2) + \alpha_i^1(\boldsymbol{x}_1, \boldsymbol{x}_2, \boldsymbol{z}, u_i) + \beta_i(\boldsymbol{y}_1, \boldsymbol{x}_2)u_i \end{aligned} \tag{6.29}$$

where r_i is the relative degree of y_i and is assumed to be known.

Eq. (6.29) can be re-written as follows:

$$\begin{aligned} y_i^{(r_i)} = \alpha_i^0(\hat{\boldsymbol{x}}_1, \boldsymbol{x}_2) + \beta_i(\hat{\boldsymbol{y}}_1, \boldsymbol{x}_2)u_i + \left[\alpha_i^0(\boldsymbol{x}_1, \boldsymbol{x}_2) - \alpha_i^0(\hat{\boldsymbol{x}}_1, \boldsymbol{x}_2)\right] \\ + \left[\beta_i(\boldsymbol{y}_1, \boldsymbol{x}_2) - \beta_i(\hat{\boldsymbol{y}}_1, \boldsymbol{x}_2)\right]u_i + \alpha_i^1(\boldsymbol{x}_1, \boldsymbol{x}_2, \boldsymbol{z}, u_i) \end{aligned}$$

which can be further simplified as

$$y_i^{(r_i)} = \alpha_i^0(\hat{\boldsymbol{x}}_1, \boldsymbol{x}_2) + \beta_i(\hat{\boldsymbol{y}}_1, \boldsymbol{x}_2)u_i + \Delta_{c,i}(\boldsymbol{x}_1, \hat{\boldsymbol{x}}_1, \boldsymbol{x}_2, \boldsymbol{z}, u_i) \tag{6.30}$$

where

$$\Delta_{c,i}\left(\boldsymbol{x}_1,\hat{\boldsymbol{x}}_1,\boldsymbol{x}_2,\boldsymbol{z},u_i\right)=\left[\alpha_i^0\left(\boldsymbol{x}_1,\boldsymbol{x}_2\right)-\alpha_i^0\left(\hat{\boldsymbol{x}}_1,\boldsymbol{x}_2\right)\right]+\left[\beta_i\left(\boldsymbol{y}_1,\boldsymbol{x}_2\right)-\beta_i\left(\hat{\boldsymbol{y}}_1,\boldsymbol{x}_2\right)\right]u_i + \alpha_i^1\left(\boldsymbol{x}_1,\boldsymbol{x}_2,\boldsymbol{z},u_i\right) \tag{6.31}$$

A. Tracking Error Dynamics

The control design objective is to design a control law as a function of available measurements such that $y_i(t)$ tracks smooth, bounded reference trajectories $y_{c,i}(t)$, $i=1,2,\cdots,m$ with bounded errors. The tracking error is defined as $e_i = y_{c,i} - y_i$, where the reference signal $y_{c,i}$ and its derivatives $\dot{y}_{c,i}, \ddot{y}_{c,i}, \cdots, y_{c,i}^{(r_i)}$ are generated by filtering a piece-wise continuous, bounded command $y_{com,i}(t)$ through asymptotically stable reference models. The r_i^{th} derivative of e_i is given by:

$$e_i^{(r_i)} = y_{c,i}^{(r_i)} - y_i^{(r_i)} = y_{c,i}^{(r_i)} - \alpha_i^0\left(\hat{\boldsymbol{x}}_1,\boldsymbol{x}_2\right) - \beta_i\left(\hat{\boldsymbol{y}}_1,\boldsymbol{x}_2\right)u_i - \Delta_{c,i}\left(\boldsymbol{x}_1,\hat{\boldsymbol{x}}_1,\boldsymbol{x}_2,\boldsymbol{z},u_i\right) \tag{6.32}$$

Assumption 6.6: $\beta_i\left(\hat{\boldsymbol{y}}_1,\boldsymbol{x}_2\right)$ is non-zero for every $\left(\boldsymbol{x},\hat{\boldsymbol{x}}_1\right)\in D_{\boldsymbol{x}}$ x $D_{\boldsymbol{x}_1}$, where $\hat{\boldsymbol{x}}_1$ evolves in the open set $D_{\boldsymbol{x}_1}\subset\Re^{n_{x1}}$ that contains the origin $\hat{\boldsymbol{x}}_1=\boldsymbol{0}$.

A feedback inversion control law for stabilizing the error dynamics in (6.32) is given by

$$u_i = \frac{\nu_i}{\beta_i\left(\hat{\boldsymbol{y}}_1,\boldsymbol{x}_2\right)} \tag{6.33}$$

where ν_i is the pseudo-control term given by

$$\nu_i = y_{c,i}^{(r_i)} - \alpha_i^0\left(\hat{\boldsymbol{x}}_1,\boldsymbol{x}_2\right) + \nu_{dc,i} - \nu_{ad,i} \tag{6.34}$$

Substituting Eqs. (6.33) and (6.34) into (6.32), we have

$$e_i^{(r_i)} = -\nu_{dc,i} + \nu_{ad,i} - \Delta_{c,i}\left(\boldsymbol{x}_1,\hat{\boldsymbol{x}}_1,\boldsymbol{x}_2,\boldsymbol{z},\nu_i\right) \tag{6.35}$$

where $\nu_{dc,i}$ is the output of a linear compensator designed to stabilize the linearized error dynamics

$$e_i^{(r_i)} = -\nu_{dc,i} \tag{6.36}$$

and $\nu_{ad,i}$ is the output of an adaptive NN designed to compensate for the modeling error function $\Delta_{c,i}\left(\boldsymbol{x}_1, \hat{\boldsymbol{x}}_1, \boldsymbol{x}_2, \boldsymbol{z}, \nu_i\right)$. Notice that we changed the last argument in $\Delta_{c,i}$ from u_i to ν_i by using (6.33).

We follow the approach in [96] for the design of $\nu_{dc,i}$ and $\nu_{ad,i}$. Defining $\boldsymbol{e}_i = \left[e_i, \dot{e}_i, \cdots, e_i^{(r_i-1)}\right]^T$, we have:

$$\begin{aligned} \dot{\boldsymbol{e}}_i &= A_{E,i}\boldsymbol{e}_i + B_{E,i}\left(\nu_{ad,i} - \Delta_{c,i}\right) \\ e_i &= C_{E,i}\boldsymbol{e}_i \end{aligned} \tag{6.37}$$

where

$$A_{E,i} = \begin{bmatrix} 0 & 1 & 0 & \cdots & 0 \\ 0 & 0 & 1 & \cdots & 0 \\ \vdots & & \vdots & & \vdots \\ 0 & 0 & 0 & \cdots & 0 \end{bmatrix}_{r_i \text{ x } r_i}, \quad B_{E,i} = \begin{bmatrix} 0 \\ 0 \\ \vdots \\ 1 \end{bmatrix}_{r_i \text{ x } 1}, \quad C_{E,i} = \begin{bmatrix} 1 & 0 & \cdots & 0 \end{bmatrix}_{1 \text{ x } r_i}$$

Since $\dot{e}_i, \cdots, e_i^{(r_i-1)}$ are not measurable, we design the following lead compensator to stabilize the error dynamics in (6.37):

$$\begin{aligned} \dot{\boldsymbol{\eta}}_i &= A_{c,i}\boldsymbol{\eta}_i + \boldsymbol{b}_{c,i}e_i \\ \nu_{dc,i} &= \boldsymbol{c}_{c,i}\boldsymbol{\eta}_i + d_{c,i}e_i \end{aligned} \tag{6.38}$$

where $\boldsymbol{\eta}_i$ has dimension $\geq r_i - 1$ [97]. This follows from the fact that the error dynamics in (6.36) has r_i poles at the origin. We assume the minimum dimension for $\boldsymbol{\eta}_i$. Defining $\boldsymbol{E}_i = \left[\boldsymbol{e}_i^T, \boldsymbol{\eta}_i^T\right]^T$, we can combine the error dynamics in (6.37) and the linear compensator dynamics in (6.38) to give:

$$\begin{aligned}\dot{\boldsymbol{E}}_i &= \bar{A}_{E,i}\boldsymbol{E}_i + \bar{B}_{E,i}\left(\nu_{ad,i} - \Delta_{c,i}\right)\\ \boldsymbol{z}_{E,i} &= \bar{C}_{E,i}\boldsymbol{E}_i = \left[e_i,\ \boldsymbol{\eta}_i^T\right]^T\end{aligned} \tag{6.39}$$

where

$$\bar{A}_{E,i} = \begin{bmatrix} A_{E,i} - B_{E,i}d_{c,i}C_{E,i} & -B_{E,i}c_{c,i} \\ \boldsymbol{b}_{c,i}C_{E,i} & A_{c,i}\end{bmatrix},\ \bar{B}_{E,i} = \begin{bmatrix} B_{E,i} \\ \boldsymbol{0}\end{bmatrix},\ \bar{C}_{E,i} = \begin{bmatrix} C_{E,i} & \boldsymbol{0} \\ \boldsymbol{0} & I\end{bmatrix} \tag{6.40}$$

The lead compensator parameters $\left(A_{c,i}, \boldsymbol{b}_{c,i}, \boldsymbol{c}_{c,i}, d_{c,i}\right)$ are designed such that the matrix $\bar{A}_{E,i}$ is Hurwitz. The $\boldsymbol{E}_i$ dynamics in (6.39) are henceforth referred to as tracking error dynamics. Since $\bar{A}_{E,i}$ is Hurwitz, then for any $Q_{E,i} > 0$, there exists a unique solution $P_{E,i} = P_{E,i}^T > 0$ of the following Lyapunov equation:

$$\bar{A}_{E,i}^T P_{E,i} + P_{E,i}\bar{A}_{E,i} = -Q_{E,i},\ \ Q_{E,i} = Q_{E,i}^T > 0 \tag{6.41}$$

B. Error Observer and Neural Network Adaptive Law

Since the complete error vector is not available in the output feedback case, we design a linear *error* observer [96] for the tracking error dynamics in (6.39). The states of the error observer are estimates of $\boldsymbol{E}_i$ and are used in the construction of the adaptive law. The error observer is given by:

$$\begin{aligned}\dot{\hat{\boldsymbol{E}}}_i &= \bar{A}_{E,i}\hat{\boldsymbol{E}}_i + \bar{K}_{E,i}\left(\boldsymbol{z}_{E,i} - \hat{\boldsymbol{z}}_{E,i}\right)\\ \hat{\boldsymbol{z}}_{E,i} &= \bar{C}_{E,i}\hat{\boldsymbol{E}}_i\end{aligned} \tag{6.42}$$

where $\bar{K}_{E,i} \neq \left[\boldsymbol{0}\right]$ is the error observer gain matrix that places the poles of the matrix $\tilde{A}_{E,i} = \bar{A}_{E,i} - \bar{K}_{E,i}\bar{C}_{E,i}$ much further to the left of the poles of the error dynamics matrix $\bar{A}_{E,i}$.

Remark 6.4: The NN adaptive law can be derived without constructing an error observer by applying the direct approach in [95]. The training signal for the NN in this case is obtained by filtering the tracking error through a strictly positive real (SPR) filter.

Defining $\tilde{\boldsymbol{E}}_i = \boldsymbol{E}_i - \hat{\boldsymbol{E}}_i$, the error dynamics of the error observer is given by:

$$\begin{aligned} \dot{\tilde{\boldsymbol{E}}}_i &= \tilde{A}_{E,i}\tilde{\boldsymbol{E}}_i + \bar{B}_{E,i}\left(\nu_{ad,i} - \Delta_{c,i}\right) \\ \tilde{\boldsymbol{z}}_{E,i} &= \bar{C}_{E,i}\tilde{\boldsymbol{E}}_i \end{aligned} \tag{6.43}$$

Consider the parameterization of the modeling error function $\Delta_{c,i}$ with a linear-in-parameters NN:

$$\begin{aligned} \Delta_{c,i}\left(\boldsymbol{x}_1, \hat{\boldsymbol{x}}_1, \boldsymbol{x}_2, \boldsymbol{z}, \nu_i\right) = \boldsymbol{W}_{c,i}^T \boldsymbol{\sigma}_c\left(\bar{\boldsymbol{\mu}}_c\right) + \varepsilon_{c,i}\left(\bar{\boldsymbol{\mu}}_c\right),\ \left\|\boldsymbol{W}_{c,i}\right\|_F \le W_{c,i}^* \le W_c^*,\ \left\|\varepsilon_{c,i}\left(\bar{\boldsymbol{\mu}}_c\right)\right\| \le \varepsilon_{c,i}^* \le \varepsilon_c^*, \\ \bar{\boldsymbol{\mu}}_c \in B_{\mu_c^*} = \left\{\bar{\boldsymbol{\mu}}_c \mid \left\|\bar{\boldsymbol{\mu}}_c\right\| \le \mu_c^*\right\},\ i = 1, 2, \cdots, m \end{aligned} \tag{6.44}$$

$\forall\left(\boldsymbol{x}_1, \boldsymbol{x}_{2,} \boldsymbol{z}, \hat{\boldsymbol{x}}_1, \nu_i\right) \in D_{g_1} \subset D_{x_1}$ x D_{x_2} x D_z x $D_{\hat{x}_1}$ x $D_{\boldsymbol{u}}$, where $D_{\boldsymbol{u}} \subset \Re$ and D_{g_1} is a compact set, the subscript 'c' stands for 'controller', $\boldsymbol{W}_{c,i} \in \Re^{N_c}$ is the ideal but unknown NN weight vector, $\varepsilon_{c,i}\left(\bar{\boldsymbol{\mu}}_c\right)$ is the NN functional approximation error, $\bar{\boldsymbol{\mu}}_c$ is the input vector, $\boldsymbol{\sigma}_c\left(\bar{\boldsymbol{\mu}}_c\right) = \left[\sigma_{c,1}\left(\bar{\boldsymbol{\mu}}_c\right), \ldots, \sigma_{c,N_c}\left(\bar{\boldsymbol{\mu}}_c\right)\right]^T$ is a vector of smooth and uniformly bounded *shifted* sigmoidal functions $\sigma_{c,i}(\cdot)$ [106, 107], N_c is the number of neurons, and W_c^* and ε_c^* are the bounds on the Frobenius norms of $\boldsymbol{W}_{c,i}$ and $\varepsilon_{c,i}$ respectively. The input vector $\bar{\boldsymbol{\mu}}_c = \bar{\boldsymbol{\mu}}_c\left(\bar{\boldsymbol{\mu}}_o(t), \hat{\boldsymbol{x}}_1(t), \boldsymbol{x}_2(t), \nu_i(t-d), d\right)$ consists of the input vector to the observer NN $\bar{\boldsymbol{\mu}}_o(t)$ given in (6.7), the estimates of the states $\hat{\boldsymbol{x}}_1$ which are the outputs of the adaptive state estimator described in the previous section, the available states $\boldsymbol{x}_2$, and the delayed values of the pseudo-control signal ν_i

$$\begin{aligned}
&\bar{\boldsymbol{\mu}}_c\left(\bar{\boldsymbol{\mu}}_o(t),\hat{\boldsymbol{x}}_1(t),\boldsymbol{x}_2(t),\nu_i(t-d),d\right)=\left[1,\bar{\boldsymbol{\mu}}_o^T(t),\ \hat{\boldsymbol{x}}_1^T(t),\boldsymbol{x}_2^T(t),\bar{\boldsymbol{v}}_{i,d}^T(t-d)\right]^T\\
&\bar{\boldsymbol{v}}_{i,d}(t-d)=\left[\Delta_d^{(0)}\nu_i(t-d),\ \ \ldots\ \ \Delta_d^{(n_3-1)}\nu_i(t-d)\right]^T
\end{aligned}\tag{6.45}$$

where $n_3 \geq n$ is a sufficiently large integer, and $d>0$ is the time delay.

From (6.44) and (6.34), $\Delta_{c,i}$ is a function of $\nu_{ad,i}$ and $\nu_{ad,i}$ is to be designed to cancel $\Delta_{c,i}$. Therefore the following assumption is introduced to guarantee existence and uniqueness of a solution for $\nu_{ad,i}$ [80], [95].

Assumption 6.7: The mapping $\nu_{ad_i} \mapsto \Delta_{c,i}$ is a contraction over the entire input domain of interest.

Assumption 6.7 is satisfied if the following two conditions are satisfied [95]:

$$\begin{aligned}
&\text{i) } \operatorname{sign}\left(\frac{\partial y_i^{(r_i)}}{\partial u_i}\right)=\operatorname{sign}\left(\frac{\partial \nu_i}{\partial u_i}\right)\Rightarrow \operatorname{sign}\left(\frac{\partial \alpha_i^1}{\partial u_i}+\beta_i\left(\boldsymbol{y}_1,\boldsymbol{x}_2\right)\right)=\operatorname{sign}\left(\beta_i\left(\hat{\boldsymbol{y}}_1,\boldsymbol{x}_2\right)\right)\\
&\text{ii) } \left|\frac{\partial \nu_i}{\partial u_i}\right|>\frac{1}{2}\left|\frac{\partial y_i^{(r_i)}}{\partial u_i}\right|>0\Rightarrow\left|\beta_i\left(\hat{\boldsymbol{y}}_1,\boldsymbol{x}_2\right)\right|>\frac{1}{2}\left|\frac{\partial \alpha_i^1}{\partial u_i}+\beta_i\left(\boldsymbol{y}_1,\boldsymbol{x}_2\right)\right|>0
\end{aligned}\tag{6.46}$$

The first condition in (6.46) implies that the estimated and actual control effectiveness have the same sign, and the second condition places a lower bound on the magnitude of the estimated control effectiveness.

Since the ideal NN weight vector $\boldsymbol{W}_{c,i}$ in (6.44) is unknown, the i^{th} NN output is given by

$$\nu_{ad,i}=\hat{\boldsymbol{W}}_{c,i}^T(t)\boldsymbol{\sigma}_c\left(\bar{\boldsymbol{\mu}}_c\right)\tag{6.47}$$

where $\hat{\boldsymbol{W}}_{c,i}(t)$ is an estimate for $\boldsymbol{W}_{c,i}$ that is updated online with the following adaptive law:

$$\dot{\hat{\boldsymbol{W}}}_{c,i} = -\Gamma_{c,i}\left(\boldsymbol{\sigma}_c\left(\bar{\boldsymbol{\mu}}_c\right)\hat{\boldsymbol{E}}_i^T P_{E,i}\bar{B}_{E,i} + \lambda_{c,i}\hat{\boldsymbol{W}}_{c,i}\right) \tag{6.48}$$

where $\Gamma_{c,i} > 0$ is the NN adaptation gain and $\lambda_{c,i} > 0$ is the sigma-mod parameter.

C. Error Boundedness Analysis

The boundedness of the integrated adaptive estimator and adaptive controller system is now shown via Lyapunov-like analysis. We consider the error analysis with respect to only the i^{th} regulated output y_i for convenience. The proof for the case of vector outputs can be obtained as a straightforward extension. Before starting the boundedness analysis, a few results are presented in the forms that are directly used in the analysis.

Define the NN weight estimation errors by $\tilde{\boldsymbol{W}}_{c,i} = \boldsymbol{W}_{c,i} - \hat{\boldsymbol{W}}_{c,i} \Rightarrow \dot{\tilde{\boldsymbol{W}}}_{c,i} = -\dot{\hat{\boldsymbol{W}}}_{c,i}$. Substituting (6.47) into Eqs. (6.39) and (6.43), we have:

$$\begin{aligned}
\dot{\boldsymbol{E}}_i &= \bar{A}_{E,i}\boldsymbol{E}_i + \bar{B}_{E,i}\left(-\tilde{\boldsymbol{W}}_{c,i}^T\boldsymbol{\sigma}_c\left(\bar{\boldsymbol{\mu}}_c\right) - \varepsilon_{c,i}\left(\bar{\boldsymbol{\mu}}_c\right)\right) \\
\dot{\hat{\boldsymbol{E}}}_i &= \tilde{A}_{E,i}\tilde{\boldsymbol{E}}_i + \bar{B}_{E,i}\left(-\tilde{\boldsymbol{W}}_{c,i}^T\boldsymbol{\sigma}_c\left(\bar{\boldsymbol{\mu}}_c\right) - \varepsilon_{c,i}\left(\bar{\boldsymbol{\mu}}_c\right)\right)
\end{aligned} \tag{6.49}$$

Since $\tilde{A}_{E,i}$ is Hurwitz, then for any $\tilde{Q}_{E,i} > 0$, there exists a unique solution $\tilde{P}_{E,i} = \tilde{P}_{E,i}^T > 0$ of the following Lyapunov equation:

$$\tilde{A}_{E,i}^T\tilde{P}_{E,i} + \tilde{P}_{E,i}\tilde{A}_{E,i} = -\tilde{Q}_{E,i}, \;\; \tilde{Q}_{E,i} = \tilde{Q}_{E,i}^T > 0 \tag{6.50}$$

Eq. (6.48) can be re-written as follows:

$$\dot{\tilde{\boldsymbol{W}}}_{c,i} = -\dot{\hat{\boldsymbol{W}}}_{c,i} = \Gamma_{c,i}\left\{\boldsymbol{\sigma}_c\left(\bar{\boldsymbol{\mu}}_c\right)\hat{\boldsymbol{E}}_i^T P_{E,i}\bar{B}_{E,i} + \lambda_{c,i}\left[\boldsymbol{W}_{c,i} - \tilde{\boldsymbol{W}}_{c,i}\right]\right\} \tag{6.51}$$

Define the following composite error vector for the integrated system

$$\boldsymbol{\zeta} = \left[\boldsymbol{\zeta}_o^T \;\; \boldsymbol{\zeta}_c^T\right]^T, \; \boldsymbol{\zeta}_c = \left[\boldsymbol{E}_i^T, \; \tilde{\boldsymbol{E}}_i^T, \; \tilde{\boldsymbol{W}}_{c,i}^T\right]^T \tag{6.52}$$

and the positive definite Lyapunov candidate function for the boundedness analysis as

$$V(\zeta) = V_o(\zeta_o) + V_c(\zeta_c) = V_o(\zeta_o) + \boldsymbol{E}_i^T P_{E,i} \boldsymbol{E}_i + \tilde{\boldsymbol{E}}_i^T \tilde{P}_{E,i} \tilde{\boldsymbol{E}}_i + \tilde{\boldsymbol{W}}_{c,i}^T \Gamma_{c_i}^{-1} \tilde{\boldsymbol{W}}_{c,i} \tag{6.53}$$

The NN approximation for the modeling error function in (6.44) is defined over a compact set D_{g_1}. In the space of the error vector ζ, consider the largest level set of $V(\zeta)$ such that its projection on the subspace of the NN input variables lies completely in D_{g_1}. Define the largest ball that lies within that level set as $B_{M_I} \triangleq \{\zeta : \|\zeta\| \le M_I\}$, where the subscript '*I*' is used to indicate that we are considering the integrated system, and let α_I be the minimum value of $V(\zeta)$ on the boundary of B_{M_I}:

$$\alpha_I \triangleq \min_{\|\zeta\| = M_I} V(\zeta) \tag{6.54}$$

Introduce the set

$$\Omega_{\alpha_I} = \{\zeta \in B_{M_I} \mid V(\zeta) \le \alpha_I\} \tag{6.55}$$

The definition of the candidate Lyapunov function (6.53) shows that there exist class K functions κ_3 and κ_4 such that

$$\kappa_3(\|\zeta\|) \le V(\zeta) \le \kappa_4(\|\zeta\|)$$

and

$$\begin{aligned} \kappa_3(\|\zeta\|) &= \kappa_1(\|\zeta_o\|) + \lambda_{\min}(P_{E,i})\|\boldsymbol{E}_i\|^2 + \lambda_{\min}(\tilde{P}_{E,i})\|\tilde{\boldsymbol{E}}_i\|^2 + \lambda_{\min}(\Gamma_{c_i}^{-1})\|\tilde{\boldsymbol{W}}_{c,i}\|^2 \\ \kappa_4(\|\zeta\|) &= \kappa_2(\|\zeta_o\|) + \lambda_{\max}(P_{E,i})\|\boldsymbol{E}_i\|^2 + \lambda_{\max}(\tilde{P}_{E,i})\|\tilde{\boldsymbol{E}}_i\|^2 + \lambda_{\max}(\Gamma_{c_i}^{-1})\|\tilde{\boldsymbol{W}}_{c,i}\|^2 \end{aligned} \tag{6.56}$$

where the class K functions κ_1 and κ_2 are defined in (6.25).

Assumption 6.8: Let

$$M_I > \kappa_3^{-1}(\kappa_4(\gamma_I)) \tag{6.57}$$

where γ_I is defined as

$$\gamma_I \triangleq \frac{\sqrt{\sum_j^m \left\{ m_{1_j}^2 + m_{4_j}^2 + \lambda_o W_o^{*2} \right\} + l_1^2 + l_2^2 + \lambda_{c,i} W_c^{*2}}}{\min\left(\sqrt{\frac{\lambda_{\min}\left(Q_1\right)}{\rho_2^2} - 2m}, \sqrt{\lambda_o - \left(m_{2_j}^2 + 2\right)}, \sqrt{\lambda_{\min}\left(Q_{E,i}\right) - 1}, \sqrt{\lambda_{\min}\left(\tilde{Q}_{E,i}\right) - 2}, \sqrt{\lambda_{c,i} - l_4^2} \right)}, \quad j = 1, 2, \cdots, m \tag{6.58}$$

where m_{1_j}, m_{2_j}, and m_{4_j} are defined in (6.28):

$$\begin{aligned} l_1 &= \left\| \tilde{P}_{E,i} \bar{B}_{E,i} \right\| \varepsilon_c^* \\ l_2 &= \left\| P_{E,i} \bar{B}_{E,i} \right\| \varepsilon_c^* \\ l_4 &= \left\| P_{E,i} \bar{B}_{E,i} + \tilde{P}_{E,i} \bar{B}_{E,i} \right\| \sqrt{N_c} \end{aligned} \tag{6.59}$$

and N_c is the number of neurons in the controller NN. Let $\lambda_{\min}\left(Q_1\right) > 2m\rho_2^2$ and $\lambda_o > \max\left\{ m_{2_1}^2 + 2, m_{2_2}^2 + 2, \cdots, m_{2_m}^2 + 2 \right\}$, $\lambda_{\min}\left(Q_{E,i}\right) > 1$, $\lambda_{\min}\left(\tilde{Q}_{E,i}\right) > 2$ and $\lambda_{c,i} > l_4^2$.

Theorem 6.2: Let Assumptions 6.1-6.8 hold and the initial error vector $\zeta\left(t_0\right) \in \Omega_{\alpha_I}$. For the system formulation in (6.4) with the normal form given by (5.3), let the adaptive estimator be given by (6.9), the adaptive controller by (6.33), (6.34), the observer NN adaptive law by (6.12), and the controller NN adaptive law by (6.48). Then the state estimation error $\tilde{\boldsymbol{x}}_1$, controller tracking errors $\boldsymbol{E}_i$ and $\tilde{\boldsymbol{E}}_i$, observer NN weight estimation errors $\tilde{\boldsymbol{W}}_{o,i}$, $i = 1, 2, \cdots, m$, and controller NN weight estimation errors $\tilde{\boldsymbol{W}}_{c,i}$, are uniformly ultimately bounded.

Proof: Refer to Appendix D.

D. Extension to the case when regulated outputs are not measured

We present an extension to the problem formulation in (5.1) by considering the case that the regulated outputs are not available directly from the measurements. An example is the problem of regulating bearing rates in the context of vision-based formation flight. Consider the i^{th} such regulated output given by

$$q_i = h_i^q\left(\boldsymbol{x}_1, \boldsymbol{x}_2\right) \tag{6.60}$$

The following additional assumption is required to address this problem.

Assumption 6.9: The nonlinear function $h_i^q\left(\boldsymbol{x}_1, \boldsymbol{x}_2\right)$ is known exactly and the relative degree of q_i equals 1.

The first part of the above assumption allows construction of estimates for q_i using the state estimates for $\boldsymbol{x}_1$

$$\hat{q}_i = h_i^q\left(\hat{\boldsymbol{x}}_1, \boldsymbol{x}_2\right) \tag{6.61}$$

The second part is required to make the mathematical analysis tractable. The bearing rates satisfy Assumption 6.9.

From Assumption 6.2, the first derivative of q_i is given as

$$\dot{q}_i = \alpha_{q_i}^0\left(\boldsymbol{x}_1, \boldsymbol{x}_2\right) + \alpha_{q_i}^1\left(\boldsymbol{x}_1, \boldsymbol{x}_2, \boldsymbol{z}, u_i\right) + \beta_{q_i}\left(\boldsymbol{y}_1, \boldsymbol{x}_2\right) u_i \tag{6.62}$$

where $\alpha_{q_i}^0\left(\boldsymbol{x}_1, \boldsymbol{x}_2\right)$ and $\beta_{q_i}\left(\boldsymbol{y}_1, \boldsymbol{x}_2\right)$ are known continuous functions, and $\alpha_{q_i}^1\left(\boldsymbol{x}_1, \boldsymbol{x}_2, \boldsymbol{z}, u_i\right)$ are unknown continuous functions. Let the tracking error be given by

$$e_i^q = y_{c,i}^q - q_i \tag{6.63}$$

where $y_{c,i}^q$, $\dot{y}_{c,i}^q$ are smooth and bounded reference signals generated by filtering the output command $q_{com,i}$ through asymptotically stable reference models of order ≥ 1. The tracking error dynamics are given by

$$\begin{aligned}\dot{e}_i^q &= \dot{y}_{c,i}^q - \alpha_{q_i}^0\left(\boldsymbol{x}_1, \boldsymbol{x}_2\right) - \alpha_{q_i}^1\left(\boldsymbol{x}_1, \boldsymbol{x}_2, \boldsymbol{z}, u_i\right) - \beta_{q_i}\left(\boldsymbol{y}_1, \boldsymbol{x}_2\right) u_i \\ &= \dot{y}_{c,i}^q - \alpha_{q_i}^0\left(\hat{\boldsymbol{x}}_1, \boldsymbol{x}_2\right) - \beta_{q_i}\left(\hat{\boldsymbol{y}}_1, \boldsymbol{x}_2\right) u_i - \Delta_{c,i}^q\left(\boldsymbol{x}_1, \hat{\boldsymbol{x}}_1, \boldsymbol{x}_2, \boldsymbol{z}, u_i\right)\end{aligned} \tag{6.64}$$

where

$$\begin{aligned}\Delta_{c,i}^q\left(\boldsymbol{x}_1, \hat{\boldsymbol{x}}_1, \boldsymbol{x}_2, \boldsymbol{z}, u_i\right) = &\left[\alpha_{q_i}^0\left(\boldsymbol{x}_1, \boldsymbol{x}_2\right) - \alpha_{q_i}^0\left(\hat{\boldsymbol{x}}_1, \boldsymbol{x}_2\right)\right] + \left[\beta_{q_i}\left(\boldsymbol{y}_1, \boldsymbol{x}_2\right) - \beta_{q_i}\left(\hat{\boldsymbol{y}}_1, \boldsymbol{x}_2\right)\right] u_i \\ &+ \alpha_{q_i}^1\left(\boldsymbol{x}_1, \boldsymbol{x}_2, \boldsymbol{z}, u_i\right)\end{aligned} \tag{6.65}$$

A feedback inversion control law for stabilizing the error dynamics in (6.64) is given by

$$u_i = \frac{\nu_i}{\beta_{q_i}\left(\hat{\boldsymbol{y}}_1, \boldsymbol{x}_2\right)}, \quad \nu_i = \dot{y}_{c,i}^q - \alpha_{q_i}^0\left(\hat{\boldsymbol{x}}_1, \boldsymbol{x}_2\right) + \nu_{dc,i} - \nu_{ad,i} \tag{6.66}$$

where ν_i is the pseudo-control term, $\nu_{dc,i}$ is the output of a linear compensator, and $\nu_{ad,i}$ is the output of an adaptive NN designed to compensate for the modeling error. Since the relative degree of q_i is 1, $\nu_{dc,i}$ can be given as the output of a proportional gain controller

$$\nu_{dc,i} = K_{q_i}\left(y_{c,i}^q - \hat{q}_i\right) = K_{q_i}\hat{e}_i^q \tag{6.67}$$

where $K_{q_i} > 0$ and $\hat{e}_i^q$ is an estimate for the tracking error e_i^q. The following identity is derived from Eqs. (6.60) and (6.61):

$$\hat{e}_i^q = e_i^q + \left(q_i - \hat{q}_i\right) = e_i^q + \left[h_i^q\left(\boldsymbol{x}_1, \boldsymbol{x}_2\right) - h_i^q\left(\hat{\boldsymbol{x}}_1, \boldsymbol{x}_2\right)\right] \tag{6.68}$$

Substituting Eqs. (6.66)-(6.68) into (6.64), we have,

$$\dot{e}_i^q = -K_{q_i} e_i^q + \left[\nu_{ad,i} - \bar{\Delta}_{c,i}^q\left(\boldsymbol{x}_1, \hat{\boldsymbol{x}}_1, \boldsymbol{x}_2, \boldsymbol{z}, u_i\right)\right] \tag{6.69}$$

where

$$\bar{\Delta}_{c,i}^{q}\left(\boldsymbol{x}_1,\hat{\boldsymbol{x}}_1,\boldsymbol{x}_2,\boldsymbol{z},u_i\right)=\Delta_{c,i}^{q}\left(\boldsymbol{x}_1,\hat{\boldsymbol{x}}_1,\boldsymbol{x}_2,\boldsymbol{z},u_i\right)+\left[h_i^{q}\left(\boldsymbol{x}_1,\boldsymbol{x}_2\right)-h_i^{q}\left(\hat{\boldsymbol{x}}_1,\boldsymbol{x}_2\right)\right] \tag{6.70}$$

The error dynamics in (6.69) has the same form as in (6.39), and since q_i is relative degree 1, there is no need for an error observer. The adaptive control design analysis in Section 6.3 can now be applied in a straight forward fashion to the control of q_i.

Remark 6.5: It is possible to relax the relative degree 1 assumption on q_i by making the Assumption 6.9 restrictive in other ways. Suppose q_i is relative degree r_i with respect to the control input u_i. Then Assumption 6.9 is modified to state that the nonlinear functions $h_i^{q}\left(\boldsymbol{x}_1,\boldsymbol{x}_2\right)$, $\dot{q}_i=\dfrac{d\left[h_i^{q}\left(\boldsymbol{x}_1,\boldsymbol{x}_2\right)\right]}{dt},\cdots q_i^{(r_i-1)}=\dfrac{d^{(r_i-1)}\left[h_i^{q}\left(\boldsymbol{x}_1,\boldsymbol{x}_2\right)\right]}{dt^{(r_i-1)}}$ are known exactly. The modified assumption would also require that the derivatives $\left[\dot{q}_i,\cdots,q_i^{(r_i-1)}\right]^T$ are not dependent on the states of the unmodeled dynamics $\boldsymbol{z}$. This could be satisfied if the relative degree of q_i with respect to u_i is equal to the relative degree with respect to the unmodeled dynamics function $\boldsymbol{g}\left(\boldsymbol{x}_1,\boldsymbol{z}\right)$.

Remark 6.6: The adaptive estimator presented in Chapter 3 is integrated with the adaptive guidance and control laws presented in Chapters 4 and 5, by replacing the LOS variables with their filtered estimates. The input vectors to the controller NNs now include the estimates of the LOS variables in addition to the delayed values of available measurements. In addition the estimates of the leader acceleration that are generated by the NN augmenting the time-varying Kalman filter can be used in the adaptive controller solution to improve performance.

6.4 Simulation Results

We integrate the adaptive estimator presented in Chapter 3, Section 4 with the time-scale separated adaptive guidance and control law presented in Chapter 4 and with the adaptive integrated guidance and control law (IGC-2) presented in Chapter 5. The former is referred to as the Integrated Adaptive Estimation with Time-Scale Separated Guidance and Control (IAETSSGC) design and the latter as the Integrated Adaptive Estimation Guidance and Control (IAEGC) design henceforth for convenience. We compare the range tracking performance of IAETSSGC and IAEGC designs for the case of the slanted 3D box maneuver of the leader aircraft described previously in Chapter 5, Section 3. The 6DOF nonlinear fixed-wing simulation model has been described in Chapter 4, Section 4.3-A. The range command is set to $R_{com} = 5$ meters, which is slightly less than 2 wing-span lengths. The bearing rate commands are nominally set to zero, and these commands are modified to prevent drifts in the bearing angles to large values using the dead-zone logic shown in Figure 23.

Figure 47 shows the range command tracking and estimation performance in meters with the IAEGC and IAETSSGC designs, with adaptation in both the estimation (NN_EKF = 1) and in the guidance and control (NN_G&C = 1). The black solid line represents the commanded range $R_{com} = 5$ meters, the blue dotted line is the range estimate, and the red dashed line represents the true range. The range estimate almost coincides with the true range. This is to be expected since we have a reasonably accurate measurement of the range by assumption of knowledge of leader wing-span length, except at large ranges. The range tracking performance with the IAEGC design is superior to that with the IAETSSGC design. The overshoots in the range due to leader maneuvers is smaller and convergence to the commanded range is faster with the IAEGC design. This figure confirms that when integrated with the adaptive estimation, the IGC-2 design retains the superiority in range tracking performance over the TSSGC design.

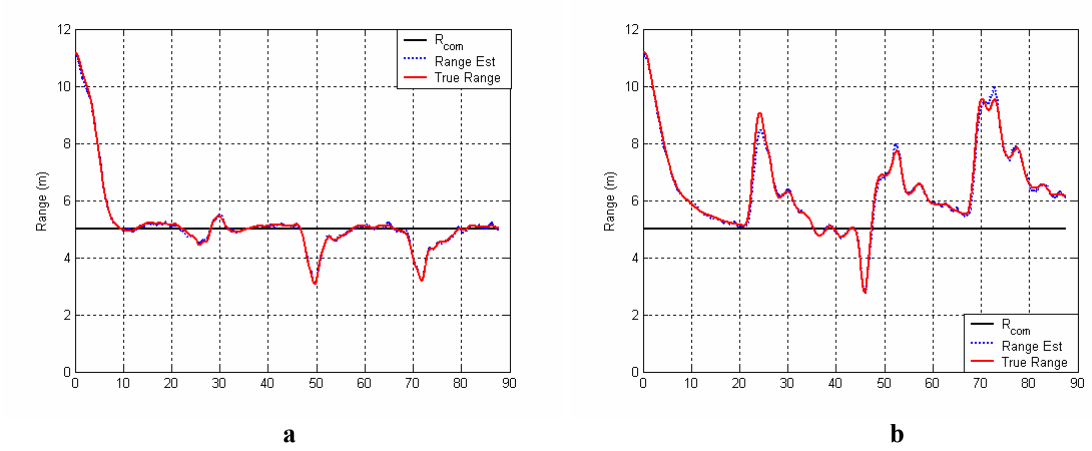

Figure 47. Range Command Tracking and Estimation Performance (meters), NN_EKF = 1, NN_G&C = 1, a) IAEGC b) IAETSSGC

Figure 48 shows the azimuth-rate time history in deg/s with adaptation in both the estimation and in the guidance and control. In the top plots, the blue dotted line is the azimuth-rate estimate, and the red solid line represents the true azimuth-rate. The corresponding estimation errors are shown in the bottom plots. The transients correspond to the start of each leader maneuver. This is due to the fact that the leader acceleration is estimated with a small delay by the adaptive estimator. The estimation performance is comparable with both designs, with the exception of one large peak with the IAETSSGC design at about 45 seconds, which is almost double in magnitude with the corresponding peak in the IAEGC design. In addition, the peak azimuth-rate with the IAEGC design (~ 30 deg/s) is much smaller compared with that of the IAETSSGC design (~ 80 deg/s). This shows that the IAEGC design does a superior job of regulating the azimuth-rate.

Figure 49 shows the elevation-rate time history in deg/s with adaptation in both the estimation and in the guidance and control. The corresponding estimation errors are

shown in the bottom plots. The estimation and tracking performances with the IAEGC and IAETSSGC designs are comparable.

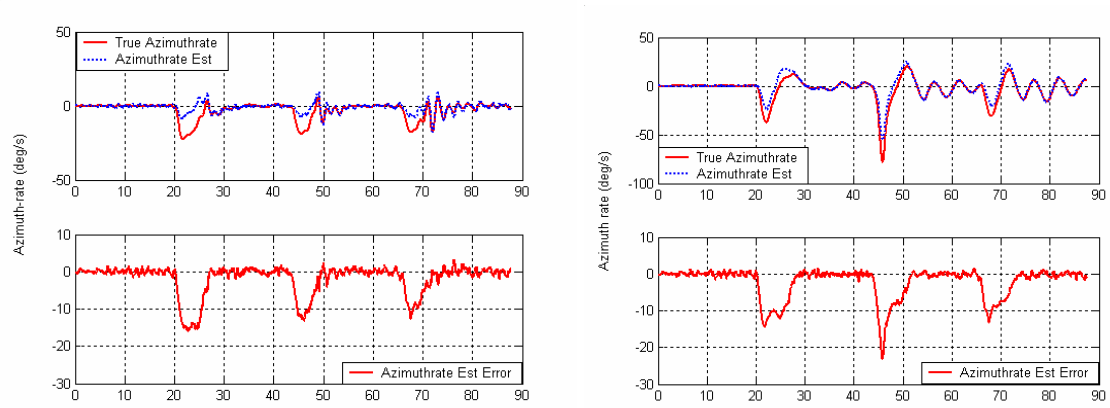

Figure 48. Azimuth-rate Estimation and Regulation (deg/s), NN_EKF = 1, NN_G&C = 1, a) IAEGC b) IAETSSGC

Figure 50 shows the leader acceleration estimation along the inertial coordinate axes in m/s^2 with adaptation in both the estimation and in the guidance and control. The blue dotted lines are the estimates and the red solid lines represent the true values. The estimates of the acceleration lag the corresponding true values. These estimates are the outputs of the observer NNs. The estimation performance with the IAEGC and IAETSSGC designs are comparable.

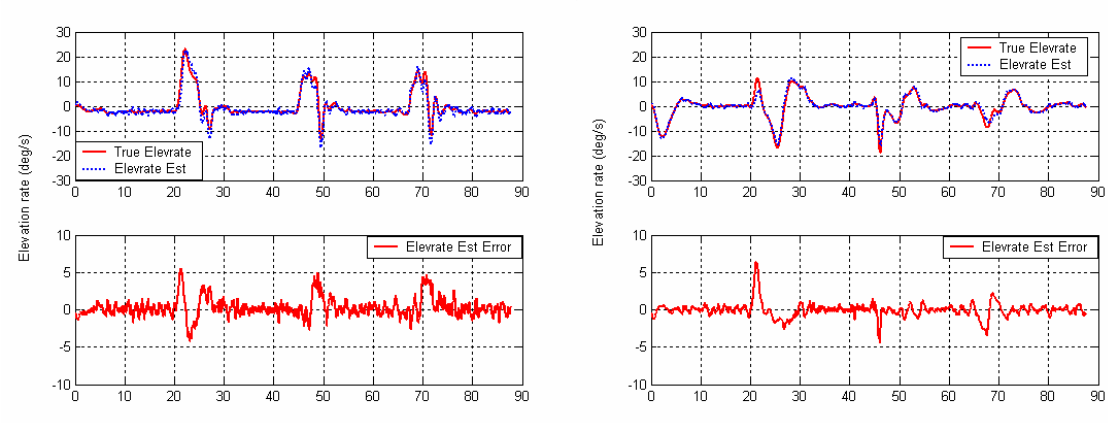

Figure 49. Elevation-rate Estimation and Regulation (deg/s), NN_EKF = 1, NN_G&C = 1, a) IAEGC b) IAETSSGC

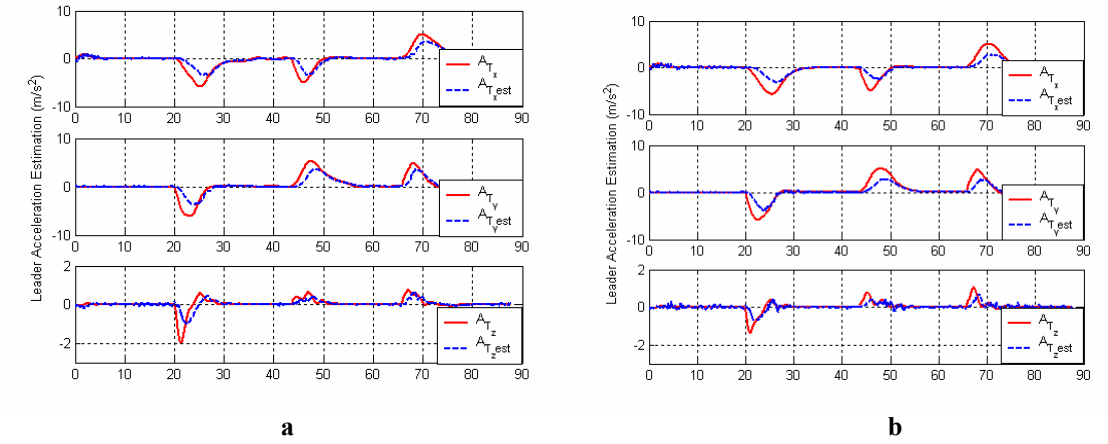

Figure 50. Leader Acceleration Estimation (m/s^2), NN_EKF = 1, NN_G&C = 1, a) IAEGC b) IAETSSGC

Figure 51 shows the actuator deflection histories with adaptation in both the estimation and in the guidance and control. The plots show that the controls have reasonable amplitude and frequency content.

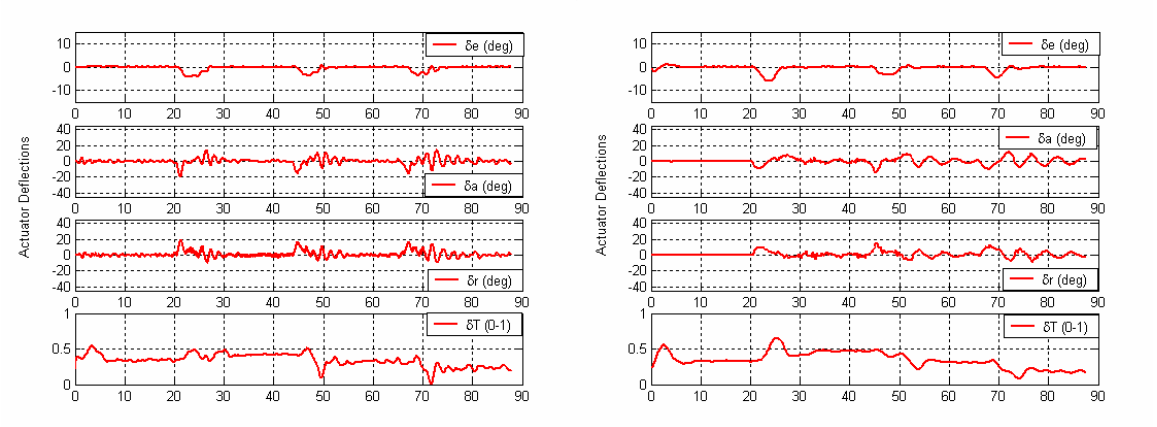

Figure 51. Actuator Deflections Histories, NN_EKF = 1, NN_G&C = 1, a) IAEGC b) IAETSSGC

The next set of results show the effect of adaptation in the integrated designs. Figure 52 shows the range command tracking and estimation performance in meters with adaptation in the guidance and control (NN_G&C = 1) and without adaptation in the estimation (NN_EKF = 0). The range estimates are not that accurate when compared to the corresponding results in Figure 47. The range tracking performance with the IAEGC design in Figure 52a is slightly worse than the corresponding result in Figure 47a. However, for the IAETSSGC design, the range tracking diverges in the absence of adaptation in the estimation. The reason for the degraded performances is that in the absence of adaptation in the estimation, the target state estimator is not compensated for the leader acceleration leading to large peaks in the state estimation error that converge to zero only when the leader maneuver ends. Figure 53 shows the range command tracking and estimation performance with adaptation in the estimation (NN_EKF = 1) and without adaptation in the guidance and control (NN_G&C = 0). The range tracking diverges for both the designs, indicating that adaptation in the guidance and control is critical to the stability of range tracking.

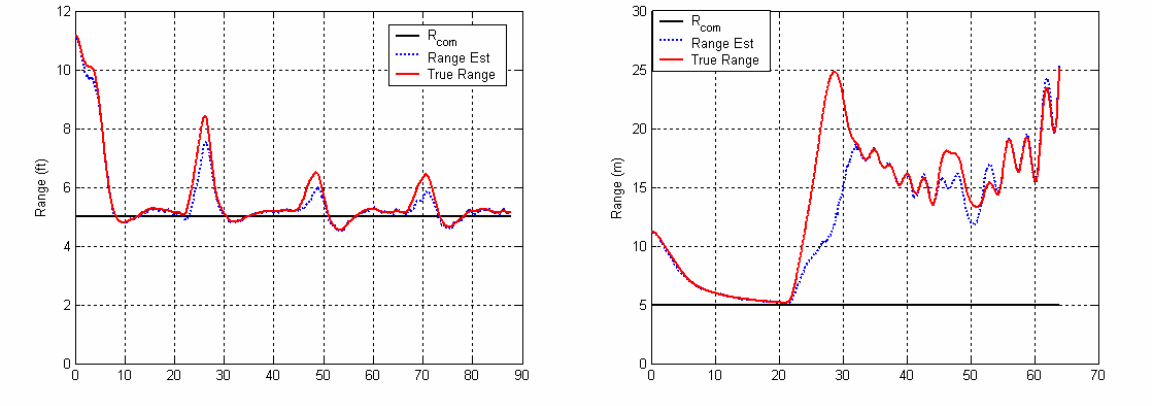

a b

Figure 52. Range Command Tracking and Estimation Performance (meters), NN_EKF = 0, NN_G&C = 1, a) IAEGC b) IAETSSGC

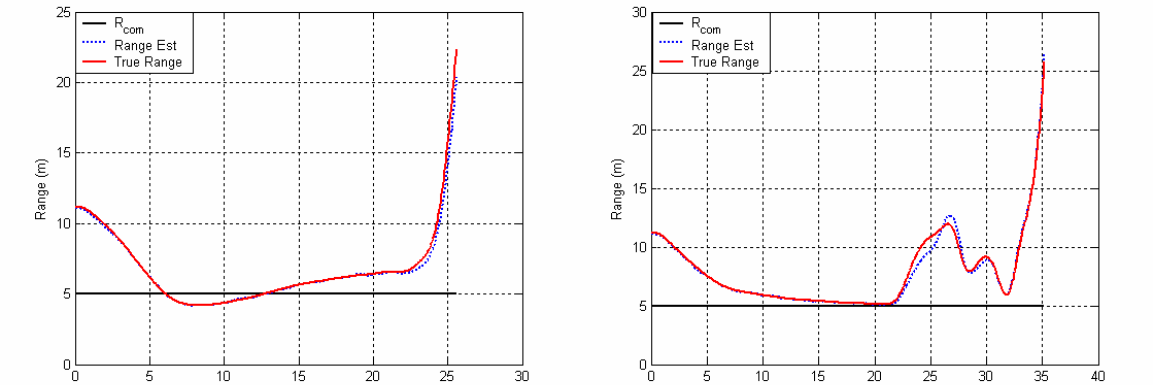

a b

Figure 53. Range Command Tracking and Estimation Performance (meters), NN_EKF = 1, NN_G&C = 0, a) IAEGC b) IAETSSGC

The results so far have been presented with the assumption that the image measurements are available at the same rate as the update rates of the G&C algorithms. The next sets of results show the effect of slower image processing update rates on the range tracking performance. The G&C system is updated at 20 Hz and the image

measurements are updated at 20 Hz, 10 Hz, 5 Hz and 4 Hz. Results are shown in Figure 54 and Figure 55 for the IAEGC design and the IAETSSGC design respectively. To handle the issue of slow image measurement update, the adaptive estimator prediction step is set up to propagate at 20 Hz, and the adaptive estimator update step occurs whenever a new measurement is received.

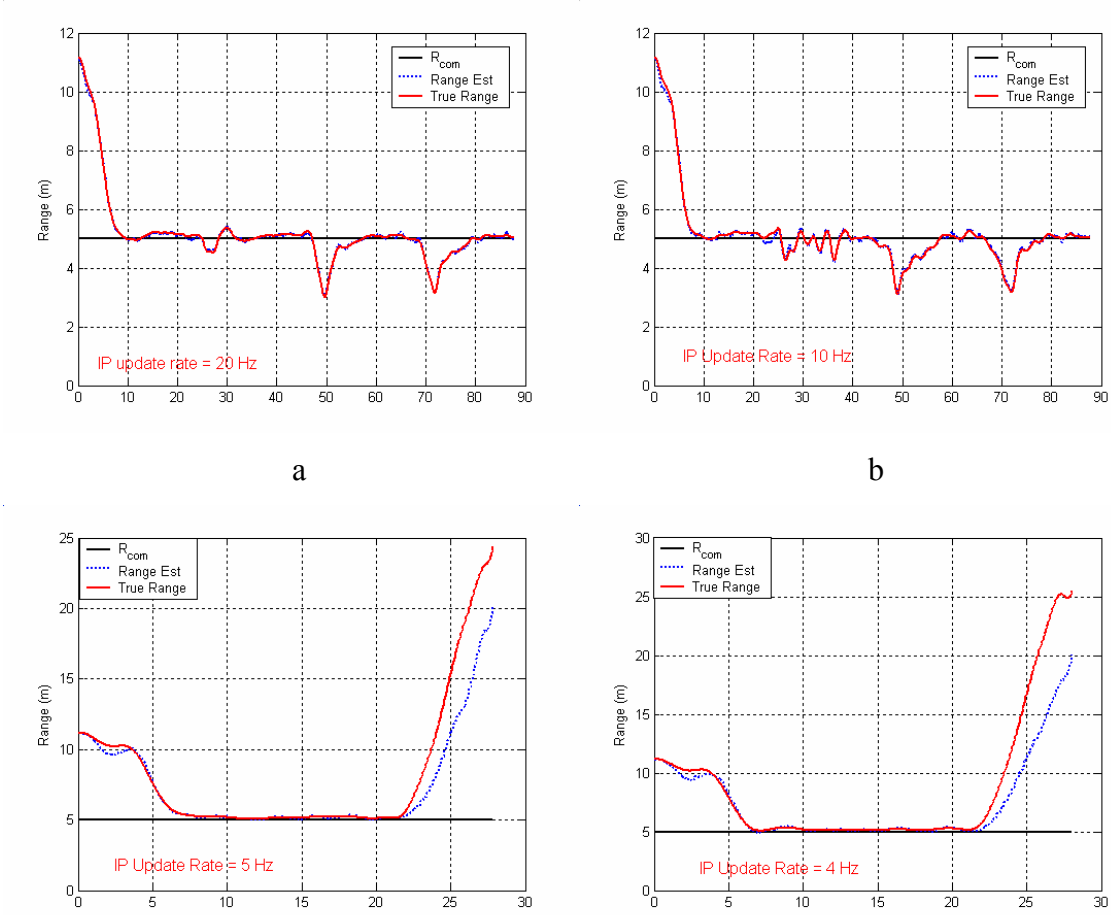

Figure 54. IAEGC Design, with varying image measurement update rates a) 20 Hz, b) 10 Hz, c) 5 Hz, d) 4 Hz

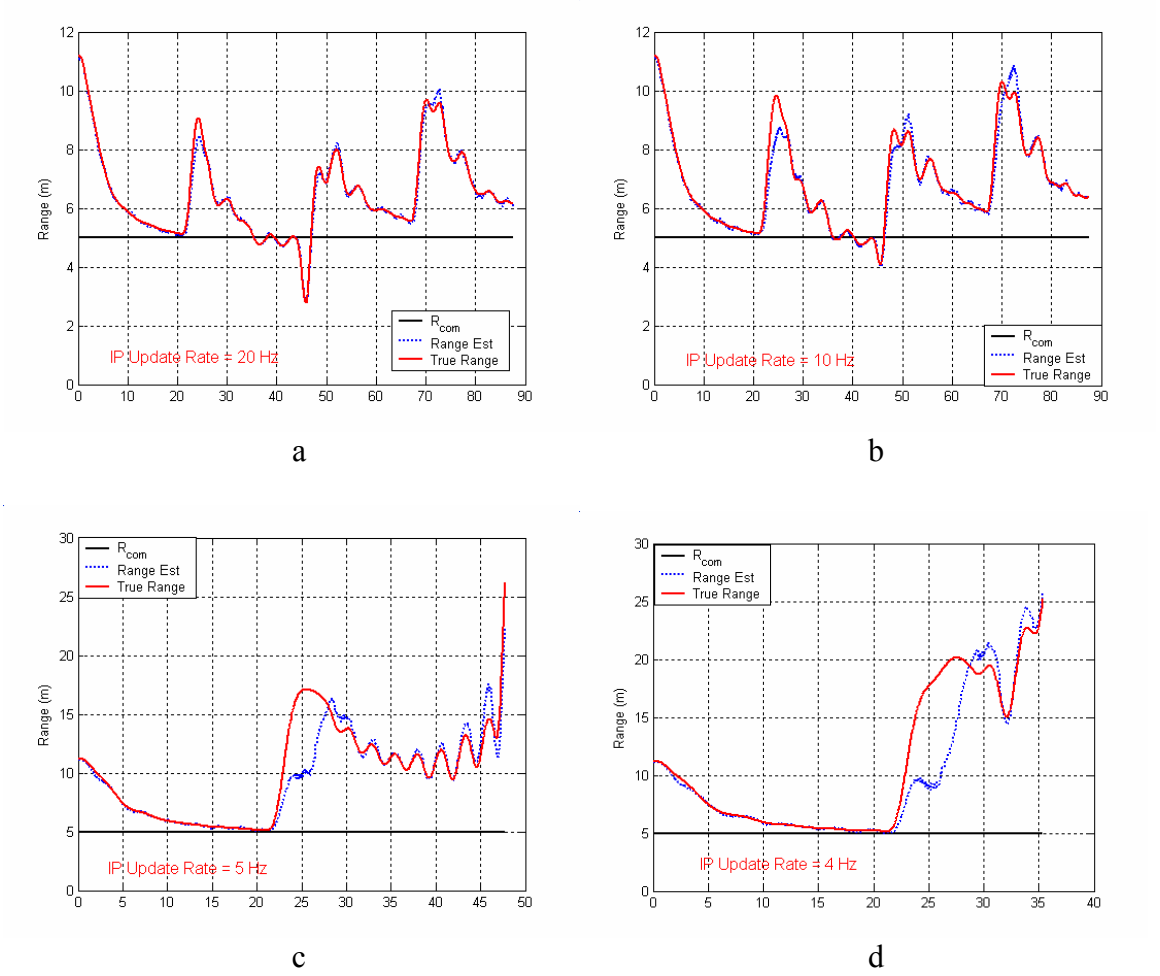

Figure 55. IAETSSGC Design, with varying image measurement update rates a) 20 Hz, b) 10 Hz, c) 5 Hz, d) 4 Hz

From Figure 54 and Figure 55, it is clear that below a critical limit for the image measurements update rate, which we found to be 10 Hz in our simulations, instability occurs in the range tracking performance. There was only marginal degradation in the range tracking and estimation performance as the image measurements update rate was decreased from 20 Hz to 10 Hz. This implies that if the image measurements update rate is significantly small relative to the estimation, guidance and control update rate, the image processing dynamics have to be considered in the overall design process.

6.5 Conclusions

This chapter has presented a method to integrate adaptive estimation and adaptive control designs for a class of nonlinear systems. The method is based on Lyapunov-like stability analysis of all the errors in the integrated closed-loop system. The developed approach is applied to integrate the adaptive estimator solution in Chapter 3 with the adaptive guidance and control solutions presented in Chapters 4 and 5 for enabling vision-based formation flight. Simulation results showed that adaptation in both estimation and guidance and control is critical to the stability and performance of the range tracking performance. When comparing between the integrated estimation, guidance and control designs, the design in which the guidance and control solution is also integrated results in superior range tracking performance compared to the design in which the guidance and control solution is designed by assuming time-scale separation.

Another conclusion is regarding the effect of the update rates of the image processing relative to that of the G&C algorithms. Below a critical limit for the image measurements update rate, instability occurs in the range tracking performance. For image measurement update rates larger than this critical value but smaller than the update rates of the estimation, guidance and control designs, there is marginal degradation in the range tracking and estimation performance. This implies that if the image measurements update rate is significantly small relative to the estimation, guidance and control update rate, the image processing dynamics have to be considered in the overall design process.

CHAPTER 7

VISION-BASED APPROACH TO MULTIPLE-AIRCRAFT FORMATION CONTROL

This chapter presents a conceptual approach to multiple-aircraft formation control. It is assumed that the aircraft utilize passive vision sensors to track neighboring aircraft and that there is little to no communication between the aircraft. Formation controllers are designed that allow each vehicle in formation to maintain separation and relative orientation with respect to neighboring vehicles, while avoiding static obstacles. These controllers are integrated with adaptive neural network augmented Kalman filters that generate estimates of the position and velocity of the neighboring aircraft. A multi-aircraft coordination scheme is proposed that does not depend on a unique leader in the formation. The resulting formations are called leaderless formations. Each aircraft in the formation maintains desired range to up to two nearest vehicles while simultaneously navigating towards a common set of waypoints and avoiding obstacles. Illustrative simulation results for a set of desired formation trajectories are shown.

Equation Chapter 7 Section 1

7.1 Formation Control Design

A. Modeling Assumptions and LOS Kinematics

The following simplifying assumptions are made to aid the design of the formation controllers:

1) The formation of vehicles is constrained to lie in the two-dimensional horizontal plane.

2) Each aircraft in formation is identical and the wing-span length is known to each aircraft. The aircraft can accelerate both along and perpendicular to the direction of motion.

3) The autopilot modeling is very simplistic. Speed and heading are considered to be the control variables from the point-of-view of the guidance law, and these are assumed to have first-order dynamics. The accelerations are treated as the actual controls for the aircraft. Limits are placed on the accelerations to prevent slowing below the stall speed, to prevent exceeding maximum bank angle limits, and maximum and minimum longitudinal acceleration limits.

Vehicle Dynamics

Consider the equations of motion of an aircraft in the horizontal plane.

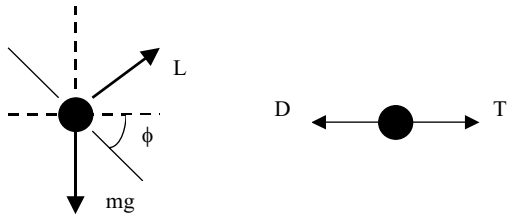

Figure 56. Banked Horizontal Turn

From Figure 56, the equations of motion are given by,

$$mV\dot{\psi} = L\sin\phi \tag{7.1}$$

$$m\dot{V} = T - D \tag{7.2}$$

$$mg = L\cos\phi \tag{7.3}$$

where ψ, V represent the heading and speed of the aircraft with respect to the North-East-Down (NED) axes which is also assumed to be the inertial coordinate axes, m, ϕ

represent the mass and bank angle, L, T, D represent the lift, thrust and drag forces on the aircraft and g is the acceleration due to gravity. Eliminating ϕ from Eqs. (7.1) and (7.3),

$$\dot{\psi} = \frac{g}{V}\sqrt{n^2 - 1} \tag{7.4}$$

$$\dot{V} = \left(\frac{T - D}{W}\right) g \tag{7.5}$$

where $n = \left(\frac{L}{W}\right)$ is the load-factor of the aircraft. Eqs. (7.4) and (7.5) can be non-dimensionalized by letting $t' = t\left(\frac{V_o}{R_o}\right)$ and $V' = V/V_o$ represent non-dimensional time and speed, where V_o and R_o are constant quantities with units of speed and distance respectively. A way to choose V_o and R_o would be to set $V_o^2 = gR_o$. Furthermore, we set $\text{mag}(V_o) = \text{mag}(R_o) \Rightarrow \text{mag}(V_o) = \text{mag}(R_o) = \text{mag}(g)$, where $\text{mag}(\cdot)$ is the magnitude operator. This implies the non-dimensionalized heading rate and longitudinal acceleration is given by:

$$\frac{d\psi}{dt'} = \frac{a_1}{V'}, \quad a_1 = \sqrt{n^2 - 1} \tag{7.6}$$

$$\frac{dV'}{dt'} = a_2 - \left(\frac{D}{W}\right), \quad a_2 = \frac{T}{W} \tag{7.7}$$

where a_1 and a_2 represent the non-dimensionalized controls. Drag is given by $D = \frac{1}{2}\rho S V^2 C_D$, and the drag coefficient C_D is given by

$$C_D = C_{D_o} + \kappa C_L^2 \tag{7.8}$$

where C_{D_o} is the profile drag coefficient, assumed to be constant, C_L is the lift coefficient and κC_L^2 is the induced drag. Eq. (7.8) can be modified to replace C_L with the load factor as follows:

$$n = \frac{L}{W} = \frac{\rho S V^2 C_L}{2W} \Rightarrow C_L = \frac{2nW}{\rho S V^2}$$

$$\Rightarrow \frac{D}{W} = \left(\frac{\rho S C_{D_o} V_o^2}{2W} \right) V'^2 + \left(\frac{2\kappa W}{\rho S V_o^2} \right) \left(\frac{n^2}{V'^2} \right)$$

$$\frac{D}{W} = k_1 V'^2 + k_2 \left(\frac{a_1^2 + 1}{V'^2} \right) \tag{7.9}$$

where $k_{1,2}$ are non-dimensional constants. So the non-dimensional speed dynamics equation is given by substituting (7.9) into (7.7):

$$\frac{dV'}{dt'} = a_2 - k_1 V'^2 - k_2 \left(\frac{a_1^2 + 1}{V'^2} \right) \tag{7.10}$$

Dropping the primes henceforth, the non-dimensionalized equations of motion for the i^{th} aircraft in formation is given by:

$$\begin{aligned} \dot{x}_i &= V_i \cos \psi_i \\ \dot{y}_i &= V_i \sin \psi_i \\ \dot{\psi}_i &= \frac{a_{i1}}{V_i} \\ \dot{V}_i &= a_{i2} - k_{i1} V_i^2 - k_{i2} \left(\frac{a_{i1}^2 + 1}{V_i^2} \right) \end{aligned} \tag{7.11}$$

where (x_i, y_i) are the position coordinates of the i^{th} aircraft in the inertial coordinate frame and ψ_i is the heading angle measured from the inertial x-axis (axis pointing towards North).

Limits on Controls

Since the controls used in our formulation are physical quantities, we need to impose realistic bounds on their values. From Eqs. (7.1), (7.3) and (7.4), we can write

$$\begin{aligned} \dot{\psi} &= \frac{g}{V}\tan\phi = \frac{g}{V}\sqrt{n^2-1} \\ \Rightarrow \tan\phi &= \sqrt{n^2-1} = a_1 \end{aligned} \tag{7.12}$$

If we set the maximum bank angle $\phi_{\max} = 60^o$, we have $n_{\max} = 2$. At low speeds, the maximum load factor is limited by the stall-limit [112] and is given by,

$$n_{\max} = \frac{L_{\max}}{W} = \frac{\rho V^2 S C_{L_{\max}}}{2W} \tag{7.13}$$

The minimum value of $n_{\max}$ is set to 1 and corresponds to straight, level flight when the lift force equals the weight. The limits for control a_1 are given below,

$$\begin{aligned} a_{1,\max} &= \min\left(\tan\phi_{\max}, \sqrt{n_{\max}^2-1}\right) \\ a_{1,\min} &= \max\left(-\tan\phi_{\max}, -\sqrt{n_{\max}^2-1}\right) \end{aligned} \tag{7.14}$$

Eq. (7.14) shows that the limits on a_1 are speed dependent. The minimum value of $n_{\max}$ is associated with a minimum speed given by

$$V_{\min} = \sqrt{\frac{2W}{\rho S C_{L_{\max}}}} \tag{7.15}$$

At this speed, no turning is possible. A similar method can be used to determine the bounds on a_2. It is assumed that the maximum and minimum values of a_2 do not vary with speed and given by:

$$\begin{aligned} a_{2,\max} &= 0.2 \\ a_{2,\min} &= 0.0 \end{aligned} \tag{7.16}$$

which indicates a reasonable assumption that the maximum thrust available is 20% of the weight of the aircraft.

Line-of-Sight Kinematics

Figure 57 shows the variables involved in describing the LOS kinematics. The LOS kinematics of the i^{th} aircraft with respect to the j^{th} aircraft is given by

$$\begin{aligned} R_{ij} &= \sqrt{\left(x_j - x_i\right)^2 + \left(y_j - y_i\right)^2} \\ \lambda_{ij} &= \operatorname{atan}\left(y_j - y_i, x_j - x_i\right) \end{aligned} \tag{7.17}$$

where R_{ij} is the range between aircraft i and j, and λ_{ij} is the angle the LOS vector from aircraft i to aircraft j makes with the inertial x-axis. Differentiating (7.17), we have,

$$\begin{aligned} \dot{R}_{ij} &= V_j \cos\left(\psi_j - \lambda_{ij}\right) - V_i \cos\left(\psi_i - \lambda_{ij}\right) \\ \dot{\lambda}_{ij} &= \frac{V_j \sin\left(\psi_j - \lambda_{ij}\right) - V_i \sin\left(\psi_i - \lambda_{ij}\right)}{R_{ij}} \end{aligned} \tag{7.18}$$

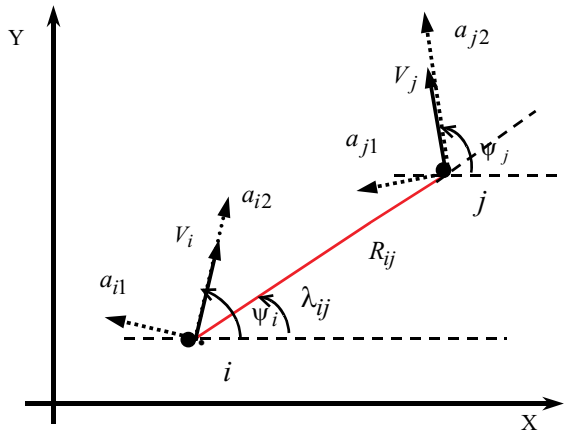

Figure 57. Line-of-Sight Kinematics

B. Formation Controller Design

We design an inverting controller for aircraft i which is augmented with the output of an adaptive target state estimator for regulating the LOS range R_{ij}. An approximate inversion of R_{ij} kinematics in (7.18) is given as follows:

$$\nu_R^{ij} = -V_i \cos\left(\psi_i - \lambda_{ij}\right) \tag{7.19}$$

where ν_R^{ij} is the pseudo-control term that represents the desired range-rate for aircraft i. Since the velocity of the j^{th} aircraft is unknown to the i^{th} aircraft, Eq. (7.19) assumes the velocity along the LOS of the j^{th} aircraft is zero. The modeling error as a result of this assumption is given by:

$$\Delta_R^{ij} = \dot{R}_{ij} - \nu_R^{ij} = V_j \cos\left(\psi_j - \lambda_{ij}\right) \tag{7.20}$$

and which is compensated for with the output of an adaptive target state estimator that estimates the leader velocity.

The pseudo-control term ν_R^{ij} is designed as discussed in Chapter 6:

$$\nu_R^{ij} = \nu_{R,crm}^{ij} + \nu_{R,dc}^{ij} - \nu_{R,ad}^{ij} \tag{7.21}$$

where $\nu_{R,crm}^{ij}$ is the reference model feedforward term, $\nu_{R,dc}^{ij}$ is the output of a linear compensator, and $\nu_{R,ad}^{ij}$ is the term designed to approximate the velocity component of aircraft j along the LOS. Since the relative degree of R_{ij} with respect to the speed and heading of aircraft i is 1, the first two components of ν_R^{ij} in (7.21) are designed using first-order reference models and proportional gain controllers as shown below:

$$\begin{aligned} \nu_{R,crm}^{ij} &= p_{R,i}\left(R_{com}^{ij} - R_c^{ij}\right), \;\; p_{R,i} > 0 \\ \dot{R}_c^{ij} &= \nu_{R,crm}^{ij} - \nu_{R,h}^{ij} \end{aligned} \tag{7.22}$$

$$\nu_{R,dc}^{ij} = k_{R,i}\left(R_c^{ij} - R_{ij}\right), \;\; k_{R,i} > 0 \tag{7.23}$$

where R_{com}^{ij} is the commanded range between aircraft i and j, R_c^{ij} is the reference range command obtained by filtering R_{com}^{ij} through the first-order, hedged reference model in (7.22), $\nu_{R,h}^{ij}$ is the hedge signal, and $p_{R,i}$ and $k_{R,i}$ are design constants. The signal $\nu_{R,ad}^{ij}$ is designed as follows:

$$\nu_{R,ad}^{ij} = \hat{V}_{j,X}\cos\hat{\lambda}_{ij} + \hat{V}_{j,Y}\sin\hat{\lambda}_{ij} \tag{7.24}$$

where $\hat{V}_{j,X}$, $\hat{V}_{j,Y}$ are estimates of the inertial velocity components of aircraft j. Construction of $\hat{V}_{j,X}$, $\hat{V}_{j,Y}, \hat{\lambda}_{ij}$ is explained in the Section 7.2.

Eq. (7.19) is solved to give speed and heading commands for aircraft i:

$$\begin{aligned} \psi_{FC,i} &= \lambda_{ij} + \theta_{des}^{ij} \\ V_{FC,i} &= -\nu_R^{ij} \Big/ \cos\left(\theta_{des}^{ij}\right) \end{aligned} \tag{7.25}$$

where θ_{des}^{ij} is a desired lead angle, and subscript '*FC*' stands for formation control. Eq. (7.25) gives a velocity vector command for aircraft i, $\boldsymbol{V}_{FC,i}$, given by:

$$\boldsymbol{V}_{FC,i} = V_{FC,i}\left(\cos\psi_{FC,i}\boldsymbol{I} + \sin\psi_{FC,i}\boldsymbol{J}\right) \tag{7.26}$$

where $\boldsymbol{I,J}$ are the unit vectors along the inertial X and Y axes respectively.

Remark 7.1: If $\theta_{des}^{ij} = 0$, then the heading command for aircraft i is oriented along the LOS to aircraft j, and results in a 'tail-chase' situation. In this case, we can interpret the pseudo-control ν_R^{ij} itself as the magnitude of a velocity vector aligned along the LOS from aircraft i to j, and write (7.26) as,

$$\begin{aligned} \boldsymbol{v}_R^{ij} &= v_R^{ij}\left(\cos\lambda_{ij}\boldsymbol{I} + \sin\lambda_{ij}\boldsymbol{J}\right) = v_R^{ij} \\ \boldsymbol{V}_{FC,i} &= -\boldsymbol{v}_R^{ij} \end{aligned} \tag{7.27}$$

In case, aircraft i is regulating range with respect to multiple neighboring aircraft, say $m > 1$, then the commanded velocity vector for aircraft i is given by the vector sum of the pseudo-controls oriented along the respective LOS:

$$\boldsymbol{V}_{FC,i} = -\sum_{j,\, j\neq i}^{m} \boldsymbol{v}_R^{ij} \tag{7.28}$$

Pseudo-Control Hedge (PCH) Signals

Since the speed and heading are treated as control variables, the speed and heading dynamics are treated as actuator dynamics and hedged in the formation control design. When tracking range with respect to 1 neighboring aircraft, the hedge signal $v_{R,h}^{ij}$ is just the difference between the commanded and achieved velocity along the LOS and is given by:

$$v_{R,h}^{ij} = v_R^{ij} - \hat{v}_R^{ij} = -V_{FC,i}\cos\left(\psi_{FC,i} - \lambda_{ij}\right) - \left[-V_i\cos\left(\psi_i - \lambda_{ij}\right)\right] \tag{7.29}$$

where $\hat{v}_R^{ij}$ is the actual LOS velocity of aircraft i.

When tracking range with respect to multiple aircraft, the situation is more complex. Eq. (7.28) shows that when commanding range with respect to $m > 1$ aircraft, we are actually trying to track m pseudo-control signals with just one control variable, the velocity vector. This means each aircraft is an underactuated system when it commands range with respect to multiple aircraft. In this case, the method of calculating the hedge signal is special. We do a non-orthogonal projection of the actual velocity vector along each of the LOS unit vector directions $\boldsymbol{u}_{ij} = \cos\lambda_{ij}\boldsymbol{I} + \sin\lambda_{ij}\boldsymbol{J}$, $j = 1,\ldots m,\, j \neq i$. Each of these projections is treated as the achieved pseudo-control along

the particular direction $\boldsymbol{u}_{ij}$. The difference between the commanded pseudo-control and the achieved pseudo-control signal is the hedge signal. The actual mathematics for doing the above calculation is shown below.

$$\boldsymbol{V}_i = -\sum_{j,j\neq i}^{m} \alpha_R^{ij}\boldsymbol{u}_{ij} = -\underbrace{\begin{bmatrix}\boldsymbol{u}_{i1} & \boldsymbol{u}_{i2} & \cdots & \boldsymbol{u}_{im}\end{bmatrix}}_{\boldsymbol{U}_i}\begin{bmatrix}\alpha_R^{i1}\\ \alpha_R^{i2}\\ \vdots\\ \alpha_R^{im}\end{bmatrix} \tag{7.30}$$

where α_R^{ij} is an estimate of the achieved pseudo-control (velocity) for aircraft i along the LOS direction $\boldsymbol{u}_{ij}$. Thus, we can solve (7.30) to obtain

$$\begin{bmatrix}\alpha_R^{i1}\\ \alpha_R^{i2}\\ \vdots\\ \alpha_R^{im}\end{bmatrix} = -\boldsymbol{U}_i^{\dagger}\boldsymbol{V}_i \tag{7.31}$$

where $\boldsymbol{U}_i^{\dagger}$ is the left pseudo-inverse of the vector $\boldsymbol{U}_i$. Eq. (7.31) provides the minimum norm solution for the achieved pseudo-control terms $\alpha_R^{ij}, j \neq i$. The corresponding expression for the hedge signal is:

$$\nu_{R,h}^{ij} = \nu_R^{ij} - \alpha_R^{ij} \tag{7.32}$$

The corresponding expression for the modeling error Δ_R^{ij} is given by

$$\Delta_R^{ij} = \dot{R}_{ij} - \alpha_R^{ij} \tag{7.33}$$

C. Obstacle Avoidance Controller

The controller design strategy for static obstacle avoidance is based on a reactive

'steer towards silhouette edge' approach. [*] The idea is to project the shape of nearby obstacles onto the local, body-fixed frame of the vehicle. If this projected shape, adjusted (enlarged) to allow for the size of the vehicle and the required 'clearance' distance, surrounds the origin of the vehicle's body-fixed frame, then some portion of the obstacle is dead ahead. The vehicle must steer away to avoid a collision, and the most efficient direction to turn is toward that portion of the projected shape that is closest to the origin.

To illustrate the concept, it is assumed that the obstacles are contained within bounding spheres (circles in 2 dimensions), and that the centers (X_{obs}, Y_{obs}) and radii (r_{obs}) of the obstacles are known. The goal of this strategy is to keep an imaginary line L_o of length $D_o \geq r_{obs}$, originating at the vehicle's current position and extending in the direction of the velocity vector, from intersecting with any obstacle boundary [113]. The length of this line is typically based upon the vehicle's speed and maneuverability. An obstacle further away than this length D_o is not an immediate threat. The obstacle avoidance strategy considers each obstacle in turn and determines if they intersect with L_o. The obstacle which intersects L_o nearest the aircraft is selected as the "most threatening" and corrective steering action is undertaken to avoid this obstacle. If no obstacle collision is imminent, no steering action is taken. Corrective steering action to avoid an obstacle involves heading change command, and possibly a speed change command too. The heading change command $\Delta\psi_{OA,i}$, '*OA*' stands for obstacle avoidance, is towards the closest projected edge of the obstacle in the local velocity fixed frame as shown in Figure 58. The output of the static obstacle avoidance controller is the commanded velocity vector $\boldsymbol{V}_{OA,i}$.

---

[*] Craig Reynolds, "Not Bumping Into Things," *http://www.red3d.com/cwr/nobump/nobump.html*

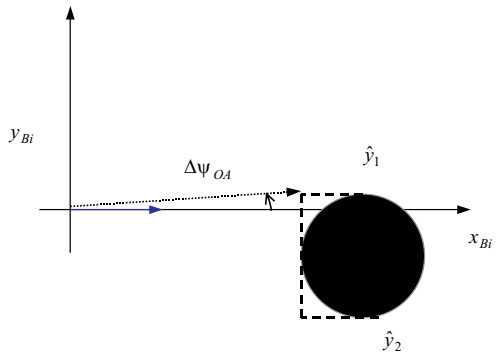

Figure 58. Heading Change Command for Static Obstacle Avoidance

D. Velocity Command for Leaderless Formations

The problem with a leader-follower formation is in the concept of a designated leader. Such a formation lacks robustness to a failure in the leader vehicle. Possibilities of failure in one or more follower vehicles further complicate this problem. So, a coordination scheme is proposed that does not depend on a unique leader, is robust to failures in one or more vehicles and allows easy scaling of the formation.

We remove the assumption of a designated leader for the formation. Each vehicle commands a nominal velocity vector when not tracking any neighboring vehicle. The nominal velocity vector is the same for all vehicles in formation. One way to choose this velocity that is in general same for all the vehicles is to choose a set of waypoints that is common to all the vehicles. The nominal velocity involves heading towards these set of waypoints at a constant known speed. The idea here is that even if one or more aircraft fall out of formation temporarily, due to obstacle avoidance or due to another mission task such as investigating a target of interest, the aircraft can rejoin the formation later and not hold up the other aircraft. The nominal velocity vector $\boldsymbol{V}_{nom,i}$ for the i^{th} aircraft is given as

$$
\begin{aligned}
\boldsymbol{V}_{nom,i} &= V_{nom,i}\left(\cos\psi_{nom,i}\boldsymbol{I} + \sin\psi_{nom,i}\boldsymbol{J}\right) \\
V_{nom,i} &= V_L \\
\psi_{nom,i} &= \text{atan2}\left(y_{WP} - y_i, x_{WP} - x_i\right)
\end{aligned} \tag{7.34}
$$

where (x_{WP}, y_{WP}) represent inertial coordinates of the waypoint under consideration. Once the vehicle comes within a specified distance of one waypoint, it starts heading towards the next waypoint. Each vehicle tracks up to two nearest vehicles depending upon the range to the vehicle. The algorithm for choosing the number of vehicles to track for the i^{th} aircraft is described below.

Let $R_{1,i}(t)$ be the distance to the closest neighboring vehicle and $R_{2,i}(t)$ be the distance to the second closest vehicle. Let $R_{\max} > 0$ be a constant and NV_i the number of vehicles tracked. Then, the logic for determining NV_i is as follows:

$$
\begin{aligned}
&\textit{If} \quad R_{1,i}(t) > R_{\max} \\
&\qquad NV_i = 0 \\
&\textit{Else If} \; R_{2,i}(t) \le R_{\max} \\
&\qquad NV_i = 2 \\
&\textit{Else} \\
&\qquad NV_i = 1 \\
&\textit{End}
\end{aligned} \tag{7.35}
$$

The formation control objective is to regulate range from NV_i number of nearest vehicles to the range command R_{com}. The value for R_{com} is such that $0 < R_{com} < R_{\max}$ and is a constant for all the vehicles in the formation.

Remark 7.2: The constant distance $R_{\max}$ could be related to the maximum distance at which the vision sensing is reasonably effective. For example, in this thesis, we assume that the subtended angle is a measurement from the vision sensing and image processing system. This measurement is inversely proportional to the range to a neighboring aircraft.

It does not make sense to maintain range from a neighboring aircraft that is at such a distance that the subtended angle measurement is very poor.

When the number of nearest neighbors NV_i changes, the control law switches. Switching of the control laws also takes place when a nearest neighbor is replaced. The formation controllers are designed to regulate range from every vehicle in the formation, but actual tracking takes place only with NV_i number of neighbors. This means that some of the formation controllers may not be in control of the aircraft for some period of time. In case the aircraft is only avoiding obstacles, then none of the formation controllers are in control of the aircraft, even if this situation is just temporary. PCH is used to hedge the range reference models in all the formation controllers, to prevent a build up of the reference model tracking error. This prevents large jumps in the velocity command signals to the velocity autopilot (discussed in Section 7.1 *E*) when switching takes place between formation controllers. Switching between the formation controllers itself can cause chattering in the control signals and poor performance. However, the switching is not a problem as long as the rate of switching is significantly smaller than the bandwidth of the autopilot. In this study, the effect of switching is mitigated by low-pass filtering of the speed and heading commands before being input to the velocity autopilot.

Since the number of vehicles tracked may change in time, the commanded velocity vector also changes. Let $\boldsymbol{u}_{i1}$ and $\boldsymbol{u}_{i2}$ denote the unit vectors along the LOS to the two closest vehicles, and $\boldsymbol{V}_{FC,i}$ the commanded velocity vectors for regulating range from one or two closest vehicles. Then, the velocity vector command for the i^{th} aircraft is given as:

$$\begin{aligned} &\text{If} \quad NV_i = 1 \\ &\boldsymbol{V}_{cmd,i} = c_{1,i}\boldsymbol{V}_{OA,i} + \left(1-c_{1,i}\right)\left(\boldsymbol{V}_{nom} - c_{2,i}\left(1-c_{1,i}\right)\left\langle \boldsymbol{V}_{nom} \bullet \boldsymbol{u}_{i1} \right\rangle \boldsymbol{u}_{i1}\right) + c_{2,i}\left(1-c_{1,i}\right)\boldsymbol{V}_{FC,i} \end{aligned} \tag{7.36}$$

$$\text{If} \quad NV_i = 2$$
$$\boldsymbol{V}_{cmd,i} = c_{1,i}\boldsymbol{V}_{OA,i} + \left(1-c_{1,i}\right)\left(\boldsymbol{V}_{nom} - c_{2,i}\left(1-c_{1,i}\right)\left[\left\langle \boldsymbol{V}_{nom} \bullet \boldsymbol{u}_{i1} \right\rangle \boldsymbol{u}_{i1} + \left\langle \boldsymbol{V}_{nom} \bullet \boldsymbol{u}_{i2} \right\rangle \boldsymbol{u}_{i2}\right]\right) \qquad (7.37)$$
$$+ c_{2,i}\left(1-c_{1,i}\right)\boldsymbol{V}_{FC,i}$$

$$\begin{aligned} &\text{If} \quad NV_i = 0 \\ &\boldsymbol{V}_{cmd,i} = c_{1,i}\boldsymbol{V}_{OA,i} + \left(1-c_{1,i}\right)\boldsymbol{V}_{nom} \end{aligned} \qquad (7.38)$$

where $\langle \bullet \rangle$ is the dot product operator, $0 \le c_{2,i} < 1$ is a tuning parameter that indicates the relative priority for formation control with respect to nominal velocity vector tracking, and $c_{1,i}$ $0 \le c_{1,i} \le 1$, is chosen such that obstacle avoidance has higher priority than both nominal velocity command tracking and formation control. One method to choose $c_{1,i}$ is as follows. Let the distance from aircraft i to the most threatening obstacle be given by

$$d_{obs,i} = \sqrt{\left(X_{obs} - x_i\right)^2 + \left(Y_{obs} - y_i\right)^2} - r_{obs} \qquad (7.39)$$

Then, $c_{1,i}$ is automatically chosen using the following logic

$$\begin{aligned} &If \quad d_{obs,i} \le D_o \\ &c_{1,i} = \exp\left(-\frac{d_{obs,i}}{D_o^{'}}\right) \\ &else \\ &c_{1,i} = 0 \\ &end \end{aligned} \qquad (7.40)$$

where $D_o^{'} > 0$ is a scaling factor. Eq. (7.40) states that once the obstacle comes within D_o distance of the aircraft, then the weight $c_{1,i}$ increases exponentially with decreasing distance, and $D_o^{'}$ is a factor that determines the rate at which $c_{1,i}$ increases or decreases.

Eqs. (7.36) and (7.37) are constructed with the objective that the velocity vectors should converge to $\boldsymbol{V}_{nom}$ when the commanded range errors are zero and there are no obstacles to avoid. This can be understood for the case $NV_i = 1$ by noting that

$\langle \boldsymbol{V}_{nom} \bullet \boldsymbol{u}_{i1} \rangle \boldsymbol{u}_{i1}$ is the projection of $\boldsymbol{V}_{nom}$ along the unit vector direction $\boldsymbol{u}_{i1}$, and $\boldsymbol{V}_{FC,i}$ is an estimate of the velocity of the closest neighbor along $\boldsymbol{u}_{i1}$ when the commanded range errors are zero. So, the desired equilibrium configuration for the formation is not reached unless $\langle \boldsymbol{V}_{nom} \bullet \boldsymbol{u}_{i1} \rangle \boldsymbol{u}_{i1} = \boldsymbol{V}_{FC,i} \Rightarrow \boldsymbol{V}_{cmd,i} = \boldsymbol{V}_{nom}$. The same logic applies if $NV_i = 2$.

E. Velocity Autopilot

The velocity vector command $\boldsymbol{V}_{cmd,i}$ is resolved into a speed command $V_{cmd,i}$ and a heading command $\psi_{cmd,i}$ that are input to an inner-loop controller. The inner-loop controller generates acceleration commands that depend on the speed and heading commands.

$$\begin{aligned} a_{i1,cmd} &= \frac{1}{\tau_\psi}\left(\psi_{c,i} - \psi_i\right)V_i \\ a_{i2,cmd} &= \frac{1}{\tau_V}\left(V_{c,i} - V_i\right) + k_{i1}V_i^2 + \frac{k_{i2}}{V_i^2}\left(a_{i1,cmd}^2 + 1\right) \end{aligned} \tag{7.41}$$

where $\tau_V > 0$, $\tau_\psi > 0$ are the time constants of the inner-loop controller, $\psi_{c,i}$ and $V_{c,i}$ are obtained by low-pass filtering of the heading command $\psi_{cmd,i}$ and magnitude limited speed command $sat\left[V_{cmd,i}\right]$ respectively, where $sat(\cdot)$ is the linear saturation operator. $V_{cmd,i}$ is limited to prevent saturating the actuators and to prevent speed commands lower than the stall speed. The acceleration commands are limited in accordance with Eqs. (7.14) and (7.16).

7.2 Target State Estimator Design

The following assumptions are made regarding the vision sensing and image processing:

1) The field-of-view (FOV) is 360^0.

2) The measurements from the vision sensor are the noisy subtended angle α_m and noisy LOS angle λ_m, where the noise is assumed to be zero-mean white noise. Since all aircraft are identical with known wing-span, α_m in effect gives a noisy range measurement R_m which is fairly accurate at close ranges.

The target tracking model considered for the design of the target state estimator is as follows:

$$\frac{d}{dt}\begin{bmatrix} V_{T_X} \\ R_X \\ V_{T_Y} \\ R_Y \end{bmatrix} = \underbrace{\begin{bmatrix} 0 & 0 & 0 & 0 \\ 1 & 0 & 0 & 0 \\ 0 & 0 & 0 & 0 \\ 0 & 0 & 1 & 0 \end{bmatrix}}_{A}\begin{bmatrix} V_{T_X} \\ R_X \\ V_{T_Y} \\ R_Y \end{bmatrix} + \underbrace{\begin{bmatrix} 1 & 0 \\ 0 & 0 \\ 0 & 1 \\ 0 & 0 \end{bmatrix}}_{B}\begin{bmatrix} a_{T_X} \\ a_{T_Y} \end{bmatrix} + \begin{bmatrix} 0 & 0 \\ 1 & 0 \\ 0 & 0 \\ 0 & 1 \end{bmatrix}\begin{bmatrix} -V_{F_X} \\ -V_{F_Y} \end{bmatrix}$$

$$\underbrace{\begin{bmatrix} y_1 \\ y_2 \end{bmatrix}}_{Y} = \underbrace{\begin{bmatrix} 0 & 1 & 0 & 0 \\ 0 & 0 & 0 & 1 \end{bmatrix}}_{C}\underbrace{\begin{bmatrix} V_{T_X} \\ R_X \\ V_{T_Y} \\ R_Y \end{bmatrix}}_{X} + \begin{bmatrix} \nu_X \\ \nu_Y \end{bmatrix} \tag{7.42}$$

where V_{T_X}, V_{T_Y} are the X, Y components of the unknown target velocity along the inertial axes, V_{F_X}, V_{F_Y} are the corresponding components of the follower velocity, R_X, R_Y are the X, Y components of the LOS range vector, a_{T_X}, a_{T_Y} are the X,Y components of the unknown target acceleration, and ν_X, ν_Y are state-dependent measurement noise terms. In (7.42), the target refers to any neighboring aircraft being tracked and follower refers to the tracking aircraft. The measurements y_1, y_2 in (7.42) are obtained as follows:

$$\begin{aligned} R_m &= \frac{b}{2\tan\left(\frac{\alpha_m}{2}\right)} \\ y_1 &= R_{X_m} = R_m \cos\left(\lambda_m\right) \\ y_2 &= R_{Y_m} = R_m \sin\left(\lambda_m\right) \end{aligned} \tag{7.43}$$

where the subscript *m* indicates the variables are measurements, and b is the target size (wing-span length), assumed constant and known for this simulation.

The design of the Kalman filter augmented with the adaptive NN is dealt in detail in Chapter 3 and is not discussed further here. In the design of the Kalman filter the target acceleration is modeled as zero-mean white process noise. The states $\hat{V}_{T_X}, \hat{V}_{T_Y}$ of the Kalman filter and $\hat{\lambda} = \text{atan2}\left(\hat{R}_Y, \hat{R}_X\right)$ are used in the construction of the $\nu_{R,ad}$ term in (7.24).

7.3 Simulation Results

The first set of results with the leaderless formation control scheme is shown for a group of 4 aircraft with identical nominal velocity vectors $\boldsymbol{V}_{nom}$ which is a sinusoidal heading profile at constant speed

$$\begin{aligned} V_{nom} &= 1.5 \\ \psi_{nom} &= \sin\left(t/5\right) \end{aligned} \tag{7.44}$$

The frequency of the sinusoidal maneuver in (7.44) is chosen such that it corresponds to 0.3 g acceleration maneuver. The value of $R_{com} = 0.5$ is approximately 2 wing-span lengths and $R_{\max} = 1.5$. The initial positions of the aircraft were chosen such that each aircraft could track all the neighboring aircraft. All the results shown do not include the effect of adaptation in the estimator design. The approximation of the modeling errors Δ_R^{ij} is quite good using just the nominal Kalman filter design. Figure 59 shows the trajectory plot for the formation. Note that the x-axis is scaled up in the plot below. The trajectories are marked with symbols (asterisks, circles, triangles, etc) every 2.5 seconds.

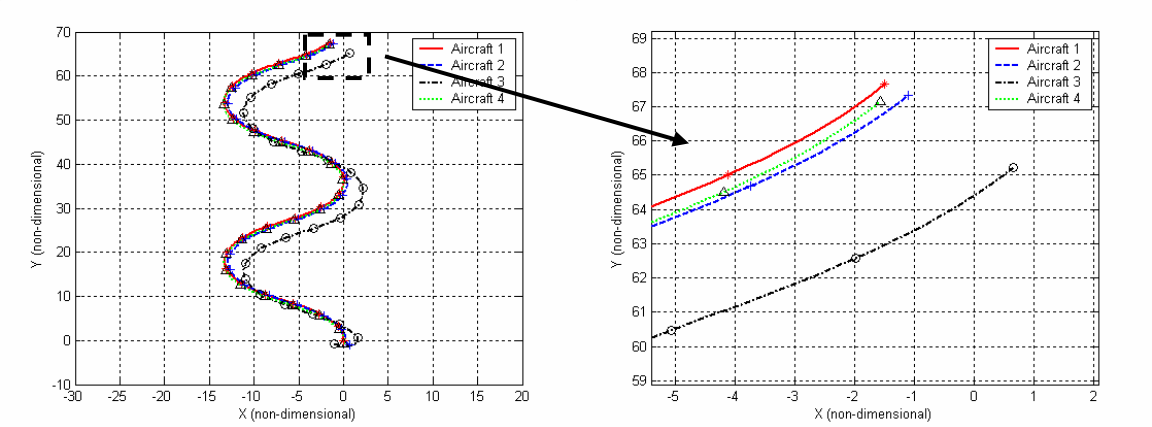

Figure 59. Leaderless Formation Trajectory, Sinusoidal Velocity Profile

Figure 60 shows the range histories for all aircraft in formation. The plot shows convergence to the commanded range R_{com} of the range from the 2 closest neighbors for Aircraft 1, 2 and 4. The initial heading of Aircraft 3 is such that its initial motion takes it away from the other aircraft in formation. Once the range from the other aircraft exceeds $R_{\max}$, Aircraft 3 does not join the formation ever.

Figure 61 shows the plot for selected inversion errors Δ_R^{ij} plotted against the corresponding estimates $\nu_{R,ad}^{ij}$. The plot shows very good tracking of the Δ_R^{ij}.

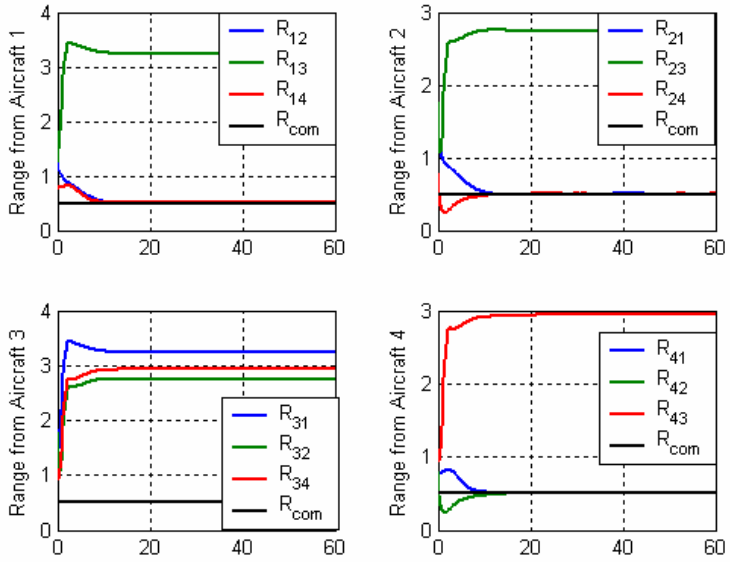

Figure 60. Range Histories (non-dimensional), Sinusoidal Velocity Profile

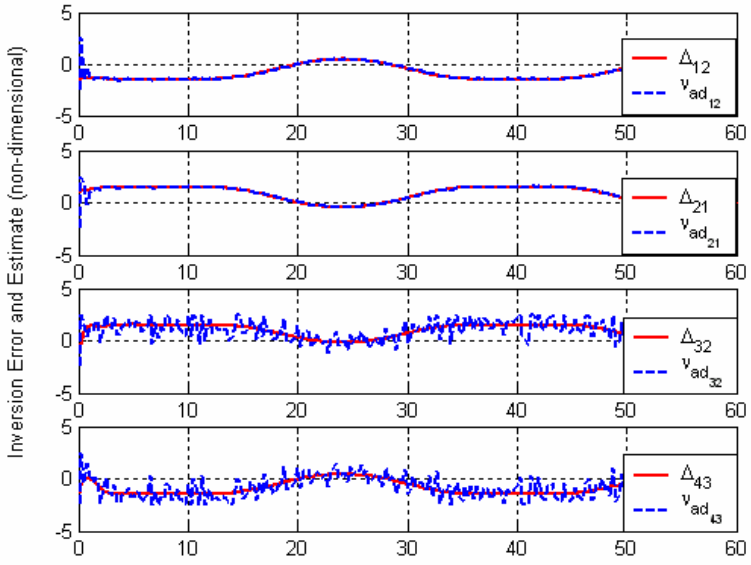

Figure 61. Inversion Error and Corresponding Estimates (non-dimensional), Sinusoidal Velocity Profile

The next set of results are shown for the nominal circular trajectory profile

$$V_{nom} = 1.5$$
$$\psi_{nom} = \int \dot{\psi}_{nom}\, dt,\ \dot{\psi}_{nom} = 5 \text{ deg/s} \tag{7.45}$$

Figure 62 shows the trajectory plot for the formation and Figure 63 shows the range histories.

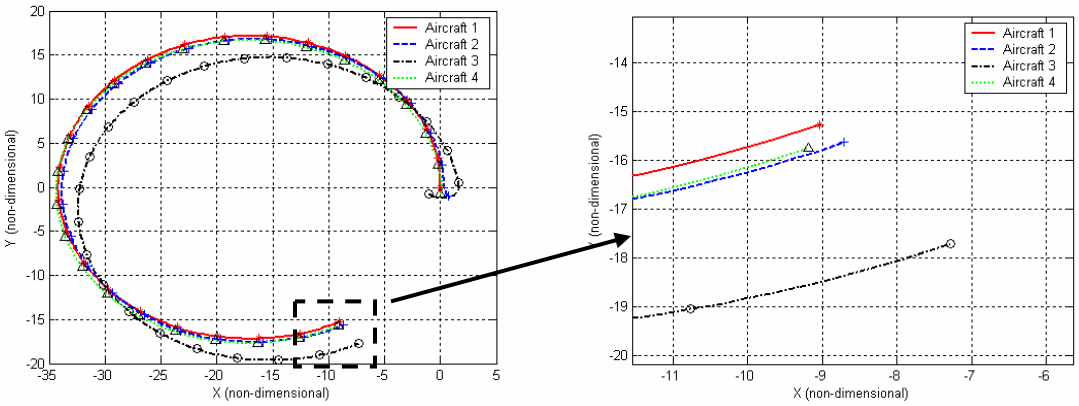

Figure 62. Leaderless Formation Trajectory, Circular Trajectory Profile

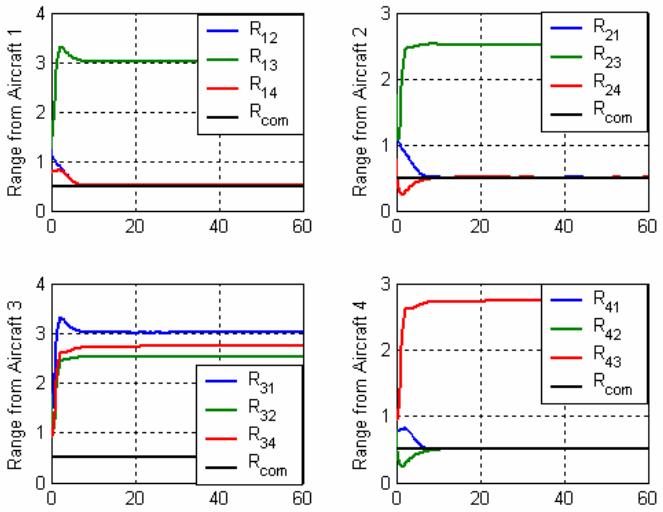

Figure 63. Range Histories (non-dimensional), Circular Trajectory Profile

Next we consider a group of 5 aircraft tracking a sequence of waypoints in the counter-clockwise direction. Waypoints are marked in the plot by red crosses. Figure 64 shows that the formation is achieved and maintained at places where there are no obstacles. The formation is also seen to split to go around an obstacle and later rejoin. Figure 65 shows the range between all pairs of aircraft in the formation. It can be concluded that the formation has again split into groups by noting that only some of the ranges go towards the commanded value R_{com}. Aircraft 3 again splits away from the rest of the aircraft.

The large spike seen between 90-100 seconds involving the range variables R_{14}, R_{24}, R_{34} and R_{45} occurs when Aircraft 4 separates from the rest of the formation at the last obstacle the formation encounters. Figure 66 shows the number of vehicles being tracked by every vehicle during the maneuver. The number of neighboring vehicles tracked is seen to change in time.

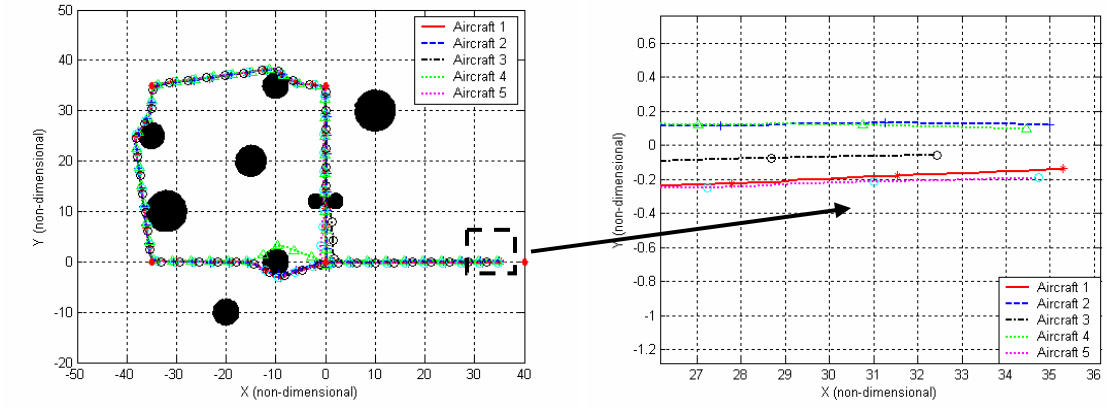

Figure 64. Leaderless Formation Trajectory, Waypoint Tracking with Obstacle Avoidance

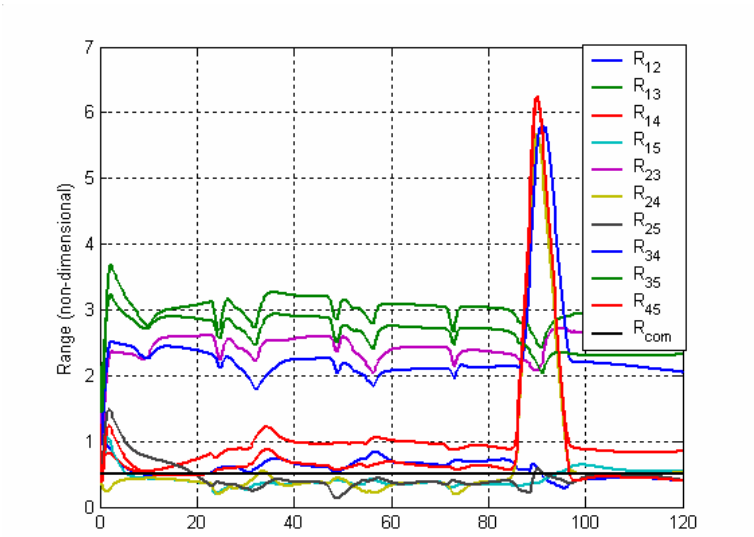

Figure 65. Range Histories (non-dimensional), Waypoint Tracking with Obstacle Avoidance

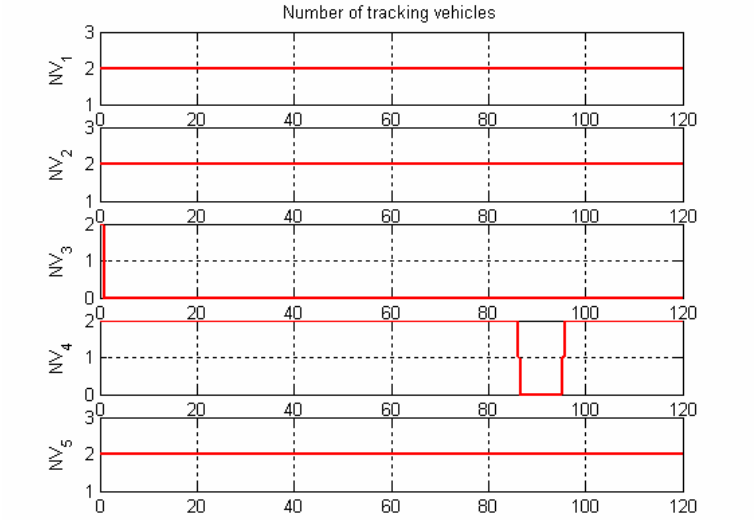

Figure 66. Number of Neighbor Vehicles (NV_i) Tracked, Waypoint Tracking with Obstacle Avoidance

7.4 Conclusions

We have formulated a decentralized adaptive guidance strategy that enables safe and coordinated motion of a group of unmanned aerial vehicles in an environment with obstacles. Little to no communication is assumed between the aircraft in formation. Passive vision sensors with 360^0 field-of-view are assumed to be onboard each aircraft to track neighboring aircraft and detect and avoid obstacles. We have implemented a leaderless formation control scheme, which is proposed as a way of dealing with the robustness issues of a leader-follower formation control scheme. Simulation results show that the aircraft in formation can track the desired nominal trajectories while simultaneously maintaining desired range from up to two nearest neighbors and avoiding obstacles.

CHAPTER 8

THESIS CONTRIBUTIONS, CONCLUDING REMARKS AND RECOMMENDED FUTURE RESEARCH

8.1 Contributions and Conclusions

This thesis considered the design of the estimation, guidance and flight control systems for application in vision-based target tracking and formation control problems. The objective was for a follower Unmanned Aerial Vehicle (UAV) to track a maneuvering leader UAV using a passive vision sensor and maintain very small commanded ranges from the leader. The leader is a non-cooperating (non-communicating) aircraft flying smooth, waypoint tracking trajectories in 3D space. The commanded ranges are of the order of two wing-span lengths of the leader aircraft. It is assumed that the vision sensor is an onboard monocular camera fixed to the body of the follower aircraft with optical axis coincident with the x-body axis. It is also assumed that there exist onboard real-time image processing algorithms that process the raw pixel measurements obtained by the vision sensor and derive measurements of the relative line-of-sight (LOS) angles and the maximum angle subtended by the leader aircraft on the image plane. These measurements are used to drive the estimation process that estimates the leader position, velocity and acceleration in inertial coordinates.

The thesis also considered an approach to multiple-aircraft formation control by assuming that there is little to no communication between the aircraft. The objective is for each aircraft in the formation to track range from up to two nearest vehicles while simultaneously tracking a nominal trajectory common to all and avoiding static obstacles. It is assumed that the formation is constrained to lie in the horizontal plane and that all aircraft in formation are identical. It is also assumed that the vision sensor onboard the

aircraft gives measurements of subtended and LOS angles to a neighboring aircraft corrupted by additive, zero-mean white noise. The field-of-view of the vision sensor is assumed to be 360^0.

The contributions and conclusions of the thesis are summarized as follows.

1. Composite Adaptation Approach to State Estimation

In Chapter 3 of this thesis, a composite adaptation approach to the partial state estimation of a class of nonlinear systems with unmodeled dynamics is presented. The state estimator is a linear, time-varying Kalman filter augmented with an adaptive neural network (NN). The key benefit of the composite adaptation approach over a conventional approach to adaptive state estimation [63] is faster and more accurate approximation of the modeling errors that degrade the accuracy of the estimation process. The modeling errors are nonlinear continuous functions of the states of both the modeled and unmodeled dynamics. This benefit of the composite adaptation approach is particularly useful in target-tracking type applications where the target acceleration is unknown. The main problem in target-tracking applications is the lag in the estimation of the target acceleration which leads to lags in the estimates of target position and velocity. These estimates are used in the implementation of the guidance and flight control laws. The smaller the lag in estimation, the better is the overall performance of the flight control system. Simulation results in this thesis show that with the composite adaptation approach, target acceleration is estimated faster and with more accuracy than with the conventional approach.

Another benefit of the adaptive approach to state estimation is the limited reliance on elaborate target maneuver models. Most conventional approaches in literature assume that the true target behavior can be adequately captured using a model or sets of models for target maneuvers. These include both probabilistic and deterministic models and range from the very simple, e.g., white noise process models, to the very sophisticated

and complex, e.g., the multiple-model approaches. While the simple model based approaches can suffer from accuracy problems when the actual target maneuver does not comply with the target model, the multiple-model type approaches may require extensive computational resources and may not be real-time implementable onboard small UAV platforms, which are the focus of this thesis. Augmenting a time-varying Kalman filter based on a simple nominal model of the target behavior with an adaptive NN is thus a complimentary design approach that is more accurate and also real-time implementable. Philosophically, one can think of the NN as providing a universal model for the target behavior, and thus best employed with a minimal complexity target model such as the model employed in this thesis.

The composite adaptation approach has been validated in both open- and closed-loop simulations in a 6 DOF leader-follower formation configuration. The adaptive estimation algorithms developed using the composite adaptation approach have been integrated with image processing algorithms in the GUST real-time simulation software [108] and validated in software-in-the-loop simulations.

2. Adaptive Integrated Guidance and Control Design for LOS Formation Flight

In Chapter 5 of the thesis, an adaptive integrated guidance and control (IGC) design for LOS formation flight using a combination of output feedback inversion and backstepping techniques is presented. It is assumed that the true values of range, LOS angles, and their rates are available for feedback. NN based online adaptation is used to compensate for modeling errors in the design process, that include, uncertainties due to unknown leader aircraft acceleration, and the modeling error due to parametric uncertainties in the aircraft aerodynamic derivatives. One key conclusion is that, when compared to an adaptive time-scale separated guidance and control (TSSGC) design, the adaptive IGC design offers an explicit advantage of achieving a higher bandwidth design for the combined guidance and flight control dynamics. This advantage of the IGC design

translates into better transient and steady-state range tracking performance as seen in the simulation results in this thesis. The bandwidths of the LOS rate command reference models also have significant effect on the range tracking performance.

A second conclusion is that adaptation in the integrated design of guidance and flight control plays a critical role in this application. It is highly unlikely that regulation at a distance of two wing-span lengths is possible for a non-cooperating maneuvering leader without adaptation. A final conclusion is that using feedback inversion alone in the design of the IGC law results in a deficiency in maintaining turn coordination. This deficiency is overcome by employing a backstepping approach for the azimuth portion of the design process. Attempting to address the full 6DOF problem using backstepping alone leads to a cumbersome design, whereas combining feedback inversion with backstepping appears leads to a complimentary design approach.

The adaptive IGC law has been validated in nonlinear 6 DOF simulations in a leader-follower formation configuration.

3. Integrated Adaptive Estimation and Adaptive Control Design

In Chapter 6, a method to integrate adaptive estimation and adaptive control designs for a class of nonlinear systems is presented. The method is based on Lyapunov-like stability analysis of all the errors in the integrated closed-loop system. The developed approach provides the theoretical foundation to integrate the adaptive estimator solution in Chapter 3 with the adaptive guidance and control solutions presented in Chapters 4 and 5 for enabling vision-based formation flight. One conclusion is that adaptation in both estimation and guidance and control is critical to the stability and performance of the range tracking performance. A second conclusion is that when comparing between the integrated estimation, guidance and control designs, the design in which the guidance and control solution is also integrated results in superior range tracking performance

compared to the design in which the guidance and control solution is designed by assuming time-scale separation.

The final conclusion is regarding the effect of the update rates of the image processing relative to that of the guidance and control designs. Below a critical limit for the image measurements update rate, instability occurs in the range tracking performance. For image measurement update rates larger than this critical value but smaller than the update rates of the estimation, guidance and control designs, there is marginal degradation in the range tracking and estimation performance. This implies that if the image measurements update rate is significantly small relative to the estimation, guidance and control update rate, the image processing dynamics have to be considered in the overall design process.

The integrated adaptive estimation and adaptive guidance and control designs have been validated in nonlinear 6 DOF simulations in a leader-follower formation configuration.

4. Acceleration Command Adaptive Guidance Design for LOS Formation Flight

In Chapter 4, an adaptive guidance law is designed for a follower aircraft maintaining range from a maneuvering leader aircraft using the theory for MIMO Adaptive Output Feedback Control [96]. The guidance law assumes that the true values of range, LOS angles, and their rates are available for feedback. NN based online adaptation is included in the guidance law design to compensate for the unknown leader aircraft maneuvers and neglected LOS kinematics. The guidance law is combined with an adaptive acceleration and bank angle command autopilot using a time-scale separation assumption.

The adaptive guidance design has the practical advantage of being simpler to analyze and implement in a situation where there is an existing acceleration autopilot.

The adaptive TSSGC design has been validated in nonlinear 6 DOF simulations in a leader-follower formation configuration.

5. Approach to Multiple-Aircraft Formation Control with Obstacle Avoidance

In Chapter 7, a decentralized guidance strategy is presented that enables safe and coordinated motion of a group of unmanned aerial vehicles in an environment with obstacles. Little to no communication is assumed between the aircraft in formation. Passive vision sensors with 360^0 field-of-view are assumed to be onboard each aircraft to track neighboring aircraft and detect and avoid obstacles. A leaderless formation control scheme is implemented to overcome some of the robustness issues associated with a leader-follower formation control scheme. Simulation results show that the aircraft in formation can track desired nominal trajectories while simultaneously maintaining desired range from up to two nearest neighbors and avoiding obstacles.

8.2 Recommended Future Research

1. Modeling of the Image Processing

The thesis assumed the use of real-time image processing algorithms and completely ignored the complexities and the dynamics of these algorithms. This could potentially have a destabilizing effect when the image processing algorithms are integrated in an *ad-hoc* fashion with the estimation, guidance and flight control algorithms. Since the image processing algorithms consist of iterative processes converging to some desired solutions, there is always a delay between the instant an image feature is captured and the instant in which useful measurements from that feature are derived for use in the target state estimation process. Secondly, there could be instances in which the image processing algorithms do not converge to any solution, and as a result there are no measurements available for some time. Finally, the noise

associated with the measurements from the image processing is non-Gaussian in nature, contrary to the assumptions made in the thesis that the measurements are corrupted with additive zero-mean white noise. One area of research is to develop state-space models of the dynamics associated with the image processing algorithms. Then these models could be taken into account when designing the estimation, guidance and flight control algorithms.

Another area of research could be to integrate the image processing and estimation algorithms, or even integrate the image processing and control algorithms. In other words, one could think of introducing feedback loops between the image processing and the estimation and control algorithms. An example of the latter approach is to control the camera motion such that the target aircraft is always in the center of the image plane. This research area is termed as "visual servoing" and is well known in the ground robotics literature [31, 32]. The idea of controlling the motion of the camera has a practical motivation in that the field-of-view (FOV) of a single camera is limited and it is possible that the target aircraft can slip out of the FOV during sharp maneuvers. So, controlling the motion of the camera offers additional control authority and increases robustness of the overall design to the disappearance of the target aircraft.

One of the assumptions in the thesis is that the apparent target size in the camera image plane is constant. However, the apparent size of the target depends on the relative orientation of the target with respect to the follower aircraft. So, additional modeling of the apparent size of the target aircraft in the image plane needs to be considered for more accurate target tracking.

2. Improved Adaptive Control and Estimation Algorithms

The benefits of a composite adaptation approach in state feedback adaptive control problems have been known for quite some time [66]-[68]. In [66], the authors interpreted the effect of an additional error signal in training the adaptive element as

having a "low-pass filtering" effect on the adaptation process. Hence the composite adaptation approach was found to be more robust to unmodeled dynamics and high frequency noise. Adaptation gains with the composite adaptation approach could also be set higher than with the conventional adaptation approach for the same reason, leading to faster rates of convergence of the tracking errors. The thesis also provided an example in which the composite adaptation approach could give dramatically improved results in the domain of adaptive state estimation.

One area of research would be to look into a composite adaptation approach for output feedback adaptive control problems. A study could also be made of other approaches to improving adaptation performance that include: i) simultaneous training of the adaptive element with both instantaneously available and stored information [114], (ii) L1 Adaptive Control theory [115] which allows incorporation of a low-pass filter within the feedback loop and consequently allows larger adaptation gains, and (iii) localized adaptive laws that address the issue of global forgetting that occurs with the use of standard leakage terms like the sigma-mod parameter [116]. Any promising approaches to improving adaptation performance could then be incorporated in the adaptive guidance and estimation algorithms presented in the thesis.

The stability proofs in this thesis established uniform ultimate boundedness of the system errors without providing means for achieving arbitrarily small ultimate bounds. Addressing this problem could be another area of theoretical research.

3. Extension to Vision-based Multi-Aircraft Formation Control

The thesis presented a conceptual approach to multiple-aircraft formation control. This research can be extended in several directions. One important area would be to develop a method of theoretical analysis of the decentralized multiple-aircraft coordination strategy presented in the thesis. Other extensions could be for practical implementation purposes. The assumptions of 360^0 field-of-view requirements of the

vision sensor, constraining the formations to be in the 2D horizontal plane, simplistic autopilot modeling, and circle-shaped static obstacles whose size is known, should all be relaxed. Image processing complexities from the point-of-view of tracking multiple targets in cluttered environments should also be considered in the application of any approach to multiple-aircraft formation control.

4. Integration with Image Processing Algorithms and Flight Test Validation

Immediate future research recommended is the integration of the adaptive estimation, guidance and control algorithms presented in this thesis with image processing algorithms in the GUST real-time simulation software [108] followed by flight test validation of the overall design.

APPENDIX A

PROOF OF THEOREM 3.1

Equation Chapter 1 Section 1

Proof: Consider the Lyapunov candidate function $V(\varsigma) = V\left(\tilde{\boldsymbol{x}}, \tilde{\boldsymbol{W}}\right)$ defined in Eq. (3.42). Differentiating $V\left(\tilde{\boldsymbol{x}}, \tilde{\boldsymbol{W}}\right)$:

$$\dot{V}\left(\tilde{\boldsymbol{x}}, \tilde{\boldsymbol{W}}\right) = \dot{\tilde{\boldsymbol{x}}}^T P^{-1}(t)\tilde{\boldsymbol{x}} + \tilde{\boldsymbol{x}}^T P^{-1}(t)\dot{\tilde{\boldsymbol{x}}} + \tilde{\boldsymbol{x}}^T \dot{P}^{-1}(t)\tilde{\boldsymbol{x}} + 2\tilde{\boldsymbol{W}}^T \Gamma_W^{-1}\dot{\tilde{\boldsymbol{W}}} \tag{A.1}$$

Substituting Eqs. (3.35), (3.36) and (3.37) in Eq. (A.1) and simplifying

$$\begin{aligned}\dot{V}\left(\tilde{\boldsymbol{x}}, \tilde{\boldsymbol{W}}\right) = &-\tilde{\boldsymbol{x}}^T \tilde{Q}(t)\tilde{\boldsymbol{x}} + 2\tilde{\boldsymbol{x}}^T P^{-1}(t) B\tilde{\boldsymbol{W}}^T \boldsymbol{\sigma}(\bar{\boldsymbol{\mu}}) + 2\tilde{\boldsymbol{x}}^T P^{-1}(t) B\varepsilon(\bar{\boldsymbol{\mu}}) \\ &+ 2\tilde{\boldsymbol{W}}^T \left[-\boldsymbol{\sigma}(\bar{\boldsymbol{\mu}}) C\tilde{\boldsymbol{x}} - \boldsymbol{q}^T(t, t_0) e_1 \right] + 2\lambda_W \tilde{\boldsymbol{W}}^T \boldsymbol{W} - 2\lambda_W \tilde{\boldsymbol{W}}^T \tilde{\boldsymbol{W}}\end{aligned} \tag{A.2}$$

$\dot{V}$ in (A.2) can be upper-bounded using (3.38) and (3.2) as shown below where the arguments of $\dot{V}$ are dropped for convenience:

$$\begin{aligned}\dot{V} \le &-\tilde{\boldsymbol{x}}^T P^{-1}(t) Q P^{-1}(t)\tilde{\boldsymbol{x}} + 2\tilde{\boldsymbol{x}}^T P^{-1}(t) B\tilde{\boldsymbol{W}}^T \boldsymbol{\sigma}(\bar{\boldsymbol{\mu}}) + 2\|\tilde{\boldsymbol{x}}\| \left\| P^{-1}(t) B \right\| \varepsilon^* \\ &-2\tilde{\boldsymbol{x}}^T C^T \tilde{\boldsymbol{W}}^T \boldsymbol{\sigma}(\bar{\boldsymbol{\mu}}) - 2\tilde{\boldsymbol{W}}^T \boldsymbol{q}^T(t, t_0) e_1 + 2\lambda_W \left\| \tilde{\boldsymbol{W}} \right\| W^* - 2\lambda_W \left\| \tilde{\boldsymbol{W}} \right\|^2\end{aligned}$$

Combining terms and expanding the expression for e_1,

$$\begin{aligned}\dot{V} \le &-\tilde{\boldsymbol{x}}^T P^{-1}(t) Q P^{-1}(t)\tilde{\boldsymbol{x}} - 2\lambda_W \left\| \tilde{\boldsymbol{W}} \right\|^2 + 2\tilde{\boldsymbol{x}}^T \left[P^{-1}(t) B - C^T \right] \tilde{\boldsymbol{W}}^T \boldsymbol{\sigma}(\bar{\boldsymbol{\mu}}) \\ &+ 2\|\tilde{\boldsymbol{x}}\| \left\| P^{-1}(t) B \right\| \varepsilon^* - \underbrace{2\tilde{\boldsymbol{W}}^T \boldsymbol{q}^T(t, t_0) \boldsymbol{q}(t, t_0) \tilde{\boldsymbol{W}}}_{\ge 0} - 2\tilde{\boldsymbol{W}}^T \boldsymbol{q}^T(t, t_0) C\Phi(t, t_0)\tilde{\boldsymbol{x}}_1(t_0) \\ &- 2\tilde{\boldsymbol{W}}^T \boldsymbol{q}^T(t, t_0)\varepsilon_f(t, t_0) + 2\lambda_W \left\| \tilde{\boldsymbol{W}} \right\| W^*\end{aligned} \tag{A.3}$$

Using the fact that $\left\| \boldsymbol{\sigma}(\bar{\boldsymbol{\mu}}) \right\| \le \sqrt{N}$, applying Eq. (3.48) and completing the squares on the last term in (A.3), we have,

$$\dot{V} \le -\frac{\lambda_{\min}(Q)}{\rho_2^2}\|\tilde{\boldsymbol{x}}\|^2 - 2\lambda_W\left\|\tilde{\boldsymbol{W}}\right\|^2 + 2m_2\|\tilde{\boldsymbol{x}}\|\left\|\tilde{\boldsymbol{W}}\right\| + 2m_1\|\tilde{\boldsymbol{x}}\| \\ + 2\left\|\tilde{\boldsymbol{W}}\right\| m_3\|C\|k\left\|\tilde{\boldsymbol{x}}_1(t_0)\right\| e^{-\lambda(t-t_0)} + 2\left\|\tilde{\boldsymbol{W}}\right\| m_3\varepsilon_f^* + \lambda_W\left\|\tilde{\boldsymbol{W}}\right\|^2 + \lambda_W W^{*2} \tag{A.4}$$

Completing the squares in the above equation, we have

$$\dot{V} \le -\|\tilde{\boldsymbol{x}}\|^2\left(\frac{\lambda_{\min}(Q)}{\rho_2^2} - 2\right) - \left\|\tilde{\boldsymbol{W}}\right\|^2\left(\lambda_W - m_2^2 - 2\right) \\ + m_1^2 + \left(m_4^2 + m_5^2\right) + \lambda_W W^{*2} \tag{A.5}$$

Thus either of the following conditions

$$\|\tilde{\boldsymbol{x}}\| > \sqrt{\frac{m_1^2 + \left(m_4^2 + m_5^2\right) + \lambda_W W^{*2}}{\frac{\lambda_{\min}(Q)}{\rho_2^2} - 2}} \tag{A.6}$$

$$\left\|\tilde{\boldsymbol{W}}\right\| > \sqrt{\frac{m_1^2 + \left(m_4^2 + m_5^2\right) + \lambda_W W^{*2}}{\lambda_W - \left(m_2^2 + 2\right)}} \tag{A.7}$$

will guarantee that $\dot{V}\left(\tilde{\boldsymbol{x}}, \tilde{\boldsymbol{W}}\right) < 0$ outside the compact set

$$B_\gamma = \left\{\varsigma \in B_M \mid \|\varsigma\| \le \gamma\right\} \tag{A.8}$$

Note that $B_\gamma \subset B_M$ from (3.46). Let β be the maximum value of the Lyapunov function V on the boundary of B_γ

$$\beta \triangleq \max_{\|\varsigma\|=\gamma} V(\varsigma) \tag{A.9}$$

Introduce the set

$$\Omega_\beta = \left\{\varsigma \mid V(\varsigma) \le \beta\right\} \tag{A.10}$$

Eq. (3.46) ensures that $\Omega_\beta \subset \Omega_\alpha$ and thus ultimate boundedness of ς with ultimate bound equal to $\kappa_1^{-1}\left(\kappa_2\left(\gamma\right)\right)$.

□

APPENDIX B

ADAPTIVE AUTOPILOT DESIGN

Design of the adaptive controllers for tracking the normal acceleration command ${}_B f_{z_{com}}$, lateral acceleration command ${}_B f_{y_{com}} = 0$, and the bank angle command Φ_{com} are presented here. The subscript B indicating the acceleration variables are defined in the body-fixed frame is dropped henceforth.

Equation Chapter 3 Section 1

A. Adaptive Normal Acceleration (f_z) Control

The control design is based on the JDAM approach to adaptive autopilot design in [111]. This approach uses an inverting controller augmented by the output of an adaptive NN for pitch rate q control in the inner-loop, and a proportional-integral (PI) controller for f_z control in the outer-loop (Figure 67). The inverting controller in the inner-loop is based on the short period approximation of the longitudinal aircraft dynamics,

$$\begin{bmatrix} \dot{\alpha} \\ \dot{q} \end{bmatrix} = \begin{bmatrix} \hat{Z}_\alpha / u_0 & 1 \\ \hat{M}_\alpha & \hat{M}_q \end{bmatrix} \begin{bmatrix} \alpha \\ q \end{bmatrix} + \begin{bmatrix} \hat{Z}_\alpha / u_0 \\ \hat{M}_{\delta e} \end{bmatrix} \delta e \tag{B.1}$$

where u_0 is the equilibrium flight speed and "^" represents an estimated quantity in the model. The true q dynamics are given by

$$\dot{q} = f_q(x, \delta e) \tag{B.2}$$

where x is the state of the plant.

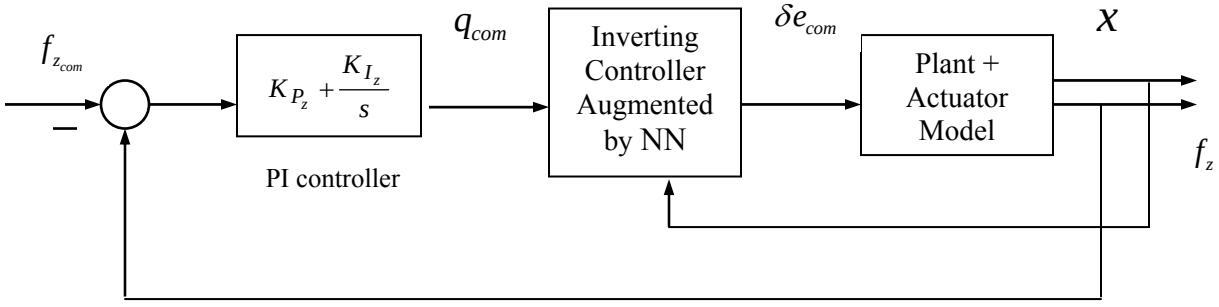

Figure 67. Adaptive Normal Acceleration Controller

Using the linear approximation to the q dynamics in (B.1), the true q dynamics can be represented as

$$\dot{q} = \hat{M}_\alpha \alpha + \hat{M}_q q + \hat{M}_\delta \delta e + \Delta_q(x, \delta e) = \nu_q + \Delta_q(x, \delta e) \tag{B.3}$$

where $\nu_q = \hat{M}_\alpha \alpha + \hat{M}_q q + \hat{M}_\delta \delta e$, is the pseudo-control signal, and $\Delta_q(x, \delta e)$ $= f_q(x, \delta e) - \nu_q$ is the modeling error. Then ν_q can be solved for the actuator command input δe_{com} as

$$\delta e_{com} = \frac{1}{\hat{M}_\delta}\left(\nu_q - \hat{M}_\alpha \alpha - \hat{M}_q q\right) \tag{B.4}$$

The pseudo-control ν_q is constructed as:

$$\nu_q = \nu_{crm,q} + K_{p,q}(q_c - q) - \nu_{ad,q} \tag{B.5}$$

$$\nu_{crm,q} = \frac{1}{\tau_q}(q_{com} - q_c) \tag{B.6}$$

where q_c is the reference pitch-rate command, obtained by filtering the raw pitch-rate command q_{com} through a first-order reference model with time constant τ_q, $\nu_{crm,q}$ is a feed-forward signal from the reference model, $K_{p,q} > 0$ is a proportional control gain,

and $\nu_{ad,q}$ is the output of an adaptive single hidden layer (SHL) NN. The NN output and update law is given in Section D below.

The reference model is hedged to prevent the adaptive law from adapting to the nonlinear actuator characteristics [89]:

$$\begin{aligned}\nu_{h,q} &= \nu_q - \hat{\nu}_q = \left[\hat{M}_\alpha \alpha + \hat{M}_q q + \hat{M}_\delta \delta e_{com}\right] - \left[\hat{M}_\alpha \alpha + \hat{M}_q q + \hat{M}_\delta \hat{\delta} e\right] \\ &= \hat{M}_\delta \left(\delta_{e_{com}} - \hat{\delta}_e\right)\end{aligned} \tag{B.7}$$

$$\dot{q}_c = \nu_{crm,q} - \nu_{h,q} \tag{B.8}$$

where $\hat{\delta} e$ is an estimate of the elevator deflection obtained by means of an actuator model and $\nu_{h,q}$ is the Pseudo-Control Hedge (PCH) signal. Figure 68 shows a block diagram representation of the adaptive pitch-rate control system.

The assumption of perfect inner-loop tracking of q_c enables the analysis and design of the PI controller in the outer-loop. Consider the following short-period approximation of the longitudinal dynamics with normal acceleration at the c.g. as the measured output:

$$\begin{bmatrix}\dot{\alpha} \\ \dot{q}\end{bmatrix} = \begin{bmatrix} Z_\alpha / u_0 & 1 \\ M_\alpha & M_q \end{bmatrix} \begin{bmatrix}\alpha \\ q\end{bmatrix} + \begin{bmatrix} Z_\alpha / u_0 \\ M_\delta \end{bmatrix} \delta e \tag{B.9}$$

$$f_z = Z_\alpha \alpha + Z_q q \tag{B.10}$$

The transfer function from δe to q is given by

$$G_{q,\delta e}(s) = \frac{M_\delta s - \left(Z_\alpha M_\delta - M_\alpha Z_\delta\right)/u_0}{s^2 - \left(Z_\alpha / u_0 + M_q\right) s + \frac{Z_\alpha M_q}{u_0} - M_\alpha} \tag{B.11}$$

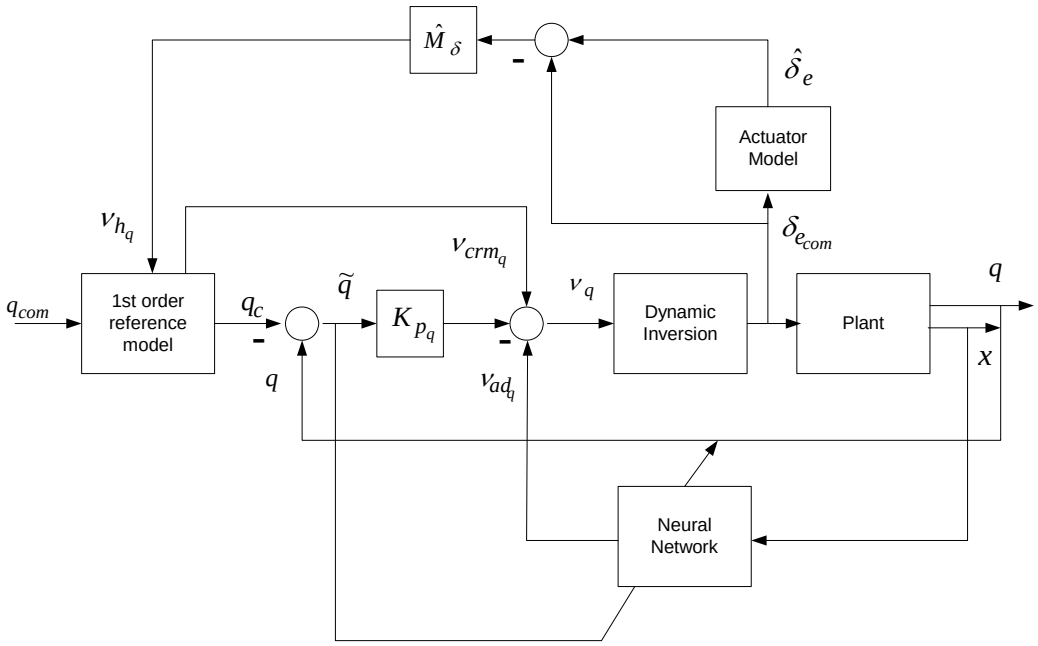

Figure 68. Block diagram representation of Adaptive pitch-rate control system

The transfer function from δe to f_z is given by

$$G_{f_z,\delta e}(s) = \frac{Z_\delta s^2 - Z_\delta M_q s + (Z_\alpha M_\delta - M_\alpha Z_\delta)}{s^2 - \left(Z_\alpha / u_0 + M_q\right)s + \frac{Z_\alpha M_q}{u_0} - M_\alpha} \tag{B.12}$$

Making the assumption $|Z_\delta| << |Z_\alpha M_\delta|$, the transfer function from q to f_z is given by

$$G_{f_z,q}(s) = \frac{G_{f_z,\delta e}(s)}{G_{q,\delta e}(s)} = \frac{Z_\alpha}{s - Z_\alpha / u_0} \tag{B.13}$$

Assuming perfect inner-loop tracking, that is, $q_c = q$, allows us to represent the transfer function from q_{com} to q as

$$\frac{q(s)}{q_{com}(s)} = \frac{q_c(s)}{q_{com}(s)} = \frac{1}{\tau_q s + 1} \tag{B.14}$$

The block diagram of Figure 67 can be idealized to the block diagram of Figure 69. The analysis of the transfer function in Figure 69 gives the loop transfer function

$$G(s) = \frac{Z_\alpha \left(K_{p_z} s + K_{I_z} \right)}{s\left(\tau_q s + 1 \right)\left(s - Z_\alpha / u_0 \right)} \tag{B.15}$$

The choice $\frac{K_{I_z}}{K_{p_z}} = -\frac{Z_\alpha}{u_0}$ results in a pole-zero cancellation, which leads to the following closed-loop transfer function

$$\frac{f_z(s)}{f_{z_{cmd}}(s)} = \frac{K_{p_z} Z_\alpha / \tau_q}{s^2 + s/\tau_q + K_{p_z} Z_\alpha / \tau_q} \tag{B.16}$$

Note that since $Z_\alpha < 0$ and $\left| \frac{Z_\alpha}{u_0} \right| >> 1$, the pole-zero cancellation in (B.15) does not cause problems despite parametric uncertainty in Z_α. The PI controller gains can be obtained by choosing a desired natural frequency ω_n and damping ratio ζ for the closed-loop transfer function in (B.16):

$$\tau_q = \frac{1}{2\zeta\omega_n},\ K_{p_z} = \frac{\omega_n}{2\zeta Z_\alpha},\ K_{I_z} = -\frac{\omega_n}{2\zeta u_0} \tag{B.17}$$

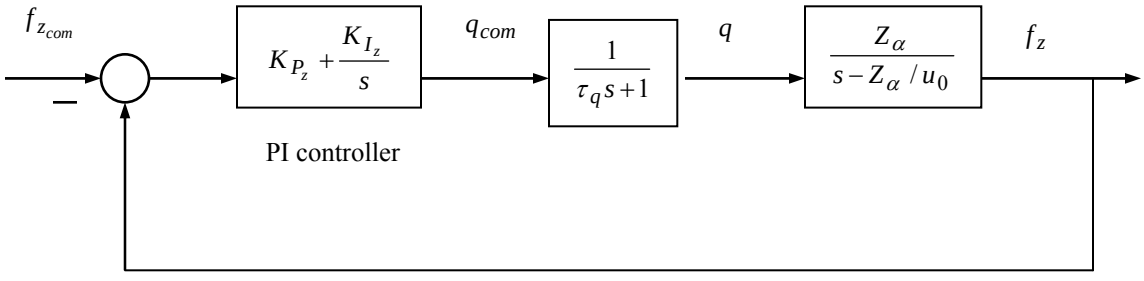

Figure 69. Idealized block diagram representation of Normal Acceleration Controller

B. Adaptive Lateral Acceleration $\left(f_y\right)$ Control

The approach to lateral acceleration control design is almost identical to that for the normal acceleration control. The difference from the normal acceleration controller lies in regulating a blended output variable $y_{lat} = \beta + C_r r$ in the inverting inner-loop controller instead of just the yaw-rate r. The reason lies in the fact that the transfer function from $\delta r(s)$ to $r(s)$ has a zero close to the origin, the effect of which is to produce a very slow mode when the dynamic inversion is inexact. By redefining the output to be controlled in the inverting inner-loop as y_{lat}, the zero of the associated transfer-function can be placed at a desirable location. The lateral acceleration command $f_{y_{cmd}} = 0$ for maintaining turn coordination. The output of the controller is the rudder deflection command δr_{com}. The reader is referred to [111] for further details.

C. Adaptive Bank Angle (Φ) Control

Compared to f_z and f_y control, adaptive bank angle control is straightforward. This is because the transfer function from the aileron δa to the bank angle Φ is minimum phase. The true bank angle dynamics can be given as

$$\ddot{\Phi} = A_\Phi x_{lat} + B_\Phi \delta a + \Delta_\Phi (x_{lat}, \delta a) \tag{B.18}$$

where $x_{lat} = \left[v, p, r, \Phi\right]^T$ represents the state vector for the lateral-directional dynamics, A_Φ and B_Φ are row vectors that come from the linear model obtained at the trim flight condition, and $\Delta_\Phi(x, \delta a)$ is the modeling error. Inversion-based control is designed as

$$\delta a_{com} = \frac{1}{B_\Phi}\left(\nu_\Phi - A_\Phi x_{lat}\right) \tag{B.19}$$

where the pseudo-control ν_Φ is given as

$$\nu_{\Phi} = \nu_{crm_{\Phi}} + K_{p_{\Phi}}\left(\Phi_c - \Phi\right) + K_{d_{\Phi}}\left(\dot{\Phi}_c - \dot{\Phi}\right) - \nu_{ad_{\Phi}} \tag{B.20}$$

where $\Phi_c, \dot{\Phi}_c$ and $\nu_{crm_{\Phi}}$ refer to the outputs of a second-order, linear reference model, $K_{p_{\Phi}} > 0,\ K_{d_{\Phi}} > 0$ are gains of a PD controller, and $\nu_{ad_{\Phi}}$ is the output of an adaptive SHL NN. The reference model is hedged to prevent the adaptive law from adapting to the nonlinear characteristics of the actuator:

$$\nu_{crm_{\Phi}} = \omega_{n_{\Phi}}^2 \Phi_{com} - \omega_{n_{\Phi}}^2 \Phi_c - 2\zeta_{\Phi}\omega_{n_{\Phi}}\dot{\Phi}_c \tag{B.21}$$

$$\begin{aligned} \nu_{h_{\Phi}} &= \nu_{\Phi} - \hat{\nu}_{\Phi} = \left[A_{\Phi}x_{lat} + B_{\Phi}\delta a_{com}\right] - \left[A_{\Phi}x_{lat} + B_{\Phi}\hat{\delta}\hat{a}\right] \\ &= B_{\Phi}\left(\delta a_{com} - \hat{\delta}\hat{a}\right) \end{aligned} \tag{B.22}$$

$$\ddot{\Phi}_c = \nu_{crm_{\Phi}} - \nu_{h_{\Phi}} \tag{B.23}$$

where $\hat{\delta}\hat{a}$ is an estimate of the aileron deflection.

D. SHL NN Output and Update Law

A SHL NN is the adaptive element in each of the control designs for f_z, f_y and Φ control. The output of each NN is given by

$$\nu_{ad,i} = \hat{W}_i^T \sigma\left(\hat{V}_i^T \bar{x}\right) \tag{B.24}$$

and the update law is given by

$$\begin{aligned} \dot{\hat{V}}_i &= -\left[\bar{x}\varsigma_i \hat{W}_i^T \hat{\sigma}' + \lambda_i \left\|\varsigma_i\right\| \hat{V}_i\right]\Gamma_{V_i} \\ \dot{\hat{W}}_i &= -\left[\left(\hat{\sigma} - \hat{\sigma}'\hat{V}_i^T \bar{x}\right)\varsigma_i + \lambda_i \left\|\varsigma_i\right\| \hat{W}\right]\Gamma_{W_i} \end{aligned} \tag{B.25}$$

where $i = 1,2,3$ refers to the controller for f_z, f_y and Φ, ς_i is the training signal to each NN, and $\Gamma_{V_i} > 0$, $\Gamma_{W_i} > 0$ and $\lambda_i > 0$ are the NN design parameters. Further details are referred to [122].

APPENDIX C

PROOF OF THEOREM 6.1

Proof: Differentiating the Lyapunov candidate function $V_o(\zeta_o)$ defined in (6.22):

$$\dot{V}_o(\zeta_o) = \dot{\tilde{x}}_1^T P_1^{-1}(t)\tilde{x}_1 + \tilde{x}_1^T P_1^{-1}(t)\dot{\tilde{x}}_1 + \tilde{x}_1^T \dot{P}_1^{-1}(t)\tilde{x}_1 + 2\sum_i^m \tilde{W}_{o,i}^T \Gamma_{o_i}^{-1} \dot{\tilde{W}}_{o,i} \tag{C.1}$$

Substituting Eqs. (6.15), (3.36) and (6.17) in Eq. (C.1)and simplifying

$$\begin{aligned}\dot{V}_o(\zeta_o) = &-\tilde{x}_1^T \tilde{Q}_1(t)\tilde{x}_1 + 2\tilde{x}_1^T \sum_i^m P_1^{-1}(t) b_i \tilde{W}_{o,i}^T \sigma_o(\bar{\mu}_o) + 2\tilde{x}_1^T \sum_i^m P_1^{-1}(t) b_i \varepsilon_{o,i}'(\bar{\mu}_o) \\ &+ 2\sum_i^m \tilde{W}_{o,i}^T \left(-\sigma_o(\bar{\mu}_o) C_{1,i}\tilde{x}_1 - Q_{fi}^T e_{na,1}\right) + 2\lambda_o \sum_i^m \tilde{W}_{o,i}^T W_{o,i} - 2\lambda_o \sum_i^m \tilde{W}_{o,i}^T \tilde{W}_{o,i}\end{aligned} \tag{C.2}$$

$\dot{V}_o$ in (C.2) can be upper-bounded using (6.18) and (6.6) as shown below:

$$\begin{aligned}\dot{V}_o \le &-\tilde{x}_1^T P_1^{-1}(t) Q_1 P_1^{-1}(t)\tilde{x}_1 + 2\tilde{x}_1^T \sum_i^m P_1^{-1}(t) b_i \tilde{W}_{o,i}^T \sigma_o(\bar{\mu}_o) + 2\sum_i^m \|\tilde{x}_1\| \left\|P_1^{-1}(t) b_i\right\| \varepsilon_o^* \\ &-2\tilde{x}_1^T \sum_i^m C_{1,i}^T \tilde{W}_{o,i}^T \sigma_o(\bar{\mu}_o) - 2\sum_i^m \tilde{W}_{o,i}^T Q_{fi}^T e_{na,1} + 2\lambda_o \sum_i^m \left\|\tilde{W}_{o,i}\right\| W_o^* - 2\lambda_o \sum_i^m \left\|\tilde{W}_{o,i}\right\|^2\end{aligned}$$

Combining terms and expanding the expression for $e_{na,1}$,

$$\begin{aligned}\dot{V}_o \le &-\tilde{x}_1^T P_1^{-1}(t) Q_1 P_1^{-1}(t)\tilde{x}_1 - 2\lambda_o \sum_i^m \left\|\tilde{W}_{o,i}\right\|^2 + 2\tilde{x}_1^T \sum_i^m \left[P_1^{-1}(t) b_i - C_{1,i}^T\right] \sigma_o^T(\bar{\mu}_o)\tilde{W}_{o,i} \\ &+ 2\sum_i^m \|\tilde{x}_1\| \left\|P_1^{-1}(t) b_i\right\| \varepsilon_o^* - 2\underbrace{\sum_i^m \tilde{W}_{o,i}^T Q_{fi}^T \left(\sum_k^m Q_{fk}\tilde{W}_{o,k}\right)}_{\ge 0} \\ &- 2\sum_i^m \tilde{W}_{o,i}^T Q_{fi}^T T\left(\tilde{x}_{na,1}(t_0), \varepsilon_{f1}', \varepsilon_{f2}', \cdots, \varepsilon_{fm}'\right) + 2\lambda_o \sum_i^m \left\|\tilde{W}_{o,i}\right\| W_o^*\end{aligned} \tag{C.3}$$

Using the fact that $\left\|\sigma_o(\bar{\mu}_o)\right\| \le \sqrt{N_o}$, applying Eq. (6.28) and completing the squares on the last term in (C.3), we have,

$$\begin{aligned}\dot{V}_o \le & -\frac{\lambda_{\min}\left(Q_1\right)}{\rho_2^2}\left\|\tilde{\boldsymbol{x}}_1\right\|^2 - 2\lambda_o\sum_i^m\left\|\tilde{\boldsymbol{W}}_{o,i}\right\|^2 + 2\sum_i^m m_{2_i}\left\|\tilde{\boldsymbol{x}}_1\right\|\left\|\tilde{\boldsymbol{W}}_{o,i}\right\| \\ & + 2\sum_i^m m_{1_i}\left\|\tilde{\boldsymbol{x}}_1\right\| + 2\sum_i^m m_{4_i}\left\|\tilde{\boldsymbol{W}}_{o,i}\right\| + \lambda_o\sum_{\boldsymbol{i}}^{\boldsymbol{m}}\left\|\tilde{\boldsymbol{W}}_{o,i}\right\|^2 + \lambda_o\sum_{\boldsymbol{i}}^{\boldsymbol{m}} W_o^{*2}\end{aligned} \tag{C.4}$$

Completing the squares in the above equation, we have

$$\dot{V}_o \le -\left\|\tilde{\boldsymbol{x}}_1\right\|^2\left(\frac{\lambda_{\min}\left(Q_1\right)}{\rho_2^2} - 2m\right) - \sum_i^m\left\|\tilde{\boldsymbol{W}}_{o,i}\right\|^2\left(\lambda_o - m_{2_i}^2 - 1\right) + \sum_i^m\left[m_{1_i}^2 + m_{4_i}^2 + \lambda_o W_o^{*2}\right] \tag{C.5}$$

Thus either of the following conditions:

$$\left\|\tilde{\boldsymbol{x}}_1\right\| > \sqrt{\frac{\sum_i^m\left\{m_{1_i}^2 + m_{4_i}^2 + \lambda_o W_o^{*2}\right\}}{\frac{\lambda_{\min}\left(Q_1\right)}{\rho_2^2} - 2m}} \tag{C.6}$$

$$\left\|\tilde{\boldsymbol{W}}_{o,i}\right\| > \sqrt{\frac{\sum_i^m\left\{m_{1_i}^2 + m_{4_i}^2 + \lambda_o W_o^{*2}\right\}}{\lambda_o - \left(m_{2_i}^2 + 2\right)}}, \quad i = 1, 2, \cdots, m \tag{C.7}$$

will guarantee that $\dot{V}_o\left(\boldsymbol{\zeta}_o\right) < 0$ outside the compact set

$$B_\gamma = \left\{\boldsymbol{\zeta}_o \in B_M \mid \left\|\boldsymbol{\zeta}_o\right\| \le \gamma\right\} \tag{C.8}$$

Note that $B_\gamma \subset B_M$ from (6.26). Let β be the maximum value of the Lyapunov function V_o on the boundary of B_γ

$$\beta \triangleq \max_{\left\|\boldsymbol{\zeta}_o\right\| = \gamma} V_o\left(\boldsymbol{\zeta}_o\right) \tag{C.9}$$

Introduce the set

$$\Omega_\beta = \left\{\boldsymbol{\zeta}_o \mid V_o\left(\boldsymbol{\zeta}_o\right) \le \beta\right\} \tag{C.10}$$

Eq. (6.26) ensures that $\Omega_\beta \subset \Omega_\alpha$ and thus ultimate boundedness of $\boldsymbol{\zeta}_o$ with ultimate bound equal to $\kappa_1^{-1}\left(\kappa_2\left(\gamma\right)\right)$.

□

APPENDIX D

PROOF OF THEOREM 6.2

Equation Chapter 4 Section 1

Proof: Differentiating the Lyapunov candidate function $V(\boldsymbol{\zeta})$ defined in (6.53):

$$\dot{V}(\boldsymbol{\zeta}) = \dot{V}_o(\boldsymbol{\zeta}_o) + \dot{V}_c(\boldsymbol{\zeta}_c) \tag{D.1}$$

where $\dot{V}_o(\boldsymbol{\zeta}_o)$ is given by (C.5). Considering only $\dot{V}_c(\boldsymbol{\zeta}_c)$, we have,

$$\dot{V}_c(\boldsymbol{\zeta}_c) = \dot{\boldsymbol{E}}_i^T P_{E,i} \boldsymbol{E}_i + \boldsymbol{E}_i^T P_{E,i} \dot{\boldsymbol{E}}_i + \dot{\tilde{\boldsymbol{E}}}_i^T \tilde{P}_{E,i} \tilde{\boldsymbol{E}}_i + \tilde{\boldsymbol{E}}_i^T \tilde{P}_{E,i} \dot{\tilde{\boldsymbol{E}}}_i + 2\tilde{\boldsymbol{W}}_{c,i}^T \Gamma_{c_i}^{-1} \dot{\tilde{\boldsymbol{W}}}_{c,i} \tag{D.2}$$

Substituting (6.49) into (D.2), we have,

$$\begin{aligned} \dot{V}_c(\boldsymbol{\zeta}_c) = & -\boldsymbol{E}_i^T Q_{E,i} \boldsymbol{E}_i - \tilde{\boldsymbol{E}}_i^T \tilde{Q}_{E,i} \tilde{\boldsymbol{E}}_i - 2\boldsymbol{E}_i^T P_{E,i} \bar{B}_{E,i} \tilde{\boldsymbol{W}}_{c,i}^T \boldsymbol{\sigma}_c(\bar{\boldsymbol{\mu}}_c) - 2\tilde{\boldsymbol{E}}_i^T \tilde{P}_{E,i} \bar{B}_{E,i} \tilde{\boldsymbol{W}}_{c,i}^T \boldsymbol{\sigma}_c(\bar{\boldsymbol{\mu}}_c) \\ & - 2\left(\boldsymbol{E}_i^T P_{E,i} + \tilde{\boldsymbol{E}}_i^T \tilde{P}_{E,i}\right) \bar{B}_{E,i} \varepsilon_c(\bar{\boldsymbol{\mu}}_c) - 2\tilde{\boldsymbol{W}}_{c,i}^T \Gamma_{c_i}^{-1} \dot{\tilde{\boldsymbol{W}}}_{c,i} \end{aligned} \tag{D.3}$$

Dropping the arguments $\bar{\boldsymbol{\mu}}_c$, substituting $\boldsymbol{E}_i = \hat{\boldsymbol{E}}_i + \tilde{\boldsymbol{E}}_i$ and rearranging terms, we have,

$$\begin{aligned} \dot{V}_c(\boldsymbol{\zeta}_c) = & -\boldsymbol{E}_i^T Q_{E,i} \boldsymbol{E}_i - \dot{\tilde{\boldsymbol{E}}}_i^T \tilde{Q}_{E,i} \tilde{\boldsymbol{E}}_i - 2\tilde{\boldsymbol{W}}_{c,i}^T \left(\boldsymbol{\sigma}_c \hat{\boldsymbol{E}}_i^T P_{E,i} \bar{B}_{E,i} + \Gamma_{c_i}^{-1} \dot{\tilde{\boldsymbol{W}}}_{c,i}\right) \\ & - 2\tilde{\boldsymbol{E}}_i^T \left(P_{E,i} \bar{B}_{E,i} + \tilde{P}_{E,i} \bar{B}_{E,i}\right) \tilde{\boldsymbol{W}}_{c,i}^T \boldsymbol{\sigma}_c - 2\boldsymbol{E}_i^T P_{E,i} \bar{B}_{E,i} \varepsilon_c - 2\tilde{\boldsymbol{E}}_i^T \tilde{P}_{E,i} \bar{B}_{E,i} \varepsilon_c \end{aligned} \tag{D.4}$$

Substituting for the controller adaptive law in (6.51) and upper bounding by using the identity $\|\boldsymbol{\sigma}_c\| \le \sqrt{N_c}$ and (6.59), we have,

$$\begin{aligned} \dot{V}_c(\boldsymbol{\zeta}_c) \le & -\lambda_{\min}\left(Q_{E,i}\right)\|\boldsymbol{E}_i\|^2 - \lambda_{\min}\left(\tilde{Q}_{E,i}\right)\|\tilde{\boldsymbol{E}}_i\|^2 - 2\lambda_{c,i}\|\tilde{\boldsymbol{W}}_{c,i}\|^2 + 2\lambda_{c,i}\tilde{\boldsymbol{W}}_{c,i}^T \boldsymbol{W}_{c,i} \\ & + 2l_4\|\tilde{\boldsymbol{E}}_i\|\|\tilde{\boldsymbol{W}}_{c,i}\| + 2l_2\|\boldsymbol{E}_i\| + 2l_1\|\tilde{\boldsymbol{E}}_i\| \end{aligned} \tag{D.5}$$

Completing the squares in the above equation and using $\|\boldsymbol{W}_{c,i}\| \le W_c^*$, we have,

$$\begin{aligned} \dot{V}_c(\boldsymbol{\zeta}_c) \le & -\|\boldsymbol{E}_i\|^2\left(\lambda_{\min}\left(Q_{E,i}\right) - 1\right) - \|\tilde{\boldsymbol{E}}_i\|^2\left(\lambda_{\min}\left(\tilde{Q}_{E,i}\right) - 2\right) - \|\tilde{\boldsymbol{W}}_{c,i}\|^2\left(\lambda_{c,i} - l_4^2\right) \\ & + l_1^2 + l_2^2 + \lambda_{c,i} W_c^{*2} \end{aligned} \tag{D.6}$$

Combining Eqs. (C.5) and (D.6) into (D.1), we have,

$$\begin{aligned}\dot{V}(\boldsymbol{\zeta}) \le & -\|\tilde{\boldsymbol{x}}_1\|^2\left(\frac{\lambda_{\min}(Q_1)}{\rho_2^2}-2m\right)-\sum_i^m\left\|\tilde{\boldsymbol{W}}_{o,i}\right\|^2\left(\lambda_o-m_{2_i}^2-1\right)\\ & -\|\boldsymbol{E}_i\|^2\left(\lambda_{\min}\left(Q_{E,i}\right)-1\right)-\left\|\tilde{\boldsymbol{E}}_i\right\|^2\left(\lambda_{\min}\left(\tilde{Q}_{E,i}\right)-2\right)-\left\|\tilde{\boldsymbol{W}}_{c,i}\right\|^2\left(\lambda_{c,i}-l_4^2\right)\\ & +\sum_i^m\left[m_{1_i}^2+m_{4_i}^2+\lambda_o W_o^{*^2}\right]+l_1^2+l_2^2+\lambda_{c,i}W_c^{*^2}\end{aligned} \tag{D.7}$$

Thus either of the following conditions:

$$\|\tilde{\boldsymbol{x}}_1\| > \sqrt{\frac{\sum_i^m\left\{m_{1_i}^2+m_{4_i}^2+\lambda_o W_o^{*^2}\right\}+l_1^2+l_2^2+\lambda_{c,i}W_c^{*^2}}{\frac{\lambda_{\min}(Q_1)}{\rho_2^2}-2m}} \tag{D.8}$$

$$\left\|\tilde{\boldsymbol{W}}_{o,i}\right\| > \sqrt{\frac{\sum_i^m\left\{m_{1_i}^2+m_{4_i}^2+\lambda_o W_o^{*^2}\right\}+l_1^2+l_2^2+\lambda_{c,i}W_c^{*^2}}{\lambda_o-\left(m_{2_i}^2+2\right)}},\quad i=1,2,\cdots,m \tag{D.9}$$

$$\|\boldsymbol{E}_i\| > \sqrt{\frac{\sum_i^m\left\{m_{1_i}^2+m_{4_i}^2+\lambda_o W_o^{*^2}\right\}+l_1^2+l_2^2+\lambda_{c,i}W_c^{*^2}}{\lambda_{\min}\left(Q_{E,i}\right)-1}} \tag{D.10}$$

$$\left\|\tilde{\boldsymbol{E}}_i\right\| > \sqrt{\frac{\sum_i^m\left\{m_{1_i}^2+m_{4_i}^2+\lambda_o W_o^{*^2}\right\}+l_1^2+l_2^2+\lambda_{c,i}W_c^{*^2}}{\lambda_{\min}\left(\tilde{Q}_{E,i}\right)-2}} \tag{D.11}$$

$$\left\|\tilde{\boldsymbol{W}}_{c,i}\right\| > \sqrt{\frac{\sum_i^m\left\{m_{1_i}^2+m_{4_i}^2+\lambda_o W_o^{*^2}\right\}+l_1^2+l_2^2+\lambda_{c,i}W_c^{*^2}}{\lambda_{c,i}-l_4^2}} \tag{D.12}$$

will guarantee that $\dot{V}(\boldsymbol{\zeta}) < 0$ outside the compact set

$$B_{\gamma_I} = \left\{\boldsymbol{\zeta} \in B_{M_I} \mid \|\boldsymbol{\zeta}\| \le \gamma_I\right\} \tag{D.13}$$

Note that $B_{\gamma_I} \subset B_{M_I}$ from (6.57). Let β_I be the maximum value of the Lyapunov function $V(\zeta)$ on the boundary of B_{γ_I}

$$\beta_I \triangleq \max_{\|\zeta\|=\gamma_I} V(\zeta) \tag{D.14}$$

Introduce the set

$$\Omega_{\beta_I} = \{\zeta \mid V(\zeta) \leq \beta_I\} \tag{D.15}$$

Eq. (6.57) ensures that $\Omega_{\beta_I} \subset \Omega_{\alpha_I}$ and thus ultimate boundedness of ζ with ultimate bound equal to $\kappa_3^{-1}(\kappa_4(\gamma_I))$.

□

REFERENCES

[1] W. Blake and D. Multhopp, "Design, performance and modeling considerations for close formation flight," *AIAA Atmospheric Flight Mechanics Conference and Exhibit*, Boston, MA, August 1998.

[2] M. Pachter, J. D'Azzo, and A. Proud, "Tight Formation Flight Control," *Journal of Guidance, Control and Dynamics,* Vol. 24, No. 2, pp. 246-254, 2001.

[3] F. Giulietti, L. Pollini, and M. Innocenti, "Autonomous Formation Flight," *IEEE Control Systems Magazine*, Vol. 20, No. 6, pp. 34-44, December 2000.

[4] A. Proud, M. Pachter, and J. D'Azzo, "Close Formation Control," *AIAA Guidance, Navigation and Control Conference*, Portland, OR, August 1999.

[5] J. D. Wolfe, D. F. Chichka and J. L. Speyer, "Decentralized Controllers for Unmanned Aerial Vehicle Formation Flight," San Diego, CA, July 1996.

[6] C. J. Schumacher, and R. Kumar, "Adaptive Control of UAVs in Close-Coupled Formation Flight," *Proc. of the American Control Conference*, Chicago, IL, June 2000.

[7] C. J. Schumacher, and S. Singh, "Nonlinear Control of Multiple UAVs in Close-Coupled Formation Flight," *AIAA Guidance, Navigation and Control Conference*, Denver, CO, August 2000.

[8] K. Misovec, "Applied Adaptive Techniques for F/A-18 Formation Flight," *AIAA Guidance, Navigation and Control Conference*, Monterrey, CA, August 2002.

[9] E. Lavretsky, "F/A-18 Autonomous Formation Flight Control System Design," *AIAA Guidance, Navigation and Control Conference*, Monterrey, CA, August 2002.

[10] E. Lavretsky, N. Hovakimyan, A. J. Calise and V. Stepanyan, "Adaptive Vortex Seeking Formation Flight Control," *AIAA Guidance, Navigation and Control Conference*, Austin, TX, August 2003.

[11] M. R. Anderson and A. C. Robbins, "Formation Flight as a Cooperative Game," *AIAA Guidance, Navigation and Control Conference*, Reston, VA, August 1998.

[12] R. Sattigeri, A. J. Calise and J. H. Evers, "An Adaptive Approach to Vision-based Formation Control," *AIAA Guidance, Navigation and Control Conference*, Austin, TX, August 2003.

[13] R. Sattigeri, A. J. Calise and J. H. Evers, "An Adaptive Vision-based Approach to Decentralized Formation Control," *AIAA Guidance, Navigation and Control Conference*, Providence, RI, August 2004.

[14] M-J Tahk, C-S Park and C-K Ryoo, "Line-of-Sight Guidance Laws for Formation Flight," *Journal of Guidance, Control and Dynamics,* Vol. 28, No. 4, pp. 708-716, 2005.

[15] A. V. Das, R. Fierro, V. Kumar, J. P. Ostrowski, J. Spletzer and C. J. Taylor, "A Vision-based Formation Control Framework," *IEEE Transactions on Robotics and Automation*, Vol. 18, No. 5, October 2002.

[16] H. Yamaguchi and T. Arai, "Distributed and Autonomous Control Method for generating Shape of Multiple Mobile Robot Group," *Proc. of the IEEE International Conference on Intelligent Robots and Systems*, Vol. 2, pp. 800-807, 1994.

[17] T. Balch and R. Arkin, "Behavior-based Formation Control for multi-robot teams," *IEEE Transactions on Robotics and Automation*, Vol. 14, December 1998.

[18] J. P. Desai, J. P. Ostrowski and V. Kumar, "Modeling and Control of Formations of Nonholonomic Mobile Robots," *IEEE Transactions on Robotics and Automation*, Vol. 17, December 2001.

[19] J. P. Desai, V. Kumar and J. P. Ostrowski, "Control of Changes in Formation for a team of Mobile Robots," *Proc. of the IEEE International Conference on Robotics and Automation*, pp. 1556-1561, 1999.

[20] J. Lawton, B. Young and R. Beard, "A Decentralized Approach to Elementary Formation Maneuvers," *Proc. of the IEEE International Conference on Robotics and Automation*, pp. 2728-2733, 2000.

[21] L. Pollini, F. Giulietti and M. Innocenti, "Robustness to Communication Failures within Formation Flight," *Proc. of the American Control Conference*, Anchorage, AK, May 2002.

[22] R. K. Mehra, J. D. Boskovic and S-M Li, "Autonomous Formation Flying of multiple UCAVs under Communication Failure," *IEEE Position Location and Navigation Symposium*, pp. 371-378, March 2000.

[23] C. Ashokkumar and D. Jeffcoat, "Cooperative Systems under Communication Delay," *AIAA Guidance, Navigation and Control Conference*, Austin, TX, August 2003.

[24] C. Sinopoli, M. Micheli, G. Donato and T. J. Koo, "Vision based Navigation for an Unmanned Aerial Vehicle," *Proc. of the IEEE International Conference on Robotics and Automation*, pp. 1757-1765, May 2001.

[25] S. Saripalli, J. F. Montgomery and G. S. Sukhatme, "Vision-based autonomous landing of an Unmanned Aerial Vehicle," *Proc. of the IEEE International Conference on Robotics and Automation*, pp. 2799-2804, May 2002.

[26] A. Proctor and E. Johnson, "Vision-only Approach and Landing," *AIAA Guidance, Navigation and Control Conference*, San Francisco, CA, August 2005.

[27] A. Proctor and E. Johnson, "Vision-only Flight Control Methods and Test Control Results," *AIAA Guidance, Navigation and Control Conference*, Providence, RI, August 2004.

[28] A. D. Wu, E. Johnson and A. Proctor, "Vision-aided Inertial Navigation for Flight Control," *AIAA Guidance, Navigation and Control Conference*, San Francisco, CA, August 2005.

[29] A. S. Watkins, R. Prazenica, A. Kurdila and G. Wiens, "RHC for Vision-based Navigation of a WMR in an Urban Environment," *AIAA Guidance, Navigation and Control Conference*, San Francisco, CA, August 2005.

[30] Y. Watanabe, E. Johnson and A. J. Calise, "Vision-based Approach to Obstacle Avoidance," *AIAA Guidance, Navigation and Control Conference*, San Francisco, CA, August 2005.

[31] N. P. Papanikolopoulos, P. K. Khosla and T. Kanade, "Visual Tracking of a Moving Target by a Camera Mounted on a Robot: A Combination of Control and Vision," *IEEE Transactions on Robotics and Automation*, Vol. 9, February 1993.

[32] S. Hutchinson, G. D. Hager, and P. I. Corke, "A Tutorial on Visual Servo Control," *IEEE Transactions on Robotics and Automation*, Vol. 12, October 1996.

[33] L. Pollini, R. Mati, M. Innocenti, G. Campa and M. Napolitano, "A Synthetic Environment for the Simulation of Vision-based Formation Flight," *AIAA Modeling and Simulation Technologies Conference and Exhibit*, Austin, TX, August 2003.

[34] L. Pollini, R. Mati and M. Innocenti, "Experimental Evaluation of Vision Algorithms for Formation Flight and Aerial Refueling," *AIAA Modeling and Simulation Technologies Conference and Exhibit*, Providence, RI, August 2004.

[35] J. Valasek, J. Kimmett, D. Hughes, K. Gunnam and J. L. Junkins, "Vision based Sensor and Navigation System for Autonomous Aerial Refueling," *AIAA's 1st Technical Conference and Workshop on Unmanned Aerospace Vehicles,* Portsmouth, VA, May 2002.

[36] M. D. Tandale, R. Bowers and J. Valasek, "Robust Trajectory Tracking Controller for Vision based Probe and Drogue Autonomous Aerial Refueling," *AIAA Guidance, Navigation and Control Conference*, San Francisco, CA, August 2005.

[37] J. Ha, C. Alvino, G. Pryor, M. Niethammer, E. Johnson and A. Tannenbaum, "Active Contours and Optical Flow for Automatic Tracking of Flying Vehicles," *Proc. of the American Control Conference*, Boston, MA, June-July 2004.

[38] A. Betser, P. Vela and A. Tannenbaum, "Automatic Tracking of Flying Vehicles using Geodesic Snakes and Kalman Filtering," *IEEE Conference on Decision and Control*, Atlantis Island, Bahamas, December 2004.

[39] AFOSR MURI # F49620-03-1-0401: Active-Vision Control Systems for Complex Adversarial 3D Environments, 1st Year Summary Report, 2004. http://controls.ae.gatech.edu/avcs

[40] Y. Bar-Shalom, X. R. Li, and T. Kirubarajan, *Estimation with Applications to Tracking and Navigation: Theory, Algorithms and Software*, Wiley-Interscience, New York, 2001.

[41] R.K Mehra, "On the Identification of Variances and Adaptive Kalman Filtering", *IEEE Transactions on Automatic Control*, AC-15, pp. 175-184, April 1970.

[42] A. Moghaddamjoo and R.L. Kirlin, "Robust Adaptive Kalman Filtering with Unknown Inputs", *IEEE Transactions on Acoustics, Speech and Signal Processing*, Vol. 37, No. 8, pp. 1166-1175, August 1989.

[43] M.E. Hough, "Improved Performance of Recursive Tracking Filters using Batch Initialization and Process Noise Adaptation", *AIAA Journal of Guidance, Control and Dynamics*, Vol. 22, No. 5, pp 675-681, 1999.

[44] R.A. Singer, "Estimating Optimal Tracking Filter Performance for Manned Maneuvering Targets", *IEEE Transactions on Aerospace and Electronic Systems*, AES-6, pp. 473-483, July 1970.

[45] Y. Bar-Shalom and K. Birmiwal, "Variable Dimension Filter for Maneuvering Target Tracking", *IEEE Transactions on Aerospace and Electronic Systems*, AES-18, pp. 621-629, 1982.

[46] H.A.P. Blom and Y. Bar-Shalom, "The Interacting Multiple-Model Algorithm for Systems with Markovian Switching Coefficients", *IEEE Transactions on Automatic Control*, AC-33, pp. 780-783, August 1988.

[47] J.A. Roecker and C.D. McGillem, "Target Tracking in Maneuver Centered Coordinates," *IEEE Transactions on Aerospace and Electronic Systems*, AES-25, pp. 836-843, November 1989.

[48] R.A. Best and J.P. Norton, "A New Model and Efficient Tracker for a Target with Curvilinear Motion," *IEEE Transactions on Aerospace and Electronic Systems*, AES-33, pp. 1030-1037, July 1997.

[49] M. Tahk and J.L. Speyer, "Target Tracking subject to Kinematic Constraints", *IEEE Transactions on Automatic Control*, AC-35, pp. 324-326, March 1990.

[50] X.R. Li and V.P. Jilkov, "Survey of Manuvering Target Tracking, Part I: Dynamic Models", *IEEE Transactions on Aerospace and Electronic Systems*, AES-39, pp. 1333 -1364, October 2003.

[51] Y.T. Chan, A.G.C. Hu and J.B. Plant, "A Kalman Filter based Tracking Scheme with Input Estimation", *IEEE Transactions on Aerospace and Electronic Systems*, AES-15, pp. 237-244, March 1979.

[52] P.L. Bogler, "Tracking a Maneuvering Target using Input Estimation", *IEEE Transactions on Aerospace and Electronic Systems*, AES-23, pp. 298-310, May 1987.

[53] H. Lee and M-J Tahk, "Generalized Input Estimation Technique for Tracking Maneuvering Targets", *IEEE Transactions on Aerospace and Electronic Systems*, AES-35, pp. 1388-1402, October 1999.

[54] X.R. Li and V.P. Jilkov, "Survey of Manuvering Target Tracking, Part IV: Decision-based Methods", *Proceedings of the SPIE Conference on Signal and Data Processing of Small Targets,* Paper 4728-60, Orlando, FL, April 2002.

[55] K. Zhou, X. Wang, M. Tomizuka, W-B Zhang, and C-Y Chan, "A New Maneuvering Target Tracking Algorithm with Input Estimation", *American Control Conference*, pp. 166-171, May 2002.

[56] A.T. Alouani, P. Xia, T.R. Rice, and W.D. Blair, "Two-Stage Kalman Estimator for Tracking Maneuvering Targets", *IEEE International Conference on Systems, Man and Cybernetics*, pp. 761-766, October 1991.

[57] K. S. Narendra and K. Parthasarathy, "Identification and Control of Dynamical Systems using Neural Networks," *IEEE Transactions on Neural Networks,* Vol. 1, pp. 4-27, 1990.

[58] Y. Kim, F.L. Lewis and C. Abdallah, "A Dynamic Recurrent Neural Network based Adaptive Observer for a Class of Nonlinear Systems," *Automatica*, 33 (8), pp. 1539-1543, 1998.

[59] J. Y. Choi and J. A. Farrell, "Observer-based Backstepping Control using On-line Approximation", *American Control Conference,* pp. 3646-3650, June 2000.

[60] N. Hovakimyan, A. J. Calise and V. Madyastha, "An Adaptive Observer Design Methodology for Bounded Nonlinear Processes," *IEEE Conference on Decision and Control*, Las Vegas, NV, December 2002.

[61] W. A. Fisher and H. E. Rauch, "Augmentation of an Extended Kalman Filter with a Neural Network," *IEEE International Conference on Neural Networks*, Vol. 2, pp. 1191-1196, June-July 1994.

[62] S. C. Stubberud, R. N. Lobbia and M. Owen, "An Adaptive Extended Kalman Filter using Artificial Neural Networks," *IEEE Conference on Decision and Control*, New Orleans, LA, December 1995.

[63] V.K. Madyastha and A.J. Calise, "An Adaptive Filtering Approach to Target Tracking", *American Control Conference,* pp. 1269-1274, June 2005.

[64] Venkatesh Madyastha, *Adaptive Estimation for Control of Uncertain Nonlinear Systems with Applications to Target Tracking*, PhD Thesis, School of Aerospace Engineering, Georgia Institute of Technology, December 2005.

[65] R. Sattigeri and A.J. Calise, "Neural Network Augmented Kalman Filtering in the Presence of Unknown System Inputs," *AIAA Guidance, Navigation, and Control Conference*, Keystone, CO, August 2006.

[66] J-J E. Slotine and W. Li, *Applied Nonlinear Control*, Prentice Hall Inc., 1991.

[67] M.A. Duarte and K.S. Narendra, "Combined Direct and Indirect Approach to Adaptive Control", *IEEE Transactions on Automatic Control,* AC-34, pp. 1071-1075, October 1989.

[68] K. Volyanskyy, A.J. Calise and B-J Yang, "A Novel Q-Modification Term for Adaptive Control", *American Control Conference*, pp. 4072-4076, June 2006.

[69] V. Stepanyan and N. Hovakimyan, "Robust Adaptive Observer Design for Uncertain Systems with Bounded Disturbances," *IEEE Conference on Decision and Control*, pp 7750-7755, December 2005.

[70] R. Sattigeri, A. J. Calise, B.S. Kim, K. Volyanskyy and N. Kim, "6 DOF Nonlinear Simulation of Vision-based Formation Flight," *AIAA Guidance, Navigation, and Control Conference*, San Francisco, CA, August 2005.

[71] P. Zarchan, *Tactical and Strategic Missile Guidance*, American Institute of Aeronautics and Astronautics, Inc., Vol. 57, 2nd Edition, 1994.

[72] B. Friedland, *Control System Design*, McGraw-Hill Inc., 1986.

[73] J. Shinar, Y. Oshman and V. Tutretsky, "On the need for Integrated Estimation/Guidance Design for Hit-to-Kill Accuracy," *American Control Conference*, pp. 402-407, Denver, CO, June 2003.

[74] I. G. Shaviv and Y. Oshman, "Guidance without Assuming Separation," *AIAA Guidance, Navigation, and Control Conference*, San Francisco, CA, August 2005.

[75] Y.H. Kim and F.L. Lewis, "Neural Network Output Feedback Control of Robot Manipulators," *IEEE Transactions on Robotics and Automation,* Vol. 15, No. 2, pp. 301-309, April 1999.

[76] J.Y. Choi and J.A. Farrell, "Adaptive Observer Backstepping Control using Neural Networks," *IEEE Transactions on Neural Networks,* Vol. 12, No. 5, pp. 1103-1112, September 2001.

[77] Y. Wang and T. Chai, "Output Feedback Control of Uncertain Nonlinear Systems using Adaptive Fuzzy Observer," *American Control Conference,* pp. 2613-2618, June 2005.

[78] N. Hovakimyan, F. Nardi, A.J. Calise and H. Lee, "Adaptive Output Feedback Control of a Class of Nonlinear Systems using Neural Networks," *International Journal of Control,* Vol. 74, No. 12, pp. 1161-1169, 2001.

[79] N. Hovakimyan, R. Rysdyk and A.J. Calise, "Dynamic Neural Networks for Output Feedback Control," *Proc of the Conference on Decision and Control,* pp. 1685-1690, December 1999.

[80] B-J. Yang, N. Hovakimyan and A.J. Calise, "Output Feedback Control of an Uncertain System using an Adaptive Observer," *Proc of the Conference on Decision and Control,* pp. 1705-1710, December 2003.

[81] P. K. Menon and E..J. Ohlmeyer, "Integrated Design of Agile Missile Guidance and Autopilot Systems," *IFAC – Control Engineering Practice*, Vol. 9, pp. 1095-1106, 2001.

[82] P. K. Menon, G. D. Sweriduk and E..J. Ohlmeyer, "Optimal Fixed-Interval Integrated Guidance-Control Laws for Hit-to-Kill Missiles," *AIAA Guidance, Navigation, and Control Conference*, Austin, TX, August 2003.

[83] I. Shkolnikov, Y. Shtessel, and D. Lianos, "Integrated Guidance-Control System of a Homing Interceptor - Sliding Mode Approach," *AIAA Guidance, Navigation, and Control Conference*, Montreal, Canada, August 2001.

[84] C.F. Lin, Q. Wang, J.H. Speyer, J.H. Evers, and J.H. Cloutier, "Integrated Estimation, Guidance and Control System Design using Game Theoretic Approach," *American Control Conference*, pp 3220-3224, 1992.

[85] N.F. Palumbo and T.D. Jackson, "Integrated Missile Guidance and Control: A State Dependent Riccati Differential Equation Approach," *IEEE International Conference on Control Applications*, Vol. 1, pp. 243-248, August 1999.

[86] M. Sharma and N. Richards, "Adaptive, Integrated Guidance and Control for Missile Interceptors," *AIAA Guidance, Navigation, and Control Conference*, Providence, RI, August 2004.

[87] M. Krstic, I. Kanellakopoulos and P. Kokotovic, *Nonlinear and Adaptive Control Design*, John Wiley & Sons, Inc., New York, 1995.

[88] E. Johnson and S. Kannan, "Adaptive Flight Control for an Autonomous Unmanned Helicopter," *AIAA Guidance, Navigation, and Control Conference*, Monterey, CA, August 2002.

[89] E. Johnson, and A.J. Calise, "Feedback Linearization with Neural Network Augmentation applied to X-33 Attitude Control," *AIAA-2000-4157 Guidance, Navigation and Control Conference*, Denver, CO, August 2000.

[90] B. S. Kim, A. J. Calise and R. Sattigeri, "Adaptive, Integrated Guidance and Control Design for Line-of-Sight based Formation Flight," *AIAA Guidance, Navigation, and Control Conference*, Keystone, CO, August 2006.

[91] E. Lavretsky, N. Hovakimyan and A.J. Calise, "Upper Bounds for Approximation of Continuous Time Dynamics using Delayed Outputs and Feedforward Neural Networks", *IEEE Transactions on Automatic Control,* AC-48, pp. 1606-1610, September 2003.

[92] K. Hornik, M. Stinchcombe and H. White, "Multi-Layer Feedforward Networks are Universal Approximators", *Neural Networks,* Vol. 2, pp. 359-366, 1989.

[93] R. G. Brown and P.Y.C. Hwang, *Introduction to Random Signals and Applied Kalman Filtering*, John Wiley and Sons Inc., 1992.

[94] K.S. Narendra and A.M. Annaswamy, "A New Adaptive Law for Robust Adaptation without Persistent Excitation", *IEEE Transactions on Automatic Control,* AC-32, pp. 134-145, 1987.

[95] A.J. Calise, N. Hovakimyan and M. Idan, "Adaptive Output Feedback Control of Nonlinear Systems Using Neural Networks," *Automatica*, 2001, vol. 37, no. 8, pp 1201-1211.

[96] N. Hovakimyan, A.J. Calise and N. Kim, "Adaptive Output Feedback Control of a Class of Multi-Input Multi-Output Systems using Neural Networks," *International Journal of Control*, October 2004, vol. 77, no. 15, pp 1318-1329.

[97] J. Brasch and J. Pearson, "Pole placement using dynamic compensators," *IEEE Transactions on Automatic Control*, pp. 34-43, AC- 15, 1970.

[98] A. Isidori, *Nonlinear Control Systems*, Springer-Verlag, Berlin, 1989.

[99] T. Y. Song and T. Y. Um, "Practical Guidance for Homing Missiles with Bearings-only Measurements," *IEEE Transactions on Aerospace and Electronic Systems*, AES-32, pp. 434-443, January 1996.

[100] G. E. Hassoun and C-C Lim, "Advanced Guidance Control System Design for Homing Missiles with Bearings-only Measurements," *Proc. of the IEEE International Conference on Industrial Technology*, pp. 250-254, December 1994.

[101] Y. Watanabe, E. Johnson and A. J. Calise, "Optimal 3-D Guidance from a 2-D Vision Sensor," *AIAA Guidance, Navigation, and Control Conference*, Providence, RI, August 2004.

[102] V. J. Aidala and S. E. Hammel, "Utilization of Modified Polar Coordinates for Bearings-only Tracking," *IEEE Transactions on Automatic Control*, AC-28, pp. 283-294, March 1983.

[103] B. Etkin, *Dynamics of Atmospheric Flight*, John Wiley & Sons, Inc., 1972.

[104] H.K. Khalil, *Nonlinear Systems*, 2nd Edition, Prentice Hall, Inc., 1996.

[105] N. Sadegh, "A nodal link perceptron network with applications to control of a non-holonomic system," *IEEE Transactions on Neural Networks*, Vol. 6, pp. 1516-1523, 1995.

[106] Y. Kim and F. Lewis, *High Level Feedback Control with Neural Networks*, World Scientific, N.J., 1998.

[107] G. Cybenko, "Approximations by superpositions of sigmoidal function," *Mathematics, Control, Signals, Systems*, Vol. 2, pp. 303-314, 1989.

[108] E.N. Johnson and D.P. Schrage, "System Integration and Operation of a Research Unmanned Aerial Vehicle," *AIAA Journal of Aerospace Computing, Communication, and Information*, 1 (1), pp. 5-18, January 2004.

[109] E.N. Johnson, A.J. Calise, Y. Watanabe, J. Ha and J.C. Neidhoefer, "Real-Time Vision-based Relative Navigation," *AIAA Guidance, Navigation, and Control Conference*, Keystone, CO, August 2006.

[110] A. Kutay, A.J. Calise and N. Hovakimyan, "Adaptive Output Feedback Control with Reduced Sensitivity to Sensor Noise," *Proc. of the American Control Conference*, Denver, CO, pp. 5141-5146, June 2003.

[111] A.J. Calise, M. Sharma and E. J. Corban, "Adaptive Autopilot Design for Guided Munitions," *Journal of Guidance, Control and Dynamics*, Vol. 23, No. 5, Sept-Oct 2000.

[112] J.D. Anderson, *Introduction to Flight*, McGraw-Hill, 4th Edition, 1999.

[113] C.W. Reynolds, "Flocks, Herds and Schools: A Distributed Behavioral Model," *Computer Graphics*, 21(4): pp. 71-87, 1987.

[114] E.N. Johnson and S-M Oh, "Adaptive Control using combined online and background learning neural network," *IEEE Conference on Decision and Control*, Paradise Island, Bahamas, pp. 5433-5438, December 2004.

[115] C. Cao and N. Hovakimyan, "Design and Analysis of a Novel L1 Adaptive Controller, Part I: Control Signal and Asymptotic Stability," *Proc. of the American Control Conference*, Minneapolis, MN, pp. 3397-3402, June 2006.

[116] Y. Zhao, J.A. Farrell, and M.M. Polycarpou, "Localized Adaptive Bounds for Online Approximation based Control," *Proc. of the American Control Conference*, Boston, MA, pp. 590-595, June-July 2004.

[117] E. Bonabeau, M. Dorigo and G. Theraulaz, *Swarm intelligence: from natural to artificial systems*, Oxford University Press, 1999.

[118] M. Mataric, *Interaction and Intelligent Behavior*, PhD thesis, MIT, EECS, 1994.

[119] P. Tabuada, G. Pappas, and P. Lima, "Feasible Formations of Multi-Agent Systems," *Proc. of the American Control Conference*, Arlington, VA, pp. 56-61, June 2001.

[120] R.W. Beard, J. Lawton, and F.Y. Hadeagh, "A Feedback Architecture for Formation Control," *Proc. of the American Control Conference*, Chicago, Il, pp. 4087-4091, June 2000.

[121] N.E. Leonard and E. Fiorelli, "Virtual Leaders, artificial potentials and coordinated control of groups," *IEEE Conference on Decision and Control*, FL, pp. 2968-2973, December 2001.

[122] M. Sharma, *A Neuro-Adaptive Autopilot Design for Guided Munitions*, PhD Thesis, Georgia Institute of Technology, School of Aerospace Engineering, April 2001.

[123] L. Wang, "Fuzzy systems are universal approximators," *IEEE Conference on Fuzzy Systems*, pp. 1163-1170, March 1992.

[124] J. Castro, "Fuzzy logic controllers are universal approximators," *IEEE Transactions on System, Man, and Cybernetics*, pp. 629-635, Vol. 25, No. 4, 1995.

[125] J.T. Spooner, M. Maggiore, R. Ordonez, and K.M. Passino, *Stable Adaptive Control and Estimation for Nonlinear Systems: Neural and Fuzzy Approximator Techniques*, John Wiley & Sons, Inc., 2002.

VITA

RAMACHANDRA J. SATTIGERI

Ramachandra Sattigeri was born on April 14, 1979, in Hubli, Karnataka, India. He secured admission into the Indian Institute of Technology (IIT), India's premier technology institute, in 1996. He was awarded the Bachelors of Technology (B.Tech) in Aerospace Engineering from IIT Mumbai in June 2000. He joined the graduate studies program in the School of Aerospace Engineering at Georgia Institute of Technology in August 2000. He was awarded the Masters of Science (MS) in Aerospace Engineering in December 2002 and began the PhD program in 2003. His research interests include adaptive control and estimation, neural network based control and estimation, flight guidance and control, target tracking and nonlinear filtering, and flight mechanics.